Modelling of an oil well cement paste from early age to hardened state : hydration kinetics and poromechanical behaviour

Marcos Samudio

HAL Id: tel-01781441
https://pastel.hal.science/tel-01781441

Submitted on 30 Apr 2018

UNIVERSITÉ PARIS-EST

École Doctorale SIE

Laboratoire Navier

Thèse

Présentée pour l'obtention du grade de
DOCTEUR DE L'UNIVERSITE PARIS-EST

par

Marcos E. Samudio Lezcano

Modélisation d'un ciment pétrolier depuis le jeune âge jusqu'à l'état durci : cinétique d'hydratation et comportement poromécanique

Spécialité : Géotechnique

Soutenue le 20 décembre 2017 devant un jury composé de :

Président	**Prof. Djimédo Kondo**	UPMC
Rapporteur	**Prof. Christian Hellmich**	TU Wien
Rapporteur	**Prof. Gilles Pijaudier-Cabot**	UPPA
Examinateur	**Prof. Patrick Dangla**	IFSTTAR
Examinateur	**Prof. Karen Scrivener**	EPFL
Directeur de thèse	**Prof. Jean Sulem**	ENPC
Co-encadrant de thèse	**Dr. Siavash Ghabezloo**	ENPC

Acknowledgements

This work would not have been possible without the generous collaboration of my supervisors Prof. Jean Sulem and Dr. Siavash Ghabezloo. Jean, I thank you for the many stimulating and enriching discussions. Siavash, I deeply appreciate the time spent together, at the lab and beyond. I have been privileged to have you both as guides throughout the journey.

I am grateful to the thesis examination committee, Prof. Djimédo Kondo, Prof. Christian Hellmich, Prof. Gilles Pijaudier-Cabot, Prof. Patrick Dangla and Prof. Karen Scrivener. I am particularly thankful to Patrick, for the hours spent at his office learning about mechanics and thermodynamics.

I am most grateful to the CERMES team of the Navier laboratory at ENPC. During my stay at ENPC, the lab has been a second home to me. I thank the researchers, technical team and lab-mates I have had the chance to spend time with over the past three years, either working, chilling over a cup of coffee or playing soccer and tennis together.

Among the cementitious geeks, I thank Nicolaine Agofack, who was a mindful guide in my early days in the cement world. The enthusiastic conversations with Sara Bahafid have also been very enriching, as together we unveiled this intriguing material.

I gratefully acknowledge the support of Total, particularly that of Christophe Urbanczyk and André Garnier, who closely followed my work. I also thank the staff of the CSTJF laboratory at Pau, notably Louis Zinsmeister and Sandrine Annet-Wable, for their help with the experiments.

I express my deepest gratitude to my dear wife Verónica, who supported me every time I felt the load was too heavy. This work would have never been possible without her. I also gratefully acknowledge the persistent encouragement of my parents and siblings.

To Federico, who came as a joyful new beginning when this work was coming to an end.

Modelling of an oil well cement paste from early age to hardened state: hydration kinetics and poromechanical behaviour

Abstract

The prediction of the performance of cement-based materials requires a holistic model integrating the progressive hydration of the material, the coupling between water consumption and strains, and the history of the applied loadings. This is particularly important when modelling the behavior of the cement sheath in oil wells which is subjected, from its earliest age and during its lifetime, to a wide range of mechanical and thermal loadings that could have a detrimental effect on its future mechanical properties.

The aim of the present thesis is to provide a complete modelling framework for the hydro-mechanical behavior of an oil well cement paste from its earliest age to its hardened state. The manuscript is divided in two parts.

Part I: hydration kinetics

The evolution of the most significant physical properties of cement-based materials is controlled by the advancement of the hydration reactions. Two different modelling approaches are presented:

- A theoretical framework for the modelling of cement hydration is developed as an extension of classical nucleation and growth models. The proposed multi-component model explicitly considers anhydrous cement and water as independent phases participating in the reaction. We also introduce a growth rate that encompasses linear as well as parabolic diffusion growth in a single continuous mathematical form. The formulation naturally introduces some of the most relevant parameters of cement paste mixtures, such as the cement powder composition, mass densities of the different phases, water to cement ratio, chemical shrinkage and hydrates properties. The different rate-controlling mechanisms can be identified and interpreted on the basis of the proposed physical model.

- A general hydration kinetics law based on the theory of solid phase transformations is proposed. This formulation is compared with the evolution laws found in the literature and helps providing a physical explanation that could shed light on the understanding of cement hydration kinetics.

In both cases, the kinetic models are calibrated over a series of experimental results in order to properly evaluate the quality of the predictions.

Part II: mechanical constitutive law

The mechanical behavior of cement paste is described in the framework of reactive porous media. The cement paste is modelled as a multi-phase porous material with an elastic-viscous-plastic constitutive law, with mechanical parameters depending on the hydration degree. Furthermore, the cement paste chemical shrinkage and pore water consumption during hydration are accounted for in the determination of the macroscopic strains. The evolution of the poroelastic parameters of the cement paste during hydration is calculated by means of a micromechanical upscaling model. An asymmetric yield surface with compressive and tensile caps is adopted for the elastoplastic regime, with hardening mechanisms considering both the cumulated plastic deformations and the hydration degree. The viscous behaviour is based on the notions of solidification theory. A water retention curve is introduced to account for the potential desaturation of the material during hydration.

The model parameters for a class G cement paste are evaluated by simulating the results of mechanical loading experiments in a device specially designed for testing the thermo-mechanical behavior of cement paste from the early stages of hydration. The results show that the proposed model predicts with good accuracy the response of a hydrating cement paste when subjected to various loading paths from its early age. The importance of the loading history is outlined, as well as the need for the accurate determination of the effective stresses throughout the life of the material.

Keywords: cement, hydration kinetics, poromechanics, oil well, cement sheath

Résumé

La prédiction des propriétés mécaniques des matériaux cimentaires nécessite d'un modèle intégrant l'hydratation progressive du matériau, le couplage entre la consommation d'eau et les contraintes et l'historique des charges appliquées. Ceci est particulièrement important lors de la modélisation du comportement de la gaine de ciment des puits pétroliers qui est soumise, dès son plus jeune âge, à une large gamme de chargements mécaniques et thermiques qui pourraient avoir un effet négatif sur ses propriétés mécaniques.

L'objectif de cette thèse est de fournir un cadre de modélisation pour le comportement hydro-mécanique d'une pâte de ciment pétrolier dès son plus jeune âge jusqu'à son état durci. Le manuscrit est divisé en deux parties.

Partie I : cinétique d'hydratation

L'évolution des propriétés physiques des matériaux cimentaires est contrôlée par l'avancement des réactions d'hydratation. Deux approches de modélisation sont présentées:

- Un cadre théorique pour la modélisation de l'hydratation du ciment est développé comme une extension des modèles de nucléation et de croissance classiques. Le modèle multi-composants proposé considère explicitement le ciment anhydre et l'eau comme des phases indépendantes participant à la réaction. Un taux de croissance est introduit qui permet de représenter sous une forme mathématique unique la croissance linéaire ainsi que la diffusion parabolique. La formulation introduit naturellement des paramètres des mélanges cimentaires tels que la composition de la poudre de ciment, les densités des différentes phases, le rapport eau/ciment, le retrait chimique et les propriétés des hydrates. Les différents mécanismes de contrôle de la réaction sont identifiés sur la base du modèle physique proposé.

- Une loi générale de la cinétique d'hydratation basée sur la théorie des transformations en phase solide est proposée. Cette formulation est comparée aux lois d'évolution trouvées dans la littérature et contribue à fournir une explication physique qui pourrait aider à la compréhension de la cinétique d'hydratation du ciment.

Dans les deux cas, les modèles cinétiques sont calés sur une série de résultats expérimentaux.

Partie II : loi de comportement mécanique

Le comportement mécanique de la pâte de ciment est décrit dans le cadre des milieux poreux réactifs. La pâte de ciment est modélisée en tant que matériau poreux multi-phases avec une loi constitutive élasto-visco-plastique, dont les paramètres dépendent du degré d'hydratation. Le retrait chimique de la pâte de ciment et la consommation d'eau pendant l'hydratation sont pris en compte dans la détermination des déformations macroscopiques. L'évolution des paramètres poroélastiques de la pâte de ciment lors de l'hydratation est calculée à l'aide d'un modèle micromécanique. Une surface de charge asymétrique avec des seuils de compression et de traction est adoptée pour le régime plastique, avec des mécanismes d'écrouissage tenant compte à la fois des déformations plastiques accumulées et du degré d'hydratation. Le comportement visqueux est basé sur les notions de la théorie de solidification. Une courbe de rétention d'eau est introduite pour tenir compte de la désaturation potentielle du matériau lors de l'hydratation.

Les paramètres du modèle pour une pâte de ciment pétrolier classe G sont évalués en simulant des expériences de chargement mécanique dans un dispositif spécialement conçu pour tester le comportement thermo-mécanique de la pâte de ciment dès le début de l'hydratation. Le modèle prédit avec une bonne précision la réponse d'une pâte de ciment en cours d'hydratation lorsqu'elle est soumise à divers chemins de chargement dès son plus jeune âge. L'importance de l'histoire de chargement est mise en évidence, ainsi que la nécessité de la détermination des contraintes effectives tout au long de la vie du matériau.

Keywords: ciment, cinétique d'hydratation, poromécanique, puits pétrolier, gaine de ciment

Contents

List of Figures

6   Mechanical behaviour of a cement paste from early age to hardened state   153

List of Tables

Chapter 1

Introduction and Fundamentals

1.1 General introduction

For over a century, oil, gas and geothermal wells have relied on the sufficiency of the cement sheath placed between the casing and the rock formation to assure the zonal isolation of geological substratum layers. In addition, the cement sheath is essential to provide well stability and guarantee the physical integrity of the casing, protecting it from corrosion [17].[1]

The cement sheath is submitted, from its earliest age and during its lifetime, to a wide range of mechanical and thermal loadings that could have a detrimental effect on its future performance. Starting from drilling and production phases, and during its long-term abandon period, the wide range of solicitations, from below-zero temperatures to 250°C and from tens to hundreds of megapascals, might compromise the material properties required to assure the proper fulfilment of the cement sheath basic roles. Furthermore, the recent advances in drilling and production technologies, e.g. hydraulic fracturing, steam injection, and high-pressure, high-temperature wells, pose new challenges and raise important questions regarding the reliability of current industry standards, demanding further investigation of the material properties under such conditions. The determination of appropriate constitutive laws describing the evolution of the material properties spanning from the early to the advanced age is required for a correct evaluation of the effect of these loadings.

The present work is inscribed in the decade-long collaboration between Total and the Ecole Nationale des Ponts et Chaussées (ENPC) regarding the mechanical behaviour of cement paste in various oil-well conditions. The results of this joint research efforts, embodied in the works of Ghabezloo [18], Vu [8] and Agofack [16], have provided fundamental experimental and modelling insight of the behaviour of a class G cement paste, the most

---

[1]The first reported use of cement for the sealing of an oil well dates to 1903, in California, USA.

common formulation used for the primary cementing job.

Ghabezloo [18] clearly demonstrated that the hardened cement paste can be considered as a poromechanics material based on an experimental campaign following classical thermo-poro-mechanical testing procedures. Vu [8] extended the analysis by considering the effects of curing temperature and pressure conditions on the early age behaviour of the material. More recently, Agofack [16] described the mechanical behaviour under various loading paths of a cement paste hydrated at low temperature based on an elastoplastic poromechanical constitutive model.

The collection of results suggests that the prediction of the performance of cement-based materials requires a holistic model integrating the progressive hydration of the material, the coupling between water consumption and strains, and the history of the applied loadings. The aim of the present thesis is to provide a comprehensive modelling framework for the mechanical behaviour of an oil well cement paste from its earliest age to its hardened state.

1.2 Outline of the manuscript

In the present chapter, a brief summary of the fundamental concepts is recalled. The remaining of the manuscript is divided in two parts. The first part, comprising Chapters 3 and 4, is dedicated to the formulation of hydration kinetics models. The evolution of the most significant physical properties of cement-based materials is controlled by the advancement of the hydration reactions. Two different modelling approaches are presented and calibrated over a series of experimental results in order to properly evaluate the quality of the predictions.

In Chapter 3, a theoretical framework for the modelling of cement hydration is developed as an extension of classical nucleation and growth models. The proposed multi-component model explicitly considers anhydrous cement and water as independent phases participating in the reaction. We also introduce a growth rate that encompasses linear as well as parabolic diffusion growth in a single continuous mathematical form. The formulation naturally introduces some of the most relevant parameters of cement paste mixtures, such as the cement powder composition, mass densities of the different phases, water to cement ratio, chemical shrinkage and hydrates properties. The different rate-controlling mechanisms can be identified and interpreted on the basis of the proposed physical model.

Chapter 4 introduces a general hydration kinetics law based on the theory of solid phase transformations. This formulation is compared with the evolution laws found in the literature and helps providing a physical explanation that could shed light on the understanding of cement hydration kinetics.

The second part, comprising Chapters 5 and 6, is dedicated to the formulation of a mechanical constitutive law and the determination of its parameters. In Chapter 5, the

mechanical behaviour of cement paste is described in the framework of reactive porous media. The cement paste is modelled as a multi-phase porous material with an elastic-viscous-plastic constitutive law, with mechanical parameters depending on the hydration degree. Furthermore, the cement paste chemical shrinkage and pore water consumption during hydration are accounted for in the determination of the macroscopic strains. The evolution of the poroelastic parameters of the cement paste during hydration is calculated by means of a micromechanical upscaling model. A yield surface with compressive and tensile caps is adopted for the elastoplastic regime, with hardening mechanisms considering both the cumulated plastic deformations and the hydration evolution. The viscous behaviour is based on the notions of solidification theory. A water retention curve is introduced to account for the potential desaturation of the material during hydration.

Chapter 6 is dedicated to the evaluation of the model predictions for a class G cement paste. The results include the simulation of the results of mechanical loading experiments in multiple experimental configurations, including a device specially designed for testing the thermo-mechanical behaviour of cement paste from the early stages of hydration. The results show that the proposed model predicts with good accuracy the response of a hydrating cement paste when subjected to various loading paths from its early age. The importance of the loading history is outlined, as well as the need for the accurate determination of the effective stresses throughout the life of the material.

Finally, the main conclusions and future work perspectives are outlined in Chapter 7.
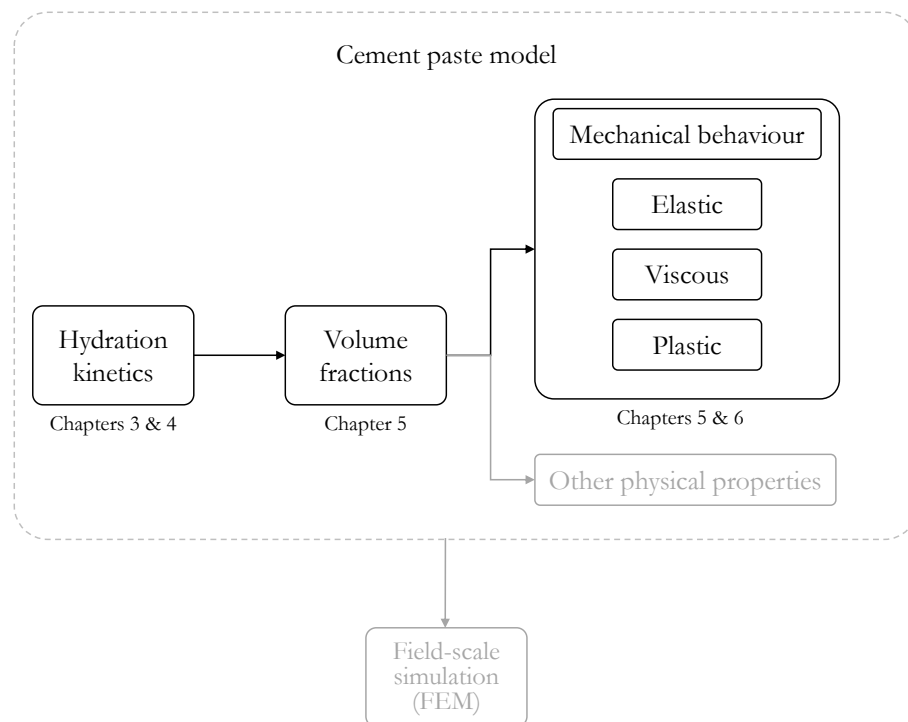
Figure 1.1: Modelling framework and manuscript structure.

Figure 1.1 summarizes the workflow of the modelling framework and the manuscript structure.

1.3 Cement powder

Anhydrous Portland cement powder is commonly composed of five main phases: alite (C_3S), belite (C_2S), aluminate (C_3A), ferrite (C_4AF) and gypsum [19]. The abbreviations follow the cement chemistry notation, where C=CaO, S=SiO_2, A=Al_2O_3, F=Fe_2O_3 and H=H_2O. The first four phases (C_3S, C_2S, C_3A and C_4AF) constitute the clinker, resulting from the partial fusion of clay and limestone at very high temperatures in the kiln. The cement powder is obtained from the fine grounding of clinker together with gypsum, added to control the reaction rates [19]. The availability of these materials (clay, limestone and gypsum) throughout the world and the well-established industrial process of cement production, together with the reliability of cementitious materials, has made of Portland cement one of the most widely manufactured materials in the planet [20].

The composition of cement powders can vary according to the specific designated use of the material. The oil well cement powders are classified on the basis of their chemical composition by the American Petroleum Institute (API) in eight main classes, A to H, to be selected according to the oil well depths and their service conditions [21]. The intended uses of each class can be found in the API documentation or literature compendiums on the subject [17]. The most extensively used classes are G and H, with nearly identical chemical compositions, class G being finer grounded, that represent over 90% of the cementing jobs, and have the typical mass composition presented in Table 1.1. Fortunately, the compositions are not too distant from that of ordinary Portland cement used in everyday applications – over 99% of the cements used worldwide [22]– hence allowing the collective inclusion and consideration of results and findings pertaining both civil and petroleum engineering literature.

Table 1.1: Typical mass composition of ordinary class G and H cement powders [17]

	Component			
	C_3S	C_2S	C_3A	C_4AF
%	50	30	5	12

1.4 Cement paste

1.4.1 Chemical reactions

The cement hydrates, main constituents of the cement paste skeleton, are the result of the reaction of the anhydrous cement powder and water. The average hydration reaction

stoichiometry of C_3S and C_2S, that account for over 70% of the cement powder mass, can be expressed in the following general form:

$$C_zS \ + \ (z - x + y)\,H \quad \rightarrow \quad C_x - S - H_y \ + \ (z - x)\,CH \tag{1.1}$$
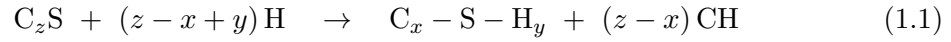
where $z = 2, 3$ for C_2S and C_3S, respectively. The parameters x and y stand for the C/S and H/S ratios, and are a function of the hydration conditions, most notably temperature [23]. At standard conditions of atmospheric pressure and 20°C their values are $x = 1.7$ and $y = 4$ [24]. The set of reactions concerning other clinker phases and gypsum has been omitted, their expressions being available in the literature [25–27].

The main hydration products resulting from the reaction are crystalline calcium hydroxide CH, also known as Portlandite, and calcium silicate hydrate, abbreviated C–S–H. The dashes in C–S–H reflect the variability of the stoichiometric composition of this amorphous phase. The complex series of reactions concerning C_4AF and C_3A result in different hydrates phases which we will summarily group as aluminate hydrates for the sake of simplicity.

1.4.2 Microstructure

In a coarse description, the cement paste can be considered as a heterogeneous mixture of anhydrous cement powder, cement hydrates and water in different physical states [7]. In addition, minor quantities of supplementary cementitious materials or impurities can also be present. Figure 1.2 schematically represents the distribution of the different phases of the cement microstructure.
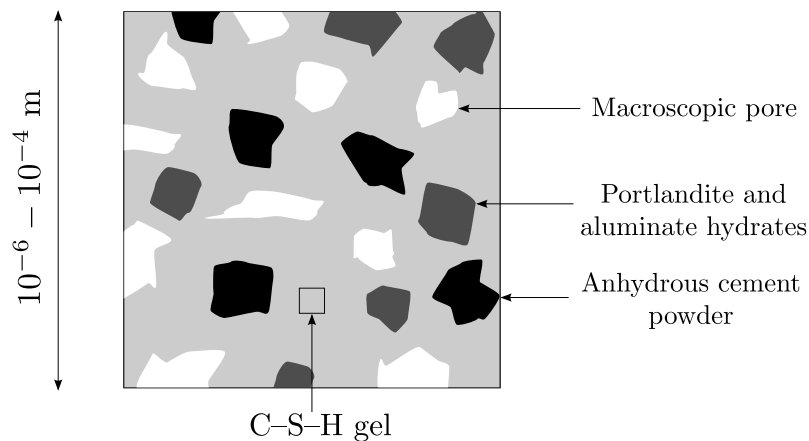
Figure 1.2: Schematic representation of the cement paste microstructure.

The most intriguing phase of the microstructure is without doubt the amorphous C–S–H gel, the main hydration product of the hydration reactions and the binder giving cement paste its characteristic cohesion. The extensive research of the C–S–H structure over the

last decades, together with the evolution of the experimental techniques and analytical tools available, are summarized in ref. [27]. The understanding of the nature of the C–S–H gel has evolved significantly, with major milestones being the pioneering work of Powers and Brownyard [28] and the models by Feldman and Sereda [29] and later Jennings [1, 26]. The main challenge in a complete material characterization resides in the extreme sensitivity of the C–S–H gel structure to hygroscopic conditions. For such reason, the study by means of new non-destructive and non-drying techniques (e.g. SANS and NMR, as in ref. [30, 31]) and the simulation of the structure at the molecular level (e.g. [32]) hold significant promise of future findings.

The microstructural model developed by Jennings [1, 26], commonly known as the Jennings model, conceives the C–S–H gel as constituted of elementary globules arranged in two colloidal nanostructures with different packing densities: low density C–S–H (LD C–S–H) and high density C–S–H (HD C–S–H). These two structures are differentiated by their amount of gel porosity, estimated to 36 and 26% for LD and HD C–S–H, respectively. According to the Jennings model, LD C–S–H is produced during the initial stages of reaction, as long as sufficiently large pore spaces are available. Later, as the growth of hydrates becomes space constrained, HD C–S–H is the main product. The globules, of around 4 nm in size, are formed of packed layers of solid C–S–H and internal water, surrounded by an adsorbed water layer.

The formulation of the Jennings model is based on the analysis of sorption isotherms performed on cement pastes. The existence of the LD and HD C–S–H gels has since been confirmed using different experimental techniques [33]. The main feature of the model is the nano-granular description based on discrete globules, while conserving the colloidal nature of the material at the level of the gel. The basic globule and C–S–H gel structure as described by the Jennings model are presented in Figure 1.3.
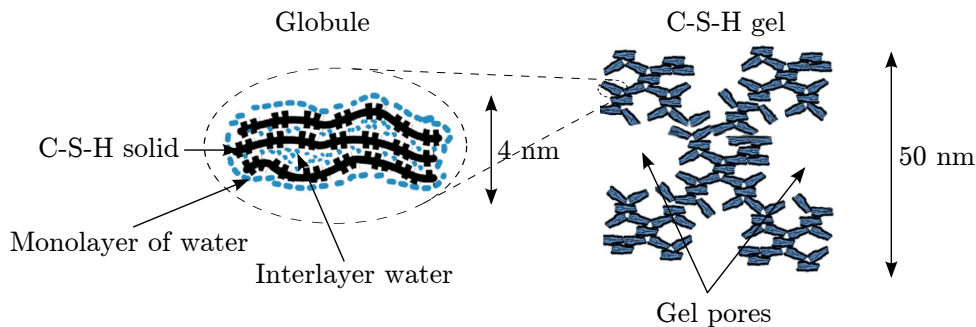
Figure 1.3: The Jennings model of C–S–H microstructure [1].

The Jennings model of C–S–H gel, together with the hydration model describing the evolution of the volume fractions of cement phases, allow us to quantitatively describe the distribution of the different phases of the cement paste microstructure at its multiple levels. The description across material length scales will be exploited by our multi-scale

model to determine the poroelastic properties of the material at macroscopic scale from its microscopic composition.

1.4.3 Hydration kinetics

The mechanisms of cement hydration have been extensively studied in the cement literature, for both their practical and fundamental scientific relevance. Indeed, the main physical properties governing the behaviour of cement-based materials (e.g. mechanical properties [7, 34–36]) are intimately related to the degree of advance of the hydration reactions.

In the case of oil well cements, an appropriate description of the hydration kinetics is of the highest priority, since the reactions are highly sensitive to pressure and temperature conditions –both of which vary in one order of magnitude in deep boreholes– calling for comprehensive models being able to properly assess the kinetics within an acceptable range of precision for the practical applications.
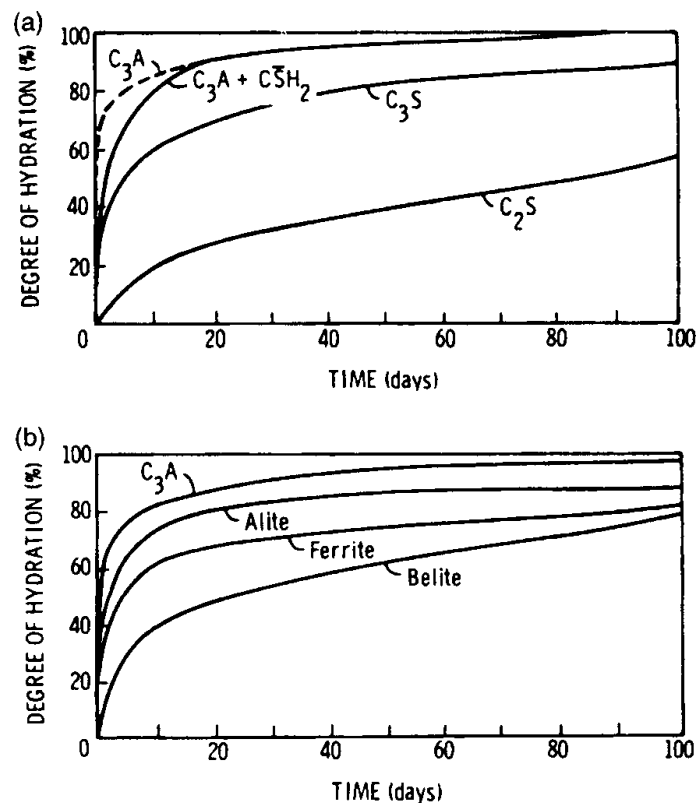
Figure 1.4: Hydration evolution for cement components a) in pure-component paste; b) in Portland cement paste. After Blackie [2].

The multiple clinker components hydrate at rates that are different from the overall observed hydration rate of the cement paste. As can be noted in Figure 1.4, the hydration kinetics of each component are slightly different when considered in its pure form, if compared to the more complex Portland cement kinetics. In an effort to simplify the

system complexity, some authors have focused on the hydration of its main component, C_3S, which represents about 2/3 of the total cement powder mass [3, 37, 38]. Furthermore, C_3S tends to dominate the early hydration and setting in well-dosed cements, where gypsum delays the large exothermal reaction of C_3A [19].

The cement hydration reaction involves diverse physico-chemical mechanisms, among which we can cite diffusion, nucleation, growth, complexation and adsorption [22]. The difficulties in modelling the hydration reaction can be traced to the strong coupling and interdependence of the different processes involved, which constitute barriers to the isolation and resolution of individual mechanisms.

The analysis is eased by schematically dividing the hydration reaction in four stages according to the reaction rate [39]: initial fast reaction, induction, acceleration and deceleration (Figure 1.5). Traditional approaches modelling the hydration of cement make use of this division in order to formulate sequences of rate controlling mechanisms. The distinction of different stages is, however, rather arbitrary and holds no strict relationship with distinct physical mechanism, with multiple classifications being attributable to different authors (e.g. refs. [22, 40, 41]).

The initial fast reaction (IR) typically lasts few minutes, and follows immediately after the contact between cement grains and water. As cement powder is brought in contact with water, the difference between the initial surface energy and the energy required for the creation of the new solid-fluid interface –the heat of wetting– is liberated, in addition to the energy released by the dissolution of the clinker phases. Therefore, the heat emission during the IR is not primarily due to the hydration of the clinker components and hence has no significant effect on the evolution of the mechanical properties of the material [41].

The induction period corresponds to a very low reaction rate, mainly due to the slow dissolution of the clinker grains, and can extend from minutes to several hours. The dissolution mechanisms depend on the concentration of the different species, which is the driving force of the reaction [42–44].

The acceleration period follows after the minimum of the hydration rate, which indicates the ending of the slow reaction period, although there seems to be no real transition in the mechanism driving the hydration evolution [41]. The duration of the acceleration period depends strongly on the curing conditions, as will be made clear in our examination of the experimental results in Chapters 3 and 4. The typical duration is between hours and days.

Finally, after the hydration rate peak, the reaction rate decelerates and the hydration proceeds at an ever diminishing rate until reaching the asymptotic hydration degree by exhaustion of the available reactants, either water or anhydrous clinker phases. The deceleration period can span over years for the typical particle size distribution of modern cements.

The total degree of hydration at the end of the induction stage is normally well under 1%
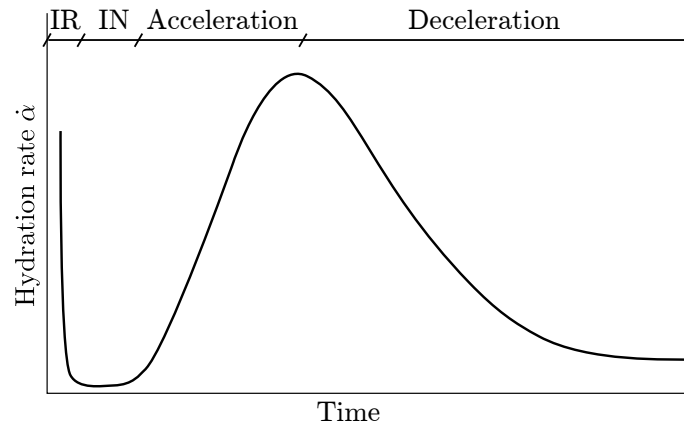
(a) Hydration rate as a function of time
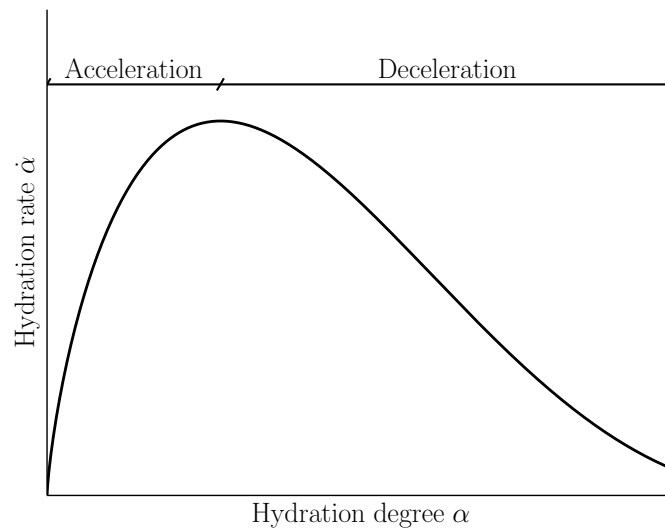
(b) Hydration rate as a function of hydration degree

Figure 1.5: Schematic representation of the hydration rate. Stages are divided in initial fast reaction (IR), induction (IN), acceleration and deceleration.

[41]. As a result, most authors disregard this contribution to the total degree of hydration and focus instead on the two final phases. This will be the approach in the present work, in which we dedicate our attention and modelling efforts on the two final phases (Chapters 3 and 4). The consideration of the two initial stages will be limited to the correct definition of the initial hydration time, which will be considered to be coincident with the acceleration period. For this definition, the effect of additives should be accounted for.

1.5   Hydration kinetics models

The efforts dedicated to the development of predictive hydration kinetics models can be traced back at least half a century, as detailed in the comprehensive reviews by Thomas et al. [45] and Scrivener et al. [46], that also include references to the most recent advances in

the field.

Among the multitude of approaches have been adopted by different authors, one can broadly distinguish those proposing empirical or semi-empirical mathematical expressions representing the different hydration stages (e.g [47–49]) and those based on more physical considerations, which attempt to describe the mechanisms of hydration reaction (e.g. [3, 37, 50]). In addition, a number of computationally-intensive tools have been developed to predict the hydration and microstructural development of the cement paste (e.g. [38, 51–53]). These computational tools are based on the same physical mechanisms suggested in analytical or semi-empirical models, but allow the consideration of discrete grains or modelling units, in an attempt to closer mimic the real physical system.

There is a general agreement on the assimilation of the early hydration phase of the cementitious materials to a nucleation and growth mechanism [41]. A transition to diffusion control is commonly assumed to take place late in the reaction because of the increase of the characteristic transport time of water with hydration [4, 37, 45, 48]. It is suggested that as the pore space is progressively reduced and the coating of hydrated material surrounding the clinker grains becomes thicker, the diffusion time of the hydration water through the material layers increases significantly, causing the shift to a diffusion-controlled reaction. Other possible reason for deceleration might be the lack of space or water [54].

In the present review, we limit our attention to the most widely used analytical models, that outline the basic physical mechanisms that will be considered in the development of the hydration models of the present work. The limitations of the current approaches will be discussed upon introduction of the hydration models in Chapters 3 and 4.

1.5.1   Nucleation and growth models

The nucleation and growth model was developed for studying the kinetics of phase change in metals, from molten fluid to solid state, and have, over the past decades, been profusely applied for modelling cement hydration kinetics [41, 55–57]. Among the main variations, we can cite the conventional nucleation and growth (NG or JMAK, by the initials of the authors) [55–57] and boundary nucleation and growth (BNG) [3, 58]. The book by Christian [59] explains the theory in extensive detail and is a recommended reference for the interested reader. The mathematical expressions constitute particular cases of the general model presented in Chapter 3, and hence their derivations are omitted.

The NG model considers a system composed of two phases, initial and transformed, each one occupying a certain fraction of the total volume. The transformation from initial to transformed phase starts from identifiable nuclei in the initial phase, in a process known as nucleation. The new transformed phase grows at the expense of the initial as the reaction progresses. The newly created regions will eventually come in contact with each other, and following this contact they are assumed to develop a common interface, across which

the growth is inhibited. In the case of a cement paste, even if the initial state is fluid and particles could separate from each other as the hydration advances, the formation of a solid structure will most certainly cause the appearance of common interfaces once the hydration is sufficiently advanced.

The hydration degree according to the original NG model is given by

$$\alpha = 1 - \exp\left(-\frac{\pi G^3 I_v t^4}{3}\right) \tag{1.2}$$

where α is the hydration degree, G is the linear growth rate of the transformed phase –assumed isotropic and constant– I_v is the nucleation rate per unit volume of the transformed phase –also assumed constant– and t is the total elapsed time. A corrective coefficient is often introduced to improve the fit quality [3, 60]. In the case of non-spherical growth, G can be considered equivalent to an averaged growth rate. Even though the model requires two input parameters, G and I_v, their effect are encapsulated by $k = G^3 I_v$.

The original NG model can be extended to the general expression [41]:

$$X = 1 - \exp(kt^m) \tag{1.3}$$

where k is a rate constant, and $m = p/s + q$. The variable p is related to the morphology of the transformed regions ($p = 1$ for needle growth, 2 for sheet growth and 3 for isotropic growth), s is related to rate-controlling process ($s = 1$ for phase-boundary control and 2 for diffusion control), and q is related to the evolution of the nucleation rate ($q = 0$ for fast exhaustion and 1 for a constant nucleation rate). The exponent m in the equation can therefore have a wide range of values $0.5 \leq m \leq 4$, in agreement with the equally scattered values reported in the cement literature [3, 61].

One of the main assumptions of the NG model is the random character of the nucleation process. In reality, nucleation often occurs preferentially at some locations. In 1956, Cahn [58] proposed the BNG model as an extension of the NG formulation in which nucleation occurred on the boundaries of the grains. The formulation has been recently brought to the attention of the cement research community by Thomas [3], who used it to model the hydration of C$_3$S. It has also been used by other authors to model Portland cement hydration [8, 16, 62]. The hydration degree is expressed as:

$$\alpha = 1 - \exp\left(-2k_g t\right) \exp\left[2k_g t \int_0^1 \exp\left(-\pi \frac{k_b^4 t^3}{k_g}\left(\frac{2x^3}{3} - x^2 + \frac{1}{3}\right)\right)\right] \mathrm{d}x \tag{1.4a}$$

where $k_b = (NB)^{1/4} G^{3/4}$ and $k_g = BG$. N is the nucleation rate per unit area, considered constant, and B is the randomly distributed specific nucleation surface per unit volume. The use of a corrective fitting factor is also common in applications [3, 8, 16].

For sufficiently small t, or if $k_b \ll k_g$, the exponential term can be estimated by its first order expansion. After integration, we obtain:

$$X = 1 - \exp\left(-\frac{\pi k_b^4 t^4}{3}\right) \tag{1.5}$$

This expression is the same as Equation (1.2), which corresponds to spatially random nucleation. The parameter k_b is associated with the nucleation at small area transformations, when nucleation sites are considerably distanced from each other and the mutual interaction of nodules is very weak. On the other hand, if we consider the case $k_b \gg k_g$ or a sufficiently large t, the expression for X becomes:

$$X = 1 - \exp\left(-2k_g t\right) \tag{1.6}$$

in which case the transformed volumes grow like slabs, with a volume $2k_g t$ at any given time t. The parameter k_g is best interpreted as the rate of growth in an advanced stage, where much of the boundary has been transformed.

The BNG formulation has several advantages over the standard NG. First and foremost, it is closer to the real physical process of cement hydration, for which the growth occurs from the grain boundaries [63]. Thomas suggested, as an additional advantage, the possibility to introduce the cement fineness in the BNG formulation through parameter B [3]. The same parameter can be introduced with equivalent ease in the NG model by defining $I_v = BN$.
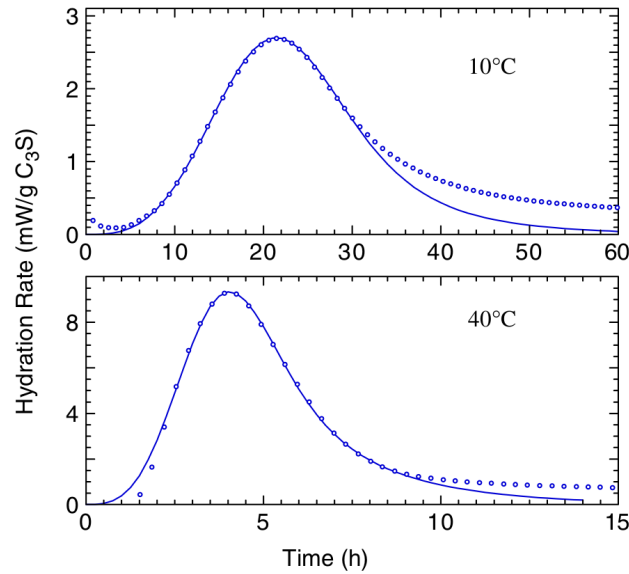
Figure 1.6: Experimental and BNG model hydration rates for C_3S paste hydrated at two different temperatures. Solid lines correspond to models, while dashed lines are experimental results. Adapted from Thomas [3].

As illustrated by Figure 1.6, the BNG model can be fit very precisely to the first part of the reaction, but it deviates from the experimental curve as the hydration advances. This is normally considered to be a consequence of the change in the rate-controlling process, as discussed in the following paragraph.

1.5.2 Long-term hydration models

It is generally assumed that the deceleration period and late hydration are dominated by diffusion mechanisms due to the hindered transport of the reactants [37, 45]. To describe the late hydration, Fuji and Kondo [37] adopted a parabolic law combined with the assumption of a spherical geometry of the grains and hydrates, in a similar way as done before by Jander [64]. The following expression by Fuji and Kondo [37] has found wide acceptance and applications:

$$(1-\alpha)^{1/3} = \frac{\sqrt{2D(t-t^*)}}{r_m} + (1-\alpha^*)^{1/3} \tag{1.7}$$

where D is the diffusion coefficient, r_m is the initial radius of the clinker grain, α^* and t^* are the hydration degree and time corresponding to the onset of diffusion control, respectively. The same approach can be applied to the diffusion problem for a spherical particle for which the thickness of the coating is evolving, modifying the parabolic law to account for the curvature of the surface, deriving in the model of Ginstling and Brounshtein [64]. An interesting comparison and discussion of these approaches, as applied to cement paste hydration, is available in ref. [65].

There are examples of attempts to integrate different rate-controlling mechanisms in order to model the short and long term reaction. Parrot and Killoh [48] propose three different rates –nucleation and growth, diffusion and shell hydration– that ought to be compared to determine the limiting process, deemed responsible for the observed reaction rate. The concatenation of successive mechanisms must be done carefully to assure smooth transitions and avoid discontinuities either of rate or rate variation that are not consistent with the observed reaction. Another example can be found in the work of Pang and Meyer [4] (Figure 1.7), who made use of a nucleation and growth model connected to a Fuji-Kondo diffusion model.

1.6 Mechanical behaviour

Immediately after mixing, the cement slurry behaves as a fluid, with no resistance to shear. As long as the solid phase of the cement paste –anhydrous grains and cement hydrates– does not percolate the medium, the material behaviour is similar to that of a bulk fluid [16].

Under controlled conditions of pressure and temperature, the main observable during
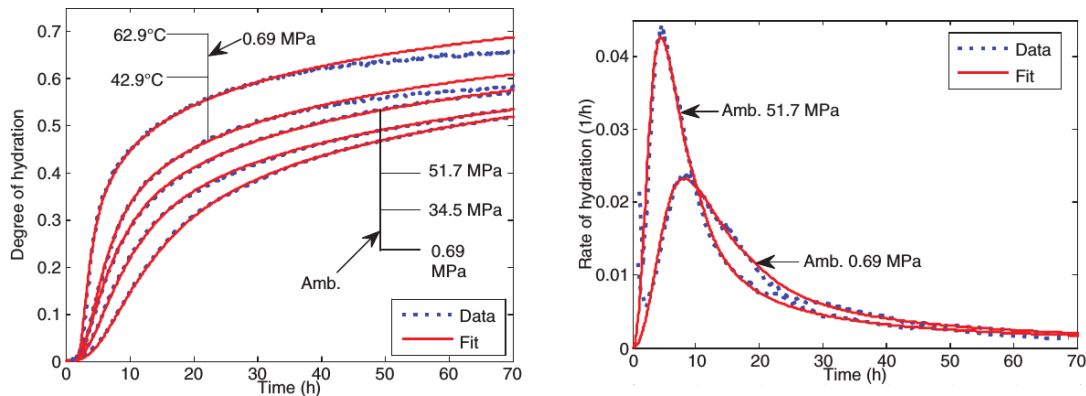
Figure 1.7: Evolution of hydration degree and rate according to the model of Pang and Meyer [4].

this initial non-percolating period is the macroscopic volumetric strain of the slurry. As demonstrated by Le Chatelier over a century ago, the cement paste volume might diminish in the order of 0.05 cm^3/g of cement powder as a result of the hydration reactions. It is now well established that the change in volume of fluid slurry is due to chemical shrinkage, i.e. volume differences among reactants and products, which might be analytically calculated or experimentally determined (see Sections 5.3.1 and 6.7.1). As long as the cement paste remains fluid, the chemical shrinkage is directly converted to macroscopic observable shrinkage.

1.6.1 Solidification model of Bažant

The percolation of the skeleton brings the transition from a fluid to fluid-saturated solid. The efforts to describe the effect of the precipitation of new hydrates on the mechanical behaviour of the material have been numerous, but perhaps none is better known and has found wider acceptance that the solidification model of Bažant and co-workers [5, 6, 66, 67]. In this approach, the evolution of the cement paste properties is described on the basis of the properties of its constituents, whose volume fractions change as a result of the hydration reactions, as stated by Bažant [67]:

> *Ageing has traditionally been treated simply as a change of the material parameters involved in the calculation (...) The mechanical properties of chemical substances are generally fixed; they do not change with time. Their change must be regarded as a change in the concentrations of various substances in concrete or hardened Portland cement paste.*

The solidification process is illustrated in Figure 1.8. The mechanical behaviour of the system is governed by the constitutive layers and their concentrations. The modelling problem is reduced to the determination of appropriate volume fraction evolution laws and
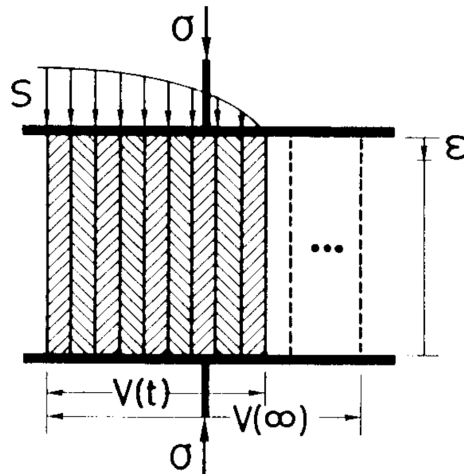
Figure 1.8: Solidification model of a hydrating cement paste with a parallel arrangement of constituent layers. The volume of constituents is V, their internal stress is given by s, and σ and ϵ are the total stress and strain, respectively [5].

the determination of the mechanical behaviour of the constitutive layers, by either inverse analysis or micromechanical tests (e.g. [68] and [69, 70]).

The model was originally formulated to predict the long term creep behaviour of cement paste and concrete. The results of the application of the solidification model in Figure 1.9 show that the effect of ageing on the viscoelastic properties of concrete is very well captured.
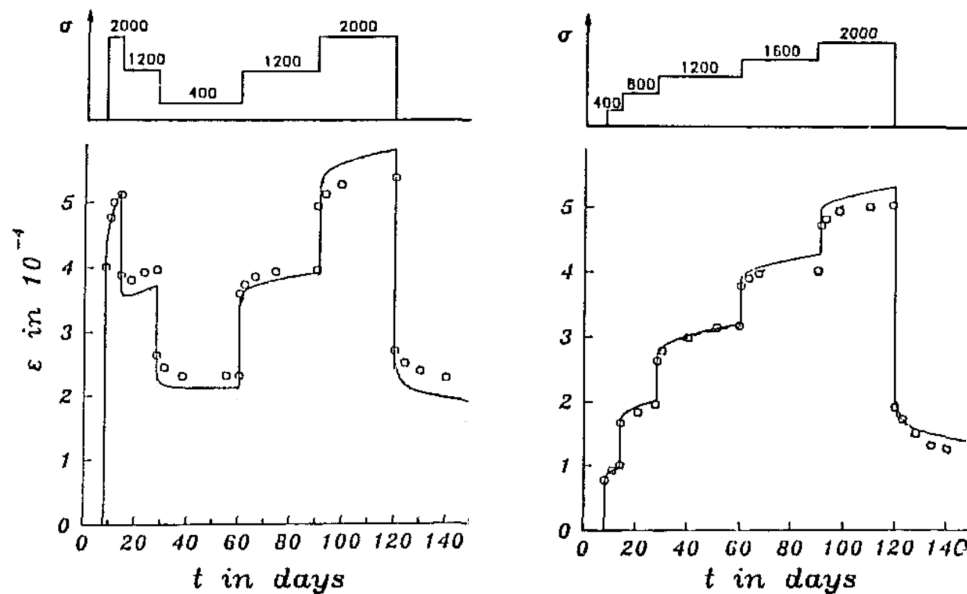
Figure 1.9: Long term evolution of strains of ageing concrete subjected to different loading paths, experimentally measured (marks) and determined from the solidification model (solid line) [6].

The model extension to a poromechanical medium with elastic, viscous and plastic behaviour will be the subject of Chapter 5 and hence the details of the formulation are omitted here.

1.6.2 Poromechanical models

Some of the most recent developments regarding the mechanical behaviour of the percolated cement paste are based on the theory of porous media developed by Biot [71, 72].

Ulm et al. [73] are among the first to describe the poroelastic properties of concrete. In their work, they determined the macroscopic properties of the material from the microscopic properties of the matrix components via micromechanical upscaling techniques adapted to the different scales and pore structures of the material.

Later, Ghabezloo and co-workers [18, 74, 75] provided experimental evidence of the poromechanical nature of a hardened cement paste. In a series of experiments in high-pressure triaxial cells, they successfully determined a complete set of compatible poroelastic parameters for a class G cement paste hydrated at 90°C.

The application of poroelastic homogenization frameworks to hydrating cement paste and concrete has seen a progressive adoption in advanced mechanical models [16, 76, 77]. An example of the dependency of a set of poroelastic parameters on the water to cement ratio determined from an upscaling model is presented in Figure 1.10. The effect of a decrease in the water to cement ratio might be regarded, amid some minor differences, as equivalent to an increase in the hydration degree.
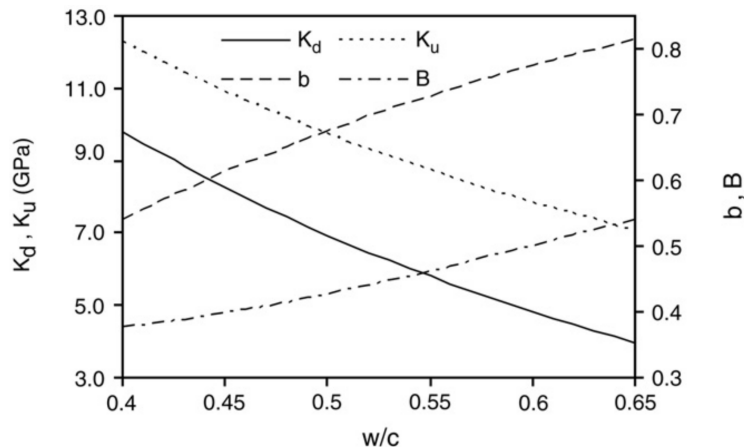
Figure 1.10: Poroelastic parameters as a function of the water to cement (w/c) ratio, determined from a micromechanical model by Ghabezloo [7]. The parameters are described in Chapter 5.

Regarding the chemo-hydro-mechanical couplings necessary to the comprehensive modelling of hydrating cementitious materials, one can trace the original work of Coussy and Ulm [78–80] as a notable source of inspiration for the more recent models available in

the literature [16, 81–83]. In their work, Coussy and Ulm considered a closed hydrating concrete (or cement) system and demonstrated that, in such scenario, the hydration degree is the single internal variable governing all evolutions. Their thermodynamic formulation reveals the origin of some of the couplings existing among the mechanical, thermal and chemical variables. The application of the model, however, is not trivial, mainly because the isolated evaluation of the parameters is not straightforward. Furthermore, the evolution of the pore pressures is not explicitly considered and hence an extension to a poromechanical framework remained lacking.

Recently, Agofack [16] proposed a chemo-poro-mechanical model that features cement paste as an elastoplastic material from its earliest age. The formulation considers the cement paste as a closed system and explicitly derives the expressions that account for the coupling of chemical, mechanical and hydraulic variables in a poromechanical framework. Among the strengths of the model is the consideration of detailed mass balance equations allowing to effectively couple the consumption of water and pore pressures, essential for the determination of the mechanical behaviour of porous materials. The evolution of the elastic properties was based on a micromechanical upscaling model, while the plastic yield followed an empirical chemical hardening law. The results outlined the importance of the loading history on the behaviour of the cement paste and the strong chemo-hydro-mechanical coupling evidenced by simulations and experimental results.

1.6.3 Effect of relative humidity and partial saturation

We believe it useful to clarify common concepts and naming conventions of the cement literature to avoid confusions and clarify the scope and reach of the formulation presented in Chapter 5.

In civil engineering, the term drying shrinkage is commonly used to designate the macroscopic volumetric strains of the cement paste observed by the decrease of the relative humidity (RH), i.e. the removal of water from the structure. In general, the cement paste is assumed to have a stalled age. In an ageing cement paste, endogenous shrinkage, as its name suggests (*endo*-within, *genous*-producing), is defined as the change in volume due exclusively to the action of internal agents, excluding changes of temperature, stress or moisture conditions originated from the exterior. In such a closed system, the internal evolutions are exclusively related to the advance of hydration reactions [78]. The hydration of a percolated cement paste, by virtue of the chemical shrinkage volume imbalance, progressively removes the water from the cement paste pores and lowers the RH, in a process known as self-desiccation. In our approach, we do not differentiate the physical mechanisms at the origin of drying or endogenous shrinkage, and interpret these as analogous, in the same way as discussed in ref. [84]. A review of the driving mechanisms of bulk volume changes is presented by Abuhaikal [85].

The mechanisms driving volumetric strains due to the change in RH of the cement paste, either by drying or self-desiccation, have been the subject of discussion by multiple authors, notably regarding their nature and physical origin (see [86], [87], [88] and [89]). Acker [89] suggests two essential mechanisms by which the change in relative humidity might affect the macroscopic strains: disjoining pressure and capillary pressure.

The disjoining pressure is the result of the interaction forces at the molecular level among C–S–H platelets and the water layers populating the space between solid particles. The magnitude of the disjoining pressure depends on the thickness of the liquid film, and therefore of RH. The increase of RH produces an increase in the repulsive force among particles, which reaches a maximum value in the saturated state. The changes in magnitude of the disjoining pressure, however, are negligible in the range of relative humidities between 50 to 100% [84, 89, 90].

The main mechanism acting for high RH, in the range of 80 to 100%, is the capillary pressure [84]. This is the range of relative humidities in which hydration reactions are possible [91], and concern the applications considered in the current work. Jennings and co-workers [90] extend the range and suggest most dimensional change from the saturated state to 50% RH is due to capillary stresses.

In addition, Hua et al. [84] judiciously recall that the meniscus effects are accurately estimated by the Kelvin-Laplace equation for pores of diameter above 10 nm. Such diameters correspond, for most cement pastes, to a RH above 80% which is, as previously mentioned, the minimum required RH for the hydration reactions to proceed. Therefore, the effects of relative humidity will be completely accounted for by means of capillary pressure effects as described by the Kelvin-Laplace equation.

Chapter 2

Materials and methods

This chapter presents the composition of the class G cement paste that will be the main subject of study of our hydration kinetics and mechanical behaviour models. The details concerning the preparation methods and conservation of the specimens are also addressed.

In addition, we describe the experimental devices, methods and procedures that will be employed to characterize the material. The interpretation of the experimental results is discussed in the concerned chapters.

2.1 Material

The cement paste is prepared using a class G cement powder with the composition presented in Table 2.1. The mixture proportioning corresponds to a water to cement ratio $w = 0.44$, and incorporates additives to optimize the slurry stability and homogeneity, as detailed in Table 2.2. In the experimental procedures requiring a setup time between the mixing and the beginning of the test (see Sections 2.2.1, 2.2.4 and 2.2.5), a retarding agent was added (commercial denomination D177). The density of the slurry after mixing is 1.91 g/cm^3. This cement paste formulation has been consistently studied in the decade-long collaboration between Total and the ENPC (consult the works of Ghabezloo [18], Vu [8] and Agofack [16]).

The cement powder has a density of 3.21 g/cm^3 and the particle size distribution (PSD) presented in Figure 2.1. The distribution features a median particle diameter of 13.5 μm, with a mean of 20.8 μm and a mode of 32 μm. The cement fineness determined from the PSD is 0.178 m^2/g, while Blaine fineness is 0.323 m^2/g. As usual, the Blaine fineness is larger, likely due to the non-spherical shape of the grains, contrary to the adopted assumption in the determination of the fineness from the PSD.

The slurries were prepared following the API recommendations [92]. For the experimental procedures that required the maturation of the samples before testing, the conservation of

Table 2.1: Composition by mass of class G cement powder. From Rietveld analysis

	Component				
	C_3S	C_2S	C_3A	C_4AF	Others
%	58.9	15.5	2.3	17.4	5.9
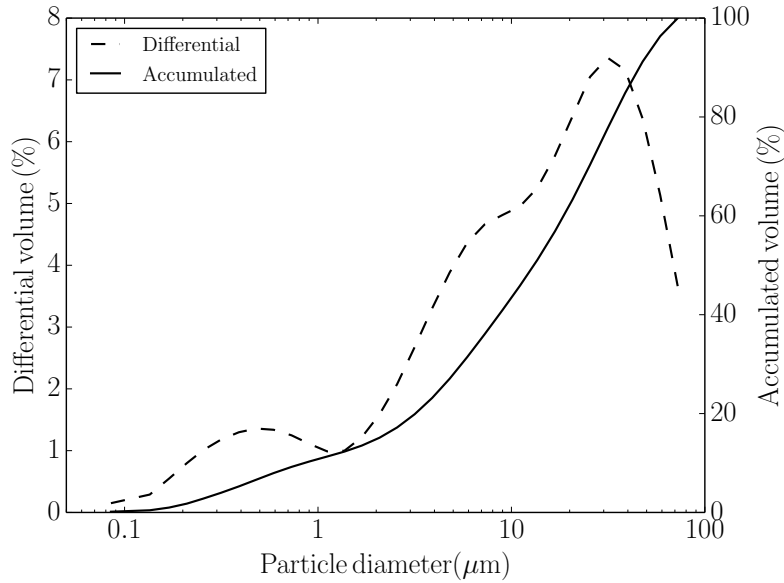
Figure 2.1: Particle size distribution of the class G cement powder. Adapted from Vu [8].

the cement paste specimens was under controlled conditions of temperature and pressure inside a lime-saturated water bath. The curing containers are sufficiently large as to assure a significant thermal inertia and avoid possible temperature shocks when manipulating the specimens. For all the experimental procedures performed in the present work, if the conservation temperature is different from the test temperature, the sample is allowed to reach the test temperature in a natural cooling process inside the container which might last from 6 to 24 hours.

Table 2.2: Composition by mass of 600 ml of cement slurry

Component	Mass (g)
Cement powder	783.53
Water	339.54
Dispersant (D604AM*)	9.47
Anti-foam (D047*)	6.27
Anti-settling (D153*)	1.18

* Commercial denominations.

The specimens for the uniaxial and triaxial experiments are cored in cylinders of 38 mm diameter and 76 mm height, providing a convenient factor of 2 that minimizes border

effects and allows the formation of complete shear bands if the material is loaded to failure. The coring was performed with diamond core drill bits and, to guarantee an even load distribution, the top and bottom surfaces are cut and their parallelism and surface quality assured by treatment with a polishing machine. Throughout the procedure, the room temperature is held constant and the sample saturated.

2.2 Experimental devices and methods

2.2.1 Isothermal calorimetry

Isothermal calorimetry provides an effective method for the quantification of the hydration evolution of the cement paste due to the highly exothermal nature of the hydration reactions. In the procedure, the heat emitted by a cement paste specimen is monitored continuously starting immediately from the minutes following the mixing. Assuming the heat release to be proportional to the consumed mass, the hydration degree α is given by:

$$\alpha(t) = \frac{Q(t)}{Q_\infty} \tag{2.1}$$

where $Q(t)$ is the cumulated heat release at time t and Q_∞ is its ultimate asymptotic value. The temperature –and in our case also the pressure– are controlled inside the calorimetric cell. The hydration rate can be directly determined from the heat emission, and hence integrated to provide the hydration degree of the specimen.

All tests were run on a Setaram BT 2.15, with maximum temperature and pressure ratings of 200 °C and 60 MPa, respectively. A summary of the experiments together with the notation conventions adopted in the following is presented in Table 2.3.

2.2.2 Triaxial experiments

Triaxial tests are commonly performed for the characterization of geomaterials, most notably soils and rocks (e.g. [93, 94]). The experimental characterization of the mechanical properties of cement pastes from a poromechanical standpoint under triaxial conditions was pioneered by Ghabezloo [18].

The schematic representation of a typical triaxial setup is presented in Figure 2.2. A cylindrical specimen is placed inside a rubber membrane, on which aluminium rings are mounted to support 6 linear variable differential transformers (LVDT) to measure displacements, 4 acting radially and 2 in the axial direction. All 4 radial LVDTs pierce through the rubber membrane and are in direct contact with the specimen via a thin aluminium sheet. The support rings are kept in contact with the membrane by metallic springs (not represented in the illustration). At the top and bottom of the sample, porous stones are placed to allow the homogeneous distribution of the pore pressures across the

Table 2.3: Isothermal calorimetry experiments

Reference	Hydration conditions		Source
	T (°C)	P (MPa)	
IC - T7P0	7	0.1	Agofack [16]
IC - T7P15	7	15	Agofack [16]
IC - T7P45	7	45	Agofack [16]
IC - T20P0	20	0.1	Current work
IC - T20P25	20	25	Current work
IC - T20P45	20	45	Current work
IC - T30P30	30	30	Agofack [16]
IC - T40P0	40	0.1	Vu [8]
IC - T40P25	40	25	Current work
IC - T40P45	40	45	Current work
IC - T60P0	60	0.1	Vu [8]
IC - T60P25	60	25	Current work
IC - T60P45	60	45	Current work
IC - T90P0	90	0.1	Current work
IC - T90P25	90	25	Current work
IC - T90P45	90	45	Current work

specimen section. The pore pressures are measured by electronic transducers, and might be controlled by hydraulic pumps if desired. The axial force is applied on the top cap by a hydraulic piston. The radial stress is controlled by a hydraulic pump. The temperatures of the triaxial cells as well as the water exchange pumps are set and regulated to 20°C for all the tests.

Different mechanical loading paths can be adopted in the triaxial cell, with thorough descriptions available in the literature [18, 94]. The mechanical tests in the present work, schematically outlined in Figure 2.3, include the following loading paths:

- *Isotropic:* drained, undrained and unjacketed

- *Deviatoric*

A summary of the experiments together with the notation conventions adopted in the following is presented in Table 2.4. The tests were performed at different effective stress levels in order to explore the effects of such variable on the material properties, as discussed in the results section of the present manuscript.

All samples were cured for at least 120 days, corresponding to a hydration degree of 85% (see Chapter 4). Although the samples were kept in lime-saturated water during their curing period, the complete pore space saturation could not be asserted with certainty before the experiments, since the specimens are exposed to room conditions of 50% relative humidity during the triaxial test setup for at least 30 minutes. To assure the complete
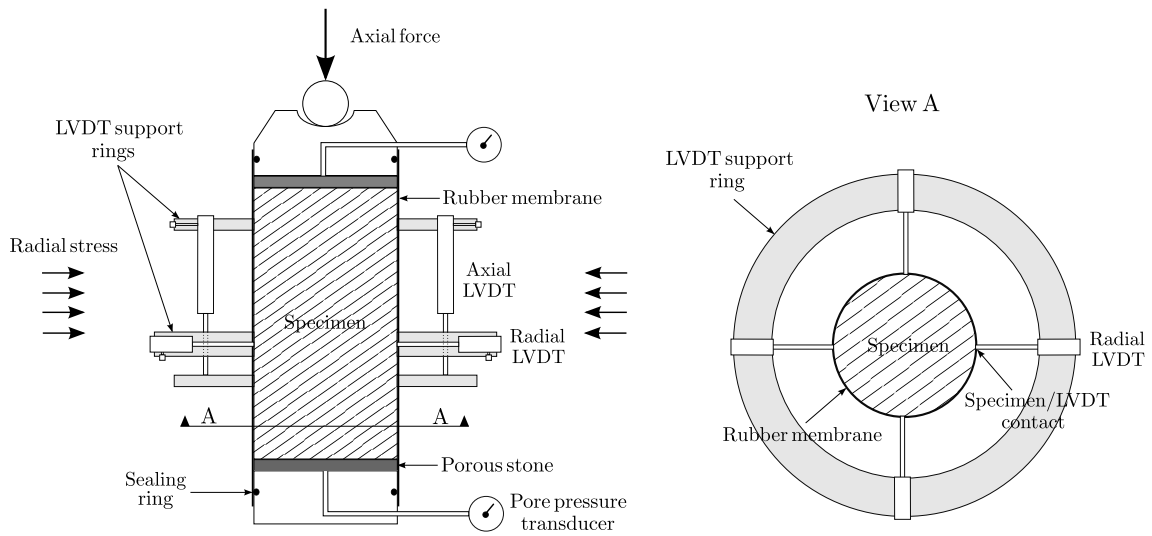
Figure 2.2: Schematic representation of the triaxial test setup. Supporting springs and axial LVDTs are not represented in the cross section for the sake of clarity.

(a) Drained isotropic

(b) Undrained isotropic

(c) Unjacketed isotropic

(d) Deviatoric
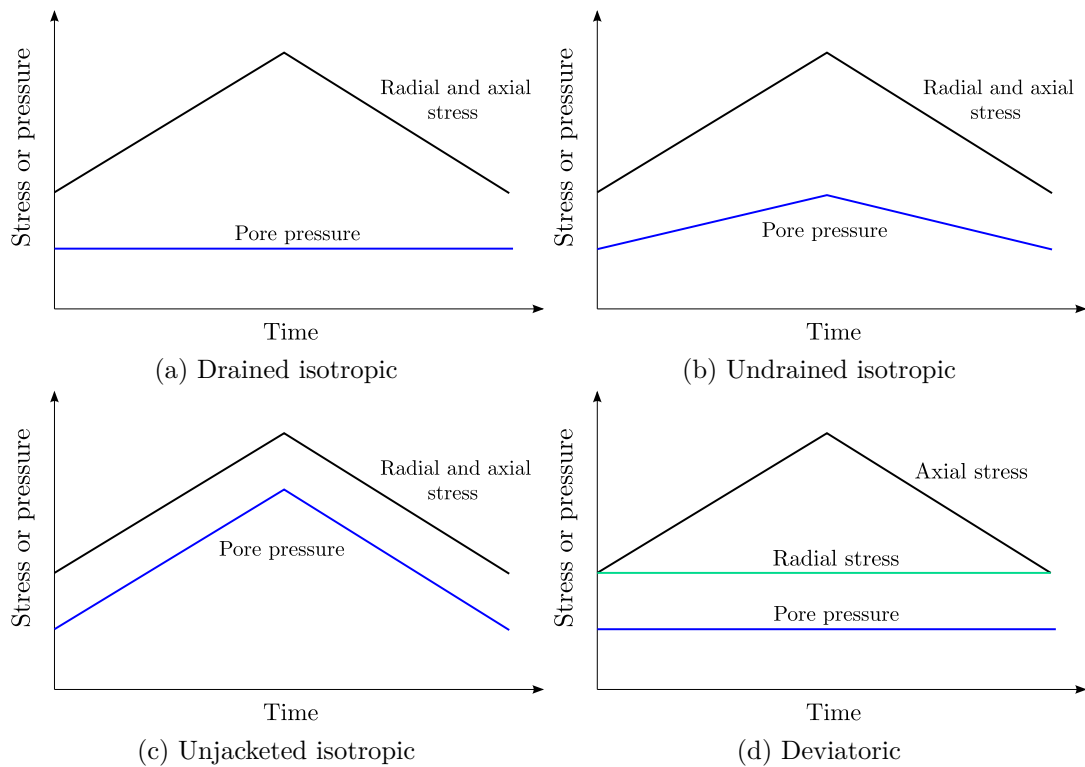
Figure 2.3: Typical loading paths of the triaxial experiments.

saturation before the execution of the experiments, the specimens inside the triaxial cell were confined under an effective stress of at least 4 MPa and a pore pressure of at least 1 MPa for 3 days before the application of the loadings. No significant fluid exchanges were recorded, suggesting the dissolution or absence of gas bubbles inside the pores of the

Table 2.4: Triaxial experiments

Reference	*Initial pressure (MPa)*		Loading	Load amplitude (MPa)	Specimen
	Confinement	Pore			
TX - D1	10	1	D	30	I
TX - D2	10	1	D	30	II
TX - D3	10	1	D	5	I
TX - D4	15	1	D	5	II
TX - D5	30	10	D	6	III
TX - D6	35	10	D	5	III
TX - D7	30	1	D	5	IV
TX - D8	43	10	D	5	III
TX - D9T20 *	4	2	D	31	V
TX - UD1	23	5	UD	16	I
TX - UD2	23	2	UD	16	II
TX - UJ1	21	11	UJ	19	I
TX - UJ2	39	5	UJ	-15	I
TX - DV1	17	8	DV	13	I
TX - DV2	15	8	DV	20-30	II
TX - DV3	13	8	DV	57	VI
TX - DV4	30	5	DV	-	VII

Loading types: D = Drained Isotropic; UD = Undrained Isotropic; UJ = Unjacketed Isotropic; DV = Deviatoric

* Cement paste hydrated at 20°C.

cement paste. The saturation degree of all specimens is hence considered to be 100%.

The adopted loading rate for the drained isotropic and unjacketed tests is of 0.01 MPa/min. The undrained loading rate is 0.015 MPa/min, with the top and bottom fluid exchange valves closed immediately after the pore pressure transducer. For deviatoric loading paths, we note that the ratio of increments of axial stress to mean stress is 1/3, and therefore the deviatoric loading rate should follow an equal ratio with respect to the isotropic loading rate. Therefore, we adopt a deviatoric loading rate of 0.03 MPa/min, although it is important to bear in mind that the previous analysis is only valid for the elastic domain, where the pore pressure and mean stress are related by the Skempton coefficient (consult Chapter 5).

The adopted loading rates are lower than those chosen by Ghabezloo [18] and Vu [8], who tested the same cement paste hydrated at higher temperatures (90 and 60°C, respectively). The decrease in loading rate accounts for the reduction of permeability of the cement paste expected as a consequence of the lower capillary porosity of the cement pastes hydrated at lower temperatures (see Section 6.2). The suitability of the loading rates has been previously discussed in the literature [18]. The loading rate in the drained, deviatoric and unjacketed tests has to be sufficiently low as to assure the dissipation of pore pressure and

its homogeneity throughout the specimen, while at the same time minimizing the viscous effects, specially significant at higher temperatures [8]. For undrained tests, the loading rate is theoretically unlimited, since the only requirement is to forbid mass exchanges of the specimen. In practice, however, the loading rate has to be limited to allow sufficient time for the transport and equilibrium of the fluid inside the pore pressure transducer connection conduits, if the pore pressure build-up is to be measured. The consideration of the dead volume of the measuring system, disregarded in the present work, leads to the correction of undrained poroelastic parameters, as discussed by Ghabezloo and Sulem [95].

2.2.3 Uniaxial experiments

Uniaxial tests are a simple mean to determine some of the basic mechanical properties of materials. A schematic representation is presented in Figure 2.4. A cylindrical sample is loaded axially under compression, whilst axial and radial strains are measured by means of strain gages.
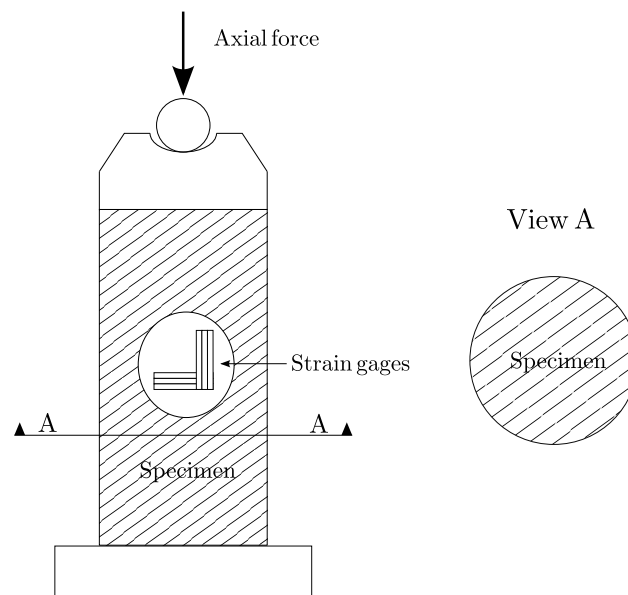
Figure 2.4: Schematic representation of the uniaxial test setup.

The adopted loading rate is of 0.025 mm/min, which corresponds to a deformation rate of 3.33×10^{-4}/min. This loading rate assures the dissipation of possible pore water over-pressures for the given specimen dimensions while minimizing the possible viscous effects by keeping the total test duration to a minimum. To minimize the fluid exchanges with the exterior, a coating of grease is applied on the surface of the specimens immediately before the experiments. This thin coating does not prevent the drainage of the sample, but serves to limit the evaporation of water through the sample surface, which is exposed to a 50% relative humidity in the testing room. The temperature of the room was regulated to 20 °C. A summary of the experiments together with the notation conventions adopted in

the following is presented in Table 2.5.

Table 2.5: Uniaxial experiments

Reference	Hydration conditions	
	T (°C)	Time (days)
UX - T7A1	7	1
UX - T7A3	7	3
UX - T7A14	7	14
UX - T7A120	7	120
UX - T20A120	20	120
UX - T60A120	60	120
UX - T90A120	90	120

2.2.4 Slurry To Cement Analyzer

The Slurry To Cement Analyzer (STCA) is an experimental device conceived for the study of the mechanical behaviour of cement paste from its earliest age in conditions of temperature and pressure that emulate those of the cement sheath in oil wells. A complete description of the different components and operation modes of the STCA is available in the works of Vu [8] and Agofack [16]. The same authors provide details of the validation, verification and calibration procedures that were performed on the device.
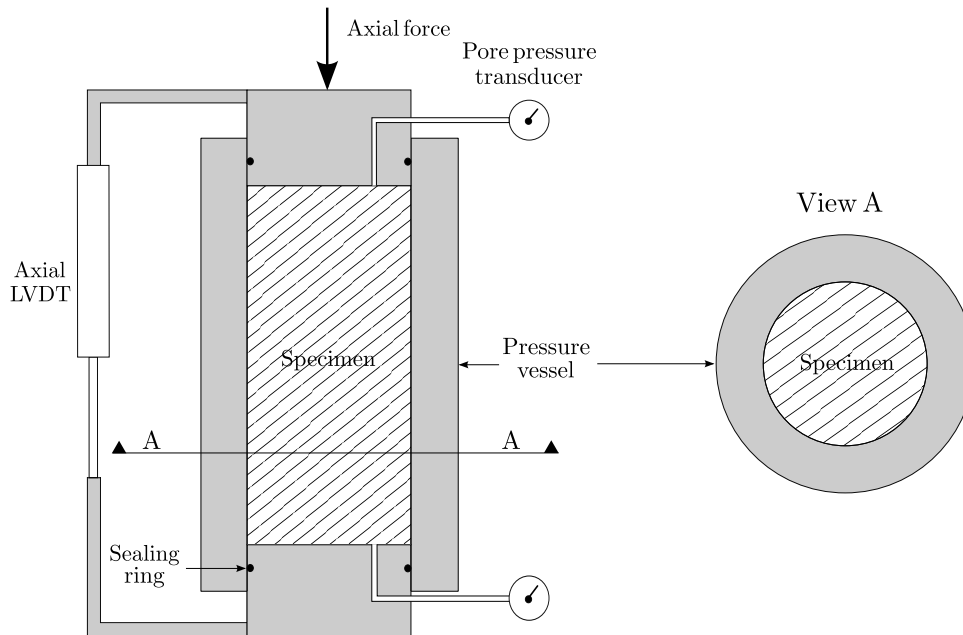
Figure 2.5: Schematic representation of the STCA oedometric test setup.

In the present work, the oedometric setup has been adopted for the study of a hydrating cement paste. A schematic representation of the device is presented in Figure 2.5. The

cylindrical pressure vessel, at controlled temperature, is filled with fresh cement slurry poured within the 5 minutes following its mixing. The specimen has a diameter of 50 mm and a height of 85 mm. The cement paste is immediately loaded by means of an axial piston with a maximum admissible stress of 120 MPa. The axial deformation is determined from the measurement of the longitudinal displacement with a LVDT. The interior surface of the steel cylinder is greased in order to minimize the friction among cell wall and specimen. As a result, the state of stress of the material can be considered homogeneous and the axial and lateral normal stresses are the principal stresses acting on the material.

A schematic illustration of the typical loading path of the oedometric STCA test is presented in Figure 2.6. The control of the experiment relies completely on the axial force. In the cyclic loading paths the loading rate is of 3 MPa/min. The lateral steel walls, 50 mm thick, are rigid enough as to be considered non-deformable, hence the oedometric or uniaxial strain designation. In all the experiments, no mass or fluid exchanges are allowed and, for a part of the experiments, the pore pressure variations were measured at both ends of the specimen.

(a) Monotonous followed by cyclic (b) Multi-cyclic
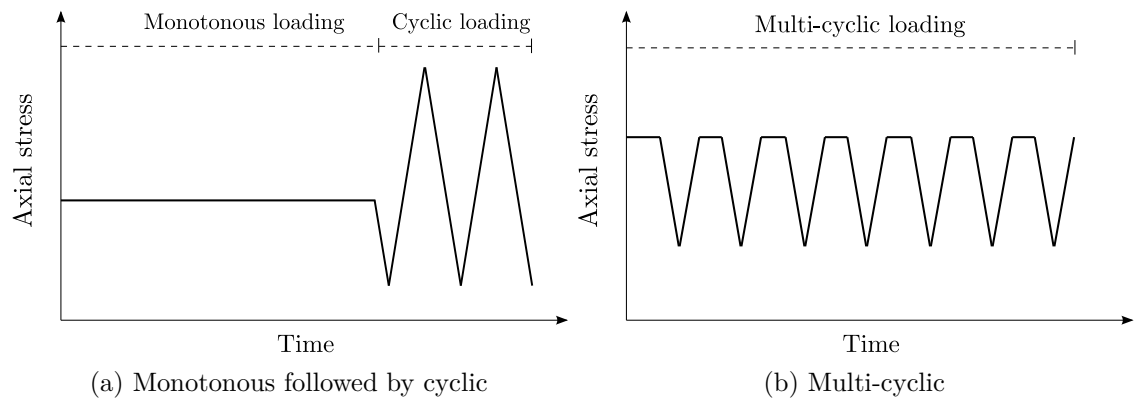
Figure 2.6: Typical loading path of the oedometric STCA experiments.

The time of application of the loading cycle depends on the hydration conditions. The load is applied when the axial strain rate becomes sufficiently small to allow the admission of a nearly constant hydration degree, simplifying the examination of the results. The summary of the experiments together with the notation convention adopted in the following is presented in Table 2.6.

Among the main features of the STCA oedometric setup is the possibility to mechanically load the cement paste from its earliest age [16]. Furthermore, the measurement of the pore pressure evolution in the sample can be related to the autogenous water consumption by hydration and the evolution of poromechanical properties of the cement paste from the onset of a percolating solid skeleton.

Table 2.6: Oedometric STCA experiments

Reference	Hydration conditions		Axial stress cycle time (hours)	Source
	Temperature (°C)	Axial stress (MPa)		
Monotonous followed by cyclic				
O - T7P3	7	3	144	Agofack [16]*
O - T7P25	7	25	144	Agofack [16]*
O - T7P45	7	45	287	Agofack [16]*
O - T20P3	20	3	60	Current work
O - T22P25	22	25	144	Agofack [16]*
O - T20P45	20	45	48	Current work
O - T60P3	60	3	24	Current work
O - T60P25	60	25	48	Current work
O - T60P45	60	45	48	Current work
O - T90P3	90	3	48	Current work
O - T90P25	90	25	48	Current work
O - T90P45	90	45	72	Current work
Multi-cyclic				
OC - T7P45	7	45	-	Agofack [16]*
OC - T20P45	20	45	-	Current work
OC - T60P45	60	45	-	Current work
OC - T90P45	90	45	-	Current work

*Pore pressure measurements not available.

2.2.5 Ultrasonic Cement Analyzer

The Ultrasonic Cement Analyzer (UCA) is an experimental device that has found a privileged place in the cement laboratories of the oil and gas industry. The device, conceived by Rao et al. [96], consists of a sealed steel vessel in which the cement slurry is hydrated under controlled temperature and pressure conditions. The longitudinal wave velocity V_L is monitored as the hydration reactions progress by means of a compressive wave pulse emitted through the sample, with recordings every 30 seconds for a duration of at least 48 hours or longer, depending on the hydration conditions. A schematic illustration is presented in Figure 2.7.

In a typical UCA test, the cement paste is poured into the cell within the 5 minutes following the mixing. The test temperature and pressure conditions are attained in no longer than 30 minutes for the target values considered in the present study. The cement hydration is retarded when necessary to allow the stabilization of the temperature and pressure conditions before the beginning of the hydration acceleration phase. The fresh slurry specimen has a diameter of 50 mm and a height of 85 mm, and rests below a 1.5 mm layer of water that serves to apply the objective pressure and allow a continuous travelling path for the ultrasonic waves. More details regarding the experimental procedure and test

setup can be found in ref. [97].
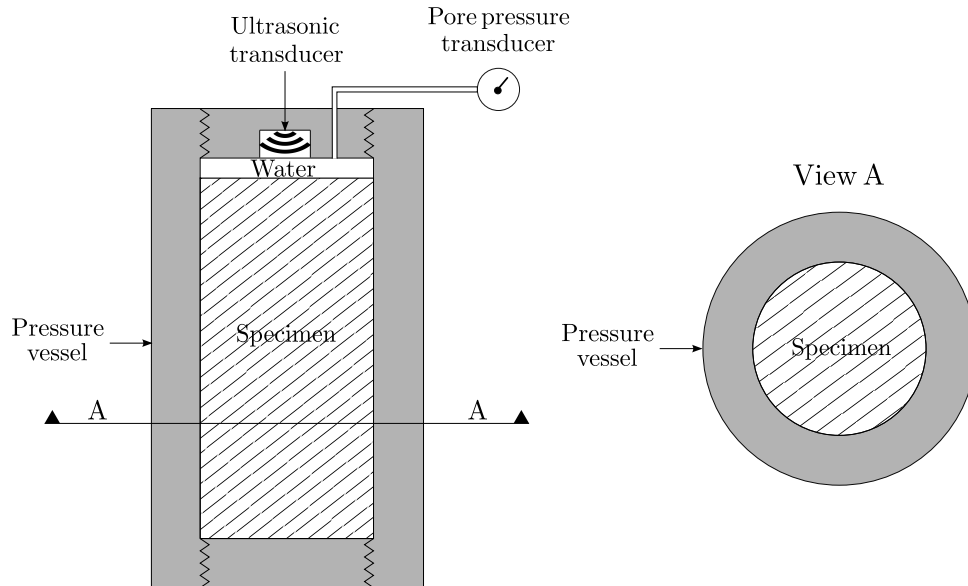
Figure 2.7: Schematic representation of the UCA setup.

The UCA is extensively employed for the estimation of the strength development of cement pastes, since wave velocity has been shown to correlate with the compressive strength of the cement paste, a guiding indicator for drilling operations in the field [96]. The correlation among these parameters has been exploited extensively in practice since, when compared with more traditional crush tests [17], the UCA tests resemble closely the hydration conditions in the well and have the advantage of being non-destructive, therefore providing continuous information with significantly less effort. In our applications, however, we will not attempt to correlate strength with velocity, but rather appeal to the determination of elastic moduli from the wave velocity according to the theory of elastic wave propagation in porous media.

The possible influence of pressure and temperature conditions on the measured wave velocity has been examined by Vu [8] for the same device used in the present work. From his experimental measurements of longitudinal wave velocity in water, determined between temperatures of 20 to 62°C and pressures from atmospheric to 42 MPa, he concluded that the discrepancies with respect to reference literature values (e.g. ref. [98]) can be estimated to be lower than 1%. These small effect will therefore be disregarded since they do not significantly change the overall results. In consequence, the experimentally determined values are considered to reflect the real values within the previously mentioned precision range.

All tests were run on a Chandler 4265-HT UCA, with maximum temperature and pressure ratings of 315°C and 135 MPa, respectively. A summary of the experimental conditions

together with the notation conventions adopted in the following is presented in Table 2.7.

Table 2.7: UCA experiments

Reference	Hydration conditions		Source
	T (°C)	P (MPa)	
UCA - T7P0	7	0.1	Vu [8]
UCA - T7P15	7	15	Agofack [16]
UCA - T7P25	7	25	Agofack [16]
UCA - T25P0	25	0.1	Vu [8]
UCA - T25P25	25	25	Current work
UCA - T25P45	25	45	Current work
UCA - T40P0	40	0.1	Current work
UCA - T40P25	40	25	Current work
UCA - T40P45	40	45	Current work
UCA - T60P0	60	0.1	Current work
UCA - T60P25	60	25	Current work
UCA - T60P45	60	45	Current work
UCA - T90P0	90	0.1	Current work
UCA - T90P25	90	25	Current work
UCA - T90P45	90	45	Current work

2.2.6 Mercury intrusion porosimetry

Mercury intrusion porosimetry (MIP) is among the most widely used experimental techniques for the analysis of the microstructure of ceramic materials [99]. It consists in the injection of fluid-state mercury under pressure into the porous space of the material specimen. Mercury is preferred because it is non-wetting and chemically inert when in contact with most tested materials. MIP constitutes a simple and efficient experimental method for probing the microstructure of the cement paste porous space requiring only three physical parameters: pore geometry, contact angle and surface tension.

The mass of the material sample is in the order of 1 gram due to the limited volume of the intrusion chamber, known as penetrometer, as well as to assure reasonable times for the penetration of the mercury throughout the tortuous pore voids. It is important, however, to use samples that remain sufficiently representative volumes to average possible heterogeneities. The similarity of sample volumes for different tests is important to assure the consistency of the results, for the same reasons mentioned above.

The preparation of the sample prior to intrusion requires the removal of the fluids in the pore space, achieved in our experiments by freeze-drying. The comprehensive comparison of cement paste drying and hydration arresting methods suggests that freeze-drying effectively removes the free water from the pores, thus arresting the chemical reaction, while causing minimal damage to the microstructure [100, 101].

Inside the penetrometer and before the injection, a very low vacuum is applied to the sample which, together with the low vapour pressure of mercury, assure a negligible gas pressure, the capillary pressure being therefore given directly by the injection pressure. Calibration runs are performed beforehand to correct the parasitic effects due to the injection chamber and mercury compression or dilation as the injection is executed.

There has been significant criticism of the MIP methodology, notably regarding the interpretation of the results [99, 102]. One of the main remarks concerns the frequent use of MIP to estimate pore size distributions, which is inappropriate mainly due to ink-bottle effects. Indeed, one can only determine pore entry distributions from the injection results, which is the main use to be made of the results in the current work. In addition, only the connected porosity can be measured by the intrusion, for which the occluded pores remain invisible.

All tests were run on an AutoPore IV 9500 Micromeritics, with a maximum pressure of 230 MPa. A summary of the experimental conditions together with the notation conventions adopted in the following is presented in Table 2.8.

Table 2.8: MIP experiments

Reference	Hydration conditions	
	T (°C)	Time (days)
MIP - T7A1	7	1
MIP - T7A3	7	3
MIP - T7A7	7	7
MIP - T7A14	7	14
MIP - T7A28	7	28
MIP - T20A1	20	1
MIP - T20A3	20	3
MIP - T20A7	20	7
MIP - T20A28	20	28
MIP - T20A60	20	60
MIP - T40A28	40	28
MIP - T60A28	60	28
MIP - T90A28	90	28

Part I

Hydration kinetics

Chapter 3

A comprehensive framework for the modelling of cement hydration kinetics: application to multi-component nucleation and diffusion-enriched growth

3.1 Introduction

In this chapter, we propose to revisit the formulation of hydration kinetics models with the aim of developing a comprehensive framework appropriately describing the fundamental physical mechanisms of the hydration reaction throughout the various steps of its evolution. In our view, a complete hydration model is the result of the combination of two essential modelling components: volume filling and growth kinetics. This chapter devotes a part to each of these components, which can be approached independently.

The first part concerns the transformation of the system volumes from reactants to hydrates with the evolution of the reaction. We present the basic rules of volume filling and interaction among phases in a multi-component domain such as a cement paste. We first introduce the notions of transformed mass and volume fractions, reviewing the underlying implicit assumptions in the traditional models. Additionally, the mechanisms of interaction among these phases in a hydrating cement are described.

The second part presents the growth kinetics models, describing the evolution of the hydrates formation. We employ profusely the concept of extended volume, defined as the transformed volume fraction without considering interactions –overlapping and impingement–

with its surrounding [56]. The hydrates are considered to grow isotropically from their nucleation sites following either a linear or parabolic-diffusion growth rate.

The result of the combination of volume filling and growth kinetics models is a comprehensive hydration kinetics model. A general framework is thus made available for the formulation and tailoring of hydration models according to desirable physical mechanisms and features, adding significant flexibility and simplifying the analysis of complex reaction processes. The proposed modelling framework overcomes the two main limitations of previous hydration kinetics models, i.e. mechanism discontinuity and single-component reaction.

Finally, we present application cases demonstrating that the comprehensive description of the entire hydration kinetics is henceforth possible with a single hydration model formulated with adequate physical features. The applications include the simulation of cement paste hydration kinetics under different conditions (hydration temperature and pressure, cement fineness, water to cement ratio), together with the examination of the resulting parameters from the fitting of the model to the experimental results.

3.2 Volume filling model

3.2.1 Volume and mass fractions of the cement paste

We consider the cement paste as composed of three main phases: anhydrous cement powder, mixing water and hydrates.[1] The volumes and masses of these components are those presented in Figure 3.1 for a unitary cement mass. These components are homogeneously distributed in the elementary representative volume, but distinct at the scale of the hydration transformations.

In the following, we adopt the naming conventions ρ_c, ρ_w and ρ_h for the cement, water and hydrates mass densities respectively. The water to cement ratio of the cement paste is given by w, while w_h is the water to cement ratio consumed in the hydration of a unitary mass of cement. In addition, the definition of the ratio $w_r = w/w_h$ will prove convenient: if $w_r \geq 1$, the mixing water is sufficient to hydrate the totality of the mixing cement powder; if $w_r \leq 1$, only a fraction w_r of the initial cement powder mass can be hydrated by the mixing water. From mass conservation of the closed system, the mass fractions of the different phases are:

$$m_c = \frac{1 - \alpha}{1 + w}; \quad m_w = \frac{w - \alpha\, w_h}{1 + w}; \quad m_h = \frac{\alpha\,(1 + w_h)}{1 + w} \tag{3.1}$$

---

[1]For simplicity, we will refer to the anhydrous cement powder simply as cement or clinker.
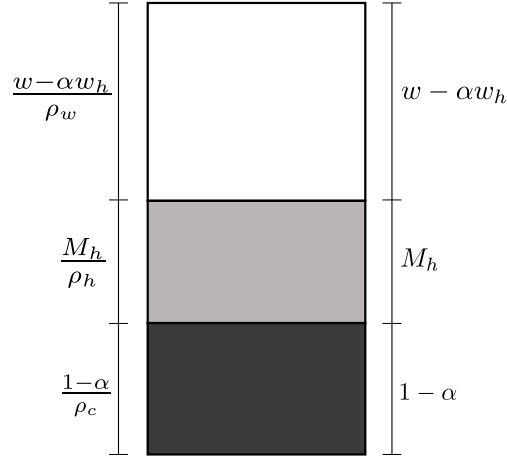
Figure 3.1: Volume (left) and mass (right) distributions for a cement paste, featuring cement powder (bottom), hydrates (middle) and water (top). For convenience, normalization is with respect to the cement powder mass.

where the hydration degree of the cement paste α is defined as

$$\alpha = 1 - \frac{M_c(t)}{M_c(t=0)} \tag{3.2}$$

with $M_c(t)$ the mass of cement powder at time t.

The volume of a system with an initially unitary volume evolves with hydration as:

$$V = 1 - \alpha\xi/V_0 \tag{3.3}$$

where $V_0 = 1/\rho_c + w/\rho_w$ is the initial volume of the cement paste per unit mass of cement powder, while ξ is the chemical shrinkage, defined in terms of volume per unit cement mass as:

$$\xi = \underbrace{\left(\frac{1}{\rho_c} + \frac{w_h}{\rho_w}\right)}_{\text{Vol. reactants}} - \underbrace{\frac{1+w_h}{\rho_h}}_{\text{Vol. products}} \tag{3.4}$$

In the previous expressions, we have assumed that the chemical shrinkage is converted to macroscopic volumetric shrinkage. This hypothesis is valid in the early stages, when the solid skeleton has not yet percolated. We revisit the consequences of this assumption in Section 3.2.3.2.

For the sake of simplicity, we will assume in the following that the chemical shrinkage is constant throughout the reaction. The previous definitions allow expressing volume fractions as:

$$v_c = \frac{1-\alpha}{\rho_c\,(V_0 - \alpha\,\xi)}; \quad v_w = \frac{w - \alpha\,w_h}{\rho_w\,(V_0 - \alpha\,\xi)}; \quad v_h = \frac{\alpha\,(1+w_h)}{\rho_h\,(V_0 - \alpha\,\xi)} \tag{3.5}$$

where hydrates mass density ρ_h is given by:

$$\rho_h = \frac{1 + w_h}{\dfrac{1}{\rho_c} + \dfrac{w_h}{\rho_w} - \xi} \tag{3.6}$$

thus also allowing to express v_h as:

$$v_h = \frac{\left(\dfrac{1}{\rho_c} + \dfrac{w_h}{\rho_w} - \xi\right)}{\left(\dfrac{1}{\rho_c} + \dfrac{w}{\rho_w} - \alpha\,\xi\right)}\, \alpha \tag{3.7}$$

The expressions we have derived can be generalized for the case of more than two reacting phases, allowing to account for different hydration products and reactant phases if so required.

Although not explicitly stated, a significant number of hydration models adopt the hypothesis of equivalence between hydration degree and volume fraction of hydrates [3, 37, 48]. We can deduce from Equation (3.5) that the hypothesis $v_h = \alpha$ is valid for its original intended application to metal solidification, where a single reacting component is present and there are no significant density changes between the initial and final components (i.e. $w = w_h = \xi = 0$). In the case of a cement paste, the validity of this assumption can be evaluated in Figure 3.2 for $w_h = 0.4$, an average value for usual cement compositions. The specific mass of clinker being nearly constant for cement compositions, the ratio is determined by parameters w_r and ξ. An increase of w_h results in larger discrepancies. It can be observed that the assumption $v_h = \alpha$ is only appropriate for the very restricted case $w_r = 1$, $\xi = 0$.

3.2.2 Model formulation

For the formulation of the space filling model, we appeal to the concept of extended volume [56], which corresponds to an imaginary volume of hydrates for which the neighbouring material is considered as invisible, thus allowing mutual impingement.

Consider a tentative growth step during which we introduce into the domain an extended volume $\mathrm{d}V^e$. In a system composed of n phases, the likelihood of a randomly chosen material point being part of the ith phase is $v_i = V_i / \sum_{j=0}^{n} V_j$, where V_i is the volume of phase i and v_i its volume fraction. The extended volume $\mathrm{d}V^e$ will thus be split among the different phases in proportions equal to their respective volume fractions. If we expect a tentative of growth into phase i to be successful with a probability p_i, we can determine the real transformed volume $\mathrm{d}V$ generated due to the introduction of the extended volume $\mathrm{d}V^e$ as:

$$\mathrm{d}V = \mathrm{d}V^e \sum_{i=0}^{n} p_i v_i \tag{3.8}$$
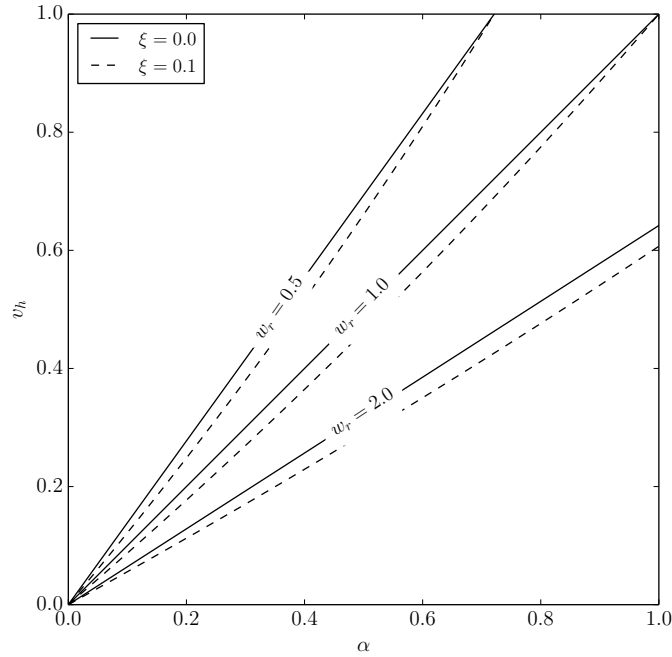
Figure 3.2: Hydration degree α and transformed volume fraction of hydrates v_h ($w_h = 0.4$).

where $\mathrm{d}V \leq \mathrm{d}V^e$ since $\sum v_i = 1$ and $p_i \leq 1$.

The growth of the newly-formed regions leads, eventually, to them coming in contact with each other. Following this contact, a pair of growing volumes might either unite in a single volume, separate and continue their independent growth, or develop a common interface, across which the growth is restricted [59]. The latter case corresponds to the hypothesis $p_i = 0$, meaning that there are no successful attempts on a given fraction. In general, although the introduction of an extended volume is always possible, its transformation into an actual physical volume depends on p_i.

Applying the previous notions to the case of solidifications of metals is straightforward. The domain is split in two phases: untransformed liquid volume l, of fraction $1 - \alpha$, and transformed solid volume s, of fraction α. If we consider all attempts of growth in the untransformed volume to be successful ($p_l = 1$), while all attempts in the transformed volume are unsuccessful ($p_s = 0$), we derive the expression employed in the NG model [56]:

$$\mathrm{d}V = \mathrm{d}V^e \left(1 - \alpha\right) \tag{3.9}$$

In the case of a cement paste Equation (3.8) becomes:

$$\mathrm{d}V_h = \mathrm{d}V_h^e \left(p_c\, v_c + p_w\, v_w + p_h\, v_h\right) \tag{3.10}$$

where $\mathrm{d}V_h$ and $\mathrm{d}V_h^e$ are the transformed and extended volume increments of the hydration

products.

As anticipated, we might regard p_c, p_w and p_h as the success rate of the growth attempts, and therefore as strictly non-negative. A wider interpretation contemplates the possibility of negative values, implying certain fractions could act as transformation inhibitors or retarders. Although not presented here, a particularly interesting case consists in assuming self-similar growth kinetics inside the hydrates, in a recursive series of steps.

For the current model, we will consider all growth attempts into hydrates as unsuccessful, i.e. $p_h = 0$. This seems to be the most appropriate hypothesis for the cement paste: even if the initial state is fluid and hydrate volumes could distance each other, the percolation of the solid structure constrains growth and leads to the appearance of common interfaces once the hydration is sufficiently advanced.

For the water and cement phases, since the hydration reaction requires the participation of two reactants, the success rate of growth attempts depends on the availability of the co-reactant phase. The likelihood of success of the growth attempt is given by the probability of finding the appropriate complementary reactant, which we will consider equal to the concentration of such reactant, i.e. $p_c = v_w$ and $p_w = v_c$. The consideration of two reactants and their interaction constitutes a distinctive feature of the present formulation.

For an initial unitary untransformed volume, for which the overall volume V evolves with the reaction, the volume of hydrates is given by $V_h = v_h V$, allowing to rewrite Equation (3.10) as:

$$\mathrm{d}(v_h\, V) = 2\, v_w v_c \, \mathrm{d}V_h^e \tag{3.11}$$

where $\mathrm{d}V_h^e$ is the extended volume increment per unit initial untransformed volume.

For any given phase, if only a fraction is available for transformation, we might divide its volume in two parts, one of which will have null success rate. This provides a simple mean to introduce the ultimate hydration degree as a function of the cement mass consumption by considering only a fraction α_u of cement powder will be consumed. Replacing the volume fractions from Equation (3.5) into Equation (3.11), the expression to integrate becomes:

$$V_h^e = \int_0^t \mathrm{d}V_h^e = \frac{z}{\alpha_u w_r} \int_0^\alpha \frac{\left(1 - \dfrac{\xi}{V_0}\bar{\alpha}\right)^2}{\left(1 - \dfrac{\bar{\alpha}}{\alpha_u}\right)\left(1 - \dfrac{\bar{\alpha}}{w_r}\right)} \, \mathrm{d}\bar{\alpha} \tag{3.12}$$

where $\bar{\alpha}$ is a dummy integration variable and the dimensionless parameter z is defined as

$$z = \frac{(1 + w_h)}{2\, w_h} \frac{\rho_w\, \rho_c}{\rho_h} V_0 \tag{3.13}$$

The previous expression can be integrated, yielding:

$$V_h^e = z \left[\left(\frac{\xi}{V_0}\right)^2 \alpha - \frac{\left(1 - \alpha_u \frac{\xi}{V_0}\right)^2}{w_r - \alpha_u} \ln\left(1 - \frac{\alpha}{\alpha_u}\right) + \frac{\left(1 - w_r \frac{\xi}{V_0}\right)^2}{w_r - \alpha_u} \ln\left(1 - \frac{\alpha}{w_r}\right) \right] \quad (3.14)$$

If the available water is completely consumed by hydration, i.e. $w_r = \alpha_u$, the expression becomes:

$$V_h^e = z \left[\left(\frac{\xi}{V_0}\right)^2 \alpha + \left(\frac{1}{\alpha_u} - \frac{\xi}{V_0}\right)^2 \frac{\alpha}{1 - \alpha/\alpha_u} - \frac{2\alpha_u \xi}{V_0} \left(\frac{1}{\alpha_u} - \frac{\xi}{V_0}\right) \ln\left(1 - \frac{\alpha}{\alpha_u}\right) \right] \quad (3.15)$$

and thus for the case $w_r = \alpha_u = 1$:

$$V_h^e = z \left[\left(\frac{\xi}{V_0}\right)^2 \alpha + \left(1 - \frac{\xi}{V_0}\right)^2 \frac{\alpha}{1 - \alpha} - \frac{2\xi}{V_0} \left(1 - \frac{\xi}{V_0}\right) \ln\left(1 - \alpha\right) \right] \quad (3.16)$$

These rich expressions consider the main characteristics of a cement paste: the multi-component nature of the mixture, the fractions of active reactants, the effects of excess water and the chemical shrinkage of the hydrates.

In practice, for typical values of ξ, terms $\mathcal{O}(\xi^2)$ might be neglected. Furthermore, completely overlooking changes of the total volume during hydration, i.e. $\xi = 0$, leads to an explicit expression for α:

$$\alpha = \frac{1 - \exp\left[\frac{(\alpha_u - w_r)}{z} V_h^e\right]}{1/\alpha_u - \exp\left[\frac{(\alpha_u - w_r)}{z} V_h^e\right] / w_r} \quad (3.17)$$

If the available water is completely consumed by hydration, i.e. $w_r = \alpha_u$, we obtain the remarkably simple expression:

$$\alpha = \frac{\alpha_u^2 V_h^e}{z + \alpha_u V_h^e} \quad (3.18)$$

and thus for $w_r = \alpha_u = 1$:

$$\alpha = \frac{V_h^e}{z + V_h^e} \quad (3.19)$$

These expressions constitute the extension of the volume filling model of Avrami to the case of a multi-component and multi-reactant system.

3.2.3 Analysis and discussion

The current section explores the main consequences and predictions of our volume filling model. We quantify the effect of model parameters by assuming the same evolution of

V_h^e –same growth kinetics– for the models we ought to compare, thus avoiding the need to effectively evaluate the extended volume from a kinetic growth model. We determine isochronous reaction degrees from reaction curves with different parameters, and compare the reaction extent to a reference reaction curve. The procedure is illustrated in Figure 3.3. In the following figures, the diagonal line with unitary slope corresponds to the reference test. In comparison, faster reactions will be above this diagonal master line, while slower reactions will be below it. We chose a reference reaction curve for which $w_h = 0.4$, $w_r = \alpha_u = 1$ and $\xi = 0$.
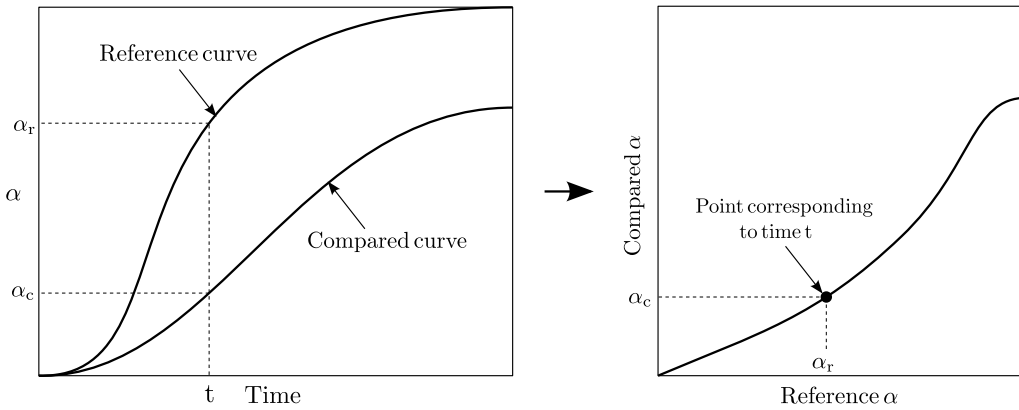
Figure 3.3: Procedure for comparing hydration curves. Left: the hydration degree of the curves to compare is determined for time t. Right: the hydration degrees are represented together.

3.2.3.1 Availability of water

The parameter w_r provides a measurement of the availability of water for the reaction. Values equal or above unity imply sufficient water is available for the complete hydration of the cement powder, while values lower than unity will limit the ultimate hydration degree to w_r. Water-diluted mixtures have large values of w_r, while dry mixtures have low values.

It is worth noting that we do not require the supersaturation of the pore solution for the precipitation of the products. In practice, a mixture with very large w_r would not precipitate because of the impossibility to reach supersaturation with respect to the hydration products [41]. In a more rigorous approach, we would correct the initial fractions to account for the initial dissolved mass before the beginning of the formation of hydrates. Furthermore, we consider the characteristic diffusion time in the pore solution as negligible when compared to nucleation, growth or diffusion processes. This will likely have an influence when the dissolution times are important, as could be the case in highly diluted mixtures.

The consequences of the lack or excess of water can be observed in Figure 3.4. If $w_r < 1$, the hydration stops at $\alpha = w_r$, while if $w_r \geq 1$ the hydration proceeds until completion. The excess water accelerates the reaction, but such acceleration is limited. The reaction

becomes progressively insensitive to an increase of w_r, with very large amounts of water needed for marginal accelerations. Indeed, for very large w_r, and for $\alpha_u = 1$, $\xi = 0$, Equation (3.14) becomes:

$$\alpha = 1 - \exp\left(-\frac{2\rho_w}{\rho_w + w_h\rho_c}V_h^e\right) \tag{3.20}$$
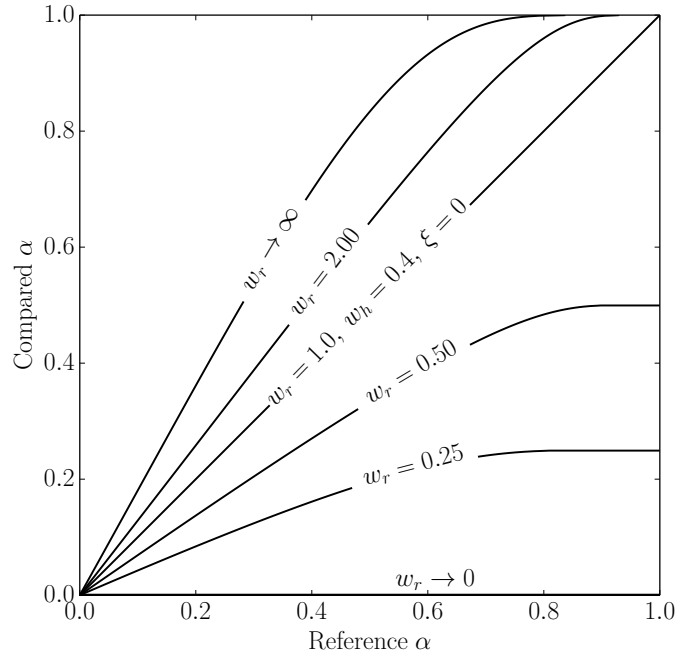
Figure 3.4: The effect of w_r on the hydration reaction.

From the previous equation, we can infer the condition leading to the NG model [56] in the case of multi-component reaction:

$$\frac{2\rho_w}{\rho_w + w_h\rho_c} = 1 \quad \rightarrow \quad \frac{w_h}{\rho_w} = \frac{1}{\rho_c} \tag{3.21}$$

The NG expression is consistent with a large excess of one of the reacting components a non-shrinking ($\xi = 0$) reaction product combining equal volumes of reactants. These very special conditions are far from those of the usual cement paste mixtures.

3.2.3.2 Properties of hydrates: water consumption, chemical shrinkage and density variations

The composition and density of the hydration products are accounted for by means of parameters w_h and ξ, whose values can be either calculated analytically or determined experimentally as discussed in Section 3.5.

The effect of the water required for hydration of the cement powder is presented in

Figure 3.5. For the reference scenario with $w_r = 1$ and $\xi = 0$, the maximum rate occurs for $w_h = \rho_w/\rho_c \approx 0.32$, corresponding to equal initial volume factions for both reactants. The difference with respect to the reference case is marginal and practically indistinguishable, and for such reason has not been represented. In practice, for typical values of $w_h \approx 0.4$, compositions requiring more water have an overall slightly slower hydration.
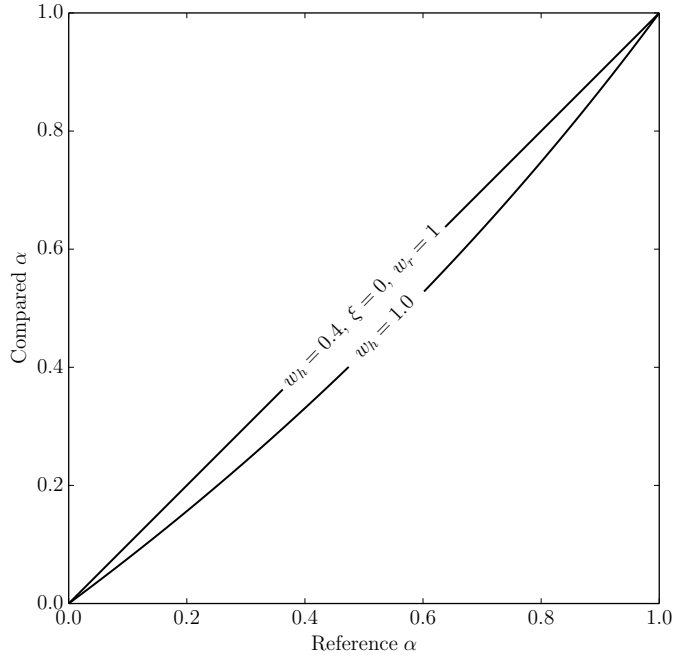
Figure 3.5: The effect of w_h on the hydration reaction.

Regarding chemical shrinkage, its effect on volume fractions will be effective as long as the solid skeleton has not percolated. After percolation, chemical shrinkage is mostly assimilated as macroscopic porosity and thus included in the volume fraction of hydrates, no longer affecting the resulting volume filling evolution. The effect of chemical shrinkage can be assessed in Figure 3.6. The chemical shrinkage results in an acceleration of the reaction which, for typical values of ξ, might be neglected for the sake of simplicity without significant consequences. We also present the effect of swelling, opposite to that of chemical shrinkage, that characterizes some special cement formulations (see, e.g. ref. [103]).

The changes of hydrate densities are useful, for instance, to assess the impact of hydration temperature on volume filling, excluding growth kinetic effects. As discussed by Gallucci et al. [104] and Bahafid et al. [23], higher densities, corresponding to higher hydration temperatures, result in variations of w_h and ξ, with effects that can be estimated from Equation (3.14) and observed in Figures 3.5 and 3.6.

In addition, the density of hydration products ρ_h might evolve as the reaction progresses, mainly due to the lack of space and physical constraints imposed on the forming skeleton [31]. To accommodate this modification, the formal mathematical statement of the problem
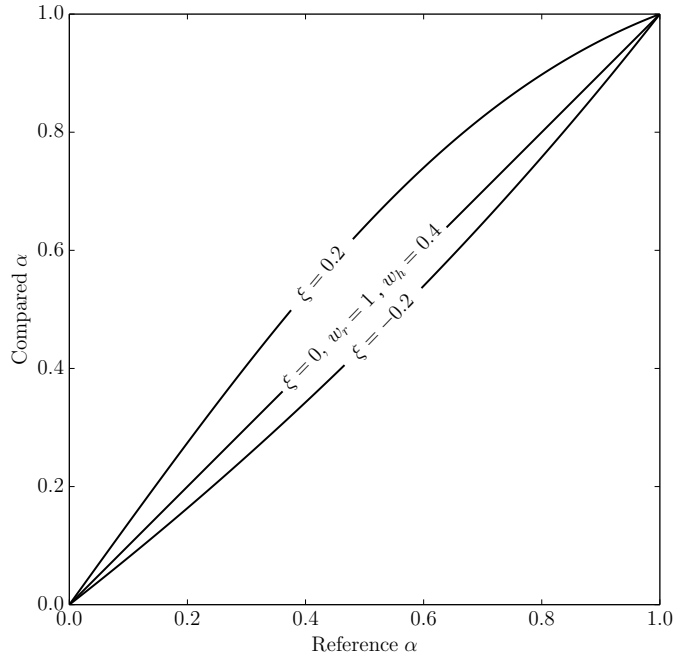
Figure 3.6: The effect of ξ on the hydration reaction.

has to be reconsidered from Equation (3.11) onwards which, together with Equation (3.7), allows expressing the differential $\mathrm{d}(v_h V)$ as:

$$\mathrm{d}(v_h V) = \left(\frac{1}{\rho_c} + \frac{w_h}{\rho_w} - \xi\right) \mathrm{d}\alpha + \alpha \left(\frac{\mathrm{d}w_h}{\rho_w} - \mathrm{d}\xi\right) \tag{3.22}$$

An increase of w_h leads to a higher volume of hydrates, while the opposite is true for increments of ξ. It is worth noting that w_h and ξ are associated to the overall hydrates production, resulting from the integration of instantaneous variations. For typical cement mixtures with small variations of product density, it is reasonable to neglect the last terms of the right hand side of Equation (3.22). The changes of hydrate density might thus be accounted by updating only the first term, so that no changes are necessary in the mathematical expressions we have previously derived.

From the previous observations, we conclude that typical hydrate density variations have minor consequences on the volume filling models. If hydrate density is to have a significant effect, as suggested by some authors [54, 105], we expect it to manifest predominantly in the growth kinetics model parameters.

3.2.3.3 Ultimate hydration degree

The hydration reaches an ultimate plateau by either water or clinker exhaustion. To limit the clinker consumption, we have incorporated only a fraction of it as consumable mass. Additionally, as previously discussed, if the water in the mixture is insufficient for hydration,

the reaction will naturally be arrested. The effective ultimate hydration degree is therefore the lowest among α_u and w_r. The influence of the parameter α_u is presented in Figure 3.7.
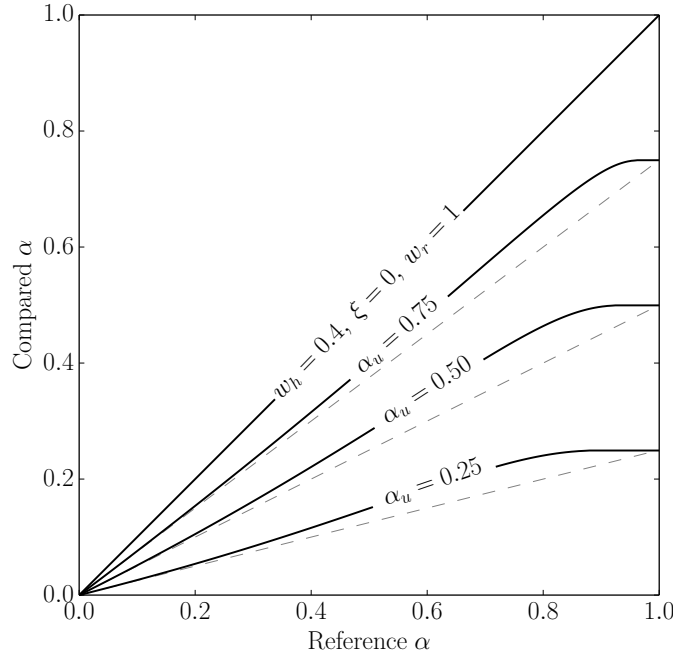
Figure 3.7: The effect of α_u on the hydration reaction. Dashed lines correspond to linear scaling by α_u.

It is important to note that the curves are not linear. This is to be contrasted with the common practice of scaling the hydration curve by a factor α_u to derive the curve corresponding to such ultimate hydration degree [106, 107] or correcting the curves by a scale factor corresponding to the transformed fraction [3, 60]. The consideration of an ultimate hydration degree in a single-reactant configuration requires rewriting Equation (3.9) as:

$$dV = (\alpha_u - \alpha) \, dV_h^e \tag{3.23}$$

for which, assuming a constant density (i.e. $\xi = 0$), we obtain the expression for the hydration degree:

$$\alpha = \alpha_u \left[1 - \frac{\exp(-V_h^e)}{\alpha_u} \right] \tag{3.24}$$

The linear scaling can only be seen as an approximation even in the simplified single-reactant configuration.

3.3 Growth kinetics model

The growth kinetics models describe the extended volume of hydrates V_h^e, requiring the definition of the the growth rate and geometry of the hydrates, as well as their nucleation

distribution in time and space.

3.3.1 Growth rate and shape of hydrates

The main product of hydration in the reaction of the clinker phases is the calcium silicate hydrate phase (C–S–H), produced along with Portlandite (CH) and some other minor hydration products [19]. Microscopic observation of the C–S–H hydrates reveals their laminar and fibrous structures [63, 108], as depicted in widely employed C–S–H microstructural models [1, 29]. It is essential, however, to note that the growth of the products is dependent on their packing and spatial distribution, rather than their underlying morphology. In the case of C–S–H, their clusters are disordered and suggest no preferential orientation, allowing the adoption of spherical hydrate volumes as the averaged result of these randomly-oriented needles. The growth of the hydration products can consequently be considered isotropic.

We propose a simple equation for the advancement of the transformed hydrates front that satisfies a phase boundary-controlled growth in the early age and later yields to diffusion control with a simple mathematical expression. Considering a germination point growing from an initial time $t = 0$, we adopt the following expression for the front advance:

$$r = \frac{Gt}{1 + \left(\dfrac{G^2 t}{2D}\right)^{1/2}} \tag{3.25}$$

The expression is particularly advantageous because it allows a smooth transition of the growth control. Indeed, consider the two extreme cases for small and large $\left(\frac{G^2}{2D}t\right)^{1/2}$:

$$r = Gt \qquad\qquad \text{for } \left(\frac{G^2}{2D}t\right)^{1/2} \ll 1 \tag{3.26a}$$

$$r = (2Dt)^{1/2} \qquad\qquad \text{for } \left(\frac{G^2}{2D}t\right)^{1/2} \gg 1 \tag{3.26b}$$

The fist expression corresponds to a boundary control growth rate, where G is the growth rate of the boundary-control mechanism. This growth rate may be itself a function of time, depending strongly on the driving force, i.e. the difference of free energy among the product and reactant configurations.

The second expression corresponds to a parabolic diffusion law, where D is the diffusion constant. Diffusion-controlled growth has often been adopted for the modelling of the late phases of cement hydration, but displayed unlimited growth rate at the mechanism-transition threshold (consult ref. [37]).

The transition of the control mechanisms and the deceleration of the advancement front is made clear in Figure 3.8, where the two characteristic slopes can be observed. Initially, the advance is boundary-controlled, with a rate G that we consider constant. As the transformation front advances, the transition of the mechanisms takes place, with an estimated transition time

$$\tau_d = \frac{2D}{G^2} \tag{3.27}$$

The two asymptotic lines represent the limiting behaviours. At any given time, these describe the position of the front according to either mechanism. The resulting advance corresponds to the slowest among these two, with a smooth transition in the intersection neighbourhood.
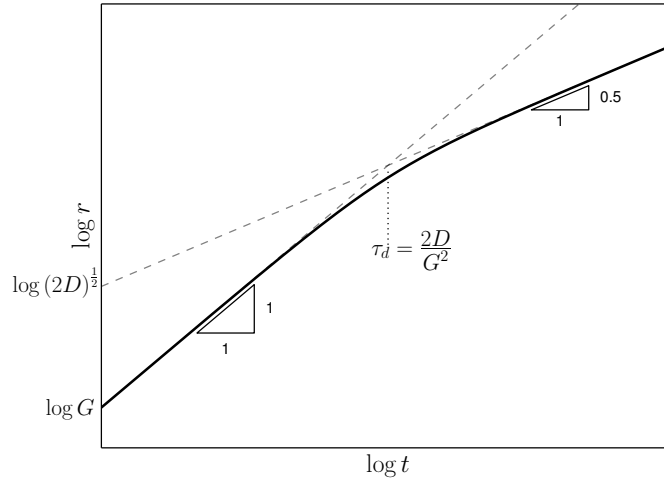
Figure 3.8: Schematic evolution of the linear dimension with time in logarithmic scale. Note the two characteristic slopes of the evolution: early age boundary control and long term diffusion control. The estimated transition time is indicated.

It is important to note that the proposed growth law expressed in Equation (3.25) possesses only two parameters: G controlling the first phase and D controlling the second phase. By adopting this hypothesis, we are implicitly imposing the transition time. In addition, we have assumed that the diffusion resistance is proportional to the coating thickness: early, when the process is boundary-controlled, the thickness is small and diffusion does not have a significant effect; only later we observe, as the layer thickens, the delaying of the growth rate due to the low permeability to ions of the hydrates coating. Finally, it is convenient to define

$$k = \left(\frac{G^2}{2D} \right)^{1/2} \tag{3.28}$$

which will lighten significantly the resulting expressions.

We will consider parameters G and D as constants throughout the hydration, although

modifications might be accommodated if their evolution is known.

3.3.2   Space and time distribution of nucleation seeds

The formation of the hydrates starts at discrete identifiable centres –nucleation seeds– from which the newly-formed hydrate grows. The location of these nuclei and their formation rate is often explained according to two different hypothesis: the volume or surface nucleation.

3.3.2.1   Volume nucleation

The consideration of the probability of reaction as equal at every location inside the volume leads to the standard NG model, originally intended for the description of the kinetics of phase change in metals, from molten fluid to solid state. Details might be found in Christian's comprehensive book on the subject [59]. In this scenario, the nuclei are assumed to be randomly distributed in the untransformed volume, with a constant rate of nucleation per unit volume. The standard form of NG is also the solution for nucleation occurring both randomly in the volume and on the product boundaries. If both the initial and the newly-formed regions have the same growth rates, the solution of the impingement problem is trivial because the offspring regions are immediately ingested.

3.3.2.2   Boundary nucleation

An important criticism of the NG model is the assumption of nucleation being distributed randomly in the volume. As an alternative, Thomas [3] made use of the Boundary Nucleation and Growth model proposed by Cahn [58]. In this model, the nucleation occurs on the surface of the grains. Although intended for the modelling of phase transition of metals, its application to alite has shown that experimental data can be correctly fitted in the early stage of reaction. In addition, the depiction seems to be in closer agreement with observed evolution of hydration under the microscope, with precipitation occurring with preference on the surfaces [63].

3.3.3   A variety of kinetic models

Combining different volume filling and growth kinetics models results in different hydration models. The most notable combinations are presented in Table 3.1.

An important feature of our framework is the ability to separate the model in its essential components, each of which can now be formulated independently from the other with convenient assumptions in accordance with the physical characteristics of the system. In the remaining of the present paper, we derive and apply a multi-component model of hydrates nucleating on the boundary, for which we consider both phase boundary and diffusion control. Other models resulting from the different combinations are presented in the Appendix.

Table 3.1: Summary of hydration kinetics models

Model	Volume filling	Growth kinetics
MCK-1	Multi-component	Boundary nucleation
MCK-2*	Multi-component	Volume nucleation
SCK-1*	Single-component	Boundary nucleation
SCK-2*	Single-component	Volume nucleation

* Derivation available in the Appendix.

3.4 MCK-1: multi-component boundary nucleation and growth with diffusion-enriched control

Among the variety of candidate hydration models, we select the one featuring most of the physical mechanisms commonly attributed to the hydration of cement paste. The model considers the cement paste as a mixture of water and anhydrous cement powder which, upon reaction, produce cement hydrates following a given stoichiometry. Each of these phases and their mutual interactions are considered independently in the volume filling model. Regarding the growth kinetics of the hydrates, these are supposed to nucleate on the boundaries and grow isotropically outwards from it. The growth rate of hydrates is first phase-boundary controlled and later becomes diffusion-controlled as the coating around the grains thickens.

3.4.1 Derivation of the model

Consider a boundary plane P of unit area, separated from plane Q by a distance y. At time t, a spherical nodule nucleated at time τ on plane P, will intersect plane Q over a surface:

$$S_\tau = \pi \left[\left(\frac{G(t-\tau)}{1 + k(t-\tau)^{1/2}} \right)^2 - y^2 \right] \quad \text{if} \quad \frac{G(t-\tau)}{1 + k(t-\tau)^{1/2}} \geq y; \text{else} \quad S_\tau = 0 \qquad (3.29)$$

The extended surface S_τ^e –analogous to the extended volume– corresponding to the total intersection area of nodules nucleated on plane P between times τ and $\tau + \mathrm{d}\tau$, without accounting for their overlapping on plane Q, is given by:

$$S_\tau^e = \pi N \left[\left(\frac{G(t-\tau)}{1 + k(t-\tau)^{1/2}} \right)^2 - y^2 \right] \mathrm{d}\tau \quad \text{if} \quad \frac{G(t-\tau)}{1 + k(t-\tau)^{1/2}} \geq y; \text{else} \quad S_\tau^e = 0 \quad (3.30)$$

where N is the nucleation rate per unit area, considered constant. Scherer et al. [109] have explored the consequences of adopting a fixed number of nuclei, a consideration that might readily be added to the current formulation if desired. The last expression can be

integrated to obtain the total extended surface on plane Q of nodules nucleated on plane P from time $t = 0$ to t. Since only nodules that have a radius larger than y at time t will intersect plane Q, the integral to be evaluated becomes:

$$S^e = \int_0^{t-\bar{t}} \pi N \left[\left(\frac{G(t-\tau)}{1 + k(t-\tau)^{1/2}} \right)^2 - y^2 \right] d\tau \tag{3.31}$$

where

$$\bar{t} = \left[\frac{ky + \sqrt{(ky)^2 + 4Gy}}{2G} \right]^2 \tag{3.32}$$

is the time required for a nodule nucleated on plane P to reach plane Q. Integration yields:

$$S^e = \pi N \left[G^2 \frac{f(k,t)}{6k^6} - y^2 (t - \bar{t}) \right] \tag{3.33}$$

where

$$f(k,t) = 3k^4 \left(t^2 - \bar{t}^2 \right) - 8k^3 \left(t^{3/2} - \bar{t}^{3/2} \right) + 18k^2 (t - \bar{t}) - 48k \left(t^{1/2} - \bar{t}^{1/2} \right) +$$
$$12 \left(\frac{1}{1 + kt^{1/2}} - \frac{1}{1 + k\bar{t}^{1/2}} \right) + 60 \ln \left(\frac{1 + kt^{1/2}}{1 + k\bar{t}^{1/2}} \right) \tag{3.34}$$

For small values of k –considering terms up to $\mathcal{O}(k^2)$– the expression simplifies to:

$$S^e = \pi N \left[G^2 \left(\frac{t^3 - \bar{t}^3}{3} - \frac{4k \left(t^{7/2} - \bar{t}^{7/2} \right)}{7} + \frac{3k^2 (t^4 - \bar{t})}{4} \right) - y^2 (t - \bar{t}) \right] \tag{3.35}$$

The consideration of the impingement problem of the hydrates precipitating on the surface of grains requires shifting the reference frame to the scale of the reactions. At this level, the transformation stoichiometry requires a unitary mass of clinker per w_h mass of water, so that $w_r = 1$.

We can calculate the real surface fraction following the same reasoning presented in Section 3.2, but with surface fractions instead of volume fractions, given the isotropic nature of the cement paste. For the sake of simplicity, we limit ourselves to the cases of negligible overall volume changes as in Equations (3.17) and (3.18) which, together with Equation (3.5), yield the real surface fraction S:

$$S = \frac{1 - \exp\left(-\dfrac{1 - \alpha_u}{z'} S^e \right)}{\dfrac{1}{\alpha_u} - \exp\left(-\dfrac{1 - \alpha_u}{z'} S^e \right)} \tag{3.36}$$

where

$$z' = \frac{\rho_w \rho_c}{2 w_h} \left(\frac{1}{\rho_c} + \frac{w_h}{\rho_w} \right)^2 \tag{3.37}$$

For the limiting case $\alpha_u = 1$, the expression reads:

$$S = \frac{S^e}{z' + S^e} \tag{3.38}$$

The real volume generated from plane P can now be calculated by integrating over the y axis to intersect all neighbour planes:

$$V = \int_0^\infty S(y) \, \mathrm{d}y = \int_0^{\frac{Gt}{1+kt^{1/2}}} S(y) \, \mathrm{d}y \tag{3.39}$$

where the integration limits have been fixed considering the predominantly one-directional growth of the products from the boundaries to the furthest reached plane at time t. The surface $S(y)$ is given by Equation (3.36). The total extended volume generated from all nucleating boundaries is therefore:

$$V_h^e = BV = B \int_0^{\frac{Gt}{1+kt^{1/2}}} S(y) \, \mathrm{d}y \tag{3.40}$$

where B is the randomly distributed specific nucleation surface per unit volume of hydrate.

The inspection of Equations (3.33) to (3.40) in the absence of diffusion, i.e. $D \to \infty$, reduces the number of effective parameters in a similar way as discussed by Cahn [58] and Thomas [3]. Indeed, we can express the extended surface area as:

$$S^e = \pi N G^2 t^3 \left(\frac{2}{3} x^3 - x^2 + \frac{1}{3} \right), \text{ where } x = \frac{y}{Gt} \tag{3.41}$$

In addition, since $\mathrm{d}y = Gt \, \mathrm{d}x$, the extended volume becomes:

$$V_h^e = BGt \int_0^1 S(x) \, \mathrm{d}x \tag{3.42}$$

where the integration limits have been appropriately updated. It is clear that only two rates dominate growth kinetics:

$$k_a = (NG^2)^{1/3}, \quad k_b = BG \tag{3.43}$$

both with units inverse of time. On the contrary, when diffusion is prevalent, i.e. $\left(\frac{G^2}{2D} t \right)^{1/2} \gg 1$, the extended surface area is:

$$S^e = \pi N D t^2 \left(\tilde{x}^2 - 1 \right)^2, \text{ where } \tilde{x} = \frac{y}{(2Dt)^{1/2}} \tag{3.44}$$

and since $dy = (2Dt)^{1/2}\, d\tilde{x}$, the extended volume becomes:

$$V_h^e = \left(2B^2 Dt\right)^{1/2} \int_0^1 S(\tilde{x})\, d\tilde{x} \tag{3.45}$$

so the two rates dominating the growth kinetics are now:

$$k_a = (ND)^{1/2}, \quad k_b = B^2 D \tag{3.46}$$

both with units inverse of time. In both limit scenarios, parameter k_a is concerned with the rate of boundary coverage, while k_b is related to the slab-like growth of hydrates, as discussed in Section 3.4.2.

The formulation of the model is now complete. The evolution of the hydration reaction will be completely determined from the choice of volume filling model among Equations (3.14) to (3.19), and the extended volume from Equation (3.40). The effect of water or clinker exhaustion, as well as the effect of kinetic parameters, can be appraised in Figure 3.9.

3.4.2 Rate-controlling mechanisms

Owing to the diversity of mechanisms featured by the model, we might observe successive transitions of the rate-controlling mechanisms as the hydration progresses.

Regarding hydration control by the rate of hydrates growth, the choice of a phase boundary control with linear growth dictates the reaction rates early in the reaction. The transition to diffusion control of the boundary growth rate can be estimated from Equation (3.25), for which transition to diffusion control is expected at a characteristic time

$$\tau_d = \frac{2D}{G^2} \tag{3.47}$$

In addition to the control operated by the rate of growth of the hydrates, two other mechanisms might control the reaction rates, here related to the mutual impingement of components.

As the hydration products grow in size, they cover nucleation sites on the grain boundaries, which will become inactive. The extensive coverage of the surface significantly inhibits the nucleation of new sites, and the growth of the hydrates proceeds thereon in the form of slabs, growing outwards from the grain boundaries [58]. The characteristic time of this process, known as nucleation site saturation, can be appraised for the MCK-1 model from the knowledge of the fraction of transformed surface S on the grain boundaries, i.e. evaluating Equation (3.36) for $y = 0$. The characteristic time can be estimated from the half-life of the transformation ($S = \alpha_u/2$, since $w_r = 1$ and $\xi = 0$), yielding:

$$S_{y=0, t=\tau_n}^e = z' \frac{\ln(2 - \alpha_u)}{1 - \alpha_u} \tag{3.48}$$
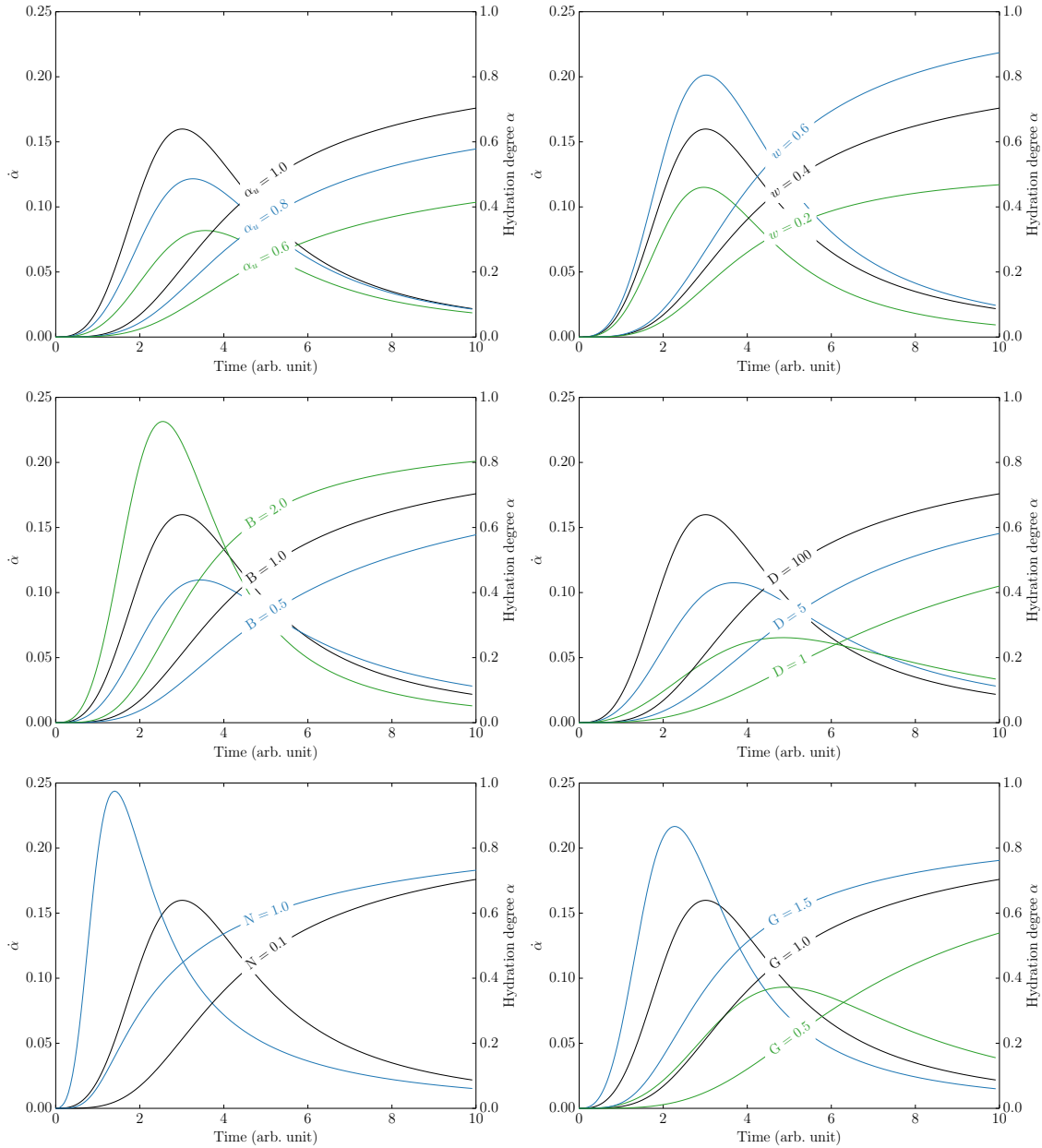
Figure 3.9: Hydration degree and rate for the MCK-1 model. Curves in black correspond to the same reference test, presented in all figures to ease comparisons.

the expression for S_e being given by Equation (3.33). In general, an estimate can be readily obtained by assuming $\alpha_u = 1$ and $k = 0$, in which case the characteristic time for nucleation site saturation is

$$\tau_n = \left(\frac{3z'}{\pi N G^2} \right)^{1/3} \tag{3.49}$$

In addition to nucleation site saturation, the filling of the volume available for product growth leads to the decrease in the rate of reaction by what we will call volume saturation.

In a similar way as previously done for the surface transformation, the characteristic time for volume saturation τ_v might be estimated as the half-life of the transformation of the total volume to hydrates ($v_h = 1/2$). This can be determined from the definition of the hydrates volume fraction in Equation (3.7) together with the definition of the hydration degree in Equation (3.17), neglecting chemical shrinkage. We obtain:

$$V^e_{h,t=\tau_v} = \frac{z}{\alpha_u - w_r} \ln\left(\frac{1/\alpha_u - 2z''}{1/w_r - 2z''}\right) \tag{3.50}$$

which, considering the case $w_r = \alpha_u = 1$, yields the simplified estimate

$$V^e_{h,t=\tau_v} = \frac{z}{2z'' - 1} \tag{3.51}$$

where

$$z'' = \frac{1/\rho_c + w_h/\rho_w}{1/\rho_c + w/\rho_w} \tag{3.52}$$

For the MCK-1 model, τ_v must be calculated from the numerical integration of the extended volume from Equation (3.40).

The definition of τ_v is valid for ordinary mixes, where the proportioning of reactants is close to the stoichiometric balance, thus leading to the filling of most of the system volume by hydrates. Although not often the case, if one of the reactants is largely in excess, the available co-reactant leftover might have control over the reaction rate. The model naturally accounts for such reaction rate control by reactant exhaustion, which can be assessed from the characteristic half-life of either reactant mass.

In summary, the initial phase boundary control can shift to either diffusion, nucleation site or volume saturation control. Each of these rate controlling mechanisms have their own characteristic times, which have to be compared in order to estimate their relative importance and the onset of their controlling stages.

3.5 Overview of model parameters

The application of the model requires the determination of the input parameters presented in the theoretical framework and summarized in Table 3.2.

The parameters related to the materials and stoichiometry account for the mixture proportioning and can be determined performing simple calculations. The cement powder mass composition is often provided by the manufacturer, from which the mass density of the cement powder can be calculated knowing the mass density of its individual components as:

$$\rho_c = \left(\sum_i \frac{m_i}{\rho_i}\right)^{-1} \tag{3.53}$$

Table 3.2: Parameters of the MCK-1 model

		Ref. values	Unit
Materials and stoichiometry of reaction			
m_i	Mass fraction of cement powder components		-
w	Water to cement mass ratio of the cement paste	0.2 - 0.6	-
w_h	Water to cement mass ratio for complete hydration	0.30 - 0.45	-
ρ_c	Mass density of cement powder	3.1 - 3.3	g/cm^3
ρ_w	Mass density of water	1.0	g/cm^3
ρ_h	Mass density of hydrates	1.8 - 2.1	g/cm^3
α_u	Ultimate hydration degree	0.6 - 1.0	-
Growth kinetics			
B	Specific nucleation surface	0.1 - 1.0	μm^{-1}
N	Nucleation rate per unit surface	0.01 - 0.10	$\left(\mu m^2 \, h\right)^{-1}$
G	Linear growth rate	0.5 - 5.0	$\mu m/h$
D	Diffusion coefficient	10 - 100	$\mu m^2/h$

where m_i and ρ_i correspond, respectively, to the mass fraction and mass density of component i = alite (C_3S), belite (C_2S), aluminate (C_3A) and ferrite (C_4AF).[2] The minor phases, such as gypsum and impurities, might also be included. When minor components are neglected or unidentified, the normalized mass fraction with respect to the main clinker components should be preferred.

The ratio of water to cement mass for complete hydration can be determined from the basic hydration reactions stoichiometry and the cement composition.

$$w_h = M_H \sum_i \frac{n_H^i m_i}{M_i}, \quad i = C_3S, C_2S, C_3A, C_4AF \tag{3.54}$$

where, for component i, M_i is its molar mass and the stoichiometric coefficient n_H^i is its number of moles participating in the reaction with a mole of water.

The density of the hydrates can be determined from knowledge of the density of reactants, the reaction stoichiometry and the chemical shrinkage ξ, according to Equation (3.6). Although the chemical shrinkage depends on a large number of parameters, most notably temperature and pressure, reference values might be determined from the basic stoichiometric reactions or experimentally measured [25, 110]. Knowing the volume changes of the reaction of individual clinker phases, the resulting overall chemical shrinkage can be determined:

$$\xi = \sum_i m_i \xi_i, \quad i = C_3S, C_2S, C_3A, C_4AF \tag{3.55}$$

where ξ_i is the chemical shrinkage per unit mass of the clinker component i.

---

[2]Cement chemistry notations: C=CaO, S=SiO$_2$, A=Al$_2$O$_3$, F=Fe$_2$O$_3$ and H=H$_2$O.

The hydration degree is often monitored by means of isothermal/isobaric calorimetry, consisting of measuring the heat flow from a hydrating sample under constant temperature and pressure [111]. Assuming the heat release to be proportional to the consumed mass, α is given by:

$$\alpha(t) = \frac{Q(t)}{Q_\infty} \tag{3.56}$$

where $Q(t)$ is the cumulated heat release at time t and Q_∞ is its ultimate asymptotic value. Q_∞ can be determined by adding the individual contribution of total heat Q_∞^i of individual clinker reacting phases:

$$Q_\infty = \sum_i m_i Q_\infty^i, \quad i = \mathrm{C_3S, C_2S, C_3A, C_4AF} \tag{3.57}$$

The ultimate hydration degree α_u can be estimated from empirical expressions. Among such expressions, the most widely used form was proposed by Mills [112]:

$$\alpha_u = \frac{1.031\,w}{0.194 + w} \tag{3.58}$$

Other authors have proposed expressions that account for the effects of temperature, particle size distribution and cement composition [113, 114]. In addition, the ultimate hydration degree is bounded by the available mixing water ratio w_r, as discussed in Section 3.2.3.1.

Table 3.3: Reference values for the material and stoichiometry of reaction parameters

	Reactants				
	C$_3$S	C$_2$S	C$_3$A	C$_4$AF	Water
$\rho\,(\mathrm{g/cm^3})$ [a]	3.15	3.28	3.03	3.73	1.00
$M\,(\mathrm{g/mol})$ [a,b]	228.32	172.24	270.20	485.96	18.02
n_H^i [a,b]	5.3	4.3	10.0	14.0	-
$Q_\infty^i\,(\mathrm{J/g})$ [c]	500	250	880	420	-
$\xi_i\,(10^{-2}\mathrm{cm^3/g})$ [d]	5.14	4.75	11.37	8.14	-

Sources: [a] Tennis and Jennings [24], [b] Bentz [52], [c] Bensted and Barnes [41]. [d] Assumed the conversion of aluminates to monosulfate.

Regarding growth kinetics parameters, the specific surface of grains B can be determined from the specific surface area per unit mass S_A of the cement powder, evaluated from Blaine fineness or calculated from the particle size distribution. In the present model, B is defined with respect to the elementary volume of reaction, thus leading to

$$B = \frac{S_A}{1/\rho_c + w_h/\rho_w} \tag{3.59}$$

It is very important to emphasize the definition of B with respect to volume of hydrates, instead of the total volume. This is a consequence of the separation of the geometric and

kinetic problem.

The remaining growth kinetics parameters N, G and D are determined from the fitting of the model to the experimental measurements.

3.6 Applications

The current section presents the application of the MCK-1 model to simulate experimental observations of the hydration kinetics of cement pastes over a wide spectrum of conditions. The modelling scenarios include hydration temperature and pressure, cement fineness and water to cement ratio effects.

For the determination of model parameters, simulated annealing [115] and basin-hopping [116] algorithms were used at first to explore large parameter domains and assure the identification of global best-fit values. In general, simple convex optimization algorithms in the neighbourhood of reference parameters (e.g. Growth kinetics, Table 3.2) should suffice to determine global optimal values.

3.6.1 Materials and experimental conditions

The cement pastes compositions and model parameters are presented in Table 3.4. The cement powder composition was determined from Rietveld analysis for cements C1, C2 and C3, and from Bogue analysis for cements C4 and C5. The specific surface area corresponds to Blaine fineness for all cements with the exception of C1, for which the particle size distribution was instead employed.

3.6.2 Effect of temperature and pressure

The hydration kinetics of an API Class H cement paste have been adapted from the experimental results of Pang et al. [9]. The slurries were prepared according to the API recommendations [92], with a water to cement ratio of 0.38. Isothermal calorimetry tests were performed at different curing conditions, constituting a rich and compatible data set with varying temperatures (T = 25, 40, 60°C) and pressures (P = 2, 15, 30, 45 MPa). The remaining parameters can be calculated following the procedure described in Section 3.5 and are presented in Table 3.4, where the cement is identified with reference C1.

The results of the model fitting are presented in Table 3.5. Figure 3.10 presents a close look of the hydration results for a temperature of 25°C and various pressures. Increments of pressure, considered equivalent to temperature increments according to activation theory [117], result in changes in the rate of reaction. It is important to observe that the variation is not homogeneous throughout the reaction. The increase in pressure results in an acceleration early in the reaction. In the long-term, however, the rate of reaction is lower

Table 3.4: Cement paste properties

				Identification reference				
	C1[a]	C2a[b]	C2b[b]	C3a[b]	C3b[b]	C3c[b]	C4[c]	C5[d]
Cement powder mass composition (%)								
C_3S	48.2	60.3	59.5	70.1	70.8	67.9	56.7	65.0
C_2S	29.4	17.2	13.2	10.3	8.2	9.1	17.2	29.7
C_3A	0.0	9.4	9.4	10.8	10.1	10.2	6.7	5.3
C_4AF	17.2	4.7	4.7	2.5	3.3	3.4	7.9	0.0
Others	5.2	8.4	13.2	6.3	7.6	9.4	11.5	0.0
Other parameters								
w	0.38	0.50	0.50	0.50	0.50	0.50	-	-
w_h	0.42	0.40	0.39	0.42	0.42	0.41	0.40	0.42
α_u *	0.68	0.74	0.74	0.74	0.74	0.74	-	-
$\rho_c\,(\text{g/cm}^3)$	3.28	3.18	3.18	3.16	3.16	3.17	3.21	3.17
$\rho_h\,(\text{g/cm}^3)$	1.95	1.95	1.97	1.92	1.93	1.94	1.96	1.93
$S_A\,(\text{m}^2/\text{g cement})$	0.254	0.395	0.618	0.357	0.495	0.663	0.312	0.317
$B\,(\mu\text{m}^{-1})$	0.349	0.549	0.871	0.482	0.675	0.913	0.438	0.429
$Q_\infty\,(\text{J/g cement})$	387	288	289	321	318	311	322	323

Sources: [a] Pang et al. [9], [b] Termkhajornkit and Barbarulo [10], [c] Danielson [11], [d] Bonavetti et al. [12].
* Determined according to Equation (3.58).

Table 3.5: Model parameters for cement paste C1

Hydration conditions		*Model parameters*		
T (°C)	P (MPa)	$N\,(\mu\text{m}^2\,\text{h})^{-1}$	$G\,(\mu\text{m}/\,\text{h})$	$D\,(\mu\text{m}^2/\text{h})$
25	2	0.025	0.592	18.38
25	15	0.029	0.669	19.68
25	30	0.033	0.770	24.07
25	45	0.039	0.887	24.25
40	2	0.052	1.193	48.29
40	45	0.076	1.774	64.86
60	2	0.101	2.645	117.26
60	15	0.122	3.066	113.35
60	30	0.146	3.496	84.93
60	45	0.172	3.988	95.89

under higher pressure or temperature, in agreement with the experimental observations.

The effect of the hydration conditions is best examined in Figure 3.11, where the capacity of the model to correctly capture the hydration kinetics and its variations with temperature and pressure is shown. The largest discrepancies correspond to hydration at high temperature, due to the appearance of the rate bump characteristic of the formation of monosulfate [19], that has a long-term effect on the hydration degree upon rate integration.

The effect of temperature on the hydration model parameters can be observed in the
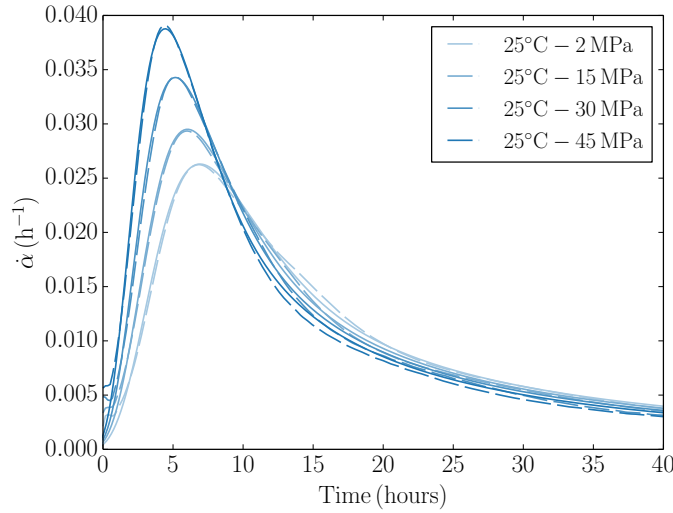
Figure 3.10: Experimental (dashed) and model (solid) hydration curves for hydration under 25°C and various pressures. Experimental data from Pang et al. [9].

Arrhenius plot of Figure 3.12a. Parameters N and G both display evolutions in accordance with a thermally-activated rate process. Their respective average activation energies are $E_N = 33.7$ kJ/mol and $E_G = 35.3$ kJ/mol. The adoption of a single average activation energy $E_a = 34.5$ kJ/mol might provide an acceptable simplifying assumption. On the other hand, the diffusion parameter D, although similarly sensitive to temperature, does not seem to follow an Arrhenius activation law.

The observations are analogous for the effect of pressure, as can be seen in the Arrhenius plot of Figure 3.12b. As for temperature, parameters N and G both display evolutions in accordance with a pressure-activated rate process. Their respective average activation volumes are $\Delta V_N = -2.90 \times 10^{-5}$ m³/mol and $\Delta V_G = -2.47 \times 10^{-5}$ m³/mol, with an average activation volume $\Delta V = -2.69 \times 10^{-5}$ m³/mol yielding a reasonable approximation for both parameters. The sensitivity of diffusion parameter D to pressure does not follow an Arrhenius activation law. Both activation parameters E_a and ΔV are within the range of commonly reported values [118–120].

The characteristic times of different mechanisms, discussed in Section 3.4.2, provide important insight on the underlying rate controlling processes. Figure 3.13a illustrates the evolution of the characteristic times of diffusion (τ_d), volume saturation (τ_v) and nucleation site saturation (τ_n) with temperature. As expected, the characteristic times decrease significantly with temperature, the sharpest changes occurring for the diffusion and nucleation site saturation. This is a consequence of the previously discussed thermal activation of the model parameters. The analogous commentary can be made regarding the effect of pressure, observable in Figure 3.13b.

Interestingly, the characteristic time scales are sufficiently distant as to allow the clear
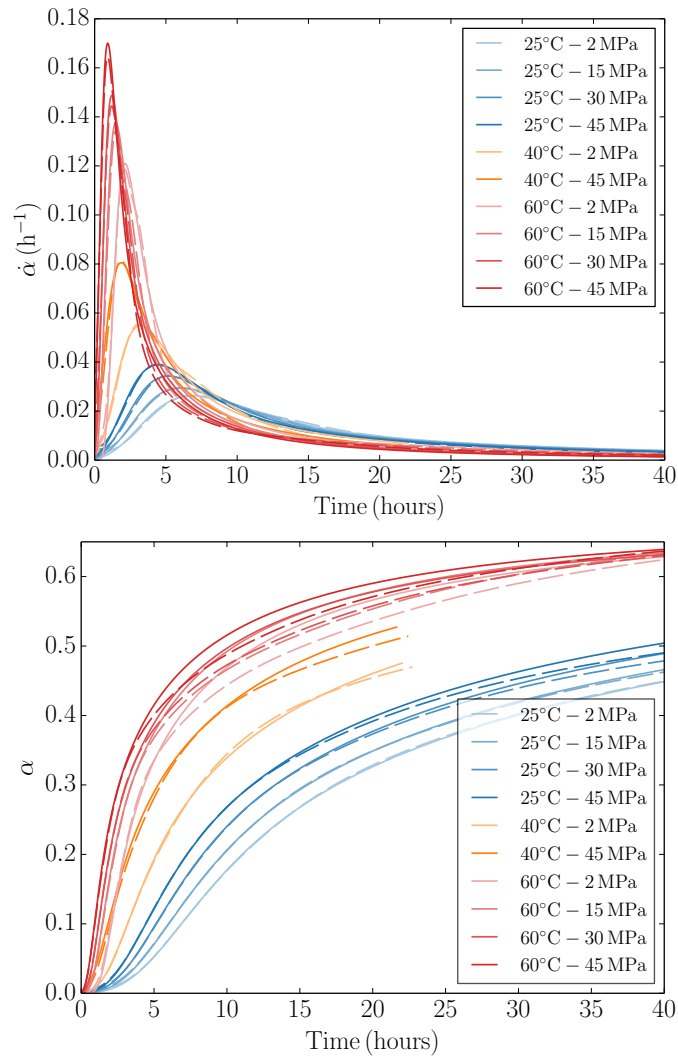
Figure 3.11: Experimental (dashed) and model (solid) hydration curves. Experimental data from Pang et al. [9].

distinction of the dominating mechanisms. In all the simulated hydration conditions, the reaction rate is first dominated by the initial linear growth rate, followed by nucleation site saturation on the boundaries and then by volume saturation. Only in the long term does diffusion takes over the reaction rate control, which it will dominate until reaching the ultimate hydration degree. The separation of scales confirms the remark of [22], who suggested that diffusion control should occur very late in the reaction.
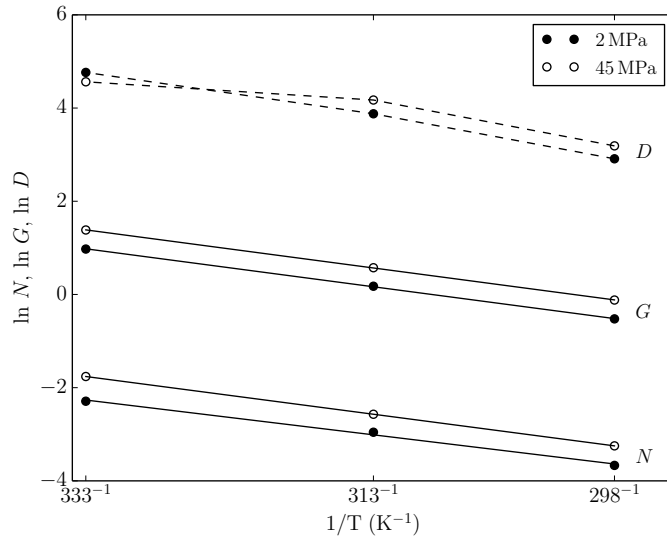
(a) Evolution of model parameters with temperature for two different hydration pressures.
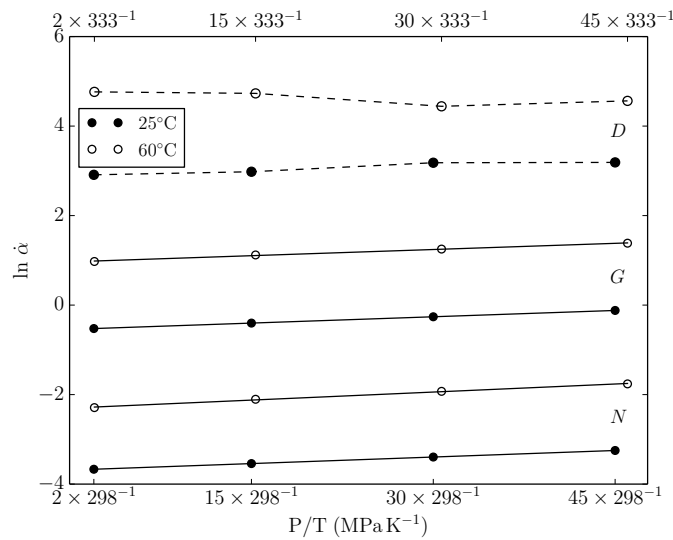
(b) Evolution of model parameters with pressure for two different hydration temperatures. Lower and upper horizontal axes corresponds to 25°C and 60°C, respectively.

Figure 3.12: Arrhenius plots portraying the effect of temperature and pressure on the model parameters. Marks correspond to experimental observations, dashed lines are drawn to guide the eye, and solid lines are linear trend fits for the determination activation parameters.
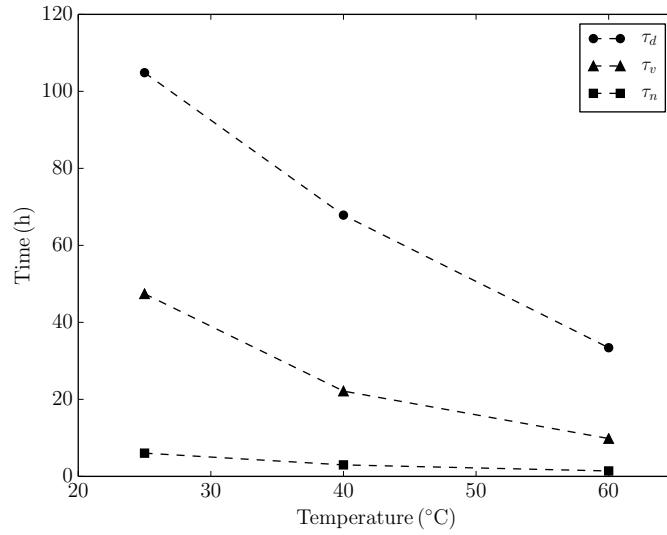
(a) Evolution of characteristic times with temperature. Constant pressure of 2 MPa.
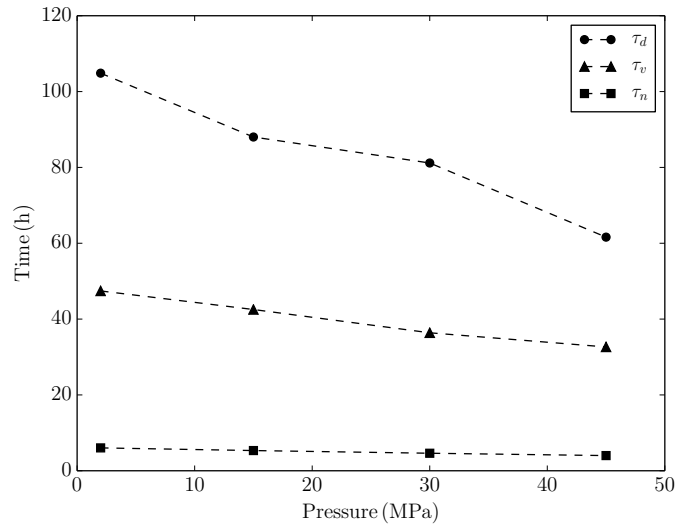
(b) Evolution of characteristic times with pressure. Constant temperature of 25°C.

Figure 3.13: Characteristic times of diffusion (τ_d), volume saturation (τ_v) and nucleation site saturation (τ_n). Marks correspond to times as determined from fitting of the experimental data while dashed lines are drawn to guide the eye.

3.6.3   Effect of cement powder fineness

In order to explore the effect of specific surface area on the hydration rates, we consider the isothermal calorimetry experiments by Termkhajornkit and Barbarulo [10] performed on mixes with cement powders of different particle size distributions, identified with references C2 and C3 in Table 3.4. The cement pastes were all hydrated at a temperature of 20°C and under atmospheric pressure. Among the variety of cement powders analysed by these authors, we selected those featuring the most significant contrasts in both mineralogical composition and specific surface area.

The model parameters for the two groups of cement pastes are presented in Table 3.6. Despite the slight difference in compositions among cements of the same reference class, the reproduction of the experiments is possible without changing the model parameters other than the specific nucleation surface B, which is updated according to the experimental measurements presented in Equation (3.59). The remaining growth kinetics parameters might also be dependent on the changes of particle size distribution and specific surface area, although we would expect a smaller relative change [54, 121]. The model results, presented in Figure 3.14, show a very close agreement with the experiments, and produce excellent estimates of the effects of specific surface on the kinetics of hydration. In both cases, the modification of the specific nucleation surface explains the essential part of the total observed variation of the kinetics of reaction.

Table 3.6: Model parameters for cement pastes with different specific surface areas

Cement reference	$N \, (\mu m^2 \, h)^{-1}$	$G \, (\mu m/ \, h)$	$D \, (\mu m^2/h)$
C2a / C2b	0.078	0.416	6.33
C3a / C3b / C3c	0.060	0.371	13.58

3.6.4   Effect of water to cement ratio

The experimental results of Danielson [11] and Bonavetti et al. [12], identified with references C4 and C5 in Table 3.4, are considered in the examination of the effect of water to cement ratio on hydration kinetics. The experiments were performed at room temperature and pressure.

Table 3.7 presents the base model parameters determined for the two cement pastes. As we did before for specific surface, we assume the growth kinetics parameters to be independent of water to cement ratio in order to capture the isolated effect of the latter on the reaction kinetics. Only the water to cement ratio parameter w has been updated for the model predictions, which we expect will account for the major part of the observed experimental differences.

The results are presented in Figure 3.15. The model predictions follow the general
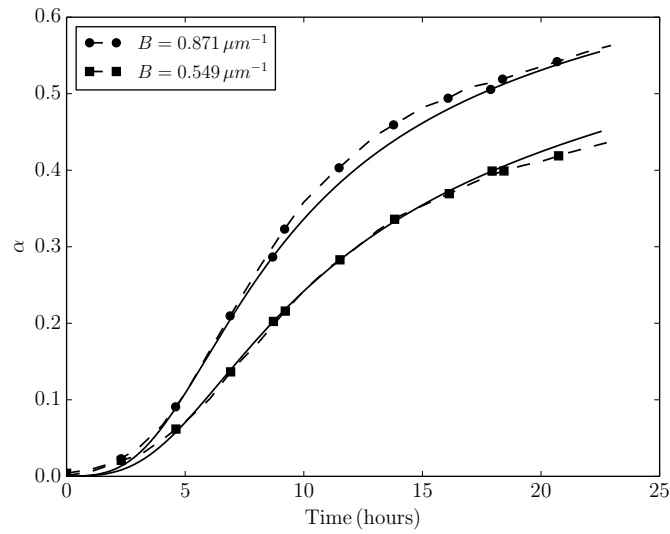
(a) Cements C2a and C2b.
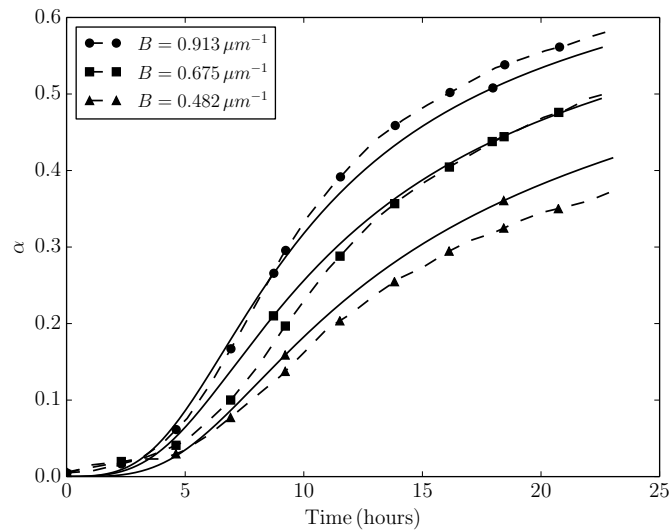
(b) Cements C3a, C3b and C3c.

Figure 3.14: Effect of fineness on hydration evolution. Dashed lines correspond to experiments while solid lines are model results obtained considering only B as variable. Experimental data from Termkhajornkit and Barbarulo [10].

trends of the experimental tests. The most important discrepancies appear early in the reaction, likely due to the effect of water availability on the kinetic parameters, which we have not considered. The long term predictions are acceptable, but sometimes below the experimental measurements. This is due to an apparent underestimation of the ultimate hydration degree by Mills' formula, as can be confirmed for the tests with the highest w, where long term experimental data is often above the calculated α_u. Overall, the model results in predictions within the range that might be expected from our overly simplified hypothesis of constant kinetic parameters.

Table 3.7: Model parameters for cement pastes with different water to cement ratios

Cement reference	$N\,(\mu\mathrm{m}^2\,\mathrm{h})^{-1}$	$G\,(\mu\mathrm{m}/\,\mathrm{h})$	$D\,(\mu\mathrm{m}^2/\mathrm{h})$
C4	0.052	0.449	5.99
C5	0.034	0.605	22.23
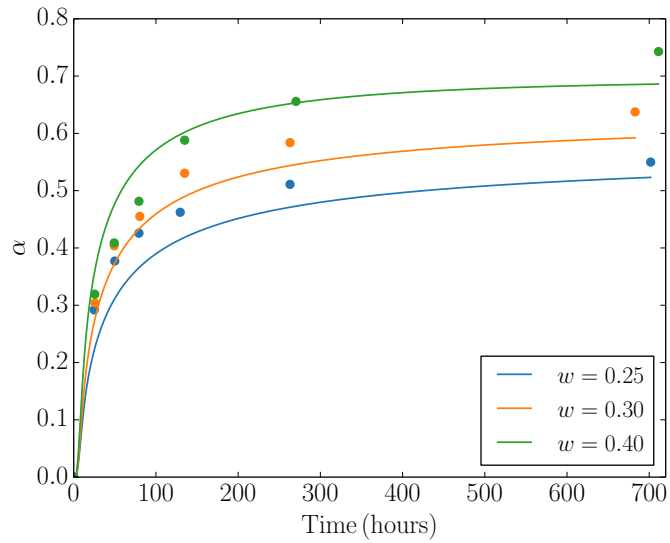
(a) Cement 4
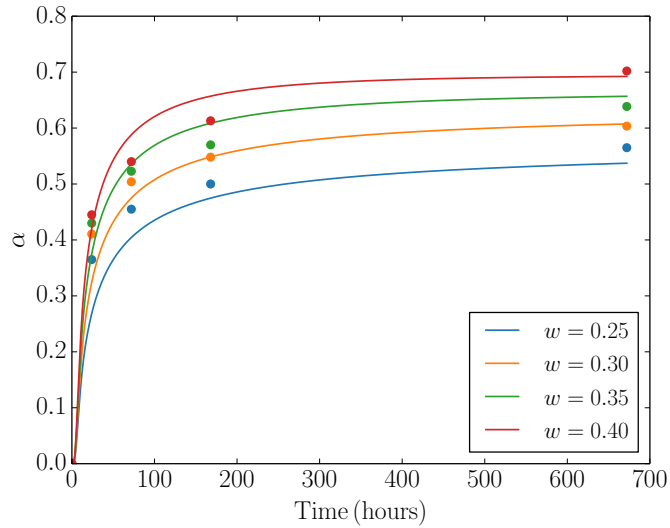
(b) Cement 5

Figure 3.15: Effect of water to cement ratio on hydration evolution. Marks correspond to experimental observations and solid lines are model results obtained considering only w as variable. Experimental data from Danielson [11] and Bonavetti et al. [12].

3.6.5   Additional modelling scenarios

For the sake of brevity, we have presented some of the most relevant applications of the hydration model in the scientific and engineering contexts. There remain, of course, a number of variables that have not been dealt with in detail, but call for consideration under the light of the new hydration model.

In our formulation, the physical mechanisms are essentially intended to model the acceleration and deceleration phases (see Figure 1.5). The consideration of the induction period, as proposed by Thomas [3], is also possible. The initial fast reaction, mainly due to the cement powder heat of wetting and initial dissolution [22], is disregarded without major consequences, since the degree of hydration at the beginning of the acceleration stage is usually below 1%, and is not attributed to the formation of the hydration products [41].

The consideration of performance enhancers additives, fine fillers and supplementary cementitious materials, subjects of intense research for their technical and economical advantages [122], is certainly possible under the current framework. The analysis of their effect on the different model parameters will provide useful information of the mechanisms by which such additions influence the cement hydration kinetics and the volume filling process in a cement paste, allowing a better design of the mixtures.

In addition, the effect of relative humidity, known to be responsible for the reduction of the reaction rate [91, 123] might be introduced in the modelling framework by reducing the water available for reaction in the same way as done for the ultimate degree of hydration.

We have demonstrated the robustness of our formulation by successfully modelling the hydration kinetics of cements pastes in different scenarios. We expect a similar performance for alite mixtures –often used as benchmarks in the literature, e.g. [37, 54, 124–126]– since experimental observations are comparable in what respects temperature and pressure [3], powder fineness [127] and water to cement ratio effects [63].

Finally, regarding the practical civil engineering applications, the extension to hydration of concrete is immediate. Thanks to the different scales of aggregates with respect to the cement powder and hydrate phases, there are likely no additional considerations to be made in either the volume filling or growth kinetics formulations.

3.7   Conclusion

We have proposed a general framework for the formulation of hydration models of cement-based materials based on two main elements: volume filling and growth kinetics models.

The volume filling model features a symmetric view of the reactants, where none of the reacting phases –cement powder or water– is privileged. The formulation naturally introduces some of the most relevant parameters of cement paste mixtures, such as the

cement powder composition, mass densities of the different phases, water to cement ratio, chemical shrinkage and hydrates properties.

The growth kinetics model proposes a single simple analytical equation describing the front advance as a boundary-controlled growth at early times, that later transitions smoothly to a diffusion control. The hydration products are considered to grow isotropically, nucleating randomly either in the volume or on the surface of the grains.

Hydration models are the result of the combination of volume filling and growth kinetics models, resulting in a multitude of possibilities of different physical complexity. The models require a reduced number of parameters, all of which have clear physical meanings. In the paper, we have explored the comprehensive and feature-rich MCK-1 model. The remaining formulations are detailed in the Appendix.

The MCK-1 model considers the cement paste as a mixture of water and cement powder which, upon reaction, produce hydrates following a given stoichiometry. The hydrates nucleate on the boundaries and grow outwards isotropically, with a growth rate that transitions from boundary to diffusion control as the coating around the grains thickens. The reaction rate can be controlled by linear boundary growth, volume space constraints, nucleation site saturation, diffusion or limiting amounts of reactants. To the best knowledge of the authors, this constitutes one of the most complete, simple and physically intuitive models of its kind to feature such a wide range of mechanisms and a powerful tool for the analysis of the kinetics of cement hydration.

The model is applied in the simulation of cement paste hydration continuously throughout the hydration reaction. We first discuss the application to the modelling of cement paste hydration under different temperature and pressure conditions, revealing the activated nature of the growth kinetics parameters. In addition, the model naturally accommodates the variations of specific surface area, yielding excellent estimates of the effects of change of particle size distribution on the kinetics of hydration. Finally, the effect of water to cement ratio can also be accounted for with minor parameter updates.

The modelling of hydration kinetics based on elementary physical considerations provides an unique opportunity to gain insight on the relevant parameters that control the reaction. The new model, as much an engineering tool as a scientific research instrument, promises to enrich the understanding of the underlying hydration processes and ultimately assist in the prediction of cement paste behaviour and optimal performance design.

3.A   Appendix: Derivation of other hydration models

We present the derivation and basic parameters of the most notable hydration models stemming from the combination of the volume filling and growth kinetics models. Naming conventions are consistent with those presented in the paper.

SCK-1: single-component boundary nucleation and growth with diffusion-enriched control

The original model by Cahn [58] can be enriched with a diffusion boundary control by reconsidering the mutual impingement of hydrates on the surface. In analogy with Equation (3.24), if only a fraction α_u of the surface is liable to transform, the transformed surface fraction is given by:

$$S = \alpha_u \left[1 - \frac{\exp(-S^e)}{\alpha_u}\right] \tag{3.A.1}$$

where S^e is given by either Equation (3.33), (3.35) or (3.41). The real volume generated from the plane P can now be calculated by integrating over the y axis:

$$V = \int_0^\infty S(y) \; \mathrm{d}y = \int_0^{\frac{Gt}{1+kt^{1/2}}} S(y) \; \mathrm{d}y \tag{3.A.2}$$

where the integration limits have been fixed considering the one-directional growth of the products from the boundaries and the furthest reached plane at time t.

Having solved the impingement of the nodules nucleated on a single surface, we now consider all the surfaces in a given volume. For a unitary volume the total extended volume generated from all nucleating boundaries is:

$$V_h^e = BV = B \int_0^{\frac{Gt}{1+kt^{1/2}}} S(y) \; \mathrm{d}y \tag{3.A.3}$$

where B is the boundary surface per unit volume of hydrate, that we assume randomly distributed. The hydration degree can be determined from Equation (3.24):

$$\alpha = \alpha_u \left[1 - \frac{\exp(-V_h^e)}{\alpha_u}\right] \tag{3.A.4}$$

The characteristic times of the diffusion control, nucleation site saturation and volume saturation can be determined in a similar way as discussed in Section 3.4.2. The characteristic time of nucleation sites saturation is:

$$\tau_n = \left(\frac{3\ln(2/\alpha_u)}{\pi NG^2}\right)^{1/3} \tag{3.A.5}$$

Volume saturation characteristic time τ_v for $\alpha = 1/2$ is:

$$V_{h,t=\tau_v}^e = \ln\left(\alpha_u - 1/2\right) \tag{3.A.6}$$

where the time τ_v has to be determined from the numerical integration of V_h^e. Diffusion

characteristic time is:

$$\tau_d = \frac{2D}{G^2} \tag{3.A.7}$$

Volume nucleation models: SCK-2 and MCK-2

The introduction of diffusion-controlled particle growth in a volume-nucleating model requires the reconsideration of the growth of hydrates. For an individual transformed region, nucleated at time τ and growing isotropically, volume at time t is given by:

$$V^\tau = \frac{4\pi}{3} \left(\frac{G(t-\tau)}{1 + k(t-\tau)^{1/2}} \right)^3 \quad \text{for } t \geq \tau; \quad V_\tau = 0 \quad \text{for } t < \tau \tag{3.A.8}$$

where we have adopted Equation (3.25) for the linear dimension in any given spatial direction.

We assume volume nuclei seeds to be randomly distributed in the untransformed volume, with a rate of nucleation per unit volume of N_v. Considering a region of unitary volume, the number of regions nucleated in a time interval $\mathrm{d}t$ is given by $N_v\,\mathrm{d}t$. The extended volume of the regions nucleated between times τ and $\tau + \mathrm{d}\tau$ is therefore given by:

$$V_h^\tau = \frac{4\pi N_v}{3} \left(\frac{G(t-\tau)}{1 + k(t-\tau)^{1/2}} \right)^3 \mathrm{d}\tau \quad \text{if } t \geq \tau; \quad V_\tau = 0 \quad \text{if } t < \tau \tag{3.A.9}$$

Assuming a constant nucleation rate N_v, the integration from time $t = 0$ to t yields the extended volume:

$$V_h^e = \frac{2\pi N_v G^3}{15} \frac{f(k,t)}{k^8} \tag{3.A.10}$$

where

$$f(k,t) = 130 + 4k^5 t^{5/2} - 15k^4 t^2 + 40k^3 t^{3/2} - 100k^2 t + 300kt^{1/2} - $$
$$\frac{140}{1 + kt^{1/2}} + \frac{10}{\left(1 + kt^{1/2}\right)^2} - 420\ln\left(1 + kt^{1/2}\right) \tag{3.A.11}$$

For small values of k –considering terms up to $\mathcal{O}(k^2)$– the expression reads:

$$V_h^e = \frac{\pi N_v G^3}{3} \left(t^4 - \frac{8kt^{9/2}}{3} + \frac{24k^2 t^5}{5} \right) \tag{3.A.12}$$

so we naturally recover the standard NG expression for $k = 0$:

$$V_h^e = \frac{\pi N_v G^3 t^4}{3} \tag{3.A.13}$$

The general expression from Equation (3.A.10) is determined by only two parameters, $N_v G^3$ and k, therefore simplifying significantly the fitting procedure and exposing the

equivalence among the kinetic parameters.

It is also worth mentioning that the comparison among the volume or surface nucleation models is straightforward by determining the volume nucleation rate $N_v = BN$.

SCK-2: single-component nucleation and growth with diffusion-enriched control

The consideration of the single-component volume filling model leads to a modified version of the original NG model. According to Equation (3.24), if only a fraction α_u of the initial volume is liable to transform, the hydration degree is given by:

$$\alpha = \alpha_u \left[1 - \frac{\exp(-V_h^e)}{\alpha_u} \right] \tag{3.A.14}$$

where V_h^e is determined by either of Equation (3.A.10), (3.A.12) or (3.A.13).

The characteristic time for volume saturation, defined as the half-life of the transformation, will be approximately given by

$$\tau_v = \left(\frac{3 \ln (2/\alpha_u)}{\pi N G^3} \right)^{1/4} \tag{3.A.15}$$

while diffusion control characteristic time is given by

$$\tau_d = \frac{2D}{G^2} \tag{3.A.16}$$

MCK-2: multi-component nucleation and growth with diffusion-enriched control

The consideration of a multiple-component reaction requires the use of the adequate volume filling model among those proposed by Equations (3.14) to (3.19) together with the definition of V_h^e given by either Equation (3.A.10), (3.A.12) or (3.A.13).

The characteristic time for volume filling neglecting chemical shrinkage is:

$$\tau_v = \left[\frac{3z N_v^{-1} G^{-3}}{\pi (\alpha_u - w_r)} \ln \left(\frac{1/\alpha_u - 2z''}{1/w_r - 2z''} \right) \right]^{1/4} \tag{3.A.17}$$

which, considering the case $w_r = \alpha_u = 1$, yields the simplified estimate

$$\tau_v = \left[\frac{3z}{\pi N_v G^3} \right]^{1/4} \tag{3.A.18}$$

while diffusion control characteristic time is given by:

$$\tau_d = \frac{2D}{G^2} \tag{3.A.19}$$

As previously discussed in Section 3.4.2, if the reactants mixture is highly disproportionate, the exhaustion of one reactant might become rate controlling. In such cases, the half-life of each of the reactants can be estimated.

This model is equivalent to the MCK-1 model once nucleation site saturation is attained in the latter.

Chapter 4

Chemical kinetics model of cement hydration

4.1 Introduction

In the present chapter, we propose a simple cement hydration kinetics model that requires a reduced number of parameters and conserves the ability to reproduce short and long term hydration reactions with accuracy. We address the modelling of cement hydration from the perspective of solid phase transformation kinetics, and determine rates of the cement hydration from the early to the advanced ages. Unlike previous kinetic models, a single mathematical expression is shown to be sufficient to describe hydration spanning all ages. The approach has the advantage of reducing the model parameters significantly and providing a smooth transition of the rate controlling mechanisms. The effects of temperature and pressure, very important for practical applications (e.g. ref. [74]), are modelled by means of the activated complex theory. The application is demonstrated for class H and G oil well cement pastes. The consequences in what regards reaction control and possible governing mechanisms are discussed.

4.2 Hydration model

4.2.1 Isoconversional formulation

Isoconversional methods [128] decompose the general form of the transformation rate $\dot{\alpha} = \dot{\alpha}(\alpha, T, P)$ as the product of functions, for which the dependence upon the parameters is self-contained in each of the independent terms, i.e.

$$\dot{\alpha} = k(T, P) \ f(\alpha) \tag{4.1}$$

where $\dot{\alpha}$ is the hydration rate, T and P are the absolute temperature and pressure, respectively. The main outcome is the independence of the conversion function $f(\alpha)$ with respect to the reaction temperature or pressure regimes, meaning that the conversion mechanism is solely dependent of the hydration degree.

Isoconversional methods have been extensively used in the prediction of the effects of temperature and pressure on the hydration kinetics of cement paste [118, 120, 129, 130]. The concepts of maturity or equivalent age of cementitious materials are also closely related [131, 132]. The widespread use of these models is based on observations supporting the validity of the hypothesis of separation, as will be shown in the following.

The complete description of the reaction requires the determination of the independent rate function $k(T, P)$ and conversion function $f(\alpha)$.

4.2.2 Rate function

The form of rate functions has long been a subject of study in chemical kinetics. The sensitivity of a reaction to its environment is modelled by means of activation theory, with the most widely accepted model being that of Arrhenius, extensively used for the description of the thermal dependency of the rate of reactions [117]. The Arrhenius equation, based on the Maxwell-Boltzmann energy distribution in homogeneous kinetics, has been shown to remain applicable to solid state kinetics, both from experimental results and theoretical energy considerations [133]. We adopt the Arrhenius thermal and pressure activated rate function:

$$k(T, P) = A \exp\left(-\frac{E_a + \Delta V P}{R T}\right) \tag{4.2}$$

where A is a pre-exponential factor, E_a and ΔV are the activation energy and activation volume respectively, and R is the gas constant. The equation remains separable in the case of isothermal and isobaric processes.

A set of activation energy and volume parameters is associated with the rate-controlling step of a specific chemical reaction. In the case of a complex process such as cement hydration, it is more appropriate to talk about apparent activation parameters because dominating mechanisms change as the transformation progresses. Therefore, in the following, activation parameters should be understood as apparent ones, unless otherwise specified.

We might introduce variations of either activation parameter to accommodate their possible evolutions as the reaction progresses. However, the exploration of the dependency of activation energy on hydration degree has shown contradictory results (see [118, 134, 135]). We analyze the evolution of E_a with hydration degree for a single cement paste in Section 4.3, where it will be shown that Equation (4.2) provides a fair description of the experimental observations.

4.2.3   Conversion function

The broad range of mechanisms of phase transformation of cementitious materials requires the consideration of different kinetic models [41]. Šesták and Berggren [136] have investigated the main mechanisms underlying the transformation processes of solid-state reactions. They propose a single mathematical expression capable of reproducing the kinetics of a wide variety of reactions, in the following form:

$$f(\alpha) = \alpha^m \left(1 - \alpha\right)^n \left(-\ln\left(1 - \alpha\right)\right)^p \tag{4.3}$$

where m, n and p are constants to be determined from experiments. A comprehensive description of the mechanisms can be found in ref. [64], with a summary available in ref. [137].

The previous expression might be divided in three elementary kernel terms: the consumed mass of reactants α, the remaining mass of reactants $(1 - \alpha)$ and the term $-\ln(1 - \alpha)$, related to the impingement and coalescence of reactants and products. In homogeneous gas kinetics, exponents m and n are interpreted as the order of reaction for the products or reactant phases, and related to the probability of collisions (order n implies n successive collisions). Following the same line of thought for heterogeneous solid kinetics, these exponents might be interpreted as derived from a branching process, as discussed in Section 4.4.

The inspection of the kernel terms in Equation (4.3) permits the simplification of the general expression. The decomposition into elementary functions is presented in Figure 4.1. It is clear, as expected from a Taylor expansion, that terms α and $\ln(1 - \alpha)$ give a similar trend for small values of α. On the other hand, the term $(1 - \alpha)$ is dominant for later stages of the reaction. In other words, we can, without loss of generality, simplify Equation (4.3) by assuming $m = 0$ and therefore reduce the number of model parameters to two.

The resulting simplified expression is rich enough as to accommodate reaction-controlling mechanisms of nucleation and growth, phase boundary advance, diffusion and order-based reactions (consult ref. [136]).

As a consequence of the isoconversional compliance of the cement hydration reaction, the general expression we will use to describe the hydration reaction rate is:

$$\dot{\alpha} = A \exp\left(-\frac{E_a + \Delta V P}{R T}\right) \left(1 - \alpha\right)^n \left(-\ln\left(1 - \alpha\right)\right)^p \tag{4.4}$$

where the the kinetic parameters are A, E_a, ΔV, n and p. A total of five parameters are needed to model hydration kinetics from early to late ages under different pressure and temperature conditions.
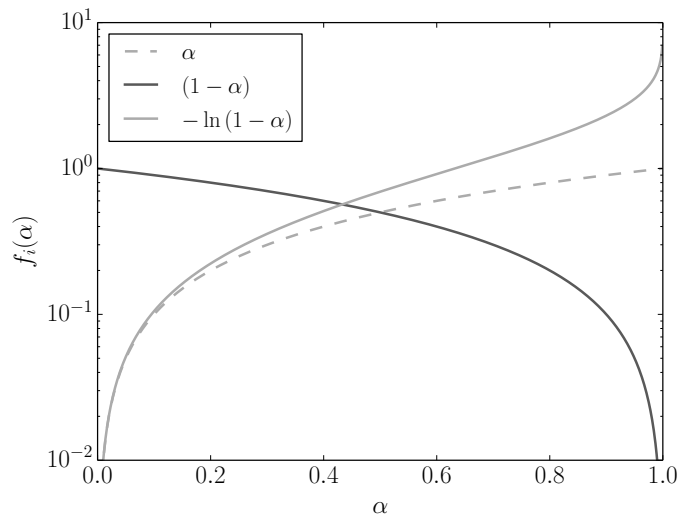
Figure 4.1: Comparison of the kernel terms of Equation (4.3).

4.3 Applications and results

The application of the model might be decomposed in two independent parts concerning the determination of: 1) the activation parameters and 2) the conversion function. The calibration procedure described might readily be applied to other cement paste compositions or curing conditions.

For the determination of the model parameters, simulated annealing [115] and basin-hopping [116] algorithms were initially used to explore large parameter domains and assure the identification of global best-fit values in case of non-convexity of the error functions. For our applications, the use of simple convex optimization algorithms in the neighbourhood of reference parameters (e.g. Table 4.2) should suffice to determine global optimal values.

4.3.1 Materials and experimental conditions

The hydration kinetics of an API Class H cement have been adapted from the experimental results of [9]. The median particle size of the clinker grains is 28.6 μm, determined by laser scattering, and the calculated specific surface is 254 m^2/kg. The slurries were prepared following the API recommendations [92], with a water to cement ratio of 0.38.

The hydration degree is determined by means of isothermal/isobaric calorimetry, consisting of measuring the heat flow from a hydrating sample while keeping the temperature and pressure constant. The method is efficient due to the highly exothermal nature of the cement hydration reaction [111]. The heat of reaction of the main components and their relative masses in the cement powder are presented in Table 4.1. The calculated ultimate heat release of our cement powder is 386.74 J/g.

Table 4.1: Composition by mass and heat of reaction - Class H cement [9]

	Component[a]				
	C_3S	C_2S	C_3A	C_4AF	Others
Rietveld composition (%)	48.2	29.4	0.0	17.2	5.2
Heat of reaction Q_∞ $(J/g)^b$	500	250	880	420	0

[a] Cement chemistry notation: $C = CaO$, $S = SiO_2$, $A = Al_2O_3$, $F = Fe_2O_3$.
[b] From ref. [41].

Isothermal calorimetry tests were performed at different curing conditions (Figure 4.2). The results constitute a rich and compatible data set with varying temperatures (25, 40, 60°C) and pressures (2, 15, 30, 45 MPa), which are in the ranges of the oil industry applications. The lower pressures concern conventional civil engineering structures.
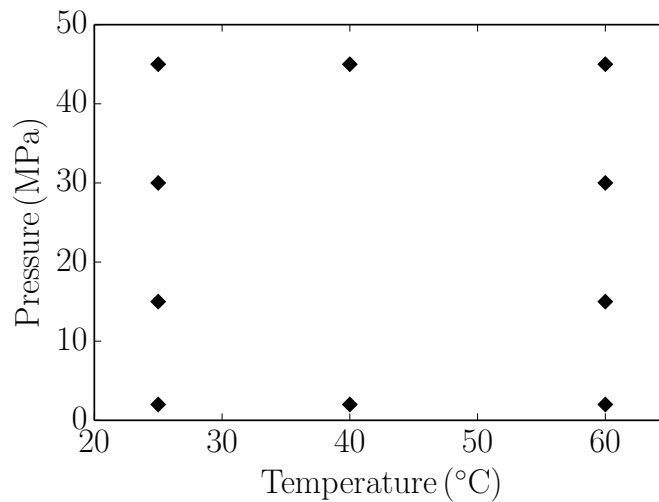
Figure 4.2: Curing conditions for isothermal calorimetry tests.

Figure 4.3a presents the corresponding hydration curves. The normalization of each test by its rate peak, shown in Figure 4.3b, reveals the isoconversional nature of the cement hydration reaction: different temperature and pressure conditions result in remarkably similar normalized hydration curves.

4.3.2 Determination of the activation parameters

From the isoconversional hypothesis, the activation parameters E_a and ΔV are independent of the function $f(\alpha)$. For a series of tests at different temperatures and constant pressure, the activation energy E_a can thus be determined, for a given hydration degree α, from a linear fit in the Arrhenius plane $\ln \dot{\alpha} - 1/T$. A similar approach is suitable for the determination of the activation volume ΔV from tests at constant temperature and different pressures, for which we expect linearity in the $\ln \dot{\alpha} - P/T$ plane.
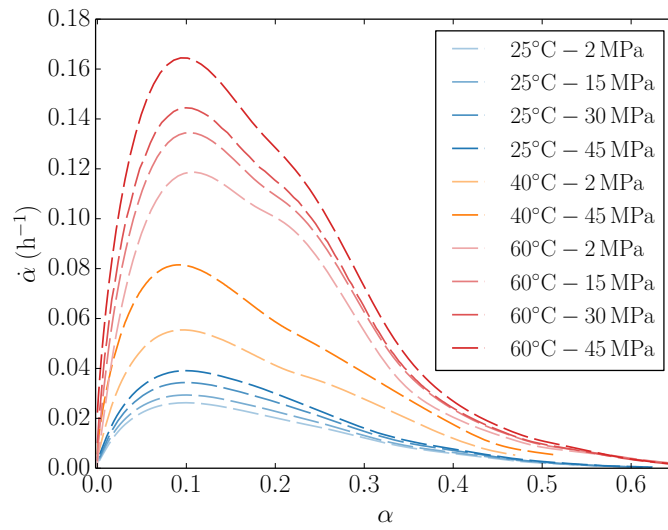
(a) Observed rate
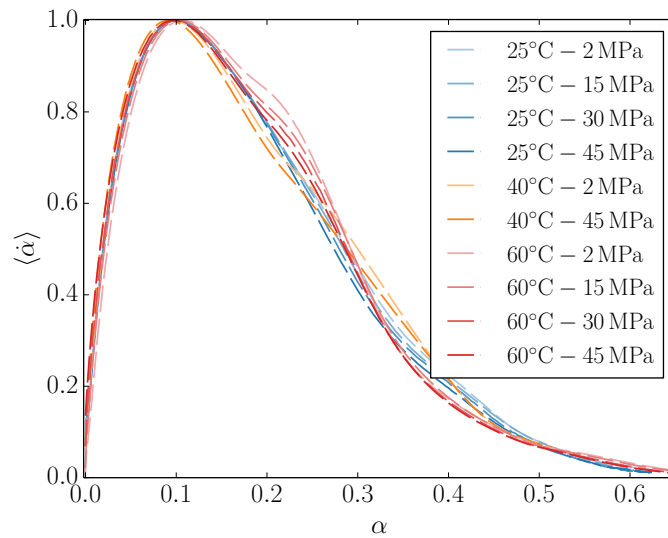
(b) Normalized rate

Figure 4.3: Hydration curves for different pressure and temperature curing conditions. Adapted from [9].

The experimental results provide evidence of the validity of the Arrhenius form of the rate function Equation (4.2). The linear fits for different isoconversional lines is presented in Figure 4.4a for tests performed at 45 MPa and temperatures of 25, 40 and 60°C. Note that, as pointed out by Laidler [117], T, 1/T and ln T are all approximately interdependent in the range of 0 to 100°C, so other activation functions might yield linear relations. We have chosen the Arrhenius equation for the reasons exposed in Section 4.2. The evolution of the activation energy throughout the reaction can be obtained from similar isoconversional lines at different degrees of hydration. It can be observed that the activation energy E_a calculated for pressures of 2 and 45 MPa is limited in range (Figure 4.4b). For our fitting

purposes, we adopt the assumption of a constant activation energy.
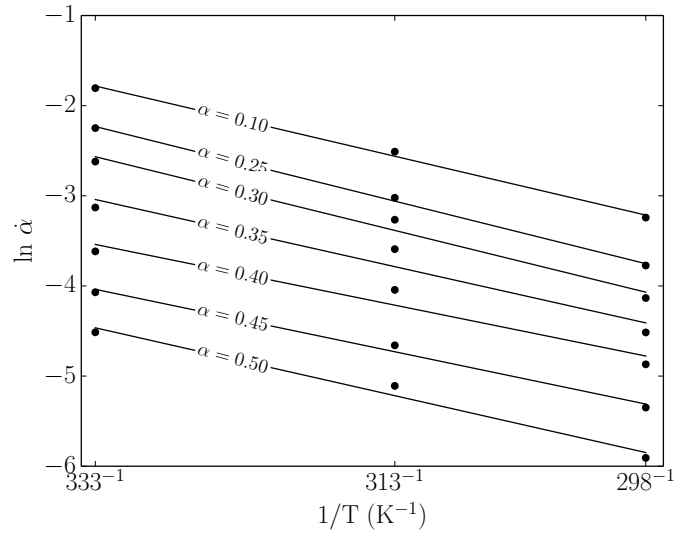
(a) Isoconversional lines for the determination of activation energy E_a for a curing pressure of 45 MPa. Marks correspond to experimental observations, solid lines to linear trend.
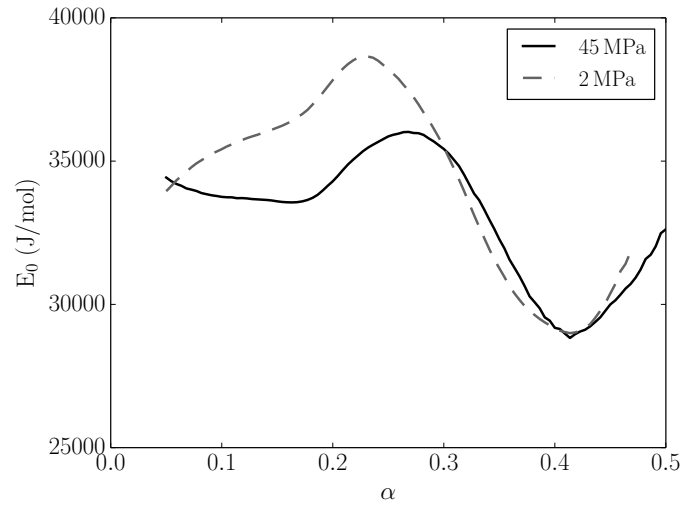
(b) Observed evolution of activation energy E_a with the hydration degree for sets of tests at constant curing pressures of 2 and 45 MPa.

Figure 4.4: Activation energy plots

Similar conclusions can be drawn regarding the activation volume ΔV. The linear fits of several isoconversional lines for a constant temperature of 60°C (333 K) and pressures of 2, 25, 30 and 45 MPa are presented in Figure 4.5a. The evolution of the activation volume during hydration for tests at 25 and 60°C is shown in Figure 4.5b. In our model calibration, the activation volume ΔV will be assumed to be constant throughout the reaction.

It is important to note that, for both the activation energy and volume, the procedure is the same: only once the Arrhenius equation is confirmed upon inspection of the linear

slopes in the appropriate plane, we can proceed to the determination of the activation parameters.
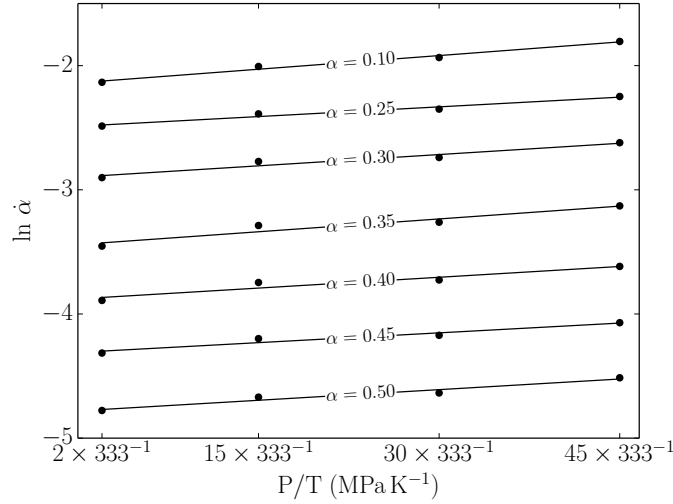
(a) Isoconversional lines for the determination of activation volume ΔV for a curing temperature of 60°C (333 K). Marks correspond to experimental observations, solid lines to linear trend.
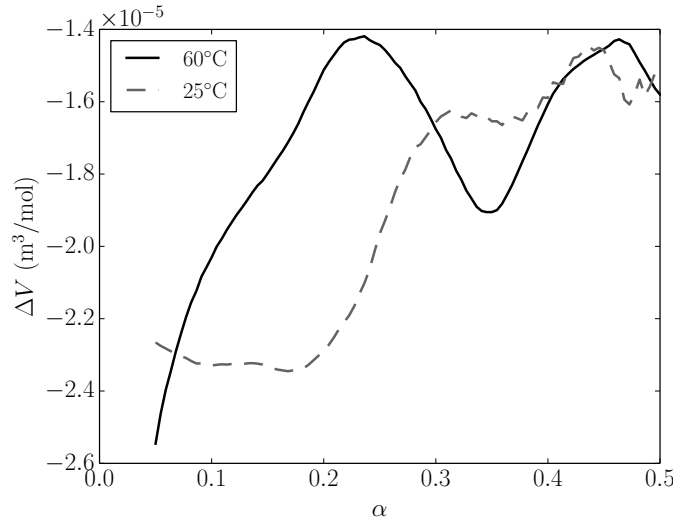
(b) Observed evolution of activation volume ΔV with the hydration degree for sets of tests at constant curing temperatures of 25 and 60°C.

Figure 4.5: Activation volume plots

For a complete set of data with multiple and combined temperature and pressure conditions, we determine the activation parameters with the aid of an optimization algorithm. Considering a set of hydration experiences, the isoconversional model (Equation (4.1)) allows expressing the reaction rate of any particular test i as:

$$\ln \dot{\alpha}_i = \ln k(T_i, P_i) + \ln f(\alpha) \tag{4.5}$$

Together with Equation (4.4), it is clear that the rate $\dot\alpha_j$ of test j at any hydration degree α can be expressed as:

$$\ln \dot\alpha_j = \ln \dot\alpha_i - \frac{E_a}{R}\left(\frac{1}{T_j} - \frac{1}{T_i}\right) - \frac{\Delta V}{R}\left(\frac{P_j}{T_j} - \frac{P_i}{T_i}\right) \tag{4.6}$$

independently of A and α. Therefore, for the model calibration, we adopt any test i as a reference and minimize the deviation between the model-estimated and the observed value of $\ln\dot\alpha_j$ over all tests and degrees of hydration. The error is defined as the absolute value of the differences.

For the class H cement we determine E_a = 34 580 J/mol and ΔV = -1.843$\times$10^{-5} m^3/mol, with an error of 6.8%. Both values are in clear correspondence to those determined instantaneously for the simpler sets of tests (see Figure 4.4b and Figure 4.5b). They are also within the range of commonly reported values [118–120].

The activation energy E_a is the energy jump required for the reactants to transition to the activated complex. A positive value implies that increments of temperature lead to increments of the rate of reaction, as observed in the experiments. The activation volume ΔV is the molar volume difference between reactants and activated complex. The negative value is interpreted as mechanical work done on the system by the surrounding pressure that helps surmount the activation energy barrier as its volume is reduced. The values of activation volume determined from experiments have been compared to chemical shrinkage measurements [9, 119], although their accordance is not predicted nor justified from activation theory. The comparison might, however, provide an order of magnitude of the expected activation volume. In our case, considering the cement powder composition (Table 4.1), the activation volume corresponds to 0.077 ml/g, similar to the measured chemical shrinkage [138].

The effects of pressure and temperature on the reaction rate as predicted by the model can be assessed in Figure 4.6a, where the rates have been normalized with respect to a reference condition of 25°C and atmospheric pressure (0.1 MPa). Pressure and temperature have similar effects of accelerating the rates of reaction. Both the spacing between isobaric curves and their slopes increase simultaneously with raising temperature and pressure: the same increment of temperature or pressure has a more significant effect at higher temperature or pressure.

For practical applications, it is useful to estimate the relative importance of changes of temperature or pressure. The equivalence of pressure and temperature changes can be determined considering iso-rate lines:

$$\frac{\partial k}{\partial P}\,dP + \frac{\partial k}{\partial T}\,dT = 0 \tag{4.7}$$
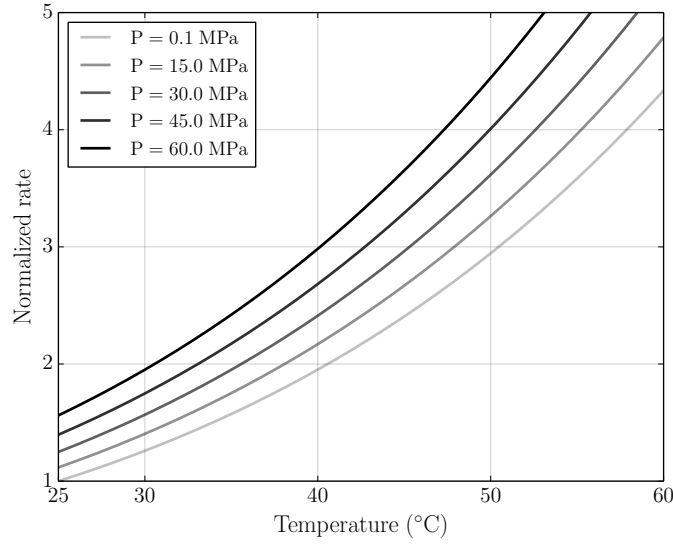
(a) Normalized reaction rates for different isobaric lines. The reference rate corresponds to 25°C and atmospheric pressure (0.1 MPa).
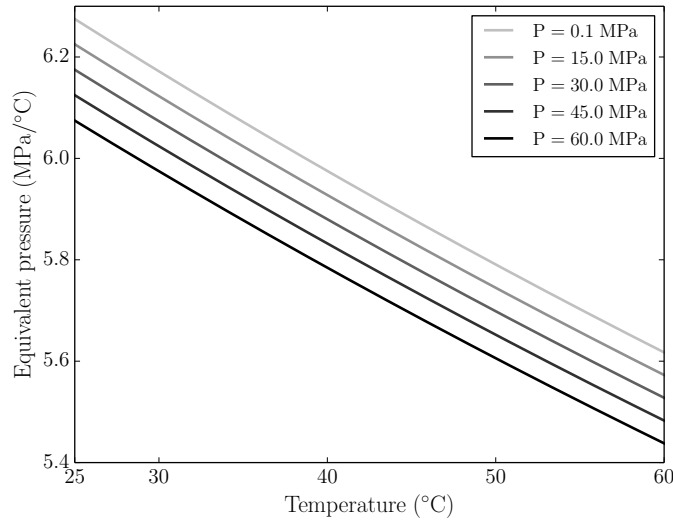
(b) Equivalent pressure changes for different isobaric lines.

Figure 4.6: Effect of pressure and temperature on reaction rate

so from Equation (4.2), the change ΔP that yields an increment of reaction rate equivalent to a change of temperature ΔT is given by

$$\Delta P = \frac{\Delta T}{T_0} \left(\frac{E_a}{\Delta V} + P_0 \right) \tag{4.8}$$

where P_0 and T_0 are the initial temperature and pressure respectively. The equivalent pressure decreases as the curing pressure or the temperature are incremented (Figure 4.6b). On average, the equivalent pressure is 5.8 MPa/°C.

For the particular case of an oil well cement sheath, changes in pressure are due to the

hydrostatic weight of the slurry or mud. Considering an average slurry density around 2 g/cm^3, the equivalent temperature increase is of 3.4°C/km due to the slurry weight. If we compare this to usual values of the naturally occurring geothermal gradient of 25°C/km [17], it becomes clear that temperature is the dominating parameter for this type of field application.

4.3.3 Determination of conversion function

The normalization of all hydration curves by their corresponding factors $k(T, P)$ causes them to collapse to a single master curve $A f(\alpha)$ (Figure 4.7). The determination of the unknowns n and p of the conversion function $f(\alpha)$ and the pre-exponential factor A is achieved in a second fitting step by minimizing the deviation over all the curves. The error is defined as the absolute value of the area between curves.
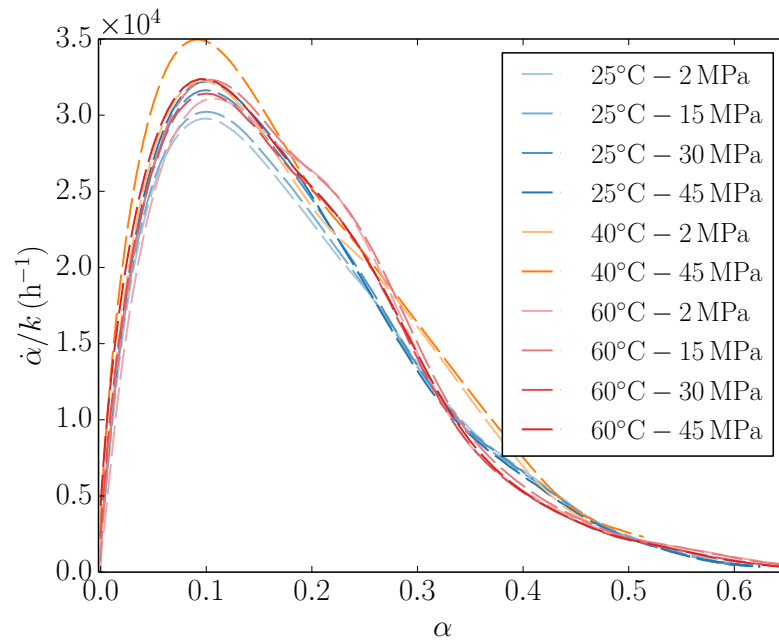
Figure 4.7: Collapsed hydration curves, normalized by the rate parameter k.

The model parameters for the class H cement are presented in Table 4.2. It is worth noting the proximity of p, as determined from global optimization, to the theoretical Nucleation and Growth model with isotropic growth and constant rate of nucleation, for which $p = 0.75$ (discussed in detail in Section 4.4). Both models adopt the same mathematical expression in the early hydration stage. The fit error for the set of parameters determined from $p = 0.75$ is very similar to that of the global optimal.

It is generally agreed that the first stages of reaction follow a nucleation and growth mechanism. Consensus regarding the mechanism has been reached over the years supported by different experimental and modelling techniques [22]. When determining chemical

reaction rates, it is important to recall that acceptable statistical model fits do not guarantee the mechanism to be properly modelled or understood. The agreement of the model parameters with the insight gained from direct observation of the products of the reaction is essential for the validation of the approach. The results presented in the following correspond to the set of parameters for imposed $p = 0.75$.

Table 4.2: Model parameters for class H cement, w/c=0.38.

Function	Parameter	No constraint	Fixed $p = 0.75$
Rate	E_a (J/mol)		34 580
	$\Delta V (10^{-5} \text{ m}^3/\text{mol})$		-1.843
	$A (10^5 \text{ h}^{-1})$	3.805	3.569
Conversion	n	7.00	6.90
	p	0.77	0.75
	Error (%)	5.30	5.32

The simulation of the experimental curing conditions show a close agreement with the measured curves, as can be seen in Figures 4.8 and 4.9, where the comparison is done on the three essential planes. The most significant deviations occur around the hydration rate bump associated to the formation of monosulfate, which is more significant at high pressures and temperatures [19].

To evaluate the model sensitivity to independent changes of the parameters, consider the logarithmic derivatives

$$\langle \dot{\alpha}_{,n} \rangle := \frac{\dot{\alpha}_{,n}}{\dot{\alpha}} = \ln(1 - \alpha); \quad \langle \dot{\alpha}_{,p} \rangle := \frac{\dot{\alpha}_{,p}}{\dot{\alpha}} = \ln\left(-\ln\left(1 - \alpha\right)\right) \tag{4.9}$$

where $\dot{\alpha}_{,x} = \frac{\partial \dot{\alpha}}{\partial x}$ and $\langle \cdot \rangle$ corresponds to normalization with respect to $\dot{\alpha}$. It is clear that the effect of p is large for small α, while the effect of n becomes more important as α increases. It is worth noting that the logarithmic derivatives are independent of the values of the parameters n and p.

In order to compare similar changes of the parameters, consider variations by a factor δ, so that $\Delta n = \delta n, \Delta p = \delta p$. The normalized variation of the rate $\langle \Delta \dot{\alpha} \rangle$ is given by:

$$\langle \Delta \dot{\alpha} \rangle = \langle \dot{\alpha}_{,n} \rangle \cdot \Delta n + \langle \dot{\alpha}_{,p} \rangle \cdot \Delta p = \delta \left(\langle \dot{\alpha}_{,n} \rangle \cdot n + \langle \dot{\alpha}_{,p} \rangle \cdot p \right) \tag{4.10}$$

This expression allows us to evaluate the proportion of the change of the rate of which each individual parameter is responsible for as the reaction progresses. As evidenced in Figure 4.10, the model is far more sensitive to changes of p for small α, while n becomes dominating for large α. For our values of n and p, they are both equally weighted at $\alpha \approx 0.17$. Regarding their impact on rate, $\langle \dot{\alpha}_{,n} \rangle$ is negative for all values of α, while $\langle \dot{\alpha}_{,p} \rangle$ is negative up to $\alpha = 1 - e^{-1} \approx 0.63$, meaning that, overall, increasing either parameter causes the rate to decrease.
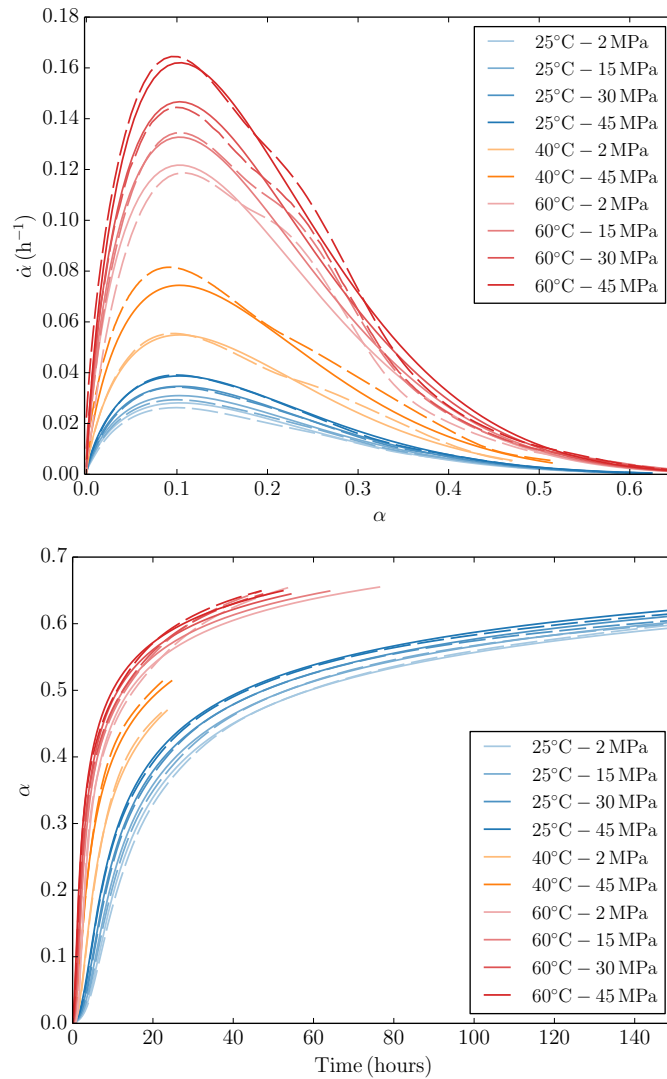
Figure 4.8: Experimental (dashed) and model (solid) hydration curves.

From the previous remarks, two important conclusions might be drawn: 1) the early stages of hydration are largely dominated by p and 2) the later stages of hydration are largely dominated by n. This is confirmed for wider variations of the parameters. Therefore, the fitting of the parameters is implicitly split in two parts, with p depending on the acceleration and n on the deceleration stages. This separation might be made explicit, and so we might fit each parameter separately.

A similar analysis is useful when considering the problem of variability and uniqueness of the model parameters. The effect of uncertainties and oscillations of the model parameters is illustrated in Figure 4.11. Over 95 % of the experimental curves lay within the range of solutions swept by a 2.5% variation of the model parameters n and p. A 4% variation is sufficient to cover all the experimental observations. Small variations of the parameters have significant effects on the rates, suggesting a narrow range of appropriate parameters
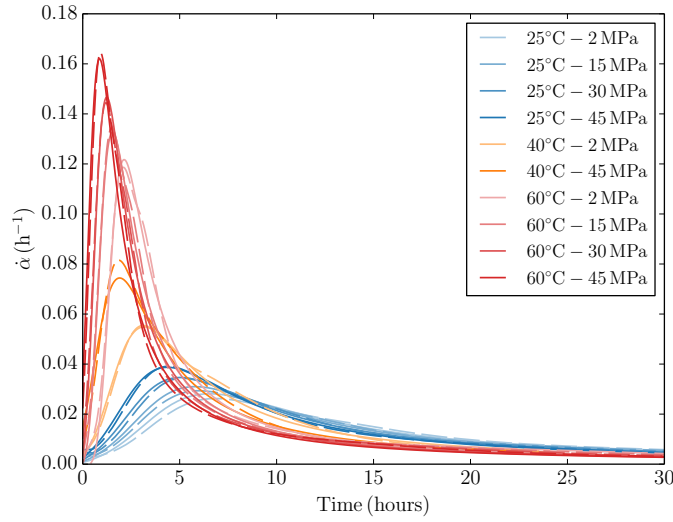
Figure 4.9: Experimental (dashed) and model (solid) hydration curves.
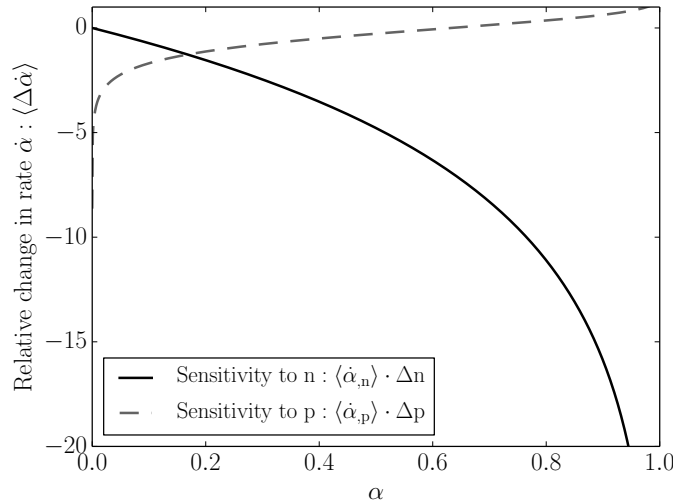
Figure 4.10: Effects of n and p on the rate of reaction ($\delta = 1$). See Equation (4.10) and text for details.

for the solution of the optimization problem. As anticipated in our sensitivity analysis, the effects of a proportional change of n and p are equivalent for $\alpha \approx 0.17$; with p dominating earlier and n later in the reaction.

The model application is straightforward for temperature and pressure conditions within the calibration domain, and likely remains accurate at curing conditions not too distant from its boundaries. Extrapolation to temperatures or pressures beyond this range might yield estimations of the reaction rates but should be done with caution, since at high temperatures and pressures chemical reactions and products might change significantly [23]. Bresson et al. [139] report structural changes for the C_3S hydration products above 120°C, while no effect was observed up to their highest testing pressure of 100 MPa. [140] observed
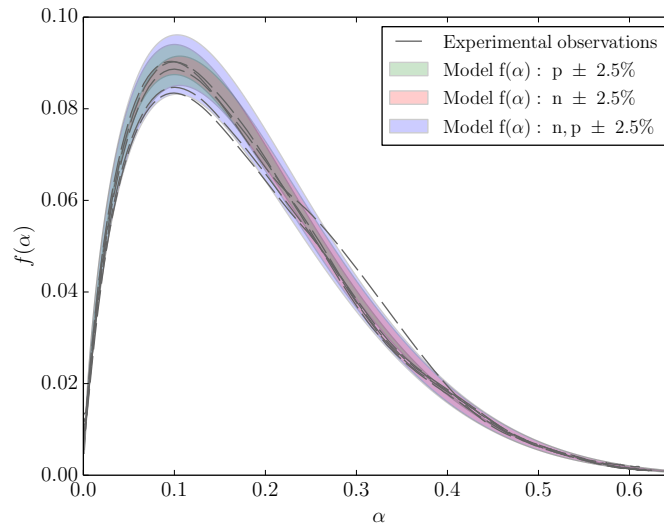
Figure 4.11: Effect of the variability of model parameters. Shaded bands cover the ranges of model responses.

significant changes starting at 110°C for a class G cement with added silica. The use of chemical additions also affect the kinetics of hydration in ways that remain unpredictable by the model without proper experimental characterization.

4.4 Discussion

4.4.1 Prediction of the hydration degree at early and advanced ages

There are several examples in the cement literature of models proposing kinetic laws based on physical solid state kinetic considerations with mechanism-control shift [47–49]. However, they require the determination of transition thresholds and multiple parameters for the reproduction of the complete reaction. Furthermore, the continuity of the mathematical formulations and their smoothness is not guaranteed, often resulting in rapid changes of rates and a seemingly unphysical response.

One of the main advantages of the present model is the continuous mathematical expression describing both the early and advanced ages. We can extend the model to include the initial fast reaction and induction period by introducing the initial time t_0 and dissolution extent α_0 that correspond to the onset of the acceleration phase. The redefinition of time and hydration degree as $\tilde{t} = t - t_0$ and $\tilde{\alpha} = \alpha - \alpha_0$ allows the use of the model (Equation (4.4)) without further modification. In a similar way, the ultimate hydration degree α_u can be introduced in the formulation as an additional parameter by redefining $\tilde{\alpha} = \alpha/\alpha_u$. The value of α_u can be determined either from expressions available in the literature (e.g. ref. [112]) or from experiments.

4.4.2   Rate controlling mechanisms

In addition to describing the evolution of the hydration degree with time, we hope to gain insight into the physical mechanisms governing the transformation and the relevant reaction parameters. Complex chemical transformations such as cement hydration are the result of the combination and interaction of simpler elementary reactions. When these reactions occur in sequence, the slowest step controls and determines the overall reaction rate.

The adopted phenomenological approach has been successful in metallurgy and pharmaceutics, and its physical premises might shed light upon the underlying mechanisms governing the hydration process. We can identify terms corresponding to different mechanisms of the reaction by decomposing

$$f(\alpha) = \underbrace{(1 - \alpha)\left(- \ln\left(1 - \alpha\right)\right)^p}_{\text{Nucleation and Growth}} \underbrace{(1 - \alpha)^{n-1}}_{\text{Order-based}} \tag{4.11}$$

The p exponent in the Nucleation and Growth (NG) equation might be decomposed as $p = 1 - 1/N$, where $N = P/S + Q$. $P = 1, 2, 3$ if the growth is in the form of needles, plates or spheres respectively; $S = 1, 2$ if the growth is boundary or diffusion controlled respectively; $Q = 0, 1$ if the nucleation is respectively instantaneous or with a constant rate [41]. In our case, the fitted value of $p = 0.75$ is only possible for a boundary-controlled advance of spherical-growing hydrates at constant nucleation rate. The microscopic observation of the cement hydrates reveals laminar and fibrous structures agglomerated in disordered clusters with no preferential orientation [63, 108]. The growth rate of the hydration products is dependent on their packing and spatial distribution, rather than their underlying morphology. The hypothesis of spherical hydrate volumes is thus a plausible result of the averaging of randomly-oriented needles.

The partial terms and the resulting conversion function can be compared in Figure 4.12 in logarithmic scale. The early reaction rate is dictated by NG with random volume nucleation and constant growth rate. The main difference with respect to a standard NG model resides in the additional rate of attenuation, represented by the parameter $(1 - \alpha)^{n-1}$, that has an insignificant effect at early age but gains more importance as the reaction advances, because of its highly non-linear character.

The order-based mechanism is proportional to the remaining mass of reactant and might be interpreted as derived from a branching process. Intuitively, it reflects the inability of the reactants to transform successfully. The deceleration of the reaction can be due to phenomena such as nucleation sites exhaustion, accumulation of diffusion barriers for the dissolved species, lack of physical space or self-desiccation as the hydrates precipitate [45, 46]. In any case, as the hydration advances, the microstructural rearrangements make the reaction of the increasingly scarce leftovers of anhydrous cement powder less likely.
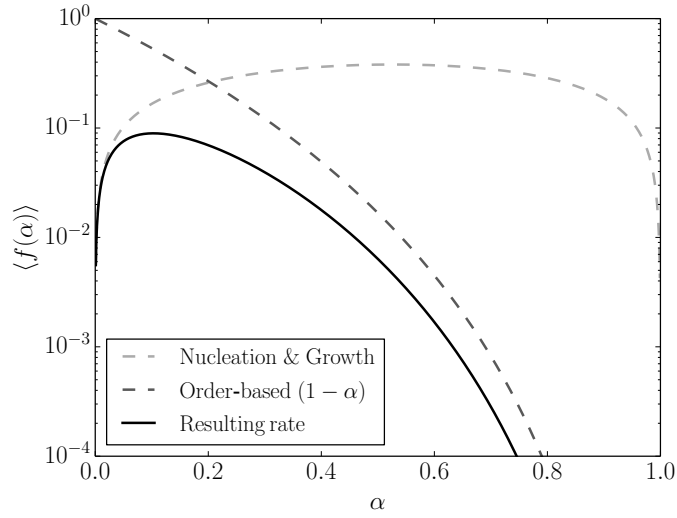
Figure 4.12: Decomposition of the rate of hydration.

The transition among mechanisms takes place around $\alpha = 0.2$, where control of the reaction is handed from NG to the order-based kinetic term. The relative importance of mechanisms shifts progressively, and a factor of 10 is found between rates at a hydration degree of $\alpha = 0.45$. As expected, the lowest rate dominates the overall observed reaction rate.

4.4.3 Comparison with other hydration models

The present model might be benchmarked against similar hydration models based on solid state kinetics found in the literature. Among such models, we can cite those of Parrot and Killoh [48], Bezjak and Jelenić [47], Krstulović and Dabić [49], Brown et al. [141], Berliner et al. [61], or more recently that of Biernacki and Xie [50]. All of these models postulate mathematical expressions describing hydration as a sequence of processes comprising nucleation and growth, diffusion –either parabolic or in the form of Jander, Ginstling-Brounshtein or Fuji and Kondo [37, 137]– and often other empirical expressions.

For comparison purposes, the model proposed by Parrot and Killoh [48] (PK) presents a high level of flexibility while remaining simple in its formulation, and has often been employed in the literature (e.g. [107, 142, 143]). The PK model proposes three different reaction rates:

$$\dot{\alpha}_1 = k_1 \left(1 - \alpha\right) \left(- \ln \left(1 - \alpha\right)\right)^{n_{pk}} \tag{4.12a}$$

$$\dot{\alpha}_2 = k_2 \frac{\left(1 - \alpha\right)^{2/3}}{1 - \left(1 - \alpha\right)^{1/3}} \tag{4.12b}$$

$$\dot{\alpha}_3 = k_3 \left(1 - \alpha\right)^{p_{pk}} \tag{4.12c}$$
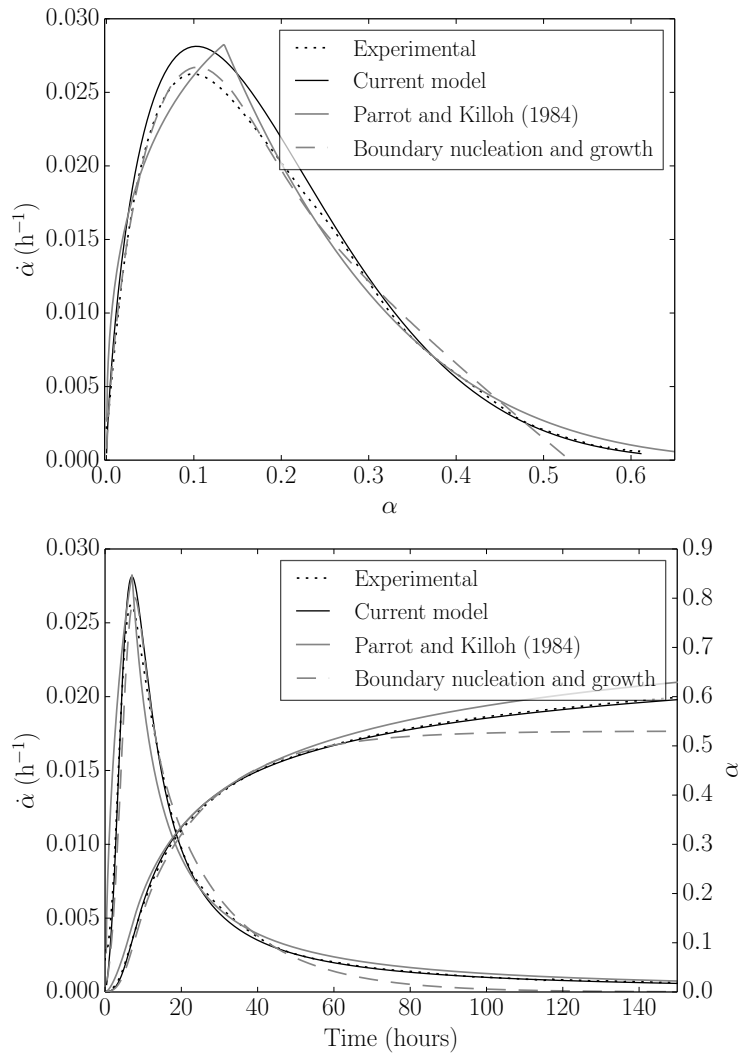
Figure 4.13: Comparison of model performances. Experimental results correspond to hydration at 2 MPa and 25°C.

with rate parameters k_1, k_2, k_3 and conversional parameters n_{pk} and p_{pk}. The first rate corresponds to nucleation and growth, the second to diffusion and the third to a process of hydration shell formation [48]. The effective reaction rate is the lowest of the three, i.e. $\dot{\alpha} = \min(\dot{\alpha}_1, \dot{\alpha}_2, \dot{\alpha}_3)$. We might assume the rate parameters are equally activated by temperature and pressure, i.e. the hydration rate follows an isoconversional formulation.

Additionally, we compare the results obtained with the Boundary Nucleation and Growth model (BNG, [3, 58]) for which hydration degree at time t is given by the expression

$$\alpha = A\left(1 - \exp\left(-X^e\right)\right) \tag{4.13}$$

where

$$X^e = 2k_g t \left[1 - \int_0^1 \exp\left(-\frac{\pi}{3} \frac{k_b^4 t^3}{k_g} \left(2x^3 - 3x^2 + 1 \right) \right) \mathrm{d}x \right] \tag{4.14}$$

The model parameters are the rates k_b and k_g and the dimensionless scalar A.

The comparison of the results for the hydration evolution at a pressure of 2 MPa and temperature of 25°C is presented in Figure 4.13. The PK model was fitted to its optimal parameters for this single test, with $k_1 = 6.68 \times 10^{-2}$ h^{-1}, $k_2 = 1.75 \times 10^{-3}$ h^{-1}, $k_3 = 5.26 \times 10^{-2}$ h^{-1}, $n_{pk} = 0.37$, $p_{pk} = 4.3$. The parameters of our model are those presented in Table 4.2, determined from the entire range of tests, and thus constrained to fit a larger set of experimental results. In terms of the model parameters, although we could draw analogies between n vs. n_{pk} and p vs. p_{pk}, the parameters are significantly different. The PK model is continuous in rate, but the transition among mechanisms is not smooth.

Regarding the BNG model, the optimal fits are $A = 0.53$, $k_b = 8.37 \times 10^{-2}$ h^{-1}, $k_g = 2.44 \times 10^{-2}$ h^{-1}. The BNG model can only reproduce the early stages of hydration, as evidenced by the value of A that sets the maximum attainable hydration degree. Beyond a hydration degree of 50%, the differences become increasingly more important.

Overall, the present model is able to reproduce the observed data more closely with a reduced number of parameters. A notable feature is the continuity of the mathematical form for both the early and advanced ages.

4.5   Model parameters for class G cement paste

The current section presents the application of the hydration model to the class G cement paste that will be the subject of study throughout the second part of the present manuscript. The cement powder properties and cement paste formulation are available in Section 2.1. The summary of the available isothermal calorimetry tests presented in Table 2.3 span over a wider range of temperatures than the results available for the class H cement paste examined before.

The model parameters have been modified as a function of temperature to better reproduce the experimental observations. The effect of pressure on the model kinetic parameters is negligible. The calibration of the model has been performed by parts, splitting the data in two ranges of temperatures (low temperatures between 7 and 40°C, and high temperatures between 60 and 90°C). Besides this caveat, the observations are analogous to those discussed in the preceding sections.

The following expressions are proposed for parameters E_a, ΔV, n and $\ln A$:

$$E_a = E_a^l + \left(E_a^h - E_a^l\right) h(T) \tag{4.15a}$$

$$\Delta V = \Delta V^l + \left(\Delta V^h - \Delta V^l\right) h(T) \tag{4.15b}$$

$$n = n^l + \left(n^h - n^l\right) h(T) \tag{4.15c}$$

$$\ln A = \ln A^l + \left[\ln A^h - \ln A^l\right] h(T) \tag{4.15d}$$

where the parameters $E_a^l = 41\,820$ J/mol, $E_a^h = 22\,810$ J/mol, $\Delta V^l = -1.34 \times 10^{-5}$ m^3/mol, $\Delta V^h = -1.67 \times 10^{-5}$ m^3/mol, $n^l = 5.14$, $n^h = 4.07$, $\ln A^l = 15.77$ and $\ln A^l = 8.21$. The l and h superscripts stand for low and high temperature, respectively. The temperature dependency is encapsulated by the function:

$$h(T) = \left[1 + \exp\left(s_G(T - T_0)\right)\right]^{-1} \tag{4.16}$$

for which $s_G = -0.2$ is a steepness constant and $T_0 = 50°$C is the assumed transition temperature. The evolution of the parameters is schematically depicted in Figure 4.14. If desired, the dependency of parameter ΔV can be dropped, a mean value being adopted instead, given the relative insensitivity of this parameter with respect to temperature. In all cases, $p = 0.75$, thus assuming a nucleation and growth rate control early in the reaction.
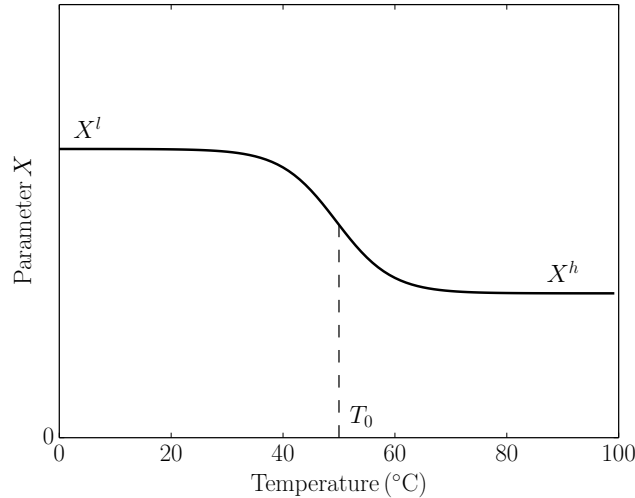
Figure 4.14: Schematic evolution of the hydration model parameters for the class G cement paste.

The experimental calorimetric measurements and the simulated hydration degrees are presented for low and high temperature ranges in Figures 4.15 and 4.16. The experimental results in the high temperature range clearly suggest heterogeneous hydration rates of the cement powder phases. The effects are also visible at moderate temperatures, although to

a minor degree. The hydration model, as formulated, is incapable of properly capturing the independent kinetics of the different components, and therefore it is not surprising that the fitting of the rates is not optimal. The overall hydration degree trend is, however, reasonably well captured, considering our intended applications.
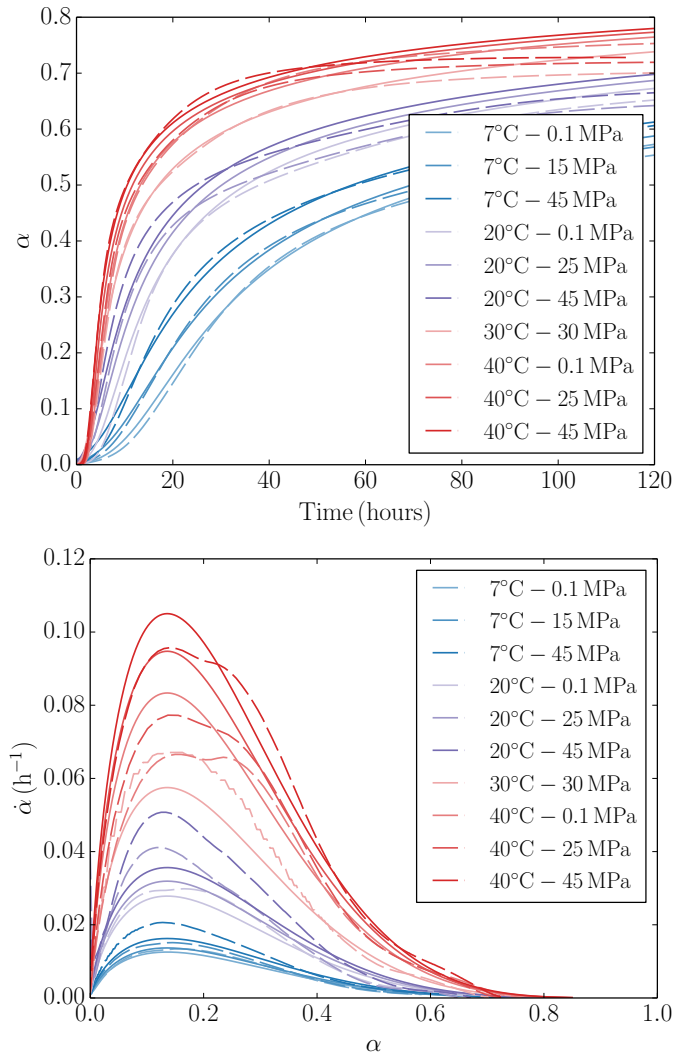
Figure 4.15: Experimental (dashed) and model (solid) hydration curves for class G cement paste. Low temperature range between 7 and 40°C.

The analysis of the hydration model reveals that the transition among mechanisms takes place at $\alpha \approx 0.25$. The complete control by the late mechanism is established around $\alpha \approx 0.5$. This observation will be useful in the formulation of our volume fraction model in Section 5.3.1, since the hydration degree corresponding to the rate mechanism shift has often been considered as an appropriate threshold for the production of different types of C–S–H hydrates (LD or HD) [8, 16, 144].
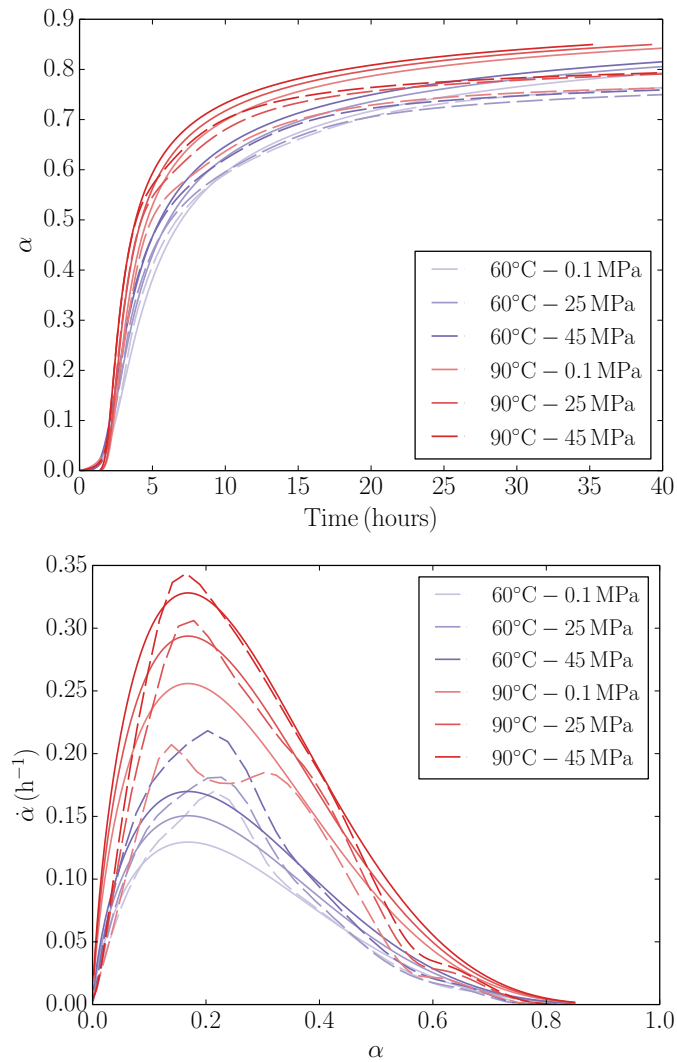
Figure 4.16: Experimental (dashed) and model (solid) hydration curves for class G cement paste. High temperature range between 60 and 90°C.

4.6 Conclusion

In this chapter, we propose a mathematical model for cement hydration based on experimental observations and chemical kinetic concepts. Hydration kinetics at different curing conditions can accurately be described with a simple mathematical expression coupling rates from activation theory (Arrhenius law) with conversion functions of solid-state kinetics. A wide spectrum of tools is available in both fields that might improve our understanding of cement hydration reactions.

The calibration procedure follows two steps for the determination of the rate and conversion functions for isothermal or isobaric hydration curves. These conditions are the most widely employed for their experimental ease and are closely related to those found in

oil wells, where the thickness of cement sheath assures short heat diffusion times and a nearly constant temperature. For conditions far from isothermal or isobaric, integration is possible to determine the model parameters. The simulation of short and long-term evolution of hydration degree under conditions of variable pressure or temperature is possible by integrating the hydration rate over time [145].

The activation parameters are $E_a = 34\,580$ J/mol and $\Delta V = -1.843 \times 10^{-5} \text{m}^3$/mol for a class H cement paste. Both temperature and pressure have the effect of increasing the reaction rates, although with different sensitivities. In the ranges of temperatures (25-60°C) and pressures (2-45 MPa) of the study, an average pressure increase of 5.8 MPa is equivalent to a temperature increase of 1°C. Temperature is therefore regarded as a far more critical parameter for both civil engineering and oil well practical applications.

A single conversion function with two kinetic parameters is sufficient to model cement hydration from early to advanced ages. The kinetic conversion parameters agree with observations of the early hydration stages, where nucleation and growth is the rate-controlling mechanism. Later, an order-based method becomes rate-controlling, owing among other reasons to the unavailability of reactants, lack of physical space and the tortuous microstructural diffusive barriers presented to the reaction paths from the hydrated shell.

The potential for future modelling is promising. Subsequent developments will be devoted to the description of hydration of individual cement powder phases and the determination of their kinetic parameters, with the ultimate objective of producing a predictive model capable of accounting for the effects of composition and curing conditions.

Part II

Poromechanical behaviour

Chapter 5

Constitutive model of the mechanical behaviour of a cement paste from early age to hardened state

5.1 Introduction

This chapter presents a comprehensive constitutive model for cement paste, from its early age to hardened state. The model is formulated in the framework of Biot's theory, considering the reactive porous medium as the superposition of solids and fluids and allowing the application of classical notions of continuum mechanics to porous materials [71, 72]. The model is inspired by the work of Agofack [16], revised, extended and reformulated according to thermomechanical principles [146]. The choice of variables and mathematical notation refers to the work of Coussy [147].

We proceed by first formulating the basic physical laws for the open cement paste system. The multiple mechanisms intervening in the system are identified, isolated and characterized independently. Finally, the mechanical constitutive laws of the solid are formulated.

5.2 Macroscopic material description and balance equations

The cement paste is constituted of a solid skeleton and a pore space. The solid skeleton, in turn, is composed of anhydrous cement powder and hydration products, in the following noted as s and h, respectively. The pore space is filled by liquid, vapour and dry air, henceforth noted respectively as l, v and a. A schematic representation is presented in Figure 5.1.
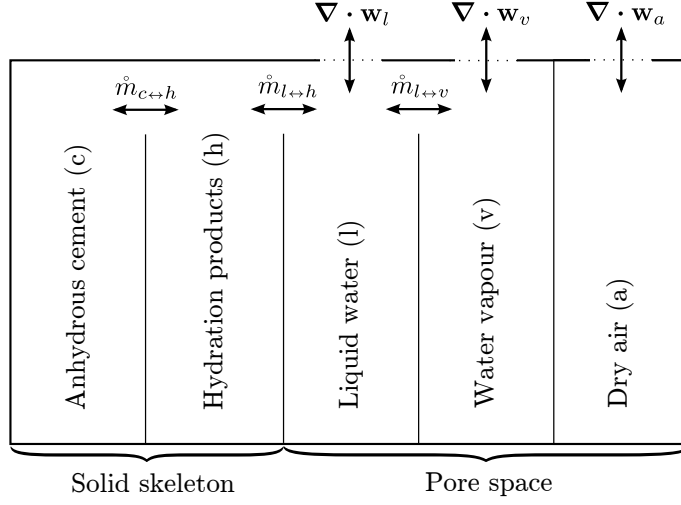
Figure 5.1: Constitution of a cement paste. Note the mass exchanges among phases and with the surroundings.

In our continuum mixture formulation all of these different phases coexist over the material volume [147]. The description is based on a Lagrangian framework with the solid skeleton as a reference configuration, a convenient choice because it allows the direct observation of the deformations. The kinematic description considers only infinitesimal transformations in a first-gradient approach. We admit only local contact forces and adopt the non-polar medium mechanical description.

We consider inertial forces sufficiently small as to be neglected. This quasi-static hypothesis conveniently lightens the mathematical expressions (examples of dynamic formulations are presented in ref. [147, 148]). Disregarding dynamic terms is acceptable since not only the solid exhibits small velocities and accelerations, but so do the fluids, due to the low permeabilities of the material.

In the following, we formulate the essential physical balance equations and laws, i.e. conservation of mass, equilibrium and thermodynamic laws of energy conservation and entropy production.

5.2.1 Mass and momentum balance

In general, the mass balance equation for phase i is expressed in its local form as:

$$\dot{m}_i = -\boldsymbol{\nabla} \cdot \mathbf{w}_i + \mathring{m}_i \tag{5.1}$$

where $m_i = \rho_i \phi_i$ is the mass content, ρ_i the intrinsic density, ϕ_i the Lagrangian porosity, $\mathbf{w}_i$ the flow of mass into the skeleton and $\mathring{m}_i$ is the net rate of local mass exchanges, all quantities being expressed per unit skeleton volume. The mass conservation of the

independent phases of the mixture are therefore expressed as:

$$\dot{m}_c = -\mathring{m}_{c \to h} \tag{5.2a}$$

$$\dot{m}_h = \mathring{m}_{c \to h} + \mathring{m}_{l \to h} = \mathring{m}_h \tag{5.2b}$$

$$\dot{m}_l = -\boldsymbol{\nabla} \cdot \mathbf{w}_l - \mathring{m}_{l \to h} - \mathring{m}_{l \to v} \tag{5.2c}$$

$$\dot{m}_v = -\boldsymbol{\nabla} \cdot \mathbf{w}_v + \mathring{m}_{l \to v} \tag{5.2d}$$

$$\dot{m}_a = -\boldsymbol{\nabla} \cdot \mathbf{w}_a \tag{5.2e}$$

Local mass exchanges are due to the transformations occurring inside the skeleton, viz. hydration reaction and phase transition. As a consequence, internal exchanges exist among solid and hydrates, while liquid can exchange with either vapour or hydrates. Regarding exchanges with the exterior, the system is open with respect to the fluids flow, i.e. liquid, vapour and dry air. Anhydrous cement and hydration products, however, remain in the interior of the system –i.e. hydrates are formed and cumulated locally– and form the skeleton of the material. This will prove useful later in the definition of the state variables.

Assuming body forces upon all phases to be equal, the local overall linear momentum conservation reads:

$$\boldsymbol{\nabla} \cdot \boldsymbol{\sigma} + \rho \mathbf{f} = \mathbf{0} \tag{5.3}$$

where ρ is the mass density of the porous medium, $\mathbf{f}$ is the body force and $\boldsymbol{\sigma}$ is the symmetric Cauchy stress tensor.[1]

5.2.2 First law of thermodynamics

The conservation of energy of a system expresses the relations existing among the kinetic and potential energy as well as the exchanges of work and heat. Considering the kinetic energy and heat radiation to be negligible, the local energy balance of our system reads:

$$\dot{E} = \boldsymbol{\sigma} : \dot{\boldsymbol{\varepsilon}} - \sum \boldsymbol{\nabla} \cdot (h_i \mathbf{w}_i) - \boldsymbol{\nabla} \cdot \mathbf{q} + \mathbf{f} \cdot \sum \mathbf{w}_i \tag{5.4}$$

where E is the overall energy density of the mixture, $\boldsymbol{\varepsilon}$ the linearized strain tensor, $\mathbf{q}$ is the heat flow and h_i the specific enthalpy of phase i. At the right-hand side, the first term is the overall mechanical work rate of the skeleton, the second term includes both the internal energy and the mechanical displacement work of mass transferred into the skeleton, the third term corresponds to the heat flow rate and the last term to the mechanical work rate of body forces.

---

[1]The decomposition in symmetric partial stress tensors acting on the mixture components is possible, as explained in ref. [149].

5.2.3 Second law of thermodynamics

The local expression of the second law of thermodynamics is given by the classic Clausius-Duhem inequality:

$$\dot{S} \geq -\sum \boldsymbol{\nabla} \cdot (s_i \mathbf{w}_i) - \boldsymbol{\nabla} \cdot \left(\frac{\mathbf{q}}{T}\right) \tag{5.5}$$

where S is the overall entropy density of the mixture and s_i is the specific entropy of phase i. We assume all phases to be in thermal equilibrium, and thus a single temperature T is sufficient to describe the temperature of all the mixture components. For this hypothesis to be valid, the mass transport time scale has to be much larger than the thermal equilibrium time scale. We might assume this to be the case in low-permeability materials such as cement paste.

Since it is often the case that we can either control or measure temperature changes, it is convenient to express the relations as functions of temperature instead of entropy. For this purpose, consider the Helmholtz free energy potential $F = E - TS$, i.e. the partial Legendre transform of internal energy with respect to dual variables S and T. Upon derivation, we obtain $\dot{F} + T\dot{S} = \dot{E} - S\dot{T}$. Combining this expression and Equation (5.4) together with Equation (5.5) gives:

$$\underbrace{\boldsymbol{\sigma} : \dot{\boldsymbol{\varepsilon}} - \sum \mu_i \boldsymbol{\nabla} \cdot \mathbf{w}_i - S\dot{T} - \dot{F}}_{\varphi_o} \underbrace{- \sum \boldsymbol{\nabla}\mu_i|_T \cdot \mathbf{w}_i + \mathbf{f} \cdot \sum \mathbf{w}_i}_{\varphi_m} \underbrace{- \frac{\mathbf{q}}{T} \cdot \boldsymbol{\nabla}T}_{\varphi_{th}} \geq 0 \tag{5.6}$$

where μ_i is the specific chemical potential of phase i, and $\boldsymbol{\nabla}\mu_i|_T$ is its gradient at constant temperature. We can identify three separate dissipation sources: φ_m due to mass transport, φ_{th} due to heat transfer and φ_o deriving from other evolutions of the reactive open system. The total dissipation Φ is the sum:

$$\Phi = \varphi_o + \varphi_m + \varphi_{th} \geq 0 \tag{5.7}$$

Because of the intrinsically different nature of the dissipative terms, each of them has to satisfy the inequality independently. Heat transfer dissipation is commonly described according to Fourier's law, while the dissipation from fluid transport is described, for a saturated porous medium, by Darcy's law or its equivalent for a partially saturated medium [150].

Considering isothermal evolutions, the dissipation φ_o of the reactive open system is:

$$\varphi_o = \boldsymbol{\sigma} : \dot{\boldsymbol{\varepsilon}} - \sum \mu_i \boldsymbol{\nabla} \cdot \mathbf{w}_i - \dot{F} \geq 0 \tag{5.8}$$

which, from the general expression of mass conservation, can be rewritten as:

$$\varphi_o = \underbrace{\boldsymbol{\sigma} : \dot{\boldsymbol{\varepsilon}} + \sum \mu_i \dot{m}_i - \dot{F}}_{\varphi} - \underbrace{\sum \mu_i \mathring{m}_i}_{\varphi_\rightarrow} \geq 0 \tag{5.9}$$

where each of the dissipation terms φ and $\varphi_\rightarrow$ satisfy the inequality independently. It is worth noting that we have yet to make use of the closure conditions of our system (Equation (5.2)). The dissipation term φ arises from the irreversible evolutions of the system. The term $\varphi_\rightarrow$ can be explicitly written as:

$$\varphi_\rightarrow = \underbrace{-\left(\mu_h \mathring{m}_h - \mu_c \mathring{m}_{c\rightarrow h} - \mu_l \mathring{m}_{l\rightarrow h}\right)}_{\varphi_h} - \underbrace{\left(\mu_v - \mu_l\right)\mathring{m}_{l\rightarrow v}}_{\varphi_t} \geq 0 \tag{5.10}$$

where we acknowledge that this dissipation results from phase transformations: φ_t due to phase transition (evaporation or condensation) and φ_h associated with the advance of the hydration reactions. Given the independence of the two different processes, φ_h and φ_t must satisfy the inequality separately.

5.3 Hydration kinetics and volume fractions evolution

The chemical reactions involved in the hydration of cement are the subject of extensive research, as discussed in Chapters 1, 3 and 4. We consider the reaction as a combination of solid and liquid reactants in some proportion to yield hydration products:

$$\nu_c C + \nu_l L \rightarrow \nu_h H \tag{5.11}$$
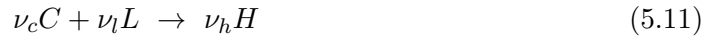
where C, L and H stand for unit masses of cement, liquid and hydrate, and ν_i is the average stoichiometric coefficient per unit mass of component i, determined from the consideration of the chemistry of the reaction (see Section 5.3.1).

Furthermore, the mass balance of the hydration reaction requires:

$$\mathring{m}_{c\rightarrow h} + \mathring{m}_{l\rightarrow h} = \mathring{m}_h \tag{5.12}$$

Following the classical ideas of physical chemistry [151], the common ratio deriving from the previous relations

$$\mathring{\alpha} = \frac{\mathring{m}_{c\rightarrow h}}{\nu_c} = \frac{\mathring{m}_{l\rightarrow h}}{\nu_l} = \frac{\mathring{m}_h}{\nu_h} \tag{5.13}$$

defines the rate of hydration α, expressing the coherent advance of the reaction. The dissipation φ_h can now be expressed as:

$$\varphi_h = (\underbrace{\nu_c \mu_c + \nu_l \mu_l}_{Reactants} - \underbrace{\nu_h \mu_h}_{Products})\mathring{\alpha} = -\Delta_r G\,\mathring{\alpha} \geq 0 \tag{5.14}$$

where $\Delta_r G$ is the reaction Gibbs energy, controlling the spontaneity of the reaction: $\Delta_r G < 0 \rightarrow \mathring{\alpha} \geq 0$, or inversely; reversible equilibrium occurs at $\Delta_r G = 0$.

Assuming the reactions occur sufficiently close to equilibrium, Onsager's principle might be invoked to formulate the dissipation function [146, 152]:

$$D_h = \frac{1}{2} A_\alpha \dot{\alpha}^2; \quad \varphi_h = \frac{\partial D_h}{\partial \dot{\alpha}} \dot{\alpha} \geq 0 \qquad (5.15)$$

where A_α is a positive semi-definite function of the local state and we recognize the thermodynamic force $-\Delta_r G = A_\alpha \dot{\alpha}$. It is worth noting that the dissipation does not require the assumption of rate-controlling mechanisms of the hydration reaction. An equivalent result was obtained by Ulm and Coussy [78] assuming diffusive dissipation, although it is known that diffusion only later governs the hydration advance. The determination of A_α and its couplings can be done as explained in ref. [79]. The evolution of the hydration degree is modelled as discussed in Chapter 4.

The consideration of mass balance (Equation (5.2)) together with the reaction extent definition (Equation (5.13)) yields

$$\dot{m}_c = -\mathring{m}_{c \to h} = -\nu_c \mathring{\alpha} \quad \text{and} \quad \dot{m}_h = \mathring{m}_h = -\nu_h \mathring{\alpha} \qquad (5.16)$$

The rate of hydration degree results in an actual time derivative, i.e. $\mathring{\alpha} = \dot{\alpha}$, because the system is closed with respect to anhydrous cement and hydrates. Rewriting the dissipation of the open system φ from Equation (5.9) results in:

$$\varphi = \boldsymbol{\sigma} : \dot{\boldsymbol{\varepsilon}} + \sum_{f=l,v,a} \mu_f \dot{m}_f + \Delta G \dot{\alpha} - \dot{F} \geq 0 \qquad (5.17)$$

where $\Delta G = \nu_h \mu_h - \nu_c \mu_c$. The change of free energy as a result of hydration is seen to be a consequence of the mass exchanges and the differences of chemical potential among reactants and products.

The enforcement of mass conservation reveals that a single state variable α is necessary to describe the free energy changes associated with the hydration reaction. The simplicity of the resulting expression is a consequence of the limits we have placed on mass exchanges of chemically active phases in our system. Among the constituents participating in the reaction, only the liquid phase is subject to mass exchanges, while solids are consumed and hydrates are precipitated *locally*. Further restriction of the mass exchanges, as in the case of a closed system, constitutes a particular case for which yet $\dot{m}_l = -\nu_l \mathring{\alpha}$ and therefore we can further reduce the number of state variables, as done, for instance, by Ulm and Coussy [78].

5.3.1 Evolution of volume fractions with hydration reactions

The evolution of the mechanical properties of the cement paste depends on its microscopic composition. The volume fractions of the different components evolve with time both as a result of the chemical reactions occurring among them and the exchanges of mass with the surroundings. In the current section, we describe the mass and volume fractions evolutions due to the chemical reactions of cement hydration, omitting exchanges with the exterior. The procedure elaborates on the work presented in refs. [7, 16, 144]. Some of the notations and definitions presented in the first part of the manuscript are repeated here for the sake clarity.

In the present description of volume fractions, the cement paste is composed of the four main clinker phases (C$_3$S, C$_2$S, C$_3$A and C$_4$AF) and the C–S–H, CH and aluminates (AFm and AFt, which we will group as Alu) hydration products. In addition, minor quantities of gypsum and impurities can also be present. This decomposition, more refined than the one presented in Figure 5.1, will provide a much more precise description for the micromechanical elastic model to be formulated later (Section 5.6.2) while adding little additional complexity.

Consider a volume of cement paste with a unitary mass of anhydrous cement powder, with components of initial mass fraction m_i^0.[2] The hydration degree α is an appropriate metric for the reactants mass consumption because the system is closed with respect to exchanges of the solid components, as discussed in the previous section. Therefore, as the result of the hydration reaction, the mass of component i is given by:

$$m_i = m_i^0 \left(1 - \alpha_i\right) \tag{5.19}$$

where α_i is the hydration degree of component i. In a similar way, the mass of water and hydrates are given by

$$m_w = w - M_w \sum_i \frac{n_w^i m_i^0}{M_i} \alpha_i \tag{5.20a}$$

$$m_h = M_h \sum_i \frac{n_h^i m_i^0}{M_i} \alpha_i \qquad i = \text{C}_3\text{S, C}_2\text{S, C}_3\text{A, C}_4\text{AF}, \qquad h = \text{C–S–H, CH} \tag{5.20b}$$

where w is the water to cement ratio of the cement paste, M_i is the molar mass of component i and the stoichiometric coefficient n_j^i is the number of moles of component j participating

---

[2]When minor components are completely neglected, the normalized mass fraction m_i' with respect to the main clinker components can be redefined as:

$$\tilde{m}_i^0 = \frac{m_i^0}{\sum\limits_i m_i^0} \qquad i = \text{C}_3\text{S, C}_2\text{S, C}_3\text{A, C}_4\text{AF} \tag{5.18}$$

in the reaction with a mole of component i.

The cement paste volume V per unit mass of cement powder is given by $V = V_0(1 - \epsilon)$, where ϵ is the volumetric strain and

$$V_0 = \frac{1}{\rho_c} + \frac{w}{\rho_w} \tag{5.21}$$

is the initial volume of the cement paste per unit mass of cement powder, $\rho_c = \left(\sum m_i^0 / \rho_i\right)^{-1}$ is the density of the cement powder.[3] The volume fractions v_i can be determined from the knowledge of the density of the different phases. For the cement powder and its components:

$$v_C = \sum_i v_i; \quad v_i = \frac{m_i^0 \left(1 - \alpha_i\right)}{\rho_i V} \quad i = C_3S, C_2S, C_3A, C_4AF \tag{5.22}$$

where v_C is the volume fraction of anhydrous clinker. An analogous calculation for water yields

$$v_w = \frac{w - M_w \sum_i \dfrac{n_w^i m_i}{M_i} \alpha_i}{\rho_w V} \quad i = C_3S, C_2S, C_3A, C_4AF \tag{5.23}$$

while for the CH and C–S–H hydration products we have

$$v_H = \sum_h v_h \qquad\qquad h = C\text{–}S\text{–}H, CH \tag{5.24a}$$

$$v_h = \frac{M_h \sum_i \dfrac{n_h^i m_i^0}{M_i} \alpha_i}{\rho_h V} \qquad\qquad i = C_3S, C_2S, C_3A, C_4AF \tag{5.24b}$$

where v_H is the total volume fraction of C–S–H and CH hydrates, and v_{CSH} corresponds to the solid phase of the C–S–H gel.

The hydration of the cement paste is accompanied by chemical shrinkage because of the difference in volume among reactants and hydration products. Assuming a percolated non-deformable skeleton, the chemical shrinkage results in a pore volume of volume fraction

$$v_\xi = \frac{\sum_i m_i^0 \xi_i \alpha_i}{V} \qquad\qquad i = C_3S, C_2S, C_3A, C_4AF \tag{5.25}$$

where the chemical shrinkage ξ_i of the phase i, measured in volume change per unit mass of clinker reactant, is given by:

$$\xi_i = \frac{1}{M_i} \left(\sum_r \frac{M_r n_r^i}{\rho_r} - \sum_h \frac{M_h n_h^i}{\rho_h} \right) \tag{5.26}$$

---

[3]We assume the reference state is unstrained, i.e. $\epsilon_0 = 0$, and thus densities should correspond to such condition.

where r should be iterated over all the participating reactants, and h over all the resulting reaction products. For the main clinker phases, C_3S and C_2S, the equation becomes

$$\xi_i = \frac{1}{\rho_i} + \frac{M_w n_w^i}{M_i \rho_w} - \sum_h \frac{M_h n_h^i}{M_i \rho_h} \quad h = \text{C–S–H, CH} \tag{5.27}$$

since only water, C–S–H and CH take part in the reaction. The aluminium-rich clinker phases, C_3A and C_4AF, hydrate in a sequence of reactions that result in diverse hydration products depending on the available reactants (see, for instance, ref. [52]). Their volume fraction is the remaining after considering all other phases:

$$v_{\text{Alu}} = 1 - \sum v_i; \quad i = w, \text{C}_3\text{S, C}_2\text{S, C}_3\text{A, C}_4\text{AF, C–S–H, CH, }\xi \tag{5.28}$$

Table 5.1: Parameters for the determination of volume fractions

	Reactants					Products	
	C_3S	C_2S	C_3A	C_4AF	w	C–S–H *	CH
$\rho\,(\text{g/cm}^3)$	3.15	3.28	3.03	3.73	1.00	2.60	2.24
$M\,(\text{g/mol})$	228.32	172.24	270.20	485.96	18.02	187.84	74.09
n_w^c	3.1	2.1	10.0	14.0	-	-	-
n_{CSH}^c	1.0	1.0	-	-	-	-	-
n_{CH}^c	1.3	0.3	-	-1.0	-	-	-
$\xi_i\,(\text{cm}^3/\text{g})$	5.14	4.75	11.37	8.14	-	-	-

Sources: Bentz [52], Tennis and Jennings [24], Bentz et al. [25] and Allen et al. [30].
* Corresponds to $C_{1.7}SH_{1.8}$

The parameters for the determination of the volume fractions are presented in Table 5.1. To complete the volume fraction model formulation, it is worth noting that the C–S–H hydrates stoichiometric coefficient and density exclude the liquid water in the gel pores. Instead, the coefficients are based on the findings by Allen and co-workers [30] regarding the density of C–S–H globules that include only physically-bound water, with chemical composition $C_{1.7}SH_{1.8}$. The gel water present inside the C–S–H hydrates can be calculated from their distribution between LD and HD C–S–H for which the gel porosities are ϕ_{HD} and ϕ_{LD}, respectively [26, 27, 33].

Including the gel water in the stoichiometric balance equations, as done by other authors [7, 16, 144], is equivalent to assuming a fixed and implicitly predetermined C–S–H gel packing density, thus ruling out the redistribution of the products according to different densities while complying with mass conservation. Indeed, knowing the density of the C–S–H globules, we can calculate the stoichiometric coefficient n_w^{gel} owed to the gel water content of the two packing densities:

$$n_w^{gel} = \frac{M_{\text{C–S–H}}}{M_w} \frac{\phi_{gel}}{(1 - \phi_{gel})} \frac{\rho_w}{\rho_{\text{C–S–H}}} \tag{5.29}$$

where ϕ_{gel} is the gel porosity of LD or HD C–S–H. Considering the gel porosities from the Jennings model (see Table 5.2), we obtain $n_w^{\text{LD}} = 2.26$ and $n_w^{\text{HD}} = 1.41$. The stoichiometric compositions of the LD and HD C–S–H gels are hence $C_{1.7}\,S\,H_{4.1}$ and $C_{1.7}\,S\,H_{3.2}$, respectively. It should be clear that, given these stoichiometric compositions, the only suitable proportioning among LD and HD packings allowing to recover the typical $C_{1.7}\,S\,H_4$ composition so consistently adopted by other authors is to produce LD C–S–H almost exclusively, and not doing so constitutes a violation of the mass balance equations.

We assume LD C–S–H is produced during the initial stages of reaction, as long as sufficiently large pore spaces are available. Later, as the growth becomes space constrained, the main product is HD C–S–H. We will assume that the LD C–S–H is formed early during the nucleation and growth control as long as $\alpha < \tilde{\alpha}_i$, where $\tilde{\alpha}_i$ is the hydration mechanism transition threshold. Later, for $\alpha \geq \tilde{\alpha}_i$ the HD C–S–H starts to form from a fraction r_{HD} of the total C–S–H globules being produced. Thus, the volume fractions of LD and HD C–S–H are given by the following relations:

$$v_{\text{CSH}}^{\text{LD}} = \frac{\sum_i v_{\text{CSH}}^i}{1 - \phi_{\text{LD}}} \left(\alpha_i - r_{\text{HD}} \langle \alpha_i - \tilde{\alpha}_i \rangle \right) \tag{5.30a}$$

$$v_{\text{CSH}}^{\text{HD}} = \frac{\sum_i v_{\text{CSH}}^i}{1 - \phi_{\text{HD}}} r_{\text{HD}} \langle \alpha_i - \tilde{\alpha}_i \rangle \qquad i = C_3S, \, C_2S \tag{5.30b}$$

where $\langle x \rangle$ is defined as:

$$\langle x \rangle = \begin{cases} x & \text{if } x > 0 \\ 0 & \text{if } x \leq 0 \end{cases} \tag{5.31}$$

The parameters governing the production of C–S–H hydrates are presented in Table 5.2.

Table 5.2: Parameters for the production of C–S–H hydrates

Parameter	Value
ϕ_{LD} *	0.26
ϕ_{HD} *	0.36
ϕ_{LD}^a **	0.10
ϕ_{HD}^a **	0
$\tilde{\alpha}$	0.5
r_{HD}	1

*Source: Jennings et al. [27]

**Similar to Jennings.

Assuming that the water in the gel pores has the same density as the bulk water [1], the distribution in capillary water with volume fraction v_w^c and gel water with volume fraction

v_w^g is straightforward:

$$v_w = v_w^c + v_w^g \tag{5.32a}$$

$$v_w^g = v_{\text{CSH}}^{\text{LD}} + v_{\text{CSH}}^{\text{HD}} - v_{\text{CSH}} \tag{5.32b}$$

Regarding the skeleton, its total volume –anhydrous phases and hydrates, including their inactive porosity– is given by:

$$v_{sk} = 1 - v_w^c - \phi_{\text{LD}}^a v_{\text{CSH}}^{\text{LD}} - \phi_{\text{HD}}^a v_{\text{CSH}}^{\text{HD}} - v_\xi \tag{5.33}$$

where ϕ^a is the active porosity, discussed in the next section. The complete determination of volume fractions is possible using Equations 5.22 to 5.33. In a first order approximation, it is reasonable to assume a constant overall volume –i.e. negligible macroscopic volume changes– and therefore $V = V_0$.

The distribution of volume fractions for our class G cement paste with $w = 0.44$ is presented in Figure 5.2 (see Section 2.1 for details on the composition of the cement paste). We have adopted the same hydration degree α and hydration threshold parameter $\tilde{\alpha} = 0.5$ for all reacting phases. We distinguish the clinker phases (C_3S, C_2S, C_3A and C_4AF), the hydration products (CH, aluminates and LD and HD C–S–H gels, including the gel porosity) and the remaining capillary water and shrinkage voids. The volume fractions of C–S–H solid and gel pores can be determined from the formulae (Equations (5.24) and (5.32)).

5.3.2 Precipitation of hydrates in the pore space

The evolution of the hydration reaction produces new hydrates that precipitate free of stress in the pore space, significantly changing the porosity of the cement paste. The poromechanical description of the material behaviour requires the identification of the active fraction of the total porosity volumes. To be considered as active, the pore space has to permit fluid displacement, because pressure changes can only be operated by mobile fluid volumes.

The wide-spanning pore sizes of cement paste, ranging over several orders of magnitude from the millimetre to the nanometre, make the definition of the active porosity a challenging endeavour. Experimental evidence suggests the activated pore volume is determined by the characteristic time scale of the physical phenomenon under consideration. A compelling analysis of the active porosity has been presented by Ghabezloo et al. [74], who found, under isotropic drained loading, an upper bound for the porosity significantly lower than the total cement paste porosity including gel pores. In his view, the active porosity would be limited to the capillary porosity. On the other hand, the analysis of creep tests by Vu et al. [153] required the activation of the entire pore volume for the reproduction of the
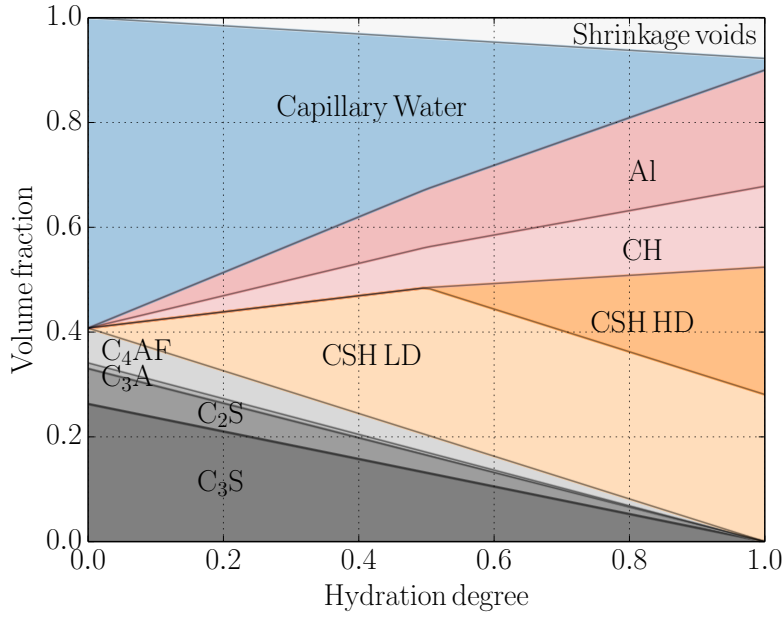
Figure 5.2: Evolution of the volume fractions of the components of a cement paste with the progress of the hydration reactions. Class G cement paste with $w = 0.44$, composition details available in Section 2.1.

experimental observations.

In general, the pore volume is given by the difference between the total cement paste volume V and the volume of the solid phases, i.e. cement powder volume V_c and hydrates volume V_h. The determination of the active porosity demands considering a corrective term due to the fraction of active porosity of the hydrates ϕ_H^a. The volume of active porosity therefore reads:

$$V_\phi^\alpha = V - V_c - (1 - \phi_H^a)V_h = V\left(1 - v_C - (1 - \phi_H^a)v_H\right) \tag{5.34}$$

where we have made use of the definitions of volume fractions from Section 5.3.1. We assume the anhydrous cement powder as non-porous. Regarding the hydrates, only the LD and HD C–S–H gels are considered porous. The active porosity of these gel phases will be treated independently.

Assuming the overall volume to remain constant ($V = V_0$) we can describe the reference Lagrangian porosity ϕ_0 according to the results of Section 5.3.1:

$$\phi_0 = 1 - v_C - v_H + \phi_{LD}^a v_{CSH}^{LD} + \phi_{HD}^a v_{CSH}^{HD} = v_w^c + v_\xi + \phi_{LD}^a v_{CSH}^{LD} + \phi_{HD}^a v_{CSH}^{HD} \tag{5.35}$$

where ϕ_{LD}^a and ϕ_{HD}^a are the active porosities of the C–S–H gel phases, satisfying

$$0 \leq \phi_{LD}^a \leq \phi_{LD}, \quad 0 \leq \phi_{HD}^a \leq \phi_{HD} \tag{5.36}$$

The observation of the active porosity of the C–S–H gels, notably under nitrogen sorption, has been pivotal in the formulation of the cement hydrates microstructural model by Jennings and co-workers [26, 27, 33]. According to this model, the HD C–S–H porosity is completely inaccessible, while a fraction of the LD C–S–H is accessible to nitrogen. In accordance with the hypothesis of Jennings' colloidal model, the HD C–S–H is considered completely inactive, i.e. $\phi_{\mathrm{HD}}^a = 0$. Regarding LD C–S–H, only a fraction of the porosity $\phi_{\mathrm{LD}}^a = \phi_{\mathrm{LD}} - \phi_{\mathrm{HD}}$ is considered active, in a similar way as hypothesized by Jennings (see Table 5.2).

The change of porosity as a function of hydration can be readily calculated differentiating Equation (5.35) assuming a homogeneous hydration degree for all components:

$$\dot{\phi}_0 = (\beta_\alpha + \beta_\xi + \beta_\phi)\,\dot{\alpha} \tag{5.37}$$

where

$$\beta_\alpha = -\frac{M_w \sum\limits_i \dfrac{n_w^i m_i}{M_i}}{\rho_w V_0} \tag{5.38a}$$

$$\beta_\xi = \frac{\sum\limits_i m_i^0 \xi_i}{V_0} \tag{5.38b}$$

$$\beta_\phi = -\left[\frac{\phi_{\mathrm{LD}} - \phi_{\mathrm{LD}}^a}{1 - \phi_{\mathrm{LD}}}\left(1 - r_{\mathrm{HD}}\frac{\langle\alpha - \tilde{\alpha}\rangle}{(\alpha - \tilde{\alpha})}\right) + \frac{\phi_{\mathrm{HD}} - \phi_{\mathrm{HD}}^a}{1 - \phi_{\mathrm{HD}}} r_{\mathrm{HD}}\frac{\langle\alpha - \tilde{\alpha}\rangle}{(\alpha - \tilde{\alpha})}\right]\frac{M_{\mathrm{CSH}}\sum\limits_j \dfrac{n_{\mathrm{CSH}}^j m_j^0}{M_j}}{\rho_{\mathrm{CSH}} V_0} \tag{5.38c}$$

where $i = \mathrm{C_3S, C_2S, C_3A, C_4AF}$ and $j = \mathrm{C_3S, C_2S}$. The first term β_α corresponds to changes in porosity due to the consumption of water via the hydration reaction to produce hydrates, assuming all C–S–H porosity as active. The term β_ξ stems from the difference in volume among reactants and products, directly proportional to the chemical shrinkage of the different reactions. The last term β_ϕ can be understood as a corrective term, corresponding to the change in porosity due to the inactive fraction of the gel porosity of the C–S–H gels, as previously discussed. If independent hydration degrees are considered for the clinker phases, each phase adopts an analogous expression for $\dot{\phi}_0^i$, the resulting porosity rate of change being given by $\dot{\phi}_0 = \sum \dot{\phi}_0^i$.

5.4 Liquid – vapour phase transition and capillary pressure

The thermodynamic equilibrium between the liquid and its vapour requires the reversibility of exchanges, i.e. $\varphi_t = 0$ and therefore $\mu_v(T, p_v) = \mu_l(T, p_l)$ according to Equation (5.10).

Assuming the vapour behaves as an ideal gas and the liquid as an incompressible fluid[4], the physicochemical equilibrium results in Kelvin's law [154]:

$$p_l - p_v = \frac{RT}{\mathcal{V}_l} \ln \mathrm{RH} \tag{5.39}$$

where R the gas constant, $\mathcal{V}_l$ the liquid specific molar volume, $\mathrm{RH} = p_v/p_{sv}(T)$ is the relative humidity, with $p_{sv}(T)$ the saturating vapour pressure at temperature T. Furthermore, according to the Laplace equation, the mechanical equilibrium of the water-gas meniscus for cylindrical pores requires

$$p_c = p_g - p_l = \frac{2\gamma \cos(\theta)}{r} \tag{5.40}$$

where γ is the surface tension at the interface of the fluids, θ the contact angle between the meniscus and the solid and r its radius.

The previous classical expressions, known as the Kelvin-Laplace equations [154], consider the presence of a meniscus at the interface when the vapour pressure is below the saturating vapour pressure. If RH=1, then $p_{sv} = p_v$, and equilibrium occurs over a meniscus of infinite radius, i.e. a flat interface. For relative humidities $\mathrm{RH} < 1$ we have $p_v > p_l$ and equilibrium can only be achieved in the presence of a meniscus.

The surface tension γ is due to the material discontinuities across the interfaces among the multiple phases coexisting in the cement paste. The effective surface tension might change with RH: at high relative humidities, the dominating interfaces are those among liquid-gas and solid-liquid; as the relative humidity is decreased, the solids are covered by fewer adsorbed water molecules and new interfaces, notably among gas and solid, are created. This effect, however, might be neglected at high relative humidities, for which the solids are and remain covered by adsorbed water [84]. The contact angle θ might also depend on the state of the interfaces in addition to other physico-chemical variables, but such effects will be neglected in the present treatment. The values adopted for these physical parameters are those typically reported in the literature (e.g. ref. [99])

In addition, from Dalton's law of partial pressures, the gas pressure results from the addition of the partial pressures of both gases, vapour and dry air, i.e.

$$p_g = p_v + p_a \tag{5.41}$$

The combination of these equations provides a relationship connecting the pore sizes to the gas and capillary pressures.

The mechanical effects of capillary pressure will be introduced in our poromechanical constitutive model by means of its associated equivalent stress, as will be made clear in

---

[4]Both fluids are assumed to be in bulk state.

5.5 Free energy of the cement paste: fluids, interfaces and solid

We are concerned with the evolution of the observable solid matrix, which is yet to be identified explicitly. After isolating the dissipation φ associated with the irreversible evolutions of the system, we express the free energy and dissipation mechanisms according to different material components of the cement paste.

5.5.1 Free energy of the fluids

Since energy is an extensive quantity of the mixture, we write:

$$F = F_{si} + \sum_{f=l,v,a} m_f F_f \tag{5.42}$$

where F_{si} is the specific free energy of the skeleton (solid and interfaces) and F_f is the specific free energy of fluid f,

The fluid-filled volume of the skeleton is described by the Lagrangian porosity ϕ, defined as the fluid volume with respect to the reference skeleton volume. The total porosity ϕ is determined by the effects of mechanical loadings and chemical processes:

$$\phi = \phi_0 + \phi_m \tag{5.43}$$

where the purely chemical changes of the reference porosity ϕ_0 are given by Equation (5.37). The stoichiometry of the hydration reaction demands the participation of liquid and, as a result, only the liquid-filled volume deforms chemically, while the gas and air volumes stand no chemical deformation, as described in Section 5.3.2. Regarding the mechanical changes of porosity, for the sake of simplicity and the lack of experimental evidence to suggest otherwise, we adopt the hypothesis of iso-deformation and assume the pore space mechanical deformation to be indifferent to the fluid it contains [155].

Since both gaseous phases occupy a common porous space, we define the gas porosity $\phi_g = \phi_v = \phi_a$. In the usual way, we define the saturation degree of the fluids as:

$$S_l = \frac{\phi_l}{\phi_0}; \quad S_g = \frac{\phi_g}{\phi_0}; \quad S_g + S_l = 1 \tag{5.44}$$

Combining the previous definitions with the expression of the dissipation from Equation (5.17), and considering the ideal fluid state equations (see, for instance, ref.[151]), we

obtain:

$$\boldsymbol{\sigma} : \dot{\boldsymbol{\varepsilon}} + \bar{p}\,\dot{\phi} - \phi\,p_c \dot{S}_l + \Delta G\,\dot{\alpha} - \dot{F}_{si} \geq 0 \tag{5.45}$$

where $\bar{p} = S_l p_l + S_g p_g$ is the average pore pressure, similar to the definition proposed by Bishop in his attempt to extend the basic ideas of soil mechanics put forward by Terzaghi to the case of partially saturated soils [156].

5.5.2 Free energy of the interface

The energy stored in the membranes at the interface of the different phases can be considered separately following the approach proposed by Dangla and Coussy [147, 157], extended here to the case of a hydrating cement paste.

We decompose the total free energy as the sum of the free energy of the solid and the interfaces. We consider the free energy of the solid to be independent of the saturation degree, and naturally adopt $\boldsymbol{\varepsilon}, \phi$ and α as the state variables. Additionally, we consider internal state variables $\boldsymbol{\chi}$ describing irreversible evolutions, i.e. $F_s = F_s(\boldsymbol{\varepsilon}, \phi, \alpha, \boldsymbol{\chi})$. Regarding the interface energy per unit volume F_i, we suppose it depends on the degree of saturation S_l and the hydration degree, while being independent of mechanical strains. We disregard irreversible behaviour –no hysteresis effects– and thus require no other internal state variables, i.e. $F_i = F_i(S_l, \alpha)$. The total free energy of solid and interfaces is hence given by:

$$F_{si} = F_s(\boldsymbol{\varepsilon}, \phi, \alpha, \boldsymbol{\chi}) + \phi F_i(S_l, \alpha) \tag{5.46}$$

From the rewriting of Equation (5.45), we obtain:

$$\boldsymbol{\sigma} : \dot{\boldsymbol{\varepsilon}} + (\bar{p} - F_i)\,\dot{\phi} + \phi\left(p_c + \frac{\partial F_i}{\partial S_l}\right)\dot{S}_l + \left(\Delta G - \phi\frac{\partial F_i}{\partial \alpha}\right)\dot{\alpha} - \dot{F}_s \geq 0 \tag{5.47}$$

The term $\partial F_i / \partial \alpha$ stems from the creation of interfaces as a result of the evolution of the hydration, responsible of the changes in the microstructure of the cement paste and the progressive refinement of the pore space.

Because the state variables are mutually independent, their rates can be chosen arbitrarily. In addition, the free energy and associated variables are also rate-independent, since an equilibrium state is completely described by its set of thermodynamic variables only [158]. Under such conditions, the inequality can only be guaranteed in a reversible evolution if:

$$\boldsymbol{\sigma} = \frac{\partial F_s}{\partial \boldsymbol{\varepsilon}}; \quad p = \frac{\partial F_s}{\partial \phi}; \quad p_c = -\frac{\partial F_i}{\partial S_l}; \quad \Delta_s G = \frac{\partial F_s}{\partial \alpha} \tag{5.48}$$

where we have defined

$$p = \bar{p} - F_i; \quad \Delta_s G = \Delta G - \phi\frac{\partial F_i}{\partial \alpha} \tag{5.49}$$

The relations (5.48) constitute the state equations of the open partially-saturated reacting

solid. From the postulate of local state, these relations are independent of the rates of state variables, and so the state equations are valid for all evolutions, reversible or irreversible.

From the third state equation in (5.48) and Equation (5.47), the dissipation of the solid can be expressed as:

$$\boldsymbol{\sigma} : \dot{\boldsymbol{\varepsilon}} + p\,\dot{\phi} + \Delta_s G\,\dot{\alpha} - \dot{F}_s \geq 0 \tag{5.50}$$

where p acts as the effective pore pressure for the skeleton, with a rate of change [147]:

$$\dot{p} = S_l\,\dot{p}_l + S_g\,\dot{p}_g \tag{5.51}$$

It is clear that p reduces to the fluid pressure in the case of a saturated material, that is, $p = p_l$ for $S_l = 1$.

Comment on the importance of rate independence

The rate-independence of the thermodynamic state is a necessary condition for the derivation of state laws. Indeed, if this is not the case, a dissipation inequality such as $\mathcal{A}\dot{a} + \mathcal{B}\dot{b} \geq 0$, where a and b are the state variables, presents singularities for each of the state variables when we choose a zero rate: at zero rate, we can say nothing of the multiplying coefficients $\mathcal{A}$ and $\mathcal{B}$ if these are rate-dependent, because they might take any finite value and still satisfy the inequality. This singularity results critical because we derive the state laws from the consideration of each state variable separately, while considering the remaining state variables as having a zero rate of change. Therefore, we can only expect the state laws to be strictly valid for all possible evolutions when the thermodynamic state is independent of the rate of its state variables.

5.5.2.1   Water retention curve and interface free energy

The water retention curve (WRC) expresses the relation among saturation degree and capillary pressure or, by Kelvin-Laplace law, the capillary meniscus radius. The WRC is an essential material parameter when considering partially saturated cement pastes. Because of its close relation with the material microstructure, the WRC of a reacting cement paste depends strongly of the hydration degree. The hydration of the cement paste significantly changes its pore structure: as the reactants are consumed and the new hydrate products precipitate, the initially coarse porous networks become more refined, with significant consequences on the WRC, schematically illustrated in Figure 5.3.

The approximation of the WRC by convenient mathematical expressions resembling the experimental measurements is useful for practical modelling applications. In their review of mathematical expressions commonly applied to soils WRC, Cornelis et al. [159] concluded that the model proposed by van Genuchten (VG) [160] constitutes the optimal choice for fine soils. The VG model has also been profusely applied in the reproduction of cement pastes WRC [147, 161–163], and is the model chosen in the current work. According to
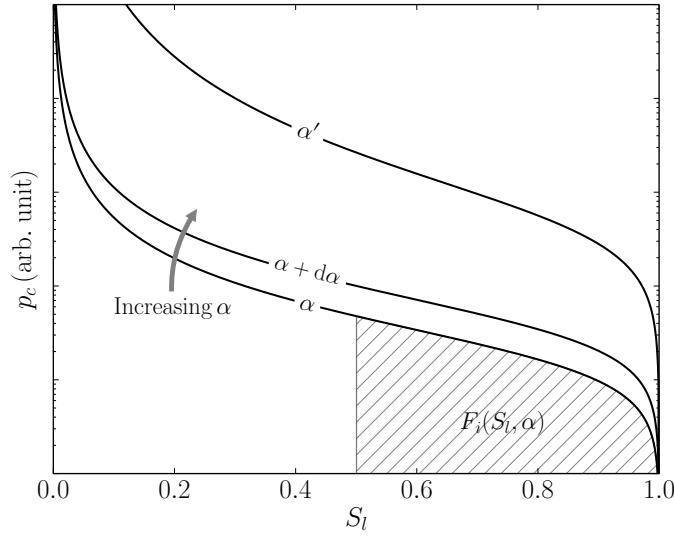
Figure 5.3: Water retention curve of a cement paste and its evolution with hydration degree. Note the change in the air entry pressure as well as the significant increment in capillary pressure, both due to the refinement of the pore structure with hydration.

the VG model, the capillary pressure is given by:

$$p_c = p_r \left(S_l^{\frac{n}{1-n}} - 1 \right)^{\frac{1}{n}} \tag{5.52}$$

where p_r is a reference pressure and $n > 1$ is a fit parameter.[5] The equation is convenient because it captures in a single analytical expression the overall shape of the WRC of materials with an unimodal pore-size distribution. A comprehensive discussion of the evolution of the WRC as well as the results of the experimental campaign aiming to characterize the WRC of a hydrating cement paste are presented in Chapter 6.

The free energy of the interface is related to the WRC by the third state equation of (5.48):

$$p_c = -\frac{\partial F_i}{\partial S_l} \tag{5.53}$$

For a constant hydration degree, the interface energy change from the reference saturated state to a given saturation degree corresponds to the shaded area under the capillary curve in Figure 5.3. The reference saturated state interface energy is equal to the total interface energy of the solid and liquids, i.e. $F_i^{sat} = S_s \gamma_{sl}$ where S_s is the specific surface of the solids and γ_{sl} the liquid-solid surface tension. The reference state, however, is not the same throughout hydration: both S_s and γ_{sl} depend on the hydration degree, because the reactions change the extent and nature of the interfaces. The area between two WRCs associated with different hydration degrees in Figure 5.3 corresponds to the change in

---

[5]Another widely used expression has been proposed by Brooks and Corey [164], for which capillary pressure is given by $p_c = p_r S_l^n$.

interface energy F_i due exclusively to the creation of liquid-gas menisci, i.e. $\phi\,\partial F_i^{lg}/\partial\alpha\,\mathrm{d}\alpha$, where F_i^{lg} is the interface energy associated to the liquid-gas interface.

It is interesting to note that the total free energy added to the system by the precipitation of the hydrates ΔG is split among the solid and the interfaces, as expressed by the fourth state law of (5.48):

$$\Delta G = \frac{\partial F_s}{\partial\alpha} + \phi\frac{\partial F_i}{\partial\alpha} \tag{5.54}$$

This result can be interpreted as a consequence of the Gibbs-Thomson effect, stating that the presence of menisci changes the chemical potential of the substance and hence the equilibrium configuration. Assuming ΔG to be independent of the saturation degree S_l, the previous expression allows us to asses the effect of desaturation on the hydration evolution. Positive values of $\partial F_s/\partial\alpha$ indicate hydrates precipitation, while negative values correspond to dissolution. The configuration in which no change of the solid free energy occurs, i.e. the ultimate hydration degree, is achieved for an interface-free material when $\Delta G = \partial F_s/\partial\alpha = 0$. As illustrated schematically in Figure 5.3, the free energy of the interfaces increases with the hydration degree. This causes a shift of the equilibrium hydration degree that results in an earlier halt of the reaction. The effect is due to the creation of new interfaces, without distinction of their nature. The effect of partial saturation is to further reduce the ultimate hydration degree (Figure 5.4), in agreement with the observations by Flatt et al. [91] and Gawin et al. [107].
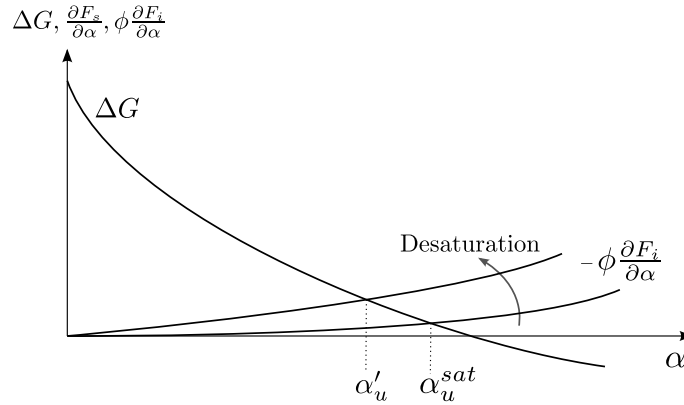
Figure 5.4: The effect of interfaces on the final hydration equilibrium configuration of the cement paste.

5.5.3 Free energy of the solid

The strains of the cement paste skeleton are diverse in nature. In addition to chemical strains (Section 5.3.2), the current model considers elastic (Section 5.6), viscous (Section 5.7) and plastic (Section 5.8) strain components. At constant hydration degree, elastic and viscous deformations are assumed to be completely recoverable.

In the framework of infinitesimal transformations, the strain and porosity rates of change are thus decomposed as:

$$\dot{\varepsilon} = \dot{\varepsilon}_e + \dot{\varepsilon}_v + \dot{\varepsilon}_p + \dot{\varepsilon}_\alpha \tag{5.55a}$$

$$\dot{\phi} = \dot{\phi}_e + \dot{\phi}_v + \dot{\phi}_p + \dot{\phi}_\alpha \tag{5.55b}$$

where the indices e, v, p and α stand for the elastic, viscous, plastic and chemical origins. The sign convention is that of the geomechanics literature, where compaction strains are positive. The volumetric strain ϵ and porosity are related by the volume balance [147]:

$$\epsilon = (1 - \phi_0)\epsilon^s - \phi + \phi_0 \tag{5.56}$$

where ϕ_0 is the reference Lagrangian porosity and ϵ^s the skeleton volumetric strain.

The elastic strains are associated to reversible mechanisms. The non-elastic deformations, of either plastic or viscous origin, are assumed to be due to the sliding of the grains that constitute the matrix, whereas the grains themselves are assumed to behave elastically, i.e. $\epsilon_v^s = \epsilon_p^s = 0$. Regarding viscous and plastic macroscopic volume changes, therefore:

$$\dot{\epsilon}_v = -\dot{\phi}_v; \qquad \dot{\epsilon}_p = -\dot{\phi}_p \tag{5.57}$$

The viscous and plastic incompressibility of the solid phase can be asserted from unjacketed tests, which allow the direct measurement of the solid phase volume changes. One such example is presented by Ghabezloo et al. [74] for a mature cement paste cured at 90°C. We extend these experimental observations to cement pastes cured at lower temperatures in Section 6.4, where it can be verified that the solid skeleton strains are completely and instantaneously reversible.

The total observable strains might be further decomposed in coupled chemo-mechanical and purely chemical components. In the case of elasticity, for instance, we have:

$$\varepsilon_e = \varepsilon_e^c + \varepsilon_e^{ch} \tag{5.58}$$

where ε_e^c is the coupled chemo-mechanical elastic strain and ε_e^{ch} is the chemical elastic strain. The nature of these components will be clearly illustrated in the following section. Analogous expressions can be formulated involving the elastic porosity, as well as the viscous and plastic strains and porosities.

The previous observations permit to postulate the form of the free energy:

$$F_s = F_e\left(\varepsilon_e^c, \phi_e^c, \alpha\right) + F_v\left(\varepsilon_v^c, \alpha\right) + F_p\left(\varepsilon_p^c, \alpha\right) + U\left(\varepsilon^{ch}, \phi^{ch}, \alpha\right) \tag{5.59}$$

where F_e, F_v and F_p are the free energies associated with the coupled elastic, viscous and

plastic mechanisms, respectively; U is the chemically-frozen mechanical energy. The main feature of this expression is the ubiquitous presence of the hydration degree, reflecting the chemical evolutions of the skeleton.

It is worth recalling that the reinforcement of the skeleton microstructure is the result of the precipitation of new hydrates with an initial stress equal to zero in a non-dissipative process. The dissipation of chemical origin, i.e. from the advance of the hydration reaction, has already been accounted for in the previous sections. For a percolated solid, since hydration does not result in chemical strains, we must have $\varepsilon_\alpha^{ch} = 0$. The changes in chemical porosity due exclusively to the hydration reaction have already been discussed and determined in Section 5.3.2 and are given by $\dot{\phi}_\alpha^{ch} = \dot{\phi}_0$.

Regarding the mechanical strains, we will only discuss the explicit decomposition in coupled and chemical terms for the elastic reversible mechanism. The analysis of the viscous and plastic mechanisms will be limited to the total observable strains. Future work will be dedicated to the determination of their coupled and chemical components.

The formulation of the elastic, viscous and plastic mechanisms follows. The seminal idea behind our model is that of Bažant's solidification theory [6, 66]: adopting a non-ageing constituent whose concentration evolves as a result of the hydration reactions. We consider the cement paste structure as the assembly of elementary mechanical components that, as a result of the advancement of the hydration reactions, accumulate and thus modify the overall macroscopic properties of the material. The evolution of the material is not due to changes of the properties of its constituents but to the change of their volume fraction. The solidification model, originally intended to model the creep of concrete, is applied to elastic and plastic mechanisms, illustrated by simple mechanical analogies that provide an intuitive understanding of the modelled phenomena.

The formulation has so far been kinematic, i.e. in strain-like state variables. Instead, we often prefer to adopt stress-like state variables, since these are more easily controlled in experiments. The change of variables is done by means of Legendre transforms, of which details are omitted for the sake of conciseness. The interested reader is referred to the literature on the subject (e.g. [165, 166]).

In our derivations, the reference state is the unstrained, unstressed state. The modifications of the expressions owing to deviations from these conditions might be obtained as shown, for instance, in ref. [147].

5.6 Elastic instantaneous reversible strains

A Legendre transform of the cement paste solid elastic free energy F_e with respect to elastic strain and porosity yields the state equations:

$$\boldsymbol{\varepsilon}_e^c = -\frac{\partial L_e}{\partial \boldsymbol{\sigma}}\left(\boldsymbol{\sigma}, p, \alpha\right); \quad \phi_e^c = -\frac{\partial L_e}{\partial p}\left(\boldsymbol{\sigma}, p, \alpha\right) \tag{5.60}$$

where $L_e = F_e - \boldsymbol{\sigma} : \boldsymbol{\varepsilon}_e^c - p\,\phi_e^c$. The elastic strain and porosity rates in terms of tangent elastic properties can be derived from the state equations adopting a stress-free reference state and accounting for the integrability conditions:

$$\dot{\boldsymbol{\varepsilon}}_e^c = \mathbf{C}^{-1}\left(\dot{\boldsymbol{\sigma}} - \mathbf{b}\,\dot{p}\right) + \left[\frac{\partial \mathbf{C}^{-1}}{\partial \alpha}\boldsymbol{\sigma} - \frac{\partial\left(\mathbf{C}^{-1}\mathbf{b}\right)}{\partial \alpha}p\right]\dot{\alpha} \tag{5.61a}$$

$$\dot{\phi}_e^c = -\mathbf{C}^{-1}\mathbf{b} : \dot{\boldsymbol{\sigma}} + \left(\mathbf{C}^{-1} : \mathbf{b}^2 + N^{-1}\right)\dot{p} + \left[-\frac{\partial\left(\mathbf{C}^{-1}\mathbf{b}\right)}{\partial \alpha}\boldsymbol{\sigma} + \frac{\partial\left(\mathbf{C}^{-1} : \mathbf{b}^2 + N^{-1}\right)}{\partial \alpha}p\right]\dot{\alpha} \tag{5.61b}$$

where $\mathbf{C}$ is the elastic stiffness tensor, $\mathbf{b}$ is Biot's tensor and N is Biot's modulus, all of which are considered to depend on α. These equations constitute the extension of the classical poroelastic mechanical framework to a reacting porous solid. As presented, they might be applied to either precipitation (reinforcement) or dissolution (weakening).

It is essential to note that, for a chemically-active elastic material, the elastic coupled strains evolve even under a constant stress state: *the effect of chemical reactions on the elastic properties of the material affect the recoverable elastic strains because of their redefinition of the stress-free configuration.*

The new elements are introduced free of stresses and strains, and therefore the macroscopic deformation does not change as a result of a chemical reaction step. Because chemical deformations can only take place if the hydration progresses, we require

$$\dot{\boldsymbol{\varepsilon}}_e|_{\boldsymbol{\sigma},p} = \dot{\boldsymbol{\varepsilon}}_e^c|_{\boldsymbol{\sigma},p} + \dot{\boldsymbol{\varepsilon}}_e^{ch} = \mathbf{0} \tag{5.62a}$$

$$\dot{\phi}_e|_{\boldsymbol{\sigma},p} = \dot{\phi}_e^c|_{\boldsymbol{\sigma},p} + \dot{\phi}_e^{ch} = 0 \tag{5.62b}$$

and therefore, the elastic chemical strains are:

$$\dot{\boldsymbol{\varepsilon}}_e^{ch} = -\left[\frac{\partial \mathbf{C}^{-1}}{\partial \alpha}\boldsymbol{\sigma} - \frac{\partial\left(\mathbf{C}^{-1}\mathbf{b}\right)}{\partial \alpha}p\right]\dot{\alpha} \tag{5.63a}$$

$$\dot{\phi}_e^{ch} = -\left[-\frac{\partial\left(\mathbf{C}^{-1}\mathbf{b}\right)}{\partial \alpha}\boldsymbol{\sigma} + \frac{\partial\left(\mathbf{C}^{-1} : \mathbf{b}^2 + N^{-1}\right)}{\partial \alpha}p\right]\dot{\alpha} \tag{5.63b}$$

and, as a result, the total observable elastic strains are:

$$\dot{\boldsymbol{\varepsilon}}_e = \dot{\boldsymbol{\varepsilon}}_e^c + \dot{\boldsymbol{\varepsilon}}_e^{ch} = \mathbf{C}^{-1}\left(\dot{\boldsymbol{\sigma}} - \mathbf{b}\,\dot{p}\right) \tag{5.64a}$$

$$\dot{\phi}_e = \dot{\phi}_e^c + \dot{\phi}_e^{ch} = -\mathbf{C}^{-1}\mathbf{b} : \dot{\boldsymbol{\sigma}} + \left(\mathbf{C}^{-1} : \mathbf{b}^2 + N^{-1}\right)\dot{p} \tag{5.64b}$$

The observable elastic strains are identical to the poroelastic equations derived for a non-reacting solid [147].

The consideration of the unidimensional chemo-elastic mechanical analogy presented in Figure 5.5 is highly instructive. In this case, the elementary mechanical unit is a spring of stiffness E_e. The initial element is loaded with a stress σ_e that induces a deformation of ε_e. A new element is then introduced, corresponding to an increase of the hydration reaction $d\alpha$. The new element bears no initial stress, and hence has no effect on either stress or strain and causes no changes of energy in the system. This is how the mechanical reinforcement of the cement microstructure is assumed to occur in the present model. Analogously, in the case of a solidifying elastic material under a multiaxial stress state, the chemical evolutions are non-dissipative.
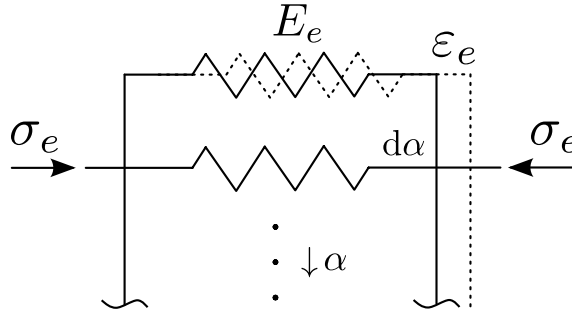
Figure 5.5: Unidimensional mechanical model of a chemically-active elastic solid.

An example response to mechanical loads and chemical reactions of this simple system is presented in Figure 5.6. In this case, an initial loading stress is first applied, followed by a chemical hydration step in which an additional element is added. Finally, the system is unloaded to its initial state of zero stress. The elastic coupled strains evolve as a result of the stress changes as well as the hydration advance. The area under the curve in this path is blocked inside the material as chemically-frozen mechanical energy U, non-recoverable by unloading. This energy is associated with the internal state of stress of the springs, that ought to be self-equilibrated in the zero-stress configuration. The elastic chemical strains counterbalance the effect of the coupled strains, and as a result no macroscopic strain is observed during the chemical reaction.

In a similar way, a cement paste hydrating under a complex state of stress stores internal energy due to the micro-heterogenous internal stresses of particles precipitated at different times in the material history. Although the observable instantaneous response of the elastic

mechanism is indifferent to the history of chemical strains (see Equation (5.64)), their effect might be very important for the estimation of the durability of the material. Indeed, the internal state of stress associated with the chemical strains has to be evaluated and considered in the analysis of long term creep or plausible degradation mechanisms such as damage and fracture.
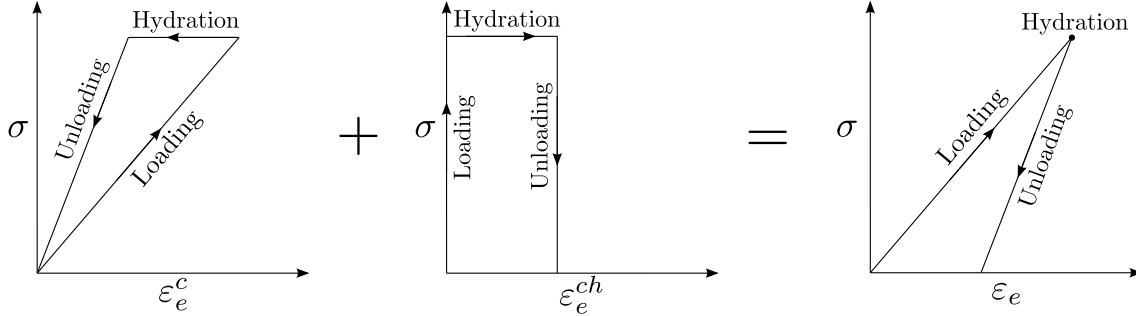
Figure 5.6: Sample stress and chemical path composed of loading, chemical reaction and unloading to initial stress.

5.6.1 Isotropic incremental form

The mechanical behaviour of isotropic materials, such as cement paste, is independent of material frame transformations, and therefore can be described as a function of the invariants of stress and strain tensors. In our description, the stress tensors invariants are

$$\sigma = \frac{\operatorname{tr}\boldsymbol{\sigma}}{3}; \quad \tau = \sqrt{\frac{\mathbf{s}:\mathbf{s}}{2}} = \sqrt{J_2} \tag{5.65}$$

where $\mathbf{s} = \boldsymbol{\sigma} - \sigma\mathbf{I}$ is the deviatoric stress tensor, σ is the mean stress and τ the deviatoric stress invariant. The mean stress is positive in compaction, according to the usual geomechanics sign convention. The strain tensor invariants are

$$\epsilon = \operatorname{tr}\boldsymbol{\varepsilon}; \quad \gamma = \sqrt{2\mathbf{e}:\mathbf{e}} \tag{5.66}$$

where $\mathbf{e} = \boldsymbol{\varepsilon} - \epsilon\mathbf{I}/3$ is the deviatoric strain tensor, ϵ is the volumetric strain and γ the deviatoric strain invariant.

In terms of stress and strain invariants, the coupled elastic strain rates are given by:

$$\dot{\epsilon}_e^c = \frac{\dot{\sigma}}{K} - \frac{b}{K}\dot{p} + \left[\frac{\partial K^{-1}}{\partial\alpha}\sigma - \frac{\partial\left(bK^{-1}\right)}{\partial\alpha}p\right]\dot{\alpha} \tag{5.67a}$$

$$\dot{\mathbf{e}}_e^c = \frac{\dot{\mathbf{s}}}{2G} + \frac{\partial\left(2G\right)^{-1}}{\partial\alpha}\mathbf{s}\,\dot{\alpha} \tag{5.67b}$$

$$\dot{\phi}_e^c = -\frac{b}{K}\dot{\sigma} + \left(\frac{b^2}{K} + \frac{1}{N}\right)\dot{p} + \left[-\frac{\partial\left(bK^{-1}\right)}{\partial\alpha}\sigma + \frac{\partial\left(b^2K^{-1} + N^{-1}\right)}{\partial\alpha}p\right]\dot{\alpha} \tag{5.67c}$$

where K and G are the bulk and shear moduli, b is Biot's effective stress coefficient and N is Biot's modulus. In a similar way, the elastic chemical strain rates are given by:

$$\dot{\epsilon}_e^{ch} = -\left[\frac{\partial K^{-1}}{\partial \alpha}\sigma - \frac{\partial \left(bK^{-1}\right)}{\partial \alpha}p\right]\dot{\alpha} \tag{5.68a}$$

$$\dot{\mathbf{e}}_e^{ch} = -\frac{\partial \left(2G\right)^{-1}}{\partial \alpha}\mathbf{s}\,\dot{\alpha} \tag{5.68b}$$

$$\dot{\phi}_e^{ch} = -\left[-\frac{\partial \left(bK^{-1}\right)}{\partial \alpha}\sigma + \frac{\partial \left(b^2 K^{-1} + N^{-1}\right)}{\partial \alpha}p\right]\dot{\alpha} \tag{5.68c}$$

and, therefore, the total observable elastic strain and porosity rates are:

$$\dot{\epsilon}_e = \frac{\dot{\sigma}}{K} - \frac{b}{K}\dot{p} \tag{5.69a}$$

$$\dot{\mathbf{e}}_e = \frac{\dot{\mathbf{s}}}{2G} \tag{5.69b}$$

$$\dot{\phi}_e = -\frac{b}{K}\dot{\sigma} + \left(\frac{b^2}{K} + \frac{1}{N}\right)\dot{p} \tag{5.69c}$$

As usual, the poroelastic parameters must satisfy the compatibility conditions [74, 147]:

$$b = 1 - \frac{K}{K_s}; \quad \frac{1}{N} = \frac{b - \phi_0}{K_s} \tag{5.70}$$

where K_s is the bulk modulus of the solid phase, considered isotropic and homogeneous.

5.6.2 Evaluation of the poroelastic parameters from a micromechanical model

The mechanical properties of the cement paste at the macroscopic scale are determined by its curing conditions and microscopic composition, which evolves with the hydration reactions. In the traditional approach of continuum mechanics, the material characterization is performed by induction: from a limited number of laboratory experiments, general constitutive laws are fit in order to best represent the material behaviour following phenomenological models [167]. In a material such as cement, traditional inductive methods would require enormous experimental characterization efforts in order to determine a constitutive law spanning all material ages.

The upscaling and homogenization techniques help surmount this challenge, allowing us to interchange the real micro-heterogeneous and evolving cement paste by homogeneous materials with an equivalent macroscopic behaviour. The heterogeneous material must be statistically homogeneous to allow the appropriate definition of an REV. In addition, the physical heterogeneities and loading mechanisms characteristic lengths must be much

smaller than the REV, to allow a clear separation of scales [167]. Both conditions are satisfied in our applications.

The homogenization scheme extending the poroelastic theory –intended for homogeneous materials– to the micro-heterogeneous cement paste is presented in the current section. The detailed derivations of the expressions can be retrieved in the literature on the subject (e.g. [35, 36, 77, 167, 168]). The main equations are recalled for the case of an isotropic material.

Consider a heterogeneous isotropic porous material composed of a total of n homogeneous phases: a pore volume and $m = n - 1$ solid phases. For any given phase i, considered isotropic and of volume fraction v_i, the bulk and shear moduli are given by K_i and G_i. The poroelastic parameters of the homogenized material are:

$$K = \sum_{i=1}^{n} v_i K_i A_i^v \tag{5.71a}$$

$$G = \sum_{i=1}^{n} v_i G_i A_i^d \tag{5.71b}$$

$$b = 1 - \sum_{i=1}^{m} v_i A_i^v \tag{5.71c}$$

$$\frac{1}{N} = \sum_{i=1}^{m} \frac{v_i \left(1 - A_i^v\right)}{K_i} \tag{5.71d}$$

where A_r^v and A_r^d are the volumetric and deviatoric strain localization coefficients, respectively. The remaining poroelastic parameters can be derived from the classic formulae (see Appendix 5.B).

For a homogenized material composed of porous heterogeneities, the previous expressions have to be modified. We assume the active pores from different scales are mutually connected, and therefore subjected to a homogeneous pore pressure. Considerations regarding the inactive porosity will be discussed later. The upscaled properties of the homogeneous material are given by:

$$b = 1 - \sum_{i=1}^{m} v_i \left(1 - b_i\right) A_i^v \tag{5.72a}$$

$$\frac{1}{N} = \sum_{i=1}^{m} v_i \left[\frac{\left(1 - b_i\right)\left(1 - A_i^v\right)}{K_i} + \frac{1}{N_i}\right] \tag{5.72b}$$

where b_i and N_i are the Biot coefficient and skeleton modulus of phase i, respectively. The expressions for the upscaling of K and G remain unchanged.

The adoption of an Eshelbian morphology [169] featuring spherical inclusions in a

reference medium allows estimating the strain coefficients A_r^v and A_r^d as:

$$A_i^v = \frac{[1 + \alpha_0 \left(K_i/K_0 - 1\right)]^{-1}}{\sum v_i \left[1 + \alpha_0 \left(K_i/K_0 - 1\right)\right]^{-1}} \tag{5.73a}$$

$$A_i^d = \frac{[1 + \beta_0 \left(G_i/G_0 - 1\right)]^{-1}}{\sum v_i \left[1 + \beta_0 \left(G_i/G_0 - 1\right)\right]^{-1}} \tag{5.73b}$$

$$\alpha_0 = \frac{3K_0}{3K_0 + 4G_0}; \quad \beta_0 = \frac{6 \left(K_0 + 2G_0\right)}{5 \left(3K_0 + 4G_0\right)} \tag{5.73c}$$

where K_0 and G_0 are the bulk and shear moduli of the reference medium, respectively. The adoption of the reference medium depends on the choice of the homogenization scheme: the Mori-Tanaka explicit scheme if a dominating percolated phase r acts as the reference medium ($K_0 = K_r, G_0 = G_r$), or the self-consistent implicit scheme if the resulting homogenized material is to be considered the reference medium ($K_0 = K, G_0 = G$).

The cement paste is a multiscale material constituted of components covering an extremely wide array of characteristic sizes, going from the sub-nanometric to the micrometric and even the millimeter range [27]. This multiscale hierarchy requires the consideration of the different scales of the heterogeneities, both solid and porous, in the upscaling scheme. In the present work, the upscaling of the poroelastic properties of the cement paste is performed in two successive steps:

- Level I: LD and HD C–S–H gel.

- Level II: cement paste.

The adopted homogenization scheme is self-consistent at both levels. The schematic idealized representation of the cement paste microstructure is presented in Figure 5.7.

The first step of the upscaling procedure is the Level I homogenization of the LD and HD C–S–H gels according to the standard expressions from Equation (5.71), valid for non-porous solid phases. The homogenization requires the definition of the elastic parameters of the C–S–H globules and the gel porosities, the latter given in Table 5.2. The result of the Level I homogenization are the poroelastic properties of LD and HD C–S–H.

The homogenization of the cement paste is performed at the Level II, in which we consider the microstructure of the cement paste as constituted of nine main phases: LD and HD C–S–H gels, Portlandite, aluminates, anhydrous clinker components C_3S, C_2S, C_3A and C_4AF, and the macro-porosity. Among these phases, Portlandite crystals, aluminates and anhydrous clinker can be considered as non-porous solids, while LD and HD C–S–H are porous solids. The upscaling procedure requires the definition of the volume fraction of each of these components, given by our volume fraction model from Section 5.3.1. The mechanical properties of the multiple phases have been collected from the literature and are given in Table 5.3. The poromechanical properties of the LD and HD C–S–H gels are
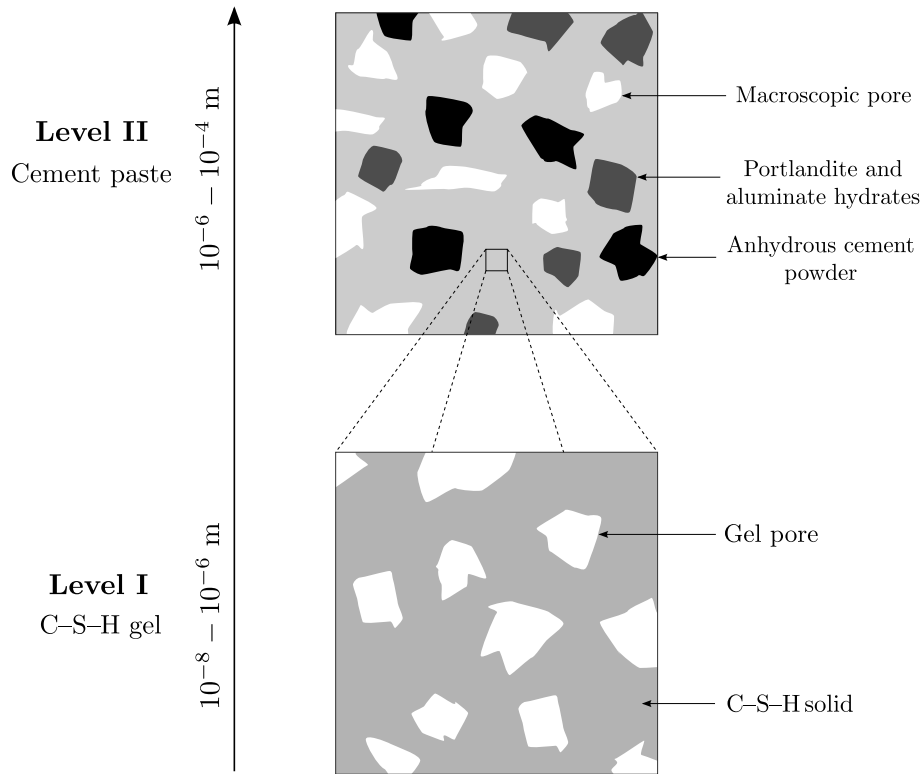
Figure 5.7: Schematic representation of the cement paste multiple microstructural scales adopted for the upscaling of the poroelastic properties of a cement paste.

determined from the Level I homogenization step. The homogenization of the poroelastic properties is performed according to the first two expressions of Equation (5.71) together with Equation (5.72), given the porous nature of some of the microstructure components.

The distinction of the active porosity of the C–S–H gels in the Level II homogenization step has an important effect on the final poroelastic properties of the cement paste. The active porosity is the porosity that participates in the transmission of pore pressures, as previously mentioned. In accordance with the Jennings model, we assumed the gel porosity of HD C–S–H to be completely inactive, while only a fraction of the LD C–S–H gel porosity is active. The details are discussed in Section 5.3.2. Therefore, in the homogenization procedure, the HD C–S–H gel behaves as a non-porous phase, with its undrained poroelastic parameters acting as effective mechanical parameters. Regarding LD C–S–H, the active volume fraction of the LD C–S–H gel is homogenized as a porous component, while its inactive part acts as non-porous with its undrained parameters.

The elastic parameters of the C–S–H globules ($K_{\text{C–S–H}}$ and $G_{\text{C–S–H}}$) are back-calculated according to our upscaling model from an inverse analysis of the poroelastic parameters obtained experimentally, as discussed in Section 6.4.5.

One of the distinguishing features of our micromechanical model is the determination

Table 5.3: Mechanical parameters for the homogenization scheme.

	K (GPa)	G (GPa)	Reference
Level I: C–S–H gel			
C–S–H globules	31.3	21.4	Inverse analysis [*]
Level II: cement paste			
C_3S	112.5	51.9	[170]
C_2S	116.7	53.8	[170]
C_3A	120.8	55.8	[170]
C_4AF	104.2	48.1	[170]
CH	32.5	14.6	[171]
Aluminates	32.5	14.6	Same as CH [**]

[*]For details, see Section 6.4.5; [**]Same hypothesis as Haecker et al. [172]
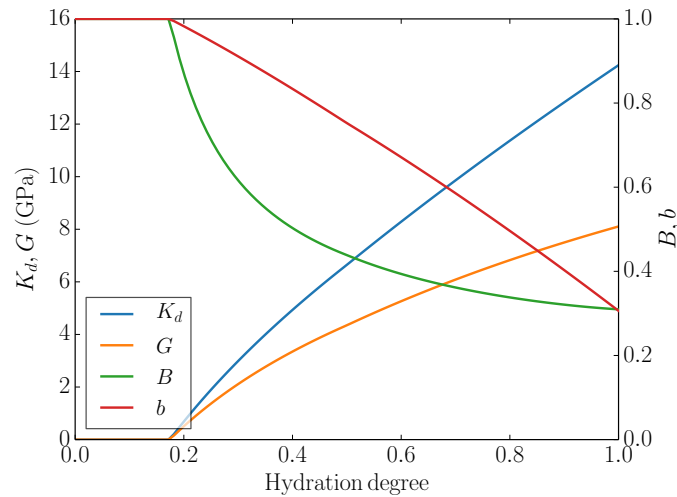
Figure 5.8: Poroelastic parameters of a class G cement paste as a function of the hydration degree.

of the volume fractions of the C–S–H gels directly from the stoichiometric formulation of the C–S–H globules, allowing the appropriate distribution of the gel in LD and HD C–S–H. In addition, the active porosity of the gels is determined directly from the Jennings model assumptions. As a result, the model is limited in terms of calibration parameters and degrees of freedom, while being in agreement with recent advances regarding the microstructure of the cement paste.

The evolution of the poroelastic parameters with hydration degree determined from our upscaling and volume fraction models is presented in Figure 5.8. Additional considerations concerning particle shape, size distributions and more complex or precise phase distributions (e.g. [34, 76, 173]), are beyond the scope of the intended applications of the present model.

The main interest of the upscaling techniques resides in the calibration of the microme-

chanical parameters –notably the elastic properties of the C–S–H globules (Table 5.3)– and the validation of the predictions of poroelastic properties and their evolution based on our volume fraction model (Section 6.7.2). The resulting calibrated tool can provide estimates of the poroelastic properties of different cement paste formulations without the need of extensive and expensive experimental campaigns (e.g [77]). Cement paste formulations can henceforth be considered in the light of the homogenization model before heading to the laboratory.

5.7   Time-dependent strains

The time-dependent viscous deformations, a characteristic feature of cementitious materials, are described according to the solidification theory of Bažant [6, 66, 174]. As essential assumptions, we recall the infinitesimal transformation hypothesis together with Boltzmann's principle of superposition, resulting in linear viscous material behaviour and independence with respect to the stresses, an acceptable hypothesis up to loadings of 70% of the failure compressive strength [175].[6] Furthermore, the intrinsic material properties are assumed non-ageing, i.e. the creep properties of the constituents are invariant with respect to time translation. The solidification of viscoelastic elements for an unidimensional material is schematically presented in Figure 5.9. The elementary mechanical unit is of the Kelvin type, composed of a spring of modulus E_v and a dashpot of viscosity $\eta = \theta E_v$. The stress acting on the spring is therefore given by $\sigma_S = E_v \varepsilon_v$, while for the dashpot $\sigma_D = \eta \dot{\varepsilon}_v$ with equilibrium requiring $\sigma_v = \sigma_D + \sigma_S$.
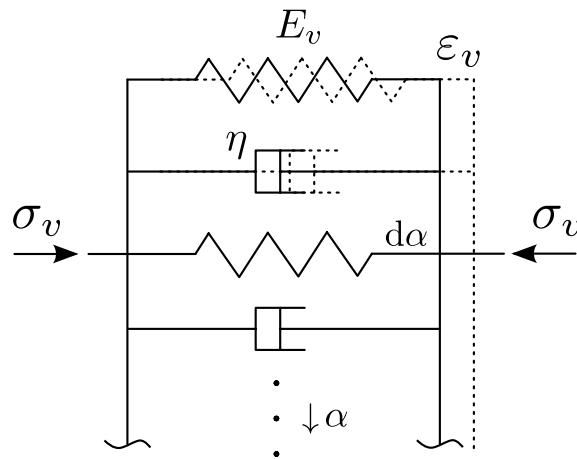
Figure 5.9: Unidimensional mechanical model of a chemically-active viscoelastic solid.

In general, the response of a non-ageing viscous material to a loading history is expressed

---

[6]Boltzmann's superposition principle implies superposition of the loadings and material behaviour. The hypothesis of infinitesimal transformations allows the superposition of responses. The problem is, therefore, completely linear, both geometrically and physically.

as

$$\varepsilon_v = \int_{\tau=t_0}^{t} J(t-\tau)\dot{\sigma}_v \, d\tau \tag{5.74}$$

where $J(t-t_0)$ is the compliance function, equal to the strain at time t produced by a load applied at time t_0. In the case of the Kelvin unit, the compliance is given by

$$J(t-t_0) = \frac{1}{E_v}\left[1 - \exp\left(-\frac{t-t_0}{\theta}\right)\right] \tag{5.75}$$

for which it is easy to verify the time-shift invariance and linearity.

The assembly of new elements in parallel results in the evolution of the macroscopic mechanical properties with the advancement of the reaction. As for elasticity, the new elements are introduced with no initial stress, and therefore have no effect on either stress or strain at their time of insertion. The evolution of the observable viscous strains is given by the second order differential equation [5]:

$$\ddot{\varepsilon}_v + \left(\frac{1}{\theta} + \frac{\dot{v}_v}{v_v}\right)\dot{\varepsilon} = \frac{\dot{\sigma}_v}{\theta v_v E_v} \tag{5.76}$$

where v_v is the volume fraction of the viscoelastic elements, which we consider equal to the volume fraction of the cement paste skeleton, i.e. henceforth $v_v = v_{sk}$.

The generalization to the case of multiaxial stress and strain conditions requires the introduction of the compliance tensor, such that

$$\boldsymbol{\varepsilon}_v = \int_{\tau=t_0}^{t} \mathbf{J}(t-\tau)\dot{\boldsymbol{\sigma}}_v \, d\tau \tag{5.77}$$

A significant simplification is possible for an isotropic material if the viscous Poisson ratio ν_v is assumed constant. For cementitious materials, this hypothesis is an acceptable approximation for saturated as well as partially saturated conditions with constant values of relative humidity, for which the creep Poisson ratio is similar to the instantaneous elastic value [175, 176]. Because the variations of relative humidity of our applications are limited in range, we adopt this hypothesis for both the saturated and partially saturated conditions.

In addition, the extension of the solidification model to porous materials requires the definition of the effective stress controlling viscous strains. In the case of a cement paste, because the solid skeleton is non-viscous under isotropic loading (see Section 5.5.3), the Terzaghi effective stress dictates the macroscopic viscous behaviour [177].

Based on the previous observations, the stress-strain relations extending the solidification model to an isotropic porous material read:

$$\ddot{\boldsymbol{\varepsilon}}_v + \left(\frac{1}{\theta} + \frac{\dot{v}_{sk}}{v_{sk}}\right)\dot{\boldsymbol{\varepsilon}}_v = \frac{(1+\nu_v)\dot{\boldsymbol{\sigma}}' - \nu_v \operatorname{tr}\left(\dot{\boldsymbol{\sigma}}'\right)\mathbf{I}}{\theta E_v v_{sk}} \tag{5.78}$$

or the equivalent expressions in terms of invariants:

$$\ddot{\epsilon}_v + \left(\frac{1}{\theta} + \frac{\dot{v}_{sk}}{v_{sk}}\right)\dot{\epsilon}_v = \frac{3\left(1 - 2\nu_v\right)}{\theta v_{sk} E_v}\dot{\sigma}' \tag{5.79a}$$

$$\ddot{\mathbf{e}}_v + \left(\frac{1}{\theta} + \frac{\dot{v}_{sk}}{v_{sk}}\right)\dot{\mathbf{e}}_v = \frac{\left(1 + \nu_v\right)}{\theta v_{sk} E_v}\dot{\mathbf{s}} \tag{5.79b}$$

or, finally, expressing the rate as:

$$\dot{\epsilon}_v = \frac{3\left(1 - 2\nu_v\right)}{E_v\left(v_{sk} + \theta\dot{v}_{sk}\right)}\dot{\sigma}' - \frac{\theta v_{sk}}{v_{sk} + \theta\dot{v}_{sk}}\ddot{\epsilon}_v \tag{5.80a}$$

$$\dot{\mathbf{e}}_v = \frac{\left(1 + \nu_v\right)}{E_v\left(v_{sk} + \theta\dot{v}_{sk}\right)}\dot{\mathbf{s}} - \frac{\theta v_{sk}}{v_{sk} + \theta\dot{v}_{sk}}\ddot{\mathbf{e}}_v \tag{5.80b}$$

The viscoelastic model might be refined by considering more appropriate compliance functions, such as the log-power law of Bažant and Prasannan [6]. The procedure would then require the determination of the Dirichlet series coefficients of the Kelvin chain that best approximate such compliance function, using for instance the continuous retardation spectrum method as explained by Bažant and Xi [68]. In addition, a further refinement might include additional material microprestresses to better model the very long term hardening [176]. Such additions might be desirable, but are nevertheless not essential for the purpose of our applications. As such, they are omitted for the sake of simplicity.

The viscoelastic behaviour relies on the volume fraction model from Section 5.3 for the determination of v_{sk} and its rate of change $\dot{v}_{sk}$. In addition, only the material viscoelastic parameters E_v and θ have to be defined, since the viscoelastic Poisson ratio ν_v can be assumed equal to the drained elastic Poisson ratio ν_d, as previously mentioned. The thermodynamic admissibility of the mechanism requires E_v and θ to be positive [174].

5.8 Plastic strains

The description of irreversible plastic strains follows the classical flow theory of plasticity applied to frictional porous materials [147, 178, 179]. The dissipation function is assumed to be rate-independent, thus resulting in the existence of a yield surface delimiting the non-plastic domain of the material [180]. Because of the assumed volumetric plastic incompressibility of the solid skeleton (see Section 5.5.3), the yield surface is defined on the stress space by the Terzaghi effective stress $\boldsymbol{\sigma}'$. In addition, the evolution of the yield threshold observed for cement-based materials is associated to a hardening force $\boldsymbol{\zeta}$. The yield surface thus reads $f(\boldsymbol{\sigma}', \boldsymbol{\zeta}) \leq 0$. Plastic deformations due to sliding rearrangements of the microstructure occur when the current state lies and remains on the yield surface, i.e. $f = 0$. Inside the yield surface, $f < 0$ and the material response is non- plastic.

As a result of the hydration reaction, the cement paste evolves from a fluid slurry to a solid material. The precipitation of the newly formed hydrates reinforces the skeleton, enlarging the elastic domain of the material. From a modelling perspective, we must require the hardening force $\boldsymbol{\zeta}$ to exhibit chemical hardening [79] which, in our case, will be described by means of the volume fraction of the cement paste skeleton v_{sk}, according to the volume fractions model described in Section 5.3.1. In addition, in accordance with most plastic models for geomaterials [179], the hardening force $\boldsymbol{\zeta}$ will depend on volumetric plastic strain ϵ_p, and therefore $\boldsymbol{\zeta} = \boldsymbol{\zeta}\left(v_{sk}, \epsilon_p\right)$.

We adopt a coaxial flow rule with coinciding principal axes of the plastic strain increment and the Cauchy stress tensor [178]. The increments of plastic strains are hence given by the evolution law

$$\dot{\boldsymbol{\varepsilon}}_p = \dot{\lambda}\frac{\partial g\left(\boldsymbol{\sigma}', \boldsymbol{\zeta}\right)}{\partial \boldsymbol{\sigma}'} \tag{5.81}$$

where the scalar $\dot{\lambda}$ is the plastic multiplier and g is the plastic flow potential, that might be different from f in a non-associated plastic model [180]. The plastic multiplier $\dot{\lambda}$ and the yield surface f must satisfy the Kuhn-Tucker conditions:

$$\dot{\lambda} \geq 0; \quad f \leq 0; \quad \dot{\lambda}f = 0 \tag{5.82}$$

For isotropic materials, only the stress and strain invariants are necessary for the material description. We neglect the effects of the third invariant, meaning the surface intersections with the deviatoric plane in Haigh-Westergaard stress space are circles (see ref.[178]). In a similar way, the hardening force is assumed invariant with respect to material rotations. The plastic strain increments are therefore given by:

$$\dot{\epsilon}_p = \dot{\lambda}\frac{\partial g}{\partial \sigma'}; \quad \dot{\gamma}_p = \dot{\lambda}\frac{\partial g}{\partial \tau} \tag{5.83}$$

5.8.1 Yield surface and plastic potential

We propose to define the yield surface and plastic potential according to the Asymmetric Cam Clay(ACC) model. This new model, an extension of the classical Modified Cam-Clay (MCC) model [181, 182], allows the displacement of the contractant-dilatant threshold. The complete derivation is presented in Appendix 5.A. The expression has the form:

$$f = \tau^2 \exp(kx) + M^2 \left(\sigma' - \sigma_c\right)\left(\sigma' + \sigma_t\right) \tag{5.84}$$

where k is the contractant-dilatant threshold (CDT) parameter[7], σ_c and σ_t are the compression and traction isotropic yield stresses, and

$$x = \frac{2\sigma' + \sigma_t - \sigma_c}{\sigma_t + \sigma_c} \tag{5.85}$$

is the normalized effective stressed with respect to the isotropic axis domain size. The surface is determined by the parameters σ_c, σ_t, k and M. Note that for $k = 0$ and $\sigma_t = 0$ we recover the MCC model.

The surface, illustrated in Figure 5.10, features volumetric and deviatoric plastic strains, isotropic traction and compression yield, purely volumetric flow under isotropic loading, frictional and mean-stress sensitive behaviour and accommodates flexible contraction or dilation responses. These features are, in our view, necessary to model a geomaterial such as cement paste. Furthermore, the ACC model remains real-valued and continuous in the real domain, fulfilling basic requirements that ease its numerical implementation.
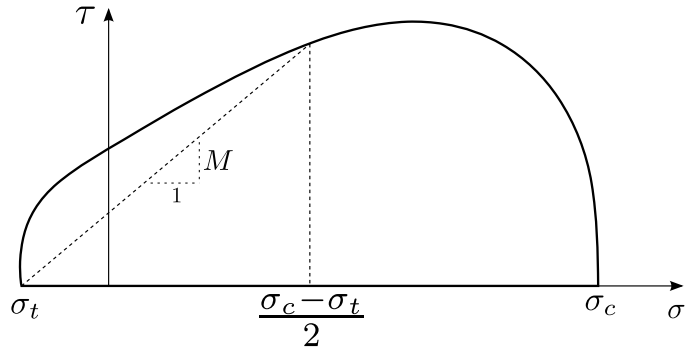
Figure 5.10: Schematic representation of the ACC yield surface.

Regarding the plastic potential, we adopt the general form:

$$g = \tau^2 \exp(kx) + N^2 (\sigma' - \sigma_c) (\sigma' + \sigma_t) \tag{5.86}$$

In the case of associated flow, $N = M$. In applications, standard associated models are preferred to non-associated models, and the latter should only considered if the material behaviour absolutely demands it, as suggested by Drucker [183]. In the case of an associated model, we only require the free energy and the dissipation potentials to completely describe the plastic behaviour of material, in agreement with the hyperplasticity framework of Houlsby and Puzrin [184].

---

[7]The contractant or dilatant character is related with the plastic flow surface. If the surface is also employed as hardening potential, it might as well be called a hardening-softening threshold.

From the plastic potential and the yield condition, the flow rule is given by:

$$\dot{\epsilon}_p = \dot{\lambda}\frac{\partial g}{\partial \sigma'} = \dot{\lambda}M^2\left(\sigma_c + \sigma_t\right)\left[\frac{k}{2}\left(1 - x^2\right) + \left(\frac{N}{M}\right)^2 x\right] \tag{5.87a}$$

$$\dot{\gamma}_p = \dot{\lambda}\frac{\partial g}{\partial \tau} = \dot{\lambda}M\exp(kx/2)\left(\sigma_c + \sigma_t\right)\left(1 - x^2\right)^{1/2} \tag{5.87b}$$

where the dependency on the stress state is completely encapsulated by x.

5.8.1.1 Thermodynamic admissibility

The total plastic work rate $\dot{W}_p$ can be decomposed as

$$\dot{W}_p = \dot{\varphi}_p + \dot{F}_p \tag{5.88}$$

where $\dot{\varphi}_p$ and $\dot{F}_p$ are the dissipation and free plastic energy, respectively. The meaning and nature of the free plastic energy F_p will become clear upon the introduction of a simplified analogy in the following section: it is the mechanical energy stored by the material in the form of microscopic stresses due to plastic hardening.

We proceed by first noting that the plastic work rate is also given by:

$$\dot{W}_p = \boldsymbol{\sigma'} : \dot{\boldsymbol{\varepsilon}}_p = \sigma'\dot{\epsilon}_p + \tau\dot{\gamma}_p \tag{5.89}$$

According to the formulae from the previous section, we can express the stresses as:

$$\sigma' = \frac{\dot{\epsilon}_p}{2\dot{\lambda}N^2} - \frac{k\tau^2\exp(kx)}{N^2\left(\sigma_c + \sigma_t\right)} + \frac{\sigma_c - \sigma_t}{2} \tag{5.90a}$$

$$\tau = \frac{\dot{\gamma}_p}{2\dot{\lambda}\exp(kx)} \tag{5.90b}$$

and combining the three previous equations, the plastic work rate can be rewritten as:

$$\dot{W}_p = \frac{\dot{\epsilon}_p^2}{2\dot{\lambda}N^2} + \frac{\dot{\gamma}_p^2}{2\dot{\lambda}\exp(kx)} - \frac{k\tau^2\exp(kx)}{N^2\left(\sigma_c + \sigma_t\right)}\dot{\epsilon}_p + \frac{\sigma_c - \sigma_t}{2}\dot{\epsilon}_p \tag{5.91}$$

The first two terms are positive for all plastic evolutions, and are thus immediately recognized as dissipative. The two remaining terms require closer examination. Imagine a plastic step in which we go from an initial to a final yield surface following two different stress paths. In the first path, we perform a purely isotropic stress step (Path A), while in the second case we allow both isotropic and shear stress components (Path B). The two cases, illustrated in Figure 5.11, produce equal changes in the yield surface, and therefore must change the stored plastic energy in the exact same amount. If it were not so, the two identical final materials would have different energy states. We can identify the last term, common to both evolutions, as corresponding to the stored energy. It is clear that

the stored plastic energy will be zero in a closed plastic strain cycle as expected, since the initial and final material states are identical. The third term, absent in path A because the shear stress is null, is not associated to the free energy rate, and must therefore also be dissipative. It is interesting to note that the ACC and MCC models both feature a critical state at the CDT where a purely dissipative frictional mechanism leads to failure.
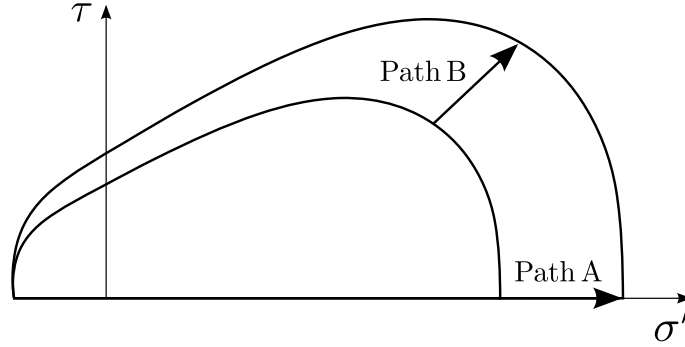

Figure 5.11: Two different stress paths with equal plastic energy increase.

The free plastic energy rate in a plastic evolution is hence given by:

$$\dot{F}_p = \frac{\sigma_c - \sigma_t}{2}\dot{\epsilon}_p \tag{5.92}$$

making it possible to identify the hardening force $\zeta = \frac{\partial F_p}{\partial \epsilon_p} = (\sigma_c - \sigma_t)/2$. From the previous derivations, it is clear that the identification of the free energy and its associated hardening force might be a non-trivial task. There are examples in the literature in which their expressions were unjustifiably –albeit correctly– assumed (e.g. [78, 185]), thus obscuring their physical origin. In addition, there are also examples of incorrect expressions (e.g. [186]).

In our analysis, no assumption has been made regarding the kinematic hardening variable. In consequence, the result places a restriction on the possible hardening mechanisms of the yield surface: *only the volumetric plastic strain rate $\dot{\epsilon}_p$ is responsible of the plastic free energy evolution, and therefore it is the only appropriate hardening variable in a MCC or ACC model.* The inclusion of other strain hardening terms, notably shear hardening, would require a different yield surface and plastic potential.

An analogous procedure can be followed to determine the appropriate hardening variables for different choices of plastic potentials, leading to the following general conclusion: *the choice of hardening variables is restricted by the free energy stored by the plastic evolution.* The mechanical modeller must strictly respect this constraint if a coherent plastic model is to be formulated. Indeed, a degenerate Legendre transform [187] reveals that only this variable can be associated to the hardening of the yield surface.

Having identified the free energy rate, the plastic dissipation can be obtained from

Equations (5.88), (5.91) and (5.92). Together with the flow rules from Equation (5.87), the plastic dissipation becomes:

$$\dot{\varphi}_p = \frac{\dot{\lambda} M^2 \left(\sigma_c + \sigma_t\right)^2}{2} \left[\frac{kx}{2} \left(1 - x^2\right) + \left(\frac{N}{M}\right)^2 x^2 + 1 - x^2 \right] \geq 0 \tag{5.93}$$

The terms outside the brackets are always positive. Assuring admissibility therefore requires the positivity of the term inside the brackets, i.e.

$$\tilde{\varphi}_p = \frac{kx}{2} \left(1 - x^2\right) + \left(\frac{N}{M}\right)^2 x^2 + 1 - x^2 \geq 0 \tag{5.94}$$

The problem is reduced to the determination of admissible combinations of k and M/N satisfying $\tilde{\varphi}_p \geq 0$ inside the reduced domain $x \in [-1, 1]$.
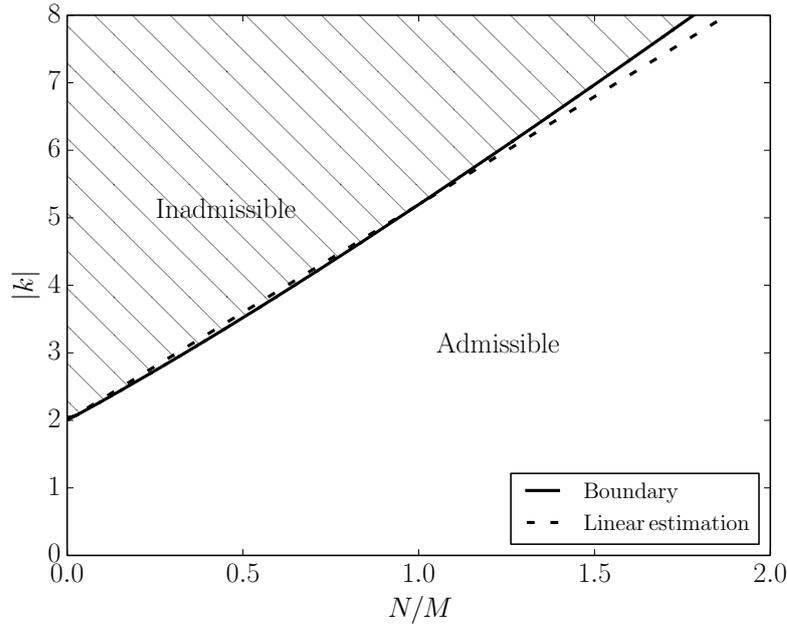
Figure 5.12: Domain of thermodynamically-admissible combinations of plastic parameters.

The boundary of admissible parameters for the general ACC model is presented in Figure 5.12. The boundary resembles a straight line, as can be observed from the plot, where we have included the line determined from $N/M = 0, k = 2$ and $N/M = 1, k = 3\sqrt{3}$, given by $k \leq 2 + \left(3\sqrt{3} - 2\right) N/M$. The line might serve as a practical guideline for limit combinations, although, in general, the parameters will likely fall well within the acceptable domain. For the particular case of the MCC model, with $k = 0$ and $N/M = 1$, the inequality is satisfied immediately. For a non-associated MCC, there are no restrictions on the ratio N/M either.

5.8.2 Chemo-mechanical hardening

The coupled chemo-mechanical hardening is best understood after considering the mechanical analogy of Figure 5.13. The elementary mechanical unit consists of a parallel assemblage of a spring with stiffness E_p and a slider with a sliding threshold p. The element behaves as perfectly rigid until we reach the slider yield stress, thereafter hardening as deformed with a hardening modulus equal to the spring stiffness. The elementary unit is considered as non-ageing, and thus reflects the intrinsic properties of the precipitating solid material.
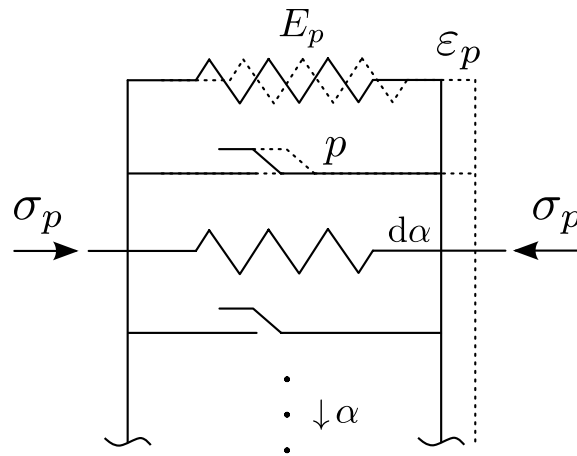

Figure 5.13: Unidimensional mechanical model of a chemically-active hardening plastic solid.

We propose a solidification approach to plastic materials inspired by the model of Bažant [6, 66], where the evolution of plastic properties is by accumulation of constituents in parallel. For the same elementary mechanical unit, the assembly in series is inappropriate because it results in the absence of chemical hardening and a decrease of the mechanical hardening modulus with hydration, both seemingly unphysical responses for a progressively reinforced solid.

Although the overall state of stress is homogeneous, the internal state of stress of the assembly is not. If the global stress is such that we remain on the yield surface, the global assemblage of elements is required to satisfy the equilibrium condition:

$$\sigma_p(t) = \int_{\tau=0}^{t} \Big[s\big(v(\tau), t\big) + p\big(v(\tau)\big) \Big] \, \mathrm{d}v\,(\tau) \qquad (5.95)$$

where, for a differential constitutive layer, s is the stress on the elastic spring and p the slider yield stress. In general, we allow the properties to depend on the solidification stage.

In addition, the system deformations ought to satisfy mutual compatibility, requiring the yield to occur simultaneously for all elements because of their parallel coupling. The strain of a single layer is given by its initial microscopic strain $\varepsilon_p^m \left(v(t_0), t_0\right)$ and the difference of

the macroscopic strain ε_p at time t and that at the time t_0 corresponding to the introduction of the layer. In view of the spring constitutive law, we must have

$$\varepsilon_p^m\left(v(t_0), t\right) = \varepsilon_p^m\left(v(t_0), t_0\right) + \varepsilon_p\left(t\right) - \varepsilon_p\left(t_0\right) = \frac{s_0(v(t_0))}{E_p(v(t_0))} + \int_{\tau=t_0}^t \frac{\mathrm{d}s\left(\tau\right)}{E_p(v(t_0))} \tag{5.96}$$

where $E_p\left(v\left(t_0\right)\right)$ is the elementary spring stiffness of the layer introduced at time t_0. If we consider the new units link to the system free of initial strain and stress, the compatibility reads:

$$\varepsilon_p\left(t\right) - \varepsilon_p\left(t_0\right) = \int_{\tau=t_0}^t \frac{\mathrm{d}s\left(\tau\right)}{E_p(v(t_0))} \tag{5.97}$$

Because the properties of the constituents are considered non-ageing, we can extract E_p from the integral and obtain the expression for the stress on a single layer:

$$s\left(v(t_0), t\right) = \int_{\tau=t_0}^t \mathrm{d}s\left(\tau\right) = E_p(v(t_0))\left(\varepsilon_p\left(t\right) - \varepsilon_p\left(t_0\right)\right) \tag{5.98}$$

that can be introduced in the equilibrium Equation (5.95) yielding:

$$\sigma_p(t) = \int_{\tau=0}^t \left[E_p\big(v(\tau)\big)\left(\varepsilon_p\left(t\right) - \varepsilon_p\left(\tau\right)\right) + p\big(v(\tau)\big)\right]\mathrm{d}v\left(\tau\right) \tag{5.99}$$

The evolution of the yield stress is obtained from the previous expression by differentiating under the integral sign recalling Leibniz's rule:

$$\dot{\sigma}_p(t) = \bar{E}_p\,\dot{\varepsilon}_p(t) + p\big(v(t)\big)\,\dot{v}(t) \tag{5.100}$$

where

$$\bar{E}_p = \int_{\tau=0}^t E_p\big(v(\tau)\big)\,\mathrm{d}v\left(\tau\right) \tag{5.101}$$

From the expression of $\dot{\sigma}_p(t)$ (Equation (5.100)), it is clear that the yield stress evolution features both a coupled chemo-mechanical hardening via $\bar{E}_p$ and a purely chemical hardening by means of p. If necessary, initial stresses in the elements might be introduced by appropriate modifications of Equation (5.96) and the subsequent derivation.[8]

We postulate analogous chemo-mechanical hardening mechanisms in the case of our multi-axial ACC plasticity model. To capture the enlargement of the elastic domain due to the precipitation of new solids, the mechanical hardening is described by means of the isotropic yields in compression σ_c and traction σ_t, while the shape ratio M reflects the changes of the frictional yield and the transition from a fluid to a solid skeleton. The CDT parameter k will be assumed constant. The resulting model displays coupled mechanical and chemical hardening in a consistent and physically-intuitive framework.

---

[8]The previous derivation explicitly shows that, to recover the hardening model of Ulm and Coussy [79], the new elements must be introduced with initial strains exactly equal to the strain of the first layer, a restrictive and physically improbable hypothesis.

From the analysis presented in the previous section, it is clear that the only possible strain hardening parameter is the volumetric plastic strain ϵ_p. The hardening force $(\sigma_c - \sigma_t)/2$, that controls the size of the yield surface, is therefore determined by both the volumetric plastic deformations and the evolving hydration of the material. We choose to describe σ_c and σ_t independently. The initial values of both σ_c and σ_t are negligible, because the incipient skeleton is non-percolating at early hydration stages. According to Equation (5.100), we must have:

$$\dot{\sigma}_c = h \, v_{sk} \, \dot{\epsilon}_p + \sigma_\infty \, \dot{v}_{sk} \tag{5.102}$$

where the hardening parameters h and σ_∞ are considered to remain constant, and depend on the hydration conditions and cement paste composition: they reflect the intrinsic plastic properties of the precipitating hydrates.

The complete definition of the yield surface position requires the determination of σ_t. The isotropic tensile yield stress σ_t increases as the cement paste progressively develops its traction resistance. The parameters σ_c and σ_t can be related by empirical correlations of uniaxial compressive and tensile strength. The ultimate resistance of cement in traction can be estimated as a fraction of the compressive strength, normally in the order of 0.06 to 0.11 [188]. Although the tension strength differs from the isotropic yield tension, the traction yield σ_t can be estimated as a similar fraction of the compressive yield stress σ_c. These parameters can be calibrated from experimental tests. We will assume $\sigma_t = f_t \sigma_c$ and hence write:

$$\dot{\sigma}_t = f_t \, \dot{\sigma}_c \tag{5.103}$$

.

The parameter M controls the shape ratio on the $\sigma' - \tau$ plane. A larger M corresponds to a higher friction coefficient with the limiting case $M \approx 0$ corresponding to the behaviour of a fluid with negligible shear yield stress. We consider M evolves from a negligible initial value to its ultimate value with the hydration of the material. As a consequence of the independence of the plastic hardening with respect to plastic shear strain γ_p, no energy is stored from frictional mechanisms. Therefore, the evolution of M is purely chemical and, according to Equation (5.100), linearly related to the precipitated solid extent:

$$\dot{M} = M_\infty \, \dot{v}_{sk} \tag{5.104}$$

where M_∞ reflects the intrinsic shear ratio of the material constituents.

The evolution of the yield surface with hydration is presented in Figure 5.14. The progressive enlargement of the isotropic yield bounds is evidenced, as well as the changes of the surface shape due to evolving frictional character of the material.
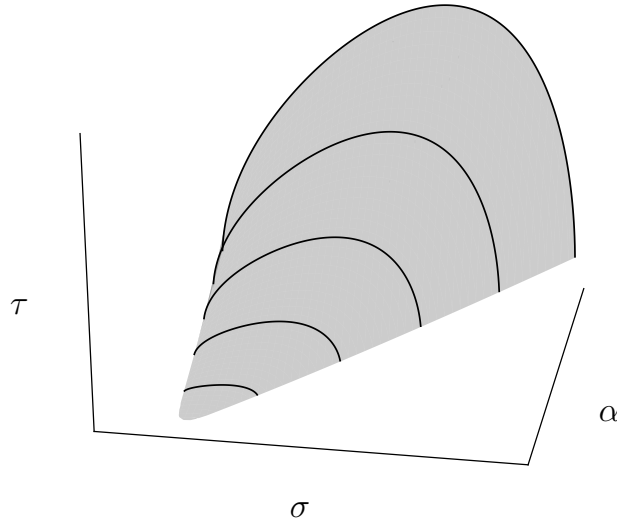
Figure 5.14: Schematic evolution of the yield surface with hydration degree. Note the change of both the size and shape of the surface.

5.9 Assembled mechanical system

The complete constitutive relations describing the mechanical behaviour of the cement paste results from the superposition of the essential mechanisms, schematically assembled in Figure 5.15. It is worth noting, however, that the illustration is limited to a one-dimensional analogy not portraying the three-dimensional nature of the model. Furthermore, it does not distinguish the different effective stresses governing the response of each of the mechanisms of our model.
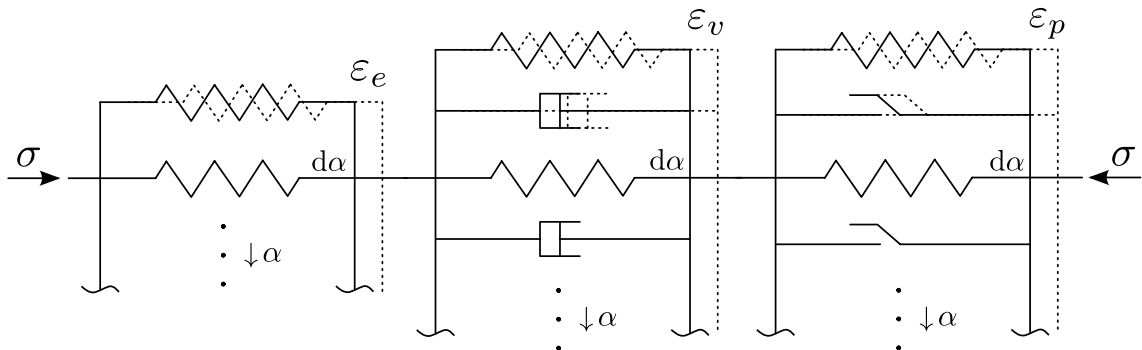

Figure 5.15: Unidimensional mechanical model of a chemically-active elasto-visco-plastic solid.

According to the expressions of the previous sections, the macroscopic strain and porosity

are given by:

$$\dot{\boldsymbol{\varepsilon}} = \dot{\boldsymbol{\varepsilon}}_e + \dot{\boldsymbol{\varepsilon}}_v + \dot{\boldsymbol{\varepsilon}}_p + \dot{\boldsymbol{\varepsilon}}_\alpha \tag{5.105a}$$

$$\dot{\phi} = \dot{\phi}_e + \dot{\phi}_v + \dot{\phi}_p + \dot{\phi}_\alpha \tag{5.105b}$$

where $\dot{\boldsymbol{\varepsilon}}_e$ and $\dot{\phi}_e$ are given by Equation (5.69), $\dot{\boldsymbol{\varepsilon}}_v$ and $\dot{\phi}_v = -\dot{\epsilon}_v$ by Equation (5.80), $\dot{\boldsymbol{\varepsilon}}_p$ and $\dot{\phi}_p = -\dot{\epsilon}_p$ by Equation (5.87) , and $\dot{\phi}_\alpha$ is given by Equation (5.37), while $\dot{\boldsymbol{\varepsilon}}_\alpha = 0$ for a percolated skeleton.

Table 5.4 summarizes the components of the model, together with its main parameters. The set of mechanical model parameters determined for our class G cement paste hydrated at different temperatures is presented in Table 5.5. The applications will be presented in the next chapter.

Table 5.4: Summary of the chemo-mechanical model components and parameters

		Ref. values	Unit
Chemistry			
	Stoichiometric and microstructural parameters	Tables 5.1 and 5.2	-
Elasticity			
	Micromechanical elastic parameters	Table 5.3	-
Viscosity			
E_v	Viscous modulus	3 - 10	GPa
θ	Relaxation time	5 - 20	h
Plasticity			
h	Chemo-mechanical hardening modulus	1 - 4	GPa
σ_∞	Chemical isotropic modulus	50 - 100	MPa
M_∞	Friction coefficient	1 - 2	-
k	Asymmetry parameter	-1 - 1	-
Partial saturation			
	Water retention curve	Section 6.3	-

Table 5.5: Chemo-mechanical model parameters determined for different temperatures

Parameter	*Hydration temperature* (°C)			
	7	20	60	90
Chemistry				
ξ (cm^3/g cement) [a]	0.047	0.045	0.036	0.030
Elasticity				
$K_{\text{C-S-H}}$ (GPa)	31.3	31.3	25.0 [b]	25.0 [b]
$G_{\text{C-S-H}}$ (GPa)	21.4	21.4	18.4 [b]	18.4 [b]
Viscosity				
E_v (GPa)	3.5	4.0	2.9	3.0
θ (h)	5	5	5	5
Plasticity				
h (GPa)	3.4	4.2	3.1	3.2
σ_∞ (MPa)	72	85	67	72
M_∞	1.5	1.7	1.5	1.9
k	0.7	0.7	0.7	0.7

[a] From Equation (6.12). [b] After Ghabezloo [7].

5.10 Closed system

The constitutive model has been derived for a system open for exchanges of fluids with the exterior. This situation is recurrent in conventional civil engineering applications, for which an exterior pressure is imposed on the gas phases. In these cases, the initial pore pressure will typically be slightly larger than the atmospheric pressure due to the hydrostatic weight of the slurry. The drop in pore pressure is affected, of course, by external sources of water, such as drying by exposure to low relative humidities or water supply by curing. If the pore pressure is depleted once the solid skeleton percolates, it might lead to the creation of gas-liquid menisci and the introduction of gas bubbles in the pore space once the material's air entry pressure p_e is reached, i.e. $p_e = p_{atm} - p_l$, since the exterior gas pressure is typically equal to the atmospheric pressure in unsealed systems. Other scenarios concerning open systems are easily accommodated.

The consideration of a closed system, completely sealed with respect to fluid exchanges, requires further examination. Moreover, its similarity to the conditions found in an oil well ought to retain our attention. The fast hydration rates at high temperatures and pressures together with the low permeability of the cement paste suggests the adoption of a closed system as a reasonable first approximation for bottom-hole conditions in the early stages.

Regarding the initial state of the fluids in a cement paste, consider the scenario of a freshly-placed slurry in an oil well. Most gas bubbles incorporated during mixing are

evacuated if the slurry has the adequate rheological properties.[9] The cement paste is initially subjected to considerable hydrostatic pressures, likely causing the complete dissolution of any remaining gas content by virtue of Henry's law [151]. The pore space can therefore be considered as completely filled with fluid. Furthermore, we can assume the surrounding formation to be saturated, a reasonable hypothesis given their usual depths, thus making the access to air impossible for the hydrating cement paste.

5.10.1   Behaviour prior to the skeleton percolation

Before percolation, the state of stress of the fluid slurry is purely hydrostatic, with $p_l = \sigma$ and $\tau = 0$. If the pressure is held constant, there is no variation in the state of stress, and the strain of solid and fluid phases remains unchanged. Early in the reaction, as long as solid skeleton has not percolated, the chemical shrinkage (see Section 5.3.1) is directly observable as a macroscopic change in volume under a constant stress state. The volumetric strain is therefore given by:

$$\dot{\epsilon} = \beta_\xi \dot{\alpha} \tag{5.106}$$

5.10.2   Evolution of gas pressure and fluid mass exchanges in a percolated system

In a closed system, after the skeleton percolation, the chemical shrinkage results in the depletion of the water pressure because the advance of hydration reactions consumes the pore water. As the hydration progresses, the drop in pore pressure due to the emptying of the pores might eventually result in the liquid phase having a pressure equal to its saturating vapour pressure, i.e. $p_l = p_{sv}$, for which both liquid and its vapour might coexist. Stable vapour bubbles, however, will only be formed once the pressure difference among vapour and liquid reaches the air entry pressure of the pore structure p_e, i.e. $p_e = p_v - p_l$. This pressure corresponds to the threshold of the meniscus size that can be accommodated by the pore structure. Once the vapour bubbles are formed, the progressive removal of water will lead to a further decrease of the menisci diameter, with an equilibrium configuration dictated by the mechanical and physicochemical balance conditions, i.e. the Kelvin-Laplace equations (Section 5.4). The evolution is depicted in Figure 5.16.

The dependency of p_{sv} with respect to temperature is presented in Figure 5.17, where we observe the increase of the p_{sv} with temperature [13]. Continuous estimates might be obtained from empirical expressions such as the Antoine equation [189]. The evolution of the equilibrium conditions according to Kelvin's law is also presented in Figure 5.17 for multiple temperatures.

We remark that the saturating vapour pressures are initially very low for the range of

---

[9]In some applications, not considered here, the air entrapment is voluntarily enhanced.
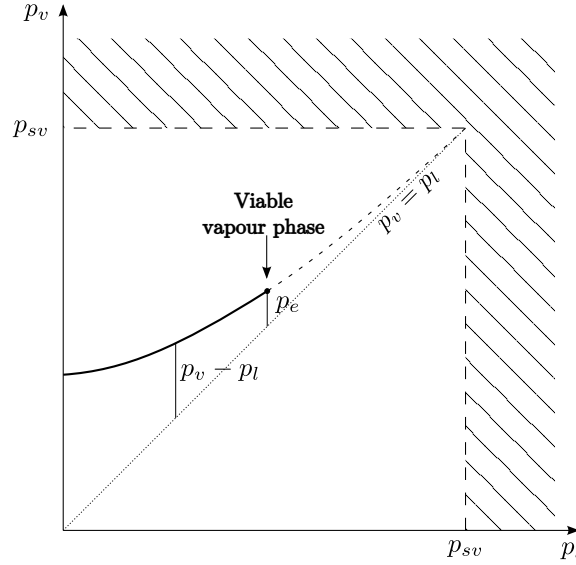
Figure 5.16: Vapour-liquid equilibrium diagram for isothermal closed system. The dashed area corresponds to impossible liquid-vapour phase co-existence, in which case the liquid phase saturates the pore space. When the liquid pressure is below the saturating vapour pressure p_{sv}, Kelvin's law expresses the thermodynamic equilibrium condition. The dashed line representing the initial part of the curve causes no effective desaturation, because the pore structure has no possibility of accommodating such large menisci. Once the air entry pressure p_e is reached, vapour bubbles are formed, the solid line representing the pressure equilibrium condition across the interface of the fluids.

temperatures expected in a well (Figure 5.17, left). In addition, the changes of vapour pressure at equilibrium with the liquid phases are several orders of magnitude smaller than the changes in pressure of the liquid phase (Figure 5.17, right). In summary, for a closed system, we can reasonably assume an initially null vapour pressure, independently of temperature, and neglect the changes in vapour pressure throughout the drying of the material if the system is assumed closed, because both the initial pressure and its variations are small, i.e. $p_{sv}(T) \approx 0$ and $\dot{p}_v \approx 0$.

Let us now consider the mass exchanges among liquid and vapour phases in a closed system, excluding exchanges of chemical origin. In such scenario, the mass of fluids in the pores remains constant, that is:

$$m_l + m_v = \phi \left[S_l \rho_l + (1 - S_l)\rho_v \right] = \phi_0 \rho_l^0 \tag{5.107}$$

where ρ_l^0 is the liquid density at its reference state, i.e. standard temperature and pressure conditions. Since changes of porosity and saturation degree are expected to be small, the fluid exchange rate can be expressed as:

$$\mathring{m}_{l \to v} \approx -\phi_0 (1 - S_l)\dot{\rho}_v \tag{5.108}$$
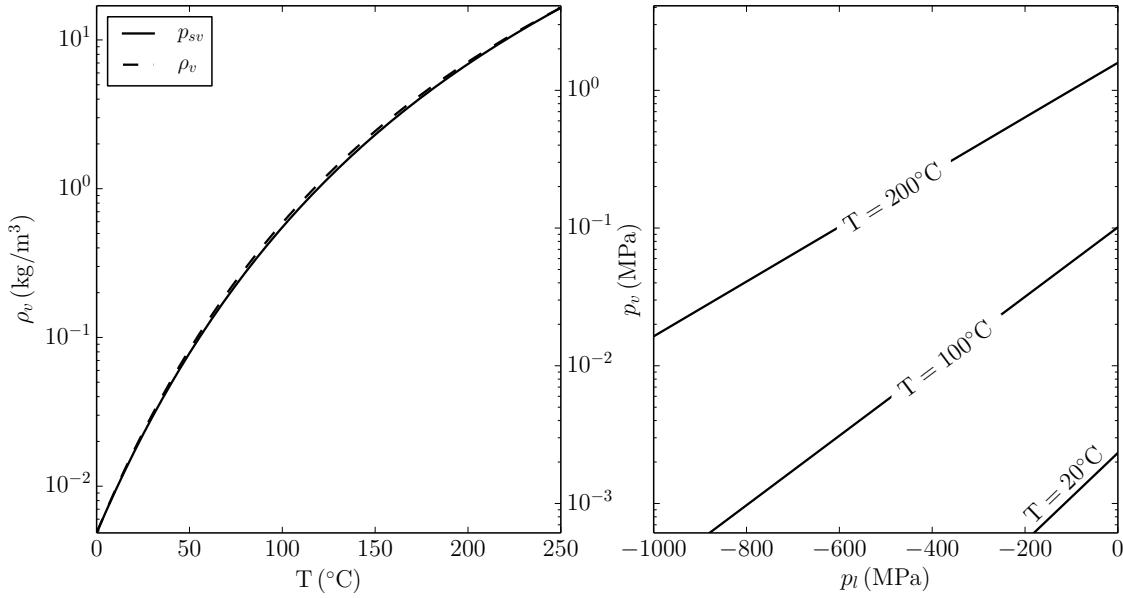
Figure 5.17: Left: temperature dependence of saturating vapour density and pressure (after the experimental measurements of Haar [13]). Right: evolution of liquid and vapour pressure according to Kelvin's law for different temperatures. Note the differences in magnitude among the two fluid pressures.

The density of the vapour phase is given by the ideal gas equation, which depends on temperature and pressure:

$$\rho_v = \frac{M_v}{RT} p_v \tag{5.109}$$

where M_v is the molar mass of the vapour. As previously mentioned, the variations of vapour pressure, which in all cases have as initial value p_{sv}, are very small, and thus so are the changes in density. The previous discussion allows the reasonable simplification $\mathring{m}_{l\to v} \approx 0$ to be applied.

In our analysis, we assume suitable vapour bubble nucleation sites are available, which is likely the case for such a microscopically disordered system as the cement paste. Experimental evidence of cavitation of closed cement paste systems was presented by Lura et al. [190], who measured acoustic emissions of a sealed cement paste and interpreted the signal as the nucleation of gas bubbles.

A certain amount of dry air is likely incorporated in the slurry by agitation at the moment of mixing and later dissolved in the pressurized cement paste, following Henry's law [151]. The effect of the dissolved gas is to lower the initial nucleation barrier and provide additional nucleation sites, facilitating the formation of gas bubbles [191]. We do not account for such effects in the present formulation. We will assume nucleation sites and rates are sufficient as to assure the equilibrium radius is instantaneously given by the Kelvin-Laplace equation throughout the skeleton.

In addition, it is worth noting that we are assuming the liquid to be pure water. In reality, the pore fluid in the cement paste contains a significant amount of dissolved ions. The effect of the pore solution composition on relative humidity has been discussed by Lura et al. [192], who suggest applying a scalar correction factor for the relative humidity. This correction can easily be accommodated in the model.

5.10.3 Mechanical response of a percolated closed system

The consideration of a closed system requires the enforcement of mass balance equations suppressing the exchanges with the exterior, modifying Equation (5.2) as:

$$\dot{m}_c = -\mathring{m}_{c \to h} \tag{5.110a}$$

$$\dot{m}_h = \mathring{m}_{c \to h} + \mathring{m}_{l \to h} \tag{5.110b}$$

$$\dot{m}_l = -\mathring{m}_{l \to h} - \mathring{m}_{l \to v} \tag{5.110c}$$

$$\dot{m}_v = \mathring{m}_{l \to v} \tag{5.110d}$$

$$\dot{m}_a = 0 \tag{5.110e}$$

The water mass exchange rate is given by:

$$\dot{m}_l = (\beta_\alpha + \beta_\phi) \, \rho_l^0 \dot{\alpha} - \mathring{m}_{l \to v} \tag{5.111}$$

where β_α and β_ϕ have been defined in Equation (5.37). In addition, the definition of the liquid mass content $m_l = \rho_l \phi S_l$ allows expressing the rate as:

$$\dot{m}_l = \dot{\rho}_l \phi S_l + \rho_l \dot{\phi} S_l + \rho_l \phi \dot{S}_l \tag{5.112}$$

The consideration of the constitutive law of the ideal liquid:

$$\frac{\dot{\rho}_l}{\rho_l} = \frac{\dot{p}_l}{K_l} \tag{5.113}$$

which leads to the ratio

$$\frac{\rho_l^0}{\rho_l} = \exp\left(\frac{p_0 - p}{K_l}\right) \tag{5.114}$$

where p_0 is the reference pressure for which $\rho_l = \rho_l^0$, i.e. the atmospheric pressure, combined together with Equation (5.111) and Equation (5.112), yield the relation

$$\frac{\rho_l^0}{\rho_l} (\beta_\alpha + \beta_\phi) \, \dot{\alpha} - \frac{\mathring{m}_{l \to v}}{\rho_l} = \frac{\phi S_l}{K_l} \dot{p}_l + \dot{\phi} S_l + \phi \dot{S}_l \tag{5.115}$$

We can now introduce the variation of porosity from Equation (5.105), which considers

porosity changes of all origins. Together with the last expression and the definitions of the individual porosity changes of different nature (Equations (5.37), (5.69), (5.80) and (5.87)), we obtain:

$$
\left[\frac{\phi}{K_l} + \left(\frac{b^2}{K} + \frac{1}{N}\right) S_l\right] \dot{p}_l + \left(\frac{b^2}{K} + \frac{1}{N}\right)(1 - S_l)\dot{p}_g = \frac{b}{K}\dot{\sigma} - \dot{\phi}_{ne} - \\
\left[\beta_\xi + (\beta_\alpha + \beta_\phi)\left(1 - \frac{\rho_l^0}{\rho_l S_l}\right)\right]\dot{\alpha} - \phi\frac{\dot{S}_l}{S_l} - \frac{\dot{m}_{l\to v}}{\rho_l S_l}
\tag{5.116}
$$

where $\dot{\phi}_{ne} = \dot{\phi}_p + \dot{\phi}_v$. Having shown in the previous section that the terms $\dot{p}_g$ and $\dot{m}_{l\to v}$ can be neglected, we can rewrite the last expression as:

$$
\left[\frac{\phi}{K_l} + \left(\frac{b^2}{K} + \frac{1}{N}\right) S_l\right] \dot{p}_l = \frac{b}{K}\dot{\sigma} - \dot{\phi}_{ne} - \left[\beta_\xi + (\beta_\alpha + \beta_\phi)\left(1 - \frac{\rho_l^0}{\rho_l S_l}\right)\right]\dot{\alpha} - \phi\frac{\dot{S}_l}{S_l}
\tag{5.117}
$$

Furthermore, because $S_l = S_l(p_c, \alpha)$, together with Equation (5.51), the previous expression becomes:

$$
\left[\frac{\phi}{K_l} + \left(\frac{b^2}{K} + \frac{1}{N}\right) S_l - \frac{\phi}{S_l}\frac{\partial S_l}{\partial p_c}\right] \dot{p}_l = \frac{b}{K}\dot{\sigma} - \dot{\phi}_{ne} - \\
\left[\beta_\xi + (\beta_\alpha + \beta_\phi)\left(1 - \frac{\rho_l^0}{\rho_l S_l}\right) + \frac{\phi}{S_l}\frac{\partial S_l}{\partial \alpha}\right]\dot{\alpha}
\tag{5.118}
$$

or, equivalently

$$
\dot{p}_l = \tilde{B}\left(\dot{\sigma} - \frac{K}{b}\dot{\phi}_{ne} - \frac{K\phi_\alpha^{eq}}{b}\dot{\alpha}\right)
\tag{5.119}
$$

where

$$
\phi_\alpha^{eq} = \beta_\xi + (\beta_\alpha + \beta_\phi)\left(1 - \frac{\rho_l^0}{\rho_l S_l}\right) + \frac{\phi}{S_l}\frac{\partial S_l}{\partial \alpha}
\tag{5.120}
$$

or also

$$
\phi_\alpha^{eq} = \beta_\xi + (\beta_\alpha + \beta_\phi)\left[1 - \exp\left(\frac{p_0 - p}{K_l}\right)/S_l\right] + \frac{\phi}{S_l}\frac{\partial S_l}{\partial \alpha}
\tag{5.121}
$$

and

$$
\tilde{B} = \frac{b}{\phi\dfrac{K}{K_l} + \left(b^2 + \dfrac{K}{N}\right) S_l - \dfrac{\phi K}{S_l}\dfrac{\partial S_l}{\partial p_c}}
\tag{5.122}
$$

For a viscous and plastically incompressible matrix $-\dot{\phi}_{ne} = \dot{\epsilon}_{ne} = \dot{\epsilon}_v + \dot{\epsilon}_p$ according to Equation (5.57). The expression becomes:

$$
\dot{p}_l = \tilde{B}\left(\dot{\sigma} + \frac{K}{b}\dot{\epsilon}_{ne} - \frac{K\phi_\alpha^{eq}}{b}\dot{\alpha}\right)
\tag{5.123}
$$

Parameter ϕ_α^{eq} is the equivalent porosity change per unit hydration degree, while $\tilde{B}$ corresponds to the effective Skempton coefficient of a partially saturated porous material.

For a saturated material, $\tilde{B}$ simplifies to the well known expression of the Skempton coefficient B [147]:

$$\tilde{B}\left(S_l = 1, \frac{\partial S_l}{\partial p_c} = 0\right) = B = \frac{b}{b^2 + K\left(\dfrac{\phi}{K_l} + \dfrac{1}{N}\right)} \tag{5.124}$$

The interplay of the chemo-hydro-mechanical evolutions and the strongly coupled nature of the closed system is made explicit in Equations (5.119) and (5.123). They clearly show that increments of mean effective stress lead to an increment in pore pressure. The increments of non-elastic strains, or decrease of porosity by non-elastic mechanisms, also increase the pore pressure. Finally, the evolution of hydration reactions will lead to a depletion of the pore pressure mainly because of chemical shrinkage, whose effect is quantified by the parameter β_ξ, depending on the reaction stoichiometry. The effect of the partial saturation, that significantly decreases the observed pore pressure rates, is also encapsulated in the expression.

5.11   Conclusion

We have formulated a comprehensive hydro-chemo-mechanical constitutive model featuring the cement paste as a multi-phase chemically-active open porous medium. The formulation rests on basic physical laws, and the mechanisms involving dissipation sources (heat and mass transport, chemical reactions, viscous and plastic strains) have been formulated in strict respect of thermodynamic principles.

The effect of the hydration degree on the volume fractions of the different cement components is quantified by a simple hydration model. The determination of these volume fractions is essential to the formulation of mechanical models and the coupling of pore pressures and chemical evolutions.

The cement paste chemical shrinkage and pore water consumption during hydration are accounted for in the determination of the macroscopic strains. The coupling among chemical reactions, fluid pressures and stresses is clearly exposed in the formulation.

A water retention curve is introduced to account for the potential desaturation of the material during hydration. The determination of appropriate expressions describing the evolution of the water retention curve will be among the subjects considered in the following chapter.

The mechanical strains of elastic, viscous and plastic nature are described based on physical analogies. The evolution of the poroelastic parameters of the cement paste during hydration is calculated by means of a micromechanical upscaling model. The viscous behaviour is based on the notions of solidification theory. An asymmetric yield surface

with compressive and tensile caps is adopted for the elastoplastic regime, with hardening mechanisms considering both the cumulated plastic deformations and the volume fraction of hydrates.

In summary, the model considers cement paste as a porous medium, chemically active, elastic, viscous, plastic and conceivably partially saturated. Applications to the modelling of experimental observations of the material behaviour from its earliest age are part of the next chapter, in which each of the aforementioned features will be shown to have a decisive role in the description of the behaviour of the material.

5.A Appendix: Derivation of the Asymmetric Cam Clay model

A large number of expressions have been proposed in the literature to represent yield surfaces and flow potentials of plastic materials (see, for instance, the review by Taiebat and Dafalias [193]). However, none of them conforms with all the features we require for the current model, namely: isotropic caps at both traction and compression with vertical tangents, a flexible contractant-dilatant behaviour and real function values for all real stress states.

We propose an alternative to the Modified Cam Clay (MCC) model that fulfils all the previous requirements: the Asymmetric Cam Clay (ACC) model. The model is isotropic and thus expressed in terms of the stress invariants. The MCC model, featuring an elliptic yield surface, is adopted as point of departure. We consider an initial ellipse centered at $\hat{x} = \hat{y} = 0$, but any desired translation can be applied without affecting the results. In order to modify the shape of the ellipse, we will change the scale of the $\hat{y}$ axis multiplying it by a function $\hat{m}(\hat{x})^{1/2}$ to be determined. The result is:

$$\frac{\hat{x}^2}{a^2} + \hat{m}(\hat{x})\frac{\hat{y}^2}{b^2} = 1 \tag{5.A.1}$$

where a and b are the semi-axis lengths over the $\hat{x}$ and $\hat{y}$ coordinates, respectively. With $\hat{m}(\hat{x}) = 1$ we recover an ellipse, while a different value results in a modified curve. We will assume that there is no scaling of $\hat{y}$ at $\hat{x} = 0$, meaning $\hat{m}(0) = 1$. This allows controlling the yield surface width by means of parameter b only. We do not intend to translate the yield surface over the $\hat{y}$-axis. If we now normalize as

$$x = \frac{\hat{x}}{a}; \; y = \frac{\hat{y}}{b} \tag{5.A.2}$$

we can rewrite:

$$x^2 + y^2 m(x) = 1 \tag{5.A.3}$$

The main interest is in displacing the contractant-dilatant threshold (CDT), corresponding to the roots of the equation $y' = 0$. The equation is:

$$y' = \frac{-m(x)^{-1}}{y}\left(x + \frac{(1 - x^2)}{2}m(x)^{-1}m'(x)\right) \tag{5.A.4}$$

Therefore, the roots we have to consider are the solutions to:

$$x + \frac{(1 - x^2)}{2}m(x)^{-1}m'(x) = 0 \tag{5.A.5}$$

from where we get

$$x = \frac{m(x)}{m'(x)} \pm \sqrt{\left(\frac{m(x)}{m'(x)}\right)^2 + 1} \tag{5.A.6}$$

Only the function m and its first derivative have an effect in the displacement of the CDT. We choose to parametrize the CDT displacement by some constant, $\frac{m(x)}{m'(x)} = 1/k$, resulting in $m(x) = C\exp(kx)$, with $C = 1$ from $m(0) = 1$, and hence $m(x) = \exp(kx)$. The normalized yield function is therefore given by:

$$x^2 + y^2\exp(kx) = 1 \tag{5.A.7}$$

The final shape of the surface, presented in Figure 5.18, has all the advantages required for its numerical implementation, while maintaining a physically sound plastic flow rule with vertical tangents at the axis intersections –isotropic traction or compression– and providing the flexibility required to reproduce the real behaviour of complex materials. The equation in stress space has the form:

$$f = \tau^2\exp(kx) + M^2\left(\sigma' - \sigma_c\right)\left(\sigma' + \sigma_t\right) \tag{5.A.8}$$

where

$$x = \frac{2\sigma' + \sigma_t - \sigma_c}{\sigma_t + \sigma_c}, \quad x \in [-1, 1] \tag{5.A.9}$$

and for the displacement of the CDT we can choose values of k. We can note that with $k = 0$ we recover the usual Modified Cam Clay model.

Other possible functions are $m(x) = (1 \pm kx)^{\pm 1}$, which have the same first-order approximation around zero, $m(x) = 1 + kx + O(x^2)$, where $O(x^2)$ is relatively small since $0 \le x \le 1$. We prefer the exponential function, derived directly from the previous analysis. Yet another choice is to set $\tilde{k} = x$ in Equation (5.A.6), i.e. the $\tilde{k}$ parameter is the normalized displacement of the peak:

$$\tilde{k} = \frac{m(x)}{m'(x)} \pm \sqrt{\left(\frac{m(x)}{m'(x)}\right)^2 + 1} \tag{5.A.10}$$
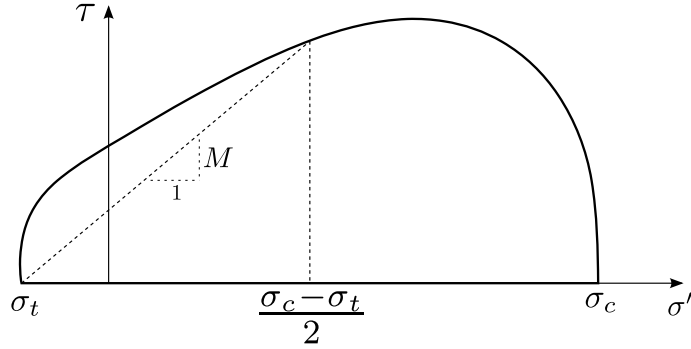
Figure 5.18: Schematic representation of the ACC yield surface.

and therefore $\frac{m(x)}{m'(x)} = \frac{\tilde{k}^2 - 1}{2\tilde{k}}$, with solution $m(x) = \exp\left(\frac{2\tilde{k}}{\tilde{k}^2 - 1} x\right)$. This formulation is also convenient, since we directly control the CDT position.

Regarding the domain convexity, the analysis of the expression reveals that the maximum absolute value of the parameter k to guarantee convexity is:

$$|k| \leq \frac{3\left(\sqrt{3} - 1\right)\left(\sqrt{2\sqrt{3}} - \sqrt{2\sqrt{3} - 3}\right)}{\left(3 - \sqrt{3}\right)^2} \approx 1.612 \tag{5.A.11}$$

5.B   Appendix: Basic poroelastic relations

An isotropic poroelastic material is defined by four poroelastic parameters, from which the remaining parameters can be determined according to the relations discussed, for instance, by Coussy [147] or Ghabezloo [74].

As an example, knowing the parameters K_d, G, K_s and K_u, we can determine E_d, ν_d and E_u, ν_u from the relations of the classical theory of elasticity. The Biot coefficient b is given by:

$$b = 1 - K_d/K_s \tag{5.A.1}$$

while the Skempton coefficient is:

$$B = \frac{1 - K_d/K_u}{b} \tag{5.A.2}$$

or, equivalently:

$$B = \frac{1/K_d - 1/K_s}{(1/K_d - 1/K_s) + \phi\left(1/K_f - 1/K_s\right)} \tag{5.A.3}$$

from which an expression for ϕ can be obtained as a function of the four original parameters:

$$\phi = \frac{(1/K_d - 1/K_s)\left(1/K_u - 1/K_s\right)}{(1/K_d - 1/K_u)\left(1/K_f - 1/K_s\right)} \tag{5.A.4}$$

Furthermore, the Biot modulus N is given by

$$\frac{1}{N} = \frac{b - \phi}{K_s} \qquad (5.A.5)$$

Any other poroelastic parameter might easily be determined from these elementary parameters following similar procedures. It is worth noting that in all our derivations we assume the knowledge of the compressibility of the pore fluid K_f.

Chapter 6

Mechanical behaviour of a cement paste from early age to hardened state: experimental characterization and model applications

6.1 Introduction

This chapter presents the summary and most relevant results of the experimental campaign pursued to characterize the mechanical behaviour of a cement paste from early age to hardened state. All the results discussed in the chapter correspond to the class G cement paste presented in Chapter 2.

The MIP results are first introduced as a tool to describe the evolution of the microstructure of a hydrating cement paste. Specifically, it provides estimates of capillary porosity that will be useful to validate the assumptions of our volume fraction model. In addition, together with water sorption isotherms from the literature, the MIP results will be essential to applications concerning partially-saturated cement pastes, allowing the determination of the evolving water retention curve for a cement paste hydrating at different temperatures.

Regarding the mechanical behaviour of the cement paste, the results of uniaxial and triaxial tests will permit the evaluation of the effect of temperature and pressure on the mechanical properties of the material.

The continuous monitoring of a hydrating cement paste will be discussed according to two complementary techniques. UCA tests will be used to determine the evolution of the

dynamic elastic parameters with hydration, together with the effect of temperature and pressure. In conjunction with STCA tests, they provide experimental information for the verification of the micromechanical model predictions as the hydration reactions advance.

Finally, we present application examples of the mechanical constitutive model, applied to the comprehensive simulation of the STCA tests under various conditions of pressure, temperature and loading paths.

6.2 Microstructure of hydrating cement paste

The MIP experiments provide the pore entry diameter distribution from the evolution of the injected volume of mercury and the applied pressure via the Young-Laplace equation, requiring the assumption of the pore geometry. Brunauer et al. [194] recommend the adoption of cylindrical pores in materials for which the precise pore geometry is unknown. This hypothesis constitutes a reasonable average between completely curved (spherical) and a completely flat (plate) pores. In our calculations, assuming cylindrical pores, the pore entry diameter is given by

$$d = -\frac{4\gamma_{Hg}\cos(\theta_{Hg})}{p_{Hg}} \tag{6.1}$$

where p_{Hg} is the intruding pressure, $\gamma_{Hg} = 0.485$ N/m is the surface tension of mercury and $\theta_{Hg} = 140°$ is the contact angle between mercury and the cement paste skeleton. The values of physical parameters have been adopted from the literature for a temperature of 25°C [99].

The results of MIP tests performed at different ages on a cement paste hydrated at 7°C are shown in Figure 6.1. The wide range of hydration degrees, spanning from 20 to 80%, is reflected in the dramatic change of the pore network of the cement paste. The total porosity, as measured by MIP, decreases nearly 30% as a result of the progressive filling of the pores by hydration products. The initial value is in agreement with the total porosity of the completely anhydrous cement paste, for which $\phi = w/(w + 1/\rho_c) = 0.59$.

The pore families are best identified in the derivative plane. For very young cement pastes, a pore family with micrometric diameter clearly dominates the pore network. A second bump, corresponding to a pore size in the order of the tenth of micron, is also visible. We observe a gradual reduction of the threshold injection diameter, interpreted as the minimum diameter present throughout the specimen, as a result of the hydration reactions. The progressive refinement of the pore space results in the shift of the dominant pore entry size towards smaller pore sizes. The large micrometer-sized pores are completely absent in extensively hydrated cement pastes. Analogous observations can be made regarding the MIP results of the cement paste hydrated at 20°C, shown in Figure 6.2.
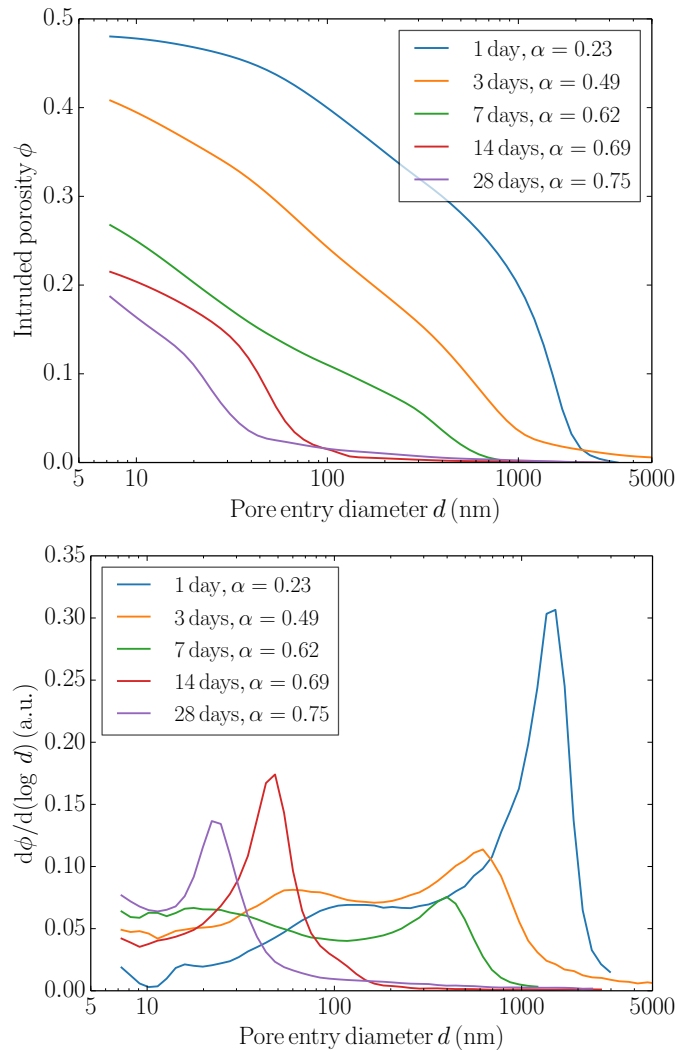
Figure 6.1: Results of MIP tests performed at different ages on a cement paste hydrated at 7°C.

The results are in agreement with the observations of Cook and Hoover [195] and Windslow and Diamond [196], who assessed both the effect of age and water to cement ratio. From the analysis of their results, we can conclude that the expected change in pore diameter distribution due to higher water content can be assimilated to a lower hydration degree by considering the modified transformed fraction.

The MIP results also allow the estimation of the capillary porosity, which can be compared to the predictions of our model for the volume fractions of cement paste presented in Section 5.3.1. Regarding the limiting pore size of capillary pores, the model of Jennings and co-workers [33, 90] adopts a lower limit threshold of 10 nm, corresponding to 35 water molecule diameters. In larger pores, the water is assumed to be in its capillary state. It is interesting to note that there is a single dominating pore family for mature cement
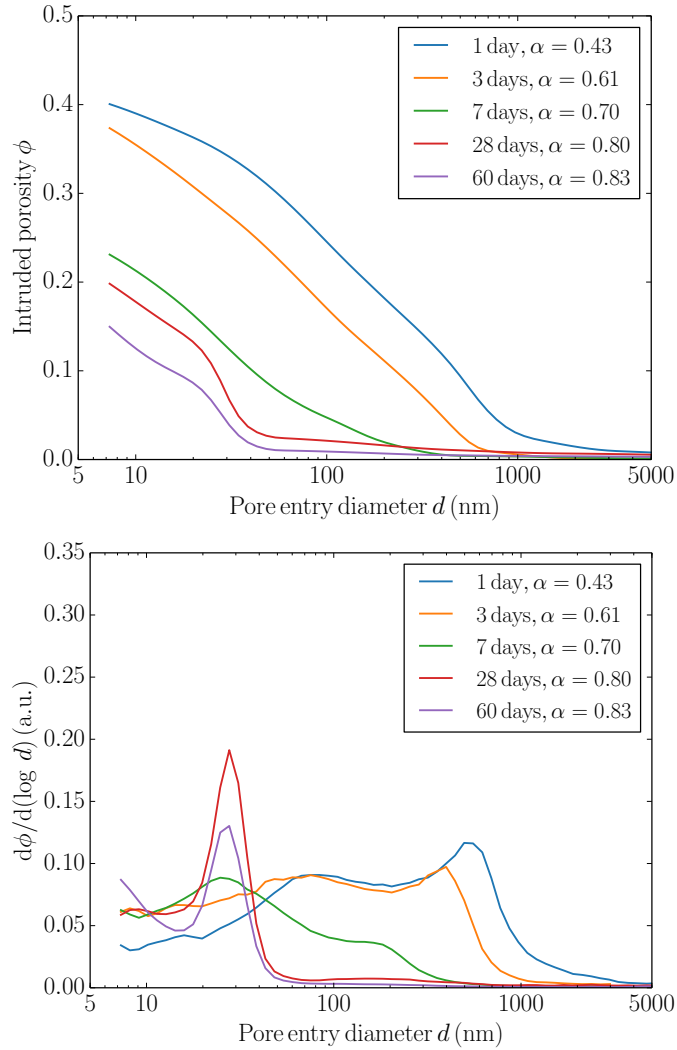
Figure 6.2: Results of MIP tests performed at different ages on a cement paste hydrated at 20°C.

pastes, with a diameter in the vicinity of 10 nm, that must therefore correspond to the main capillary pore network.

The capillary porosity determined from MIP at a pore entry diameter of 10 nm is presented in Figure 6.3, together with the prediction of our volume fraction model. The model adequately captures the change in capillary porosity, which excludes all hydrates intrinsic porosity.

For high hydration temperatures, capturing the evolution of the pore structure with MIP requires arresting the hydration very precisely. Indeed, because the hydration rate is exponentially accelerated by temperature, the evolution of the microstructure is very fast, hindering the observation of gradual changes. Besides, the rapid cooling of early-age samples hydrating at high temperature comes with considerable risk of damaging the fragile
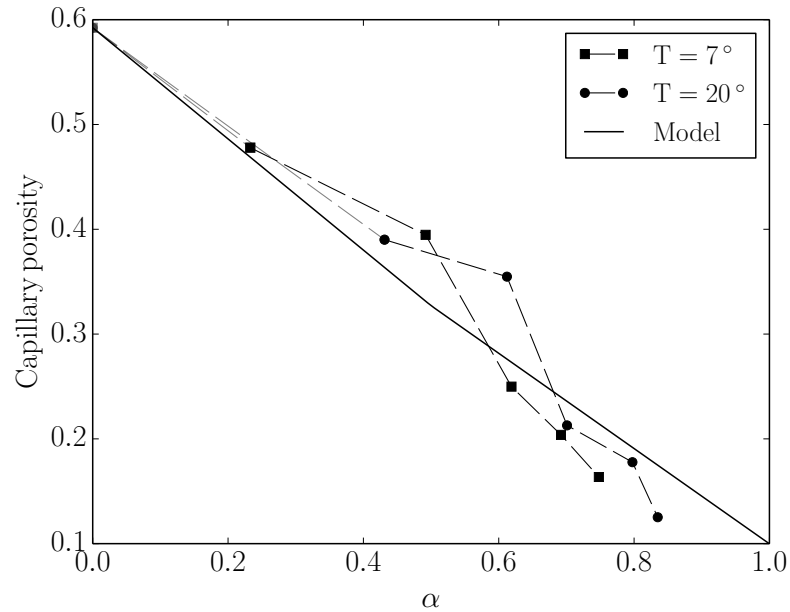
Figure 6.3: Capillary porosity as a function of hydration degree. Marks correspond to experimental observations determined from MIP and solid lines are model results. Dashed lines are drawn to guide the eye. Threshold pore diameter is 10 nm [1, 33].

microstructure. In any case, the changes are expected to follow trends similar to those obtained at lower temperatures, despite the differences in the final distributions, to be discussed in the following.

The results of MIP for mature cement pastes hydrated at different temperatures are presented in Figure 6.4. All the samples are 28 days old, with hydration degrees between 77 and 85%. There is a slight increase in the total MIP porosity with temperature for cement pastes hydrated up to 40°C, with a dominating pore family in the range of tens of nanometers. The differences become more significant for higher temperatures (60 and 90°C), for which the total MIP porosity is greater and the dominating pore family is shifted towards larger diameters, reflecting the coarsening of the pore network. The increase of porosity is in agreement with the experimental results reported in the literature [134]. Gallucci at al. [104] concluded that the higher porosity and more open porous network observed in cement pastes hydrated at higher temperature are the consequence of denser hydration products. The effect of temperature on the capillary porosity can be assessed in Figure 6.5, where the increase of the capillary pores is apparent. The volume fraction model estimate corresponds to an average hydration degree. Although the model could account for the variation of density and its effect on the volume fractions, we neglect such variations and consider equal parameters for all temperatures for the sake of simplicity.

Regarding hydration pressure, Bresson et al. [139] observed no effect of pressures up to 100 MPa on the microstructure of alite pastes. MIP experiments of cement pastes
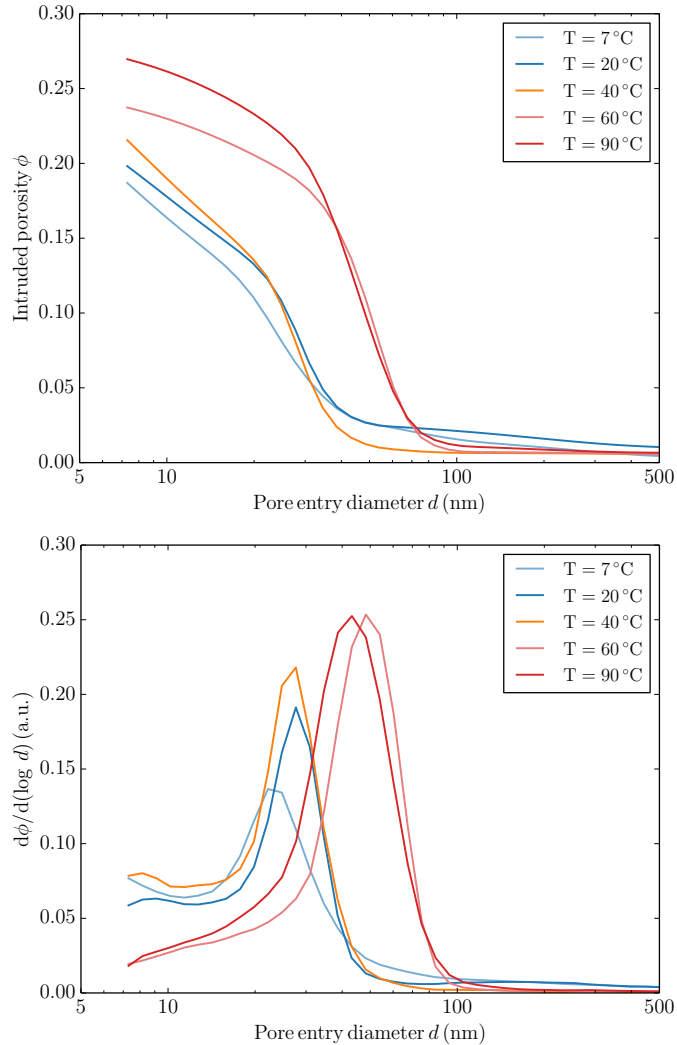
Figure 6.4: Results of MIP tests performed on cement pastes hydrated at different temperatures. All specimens are 28 days old.

hydrated at different pressures show no appreciable change in the injection curves [8]. As an explanation, we propose to consider the effect of pressure from two different perspectives. First, from a reaction-rate point of view, we have seen in Chapter 4 that the hydration kinetics acceleration due to a 5 MPa increment of pressure is roughly equivalent to a 1°C increment of temperature. In consequence, if the microstructural effects of pressure were associated to hydration kinetics, they would be significantly smaller than those due to temperature. Postulating an equivalence of pressure and temperature is, in any case, only a first order approach, but provides an initial estimate of the order of magnitude of the changes to be expected. Second, if considered in a poromechanical framework, it is the effective pressure, rather than the total external pressure, that could potentially have an effect on the microstructure. Under controlled external pressure, the pore pressure is the only variable responsible for changes of effective stress. The changes of pore pressure, however,
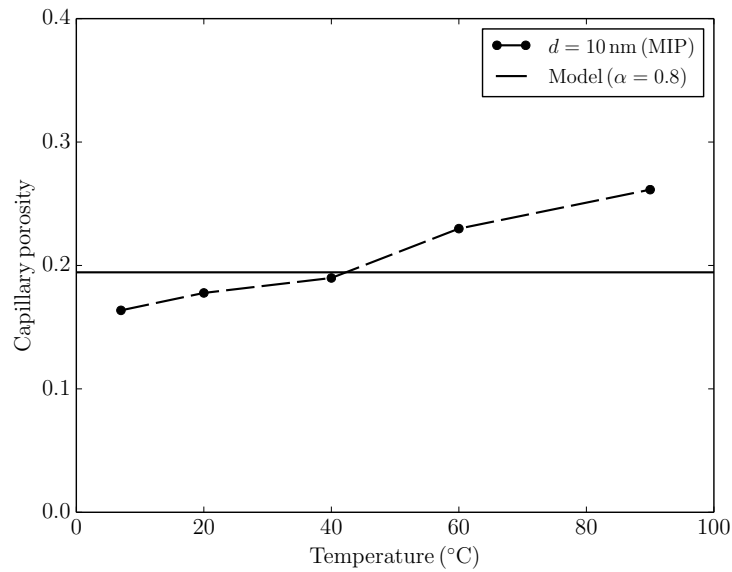
Figure 6.5: Capillary porosity of mature cement pastes hydrated at different temperatures. Marks correspond to experimental observations determined from MIP and solid lines are model results. Dashed lines are drawn to guide the eye. Threshold pore diameter is 10 nm [1, 33]

are not sufficient to generate stresses capable of significantly changing the microstructure (see Section 6.8).

6.3 Water retention curve of hydrating cement paste

As discussed in Section 5.5.2, the water retention curve (WRC), relating the saturation degree to the capillary pressure, is necessary for the determination of the effective stresses in a partially saturated porous medium. In the current section, we present and discuss experimental and modelling procedures that help describe the WRC of a cement paste from its earliest age and the effect of the hydrating conditions, notably temperature, on the water retention properties of the hardened material.

The WRC of a hardened cement paste can be determined from the water sorption isotherm (WSI), obtained from the measurement of equilibrium moisture contents corresponding to different relative humidities [197]. In the following applications, we present the WRC determined from the desorption branches of the WSI following Kelvin's equation (Equation (5.39)) although other approaches considering the multilayer adsorption of water molecules are preferred at low relative humidities (see, for instance, [197, 198]). Hysteresis effects are not considered.

Yavari [14] and Bahafid [15] have determined the WSI of mature samples of our class G cement for hydrating temperatures of 7, 20, 60 and 90°C following a gravimetric procedure.

The relative humidity inside a sealed desiccator was controlled by means of saturated salt solutions, and the mass exchanges of the cement paste samples were recorded for a minimal equilibrium time of 4 months, after which the changes in water content became negligible. In all cases, the environment temperature was 20°C. The samples, circular discs of 10 cm diameter and 4 mm thickness, are large enough as to remain representative of the average material properties while conserving a short drainage path that demanded reasonable equilibration times.

Figure 6.6 presents the WRCs for the four temperatures and the results of a non-parametric regression fit (dashed lines). We note the similarity between the curves determined at 7 and 20°C, confirming the small effect of temperature on the paste microstructure at the lower range of temperatures. At higher hydrating temperatures (60 and 90°C), however, the effect of the curing conditions on the paste microstructure becomes more significant. The very large capillary pores resulting from the densification of the solid skeleton cause a significant decrease in saturation with a negligible capillary pressure. The effect is enhanced by higher curing temperature.
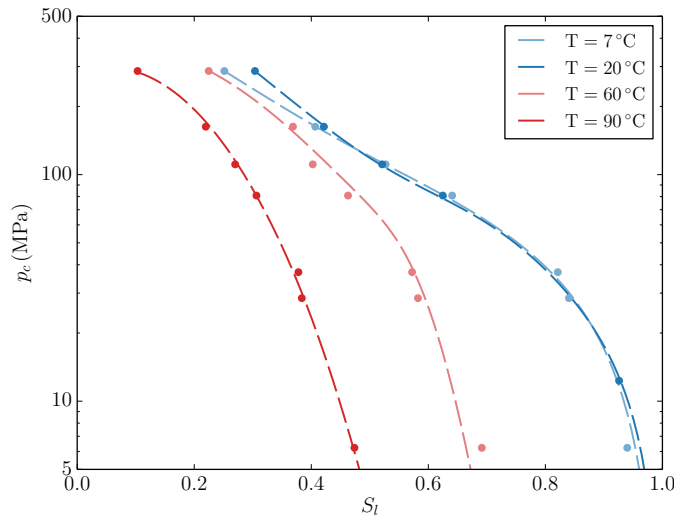
Figure 6.6: Water retention curves determined from water sorption isotherms for cement paste hydrated at different temperatures. Marks correspond to experimental observations and dashed lines are non-parametric regressions. After refs. [14, 15].

Water sorption isotherms, based on the thermodynamic equilibrium of adsorbed and vapour water, typically require a significant time to attain equilibrium configurations, mainly due to the size and low permeability of the samples. The determination of the WRC from WSI is therefore only appropriate for a thoroughly hydrated cement paste, where negligible microstructural changes are expected due to chemical reactions. Indeed, unless the hydration is arrested or significantly slowed down, the water vapour transport times are considerably larger than hydration reaction characteristic times. As a result, the WSI does not reflect the instantaneous microstructure of an early-age cement paste

because of the gradually progressing reactions. To overcome this inconvenience, we propose to calculate the WRC curve from the MIP results.

The emptying of water-filled pores of a cement paste in desorption and the filling of pores by mercury in MIP are similar in their principle of invasion of the pore space by a non-wetting fluid [84]. The determination of the WRC from MIP tests is based on the analogy that can be drawn between the roles of air in water depression and mercury in MIP. The procedure has been applied before in the field of soil mechanics as a mean to determine water retention properties of fine-grained materials [199]. The capillary pressure in the water-air interface can be related to that of the air-mercury interface by:

$$p_c = -\frac{\gamma_w \cos(\theta_w)}{\gamma_{Hg} \cos(\theta_{Hg})} p_{Hg} \tag{6.2}$$

from which the determination of the WRC is straightforward since the intruded porosity is known for each pressure level.

The experimental results of MIP tests performed at different ages and the WSI of mature cement pastes at 7 and 20°C are translated to their corresponding WRCs in Figure 6.7. As the hydration advances, there is a consistent tendency of increase of the pore entry pressure and the capillary pressure at constant saturation degree, a clear consequence of the pore structure refinement. The asymptotic evolution of the MIP-based curves towards the ultimate WSI-based WRC determined for advanced age gives confidence in the compatibility among both procedures.

6.3.1 Modelling of the evolving water retention curve

According to the van Genuchten (VG) expression (see Section 5.5.2), the capillary pressure is given by:

$$p_c = p_r \left(S_r^{\frac{n}{1-n}} - 1 \right)^{\frac{1}{n}} \tag{6.3}$$

where p_r is a reference pressure and $n > 1$ is a fit parameter. The result of fitting the VG model parameters p_r and n to the WRCs for cement pastes hydrated at 7 and 20°C is depicted in Figure 6.7. The evolution of the fitted model parameters with hydration degree is shown in Figure 6.8. From the optimal fit, shown in grey, we can appreciate the very small changes of parameter n with hydration. It seems therefore reasonable to neglect the dependency of n with respect to the reaction evolution and adopt a constant value. On the other hand, parameter p_r shows a significant dependency on α. A simplified fitting routine, considering n constant, is shown in the same figure. The evolution of parameter p_r can be very well estimated with an exponential function of the form $p_r = p_r^0 \exp(k_\alpha \alpha)$,
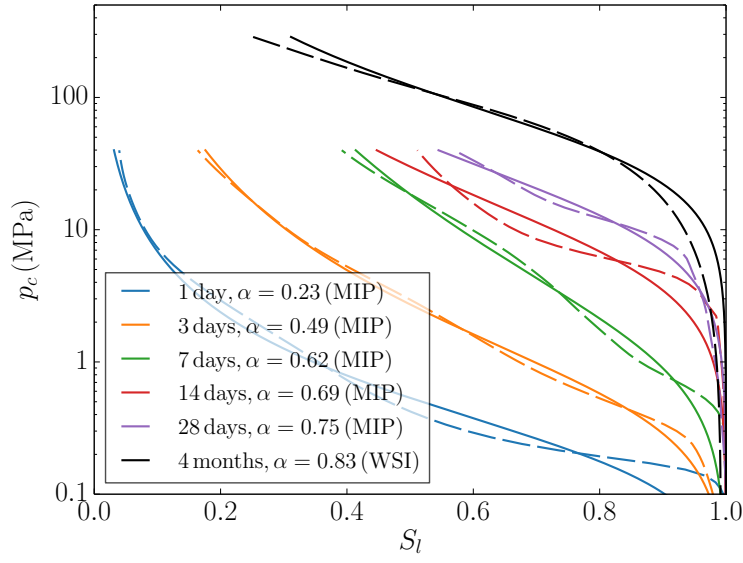
(a) Hydration temperature of 7°C
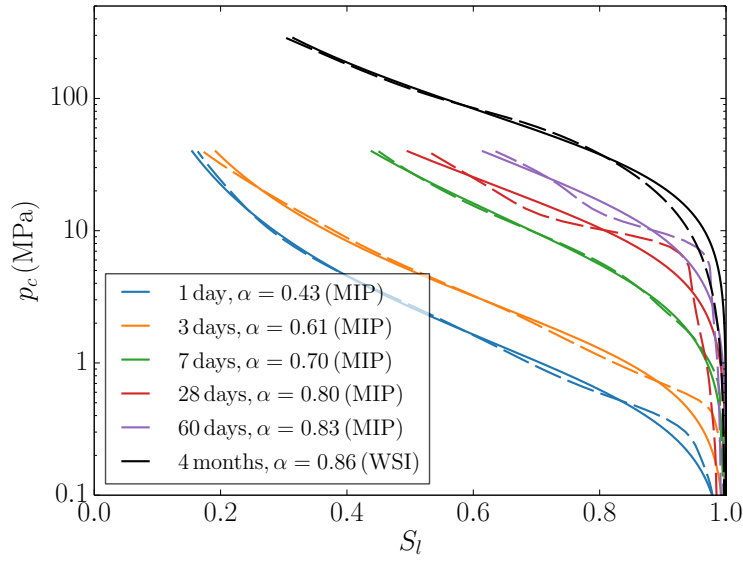
(b) Hydration temperature of 20°C

Figure 6.7: Water retention curves evaluated from MIP at different ages and from WSI for a mature cement paste. Dashed lines correspond to experimental results, while solid lines correspond to model.

the final expression therefore being

$$p_c = p_r(\alpha) \left(S_r^{\frac{n}{1-n}} - 1 \right)^{\frac{1}{n}} = p_r^0 \exp(k_\alpha \alpha) \left(S_r^{\frac{n}{1-n}} - 1 \right)^{\frac{1}{n}} \tag{6.4}$$

For cement pastes cured at 7 and 20°C, we determined $n = 1.48$, $p_r^0 = 0.011$ MPa and $k_\alpha = 9.24$.
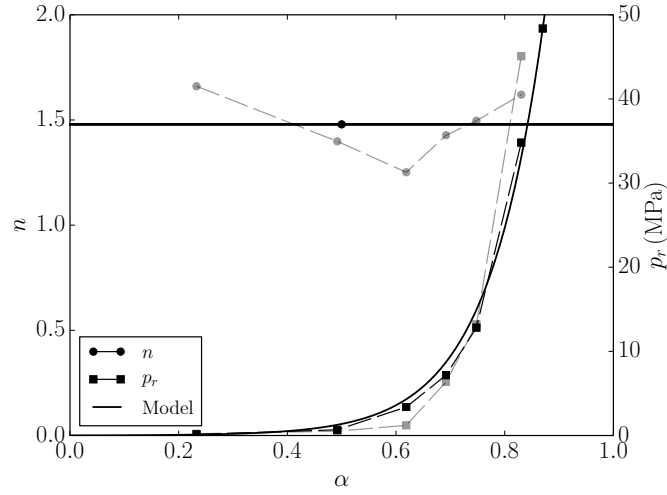
(a) Hydration temperature of 7°C
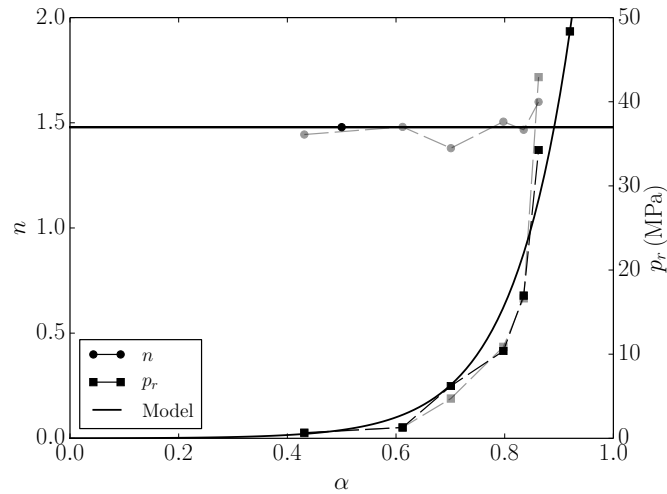
(b) Hydration temperature of 20°C

Figure 6.8: Evolution of the fitting parameters of the VG model with hydration degree. The grey marks correspond to best fits when model parameters n and p_r are both free. Black marks correspond to the best fits assuming a constant value of n. Solid lines correspond to model predictions from Equation (6.4). Dashed lines are guides to the eye.

The evolution of the model WRC is depicted in Figure 6.9. According to the previous expression, the separation among WRCs is directly proportional to the hydration degree in a logarithmic scale:

$$\ln(p_c) = k_\alpha \alpha + f(S_l) \tag{6.5}$$

where $f(S_l) = \ln \left[p_r^0 \left(S_r^{\frac{n}{1-n}} - 1 \right)^{\frac{1}{n}} \right]$. All the WRCs are geometrically identical, separated by a factor $k_\alpha \Delta \alpha$, where $\Delta \alpha$ is the difference of hydration degree.

So far, we have considered the effect of hydration degree on WRCs for cement pastes
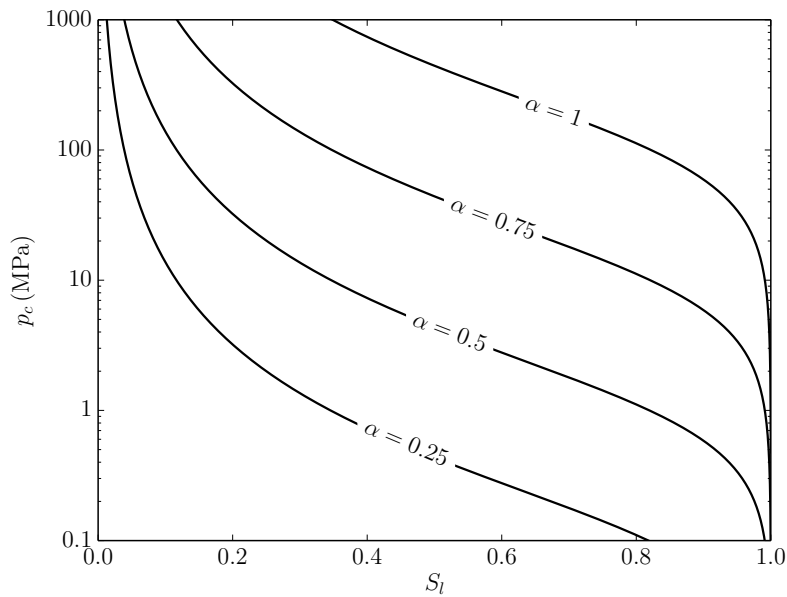
Figure 6.9: Evolution of the water retention curve for hydration temperatures between 7 and 20°C.

hydrated at relatively low temperatures (7 and 20°C). For higher hydration temperatures, however, we do not dispose of MIP results for significantly different hydration degrees, for the reasons mentioned in the previous section.

For mature cement pastes hydrated at high temperatures, the large capillary pores that permeate the material result in significant desaturation at negligible capillary pressure, as seen in Figure 6.6. A saturation degree in the order of 70% is necessary in order to reach capillary pressures significant enough to produce non-negligible mechanical effects on the cement skeleton. In traditional cement paste mixes –even for mixes with low water to cement ratios– such low degrees of partial saturation are not attainable by water consumption due to hydration.

In addition, it is reasonable to suppose that the WRC determined from WSI for a mature cement paste corresponds to the asymptotic WRC for the hydrating cement paste, in agreement with the trends observed at lower temperatures. Hence, for any given hydration condition, we expect a lower capillary pressure at identical degree of saturation for a lower degree of hydration.

As a result of the previous observations, we do not expect significant stresses to develop in a cement paste hydrating at high temperature when no exchanges with the exterior are allowed. Furthermore, even if drying due to external action is expected, the usual characteristic times of such drying processes are much larger than the characteristic times for hydration reactions at high temperature. In all practical applications, therefore, the final WRC, as determined from WSI, will be sufficient for describing the effect of partial

saturation at high temperatures.

In oil well applications, in particular, reaching the low saturation levels required to produce significant capillary pressures in cement pastes hydrated at high temperatures is very unlikely, given the usual service conditions of high depths and, hence, high fluid pressures. Therefore, the consideration of stresses associated to partial saturation for cement pastes hydrated at high temperatures –above 60°C– does not seem necessary. For intermediate temperatures between 20 and 60°C we suggest the interpolation of the model results.

6.3.2 Consequences for permeability

The VG curve has the additional advantage of being integrable if considered in Mualem's expression of relative liquid permeability [200]. Therefore, knowing the evolution of the WRC through the VG expression, we can obtain an analytical expression describing the evolution of the relative water permeability of the cement paste. According to Mualem [200], the ratio of liquid permeability k_l for the VG model is given by:

$$\frac{k_l(S_l)}{k_l(1)} = S_l^{1/2} \left[1 - \left(1 - S_l^{\frac{1}{m}} \right)^m \right]^2 \tag{6.6}$$

where $m = 1 - 1/n$. The validity of Mualem's relative permeability expression has been verified by Savage and Janssen for mature concrete [201]. The same expression has been applied for the modelling of cement paste permeability by other authors [163, 202, 203]. Following our determination of the model parameters, an important prediction deriving from the previous result is that, because n is independent of hydration degree, the relative permeabilities are insensitive to variations of hydration degree, at least to a first approximation. The measurements of permeability of a mature paste, simpler to perform than those on a hydrating cement paste, can therefore serve to estimate the relative permeability of a hydrating partially saturated cement paste. A similar conclusion can be drawn regarding gas transport, for which relative permeability can be estimated by [204]:

$$\frac{k_g(S_l)}{k_g(1)} = (1 - S_l)^{1/2} \left(1 - S_l^{\frac{1}{m}} \right)^{2m} \tag{6.7}$$

which can be considered independent of hydration degree as a first approximation. These estimates remain to be verified experimentally.

6.4 Evaluation of the poroelastic parameters of a mature cement paste from triaxial tests

In this section, we present and discuss the results of poromechanical tests performed on mature cement pastes hydrated at 7°C. Following a similar testing campaign, a complete set of poroelastic parameters was determined by Ghabezloo [18] for the same cement paste hydrated at 90°C. The current work hence extends the results to a lower range of temperatures, likely also valid for standard room temperatures in the order of 20°C.

6.4.1 Drained isotropic compression tests

The drained bulk modulus K_d, given by the slope in the volumetric strain – effective confining stress plane, can be directly determined from drained isotropic compression tests (see Chapter 5). In the first test TX - D1, a complete loading-unloading cycle was performed to assess the reversibility of the strains. Test TX - D2 serves to confirm the repeatability of the measurements. The remaining tests have a much smaller load amplitude, and provide evaluations of the bulk moduli as a function of the effective stress under diverse conditions of confining and pore pressure.
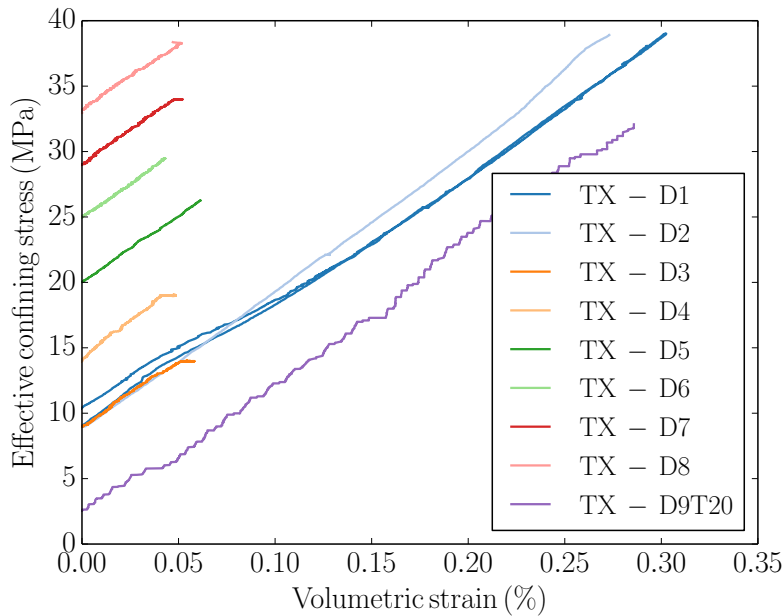
Figure 6.10: Effective confining stress – volumetric strain curves for drained isotropic tests. The slopes correspond to drained bulk modulus K_d. TX - D9T20 corresponds to hydration at 20°C.

The drained bulk modulus K_d determined over load intervals of 5 MPa are presented as a function of the effective stress in Figure 6.11. The overall insensitivity to effective stress leads us to postulate the independence of the drained bulk modulus with respect to the

Terzaghi effective stress in the range of values considered in the present study, i.e. below 40 MPa. We therefore adopt the average value $K_d = 10.5$ GPa.
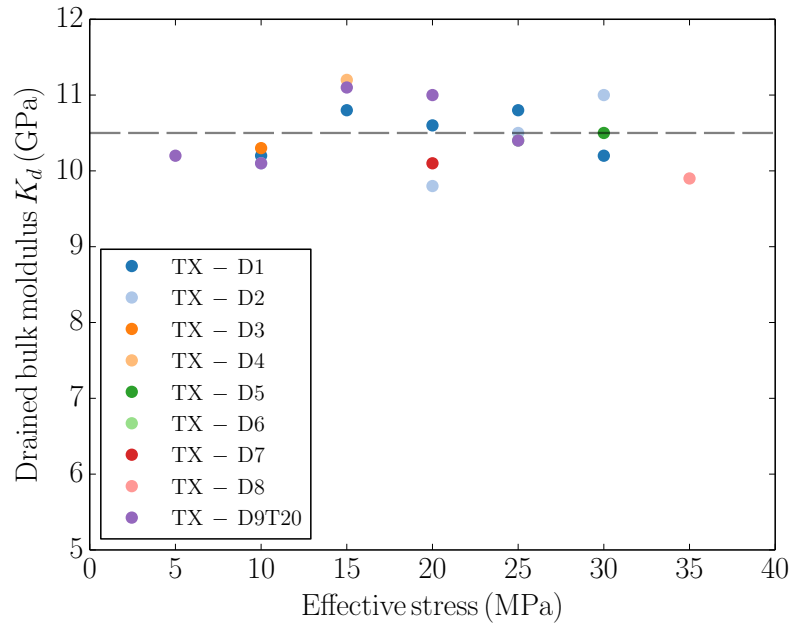

Figure 6.11: Effective confining stress – drained bulk modulus K_d. The dashed line corresponds to the average.

In addition to the evaluation of the bulk modulus for cement pastes hydrated at 7°C, an isotropic drained test was performed on a cement paste hydrated at 20°C and tested at the same temperature (TX - D9T20). The measured bulk modulus is $K_d =$ 10.6 GPa, thus leading to conclude, as expected, that the elastic properties do not change significantly in this reduced range of temperatures. This result suggests that the poromechanical properties determined in the current section are applicable to the same cement paste hydrated at room temperature.

6.4.2 Undrained isotropic compression tests

The undrained isotropic compression tests provide the undrained bulk modulus K_u, given by the slope in the volumetric strain – confining stress plane (see Chapter 5). In addition, if the pore pressure increase is measured, the Skempton coefficient B can be determined from the variations of pore pressure as a function of confining stress.

The two undrained tests TX - UD1 and TX - UD2 were performed over large loading cycles of 16 MPa, with the same initial confining pressures but different pore pressures. The results, presented in Figures 6.12 and 6.13, confirm the excellent repeatability of the measurements.

From the inspection of the experimental results, we can assume the undrained bulk
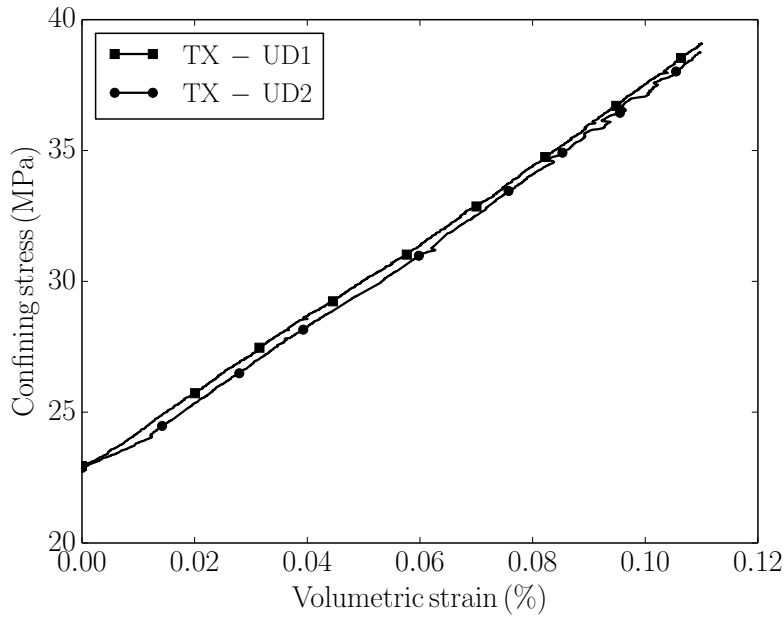
Figure 6.12: Confining stress – volumetric strain curves for isotropic undrained tests. The slopes correspond to undrained bulk modulus K_u.
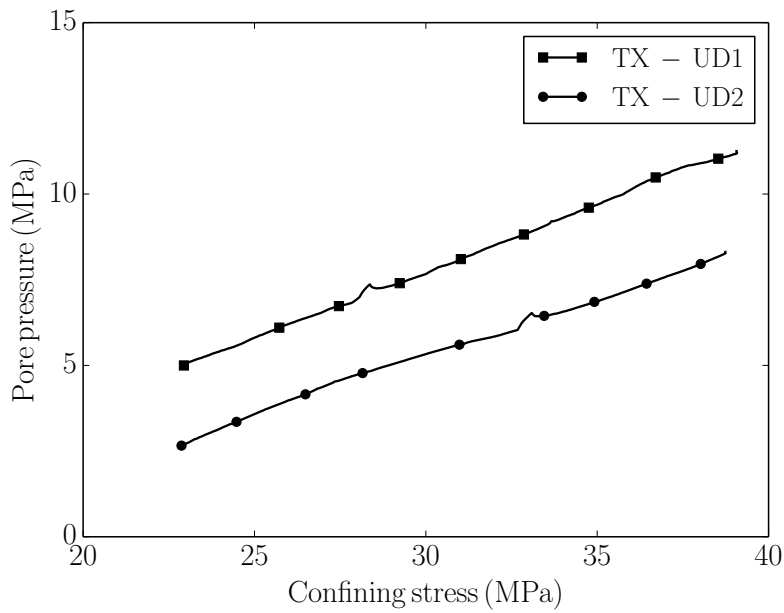

Figure 6.13: Confining stress – pore pressure curves for isotropic undrained tests. The slopes correspond to Skempton coefficient B.

modulus is independent of the confining stress, as done before for the drained modulus. The average value of the undrained bulk modulus determined over the complete loading path for both tests is $K_u = 14.5$ GPa. Regarding the Skempton coefficient, the average value is $B = 0.36$.

6.4.3 Unjacketed isotropic compression tests

The unjacketed isotropic compression tests serve to measure the bulk modulus of the solid phase K_s, given by the slope in the volumetric strain – confining stress plane (see Chapter 5).[1]

The two unjacketed tests TX - UJ1 and TX - UJ2 were performed over large loading cycles of 15 and 19 MPa respectively, with different initial confining and pore pressures (11 and 5 MPa, respectively). The results, presented in Figure 6.14 display an excellent agreement between the two measurements.
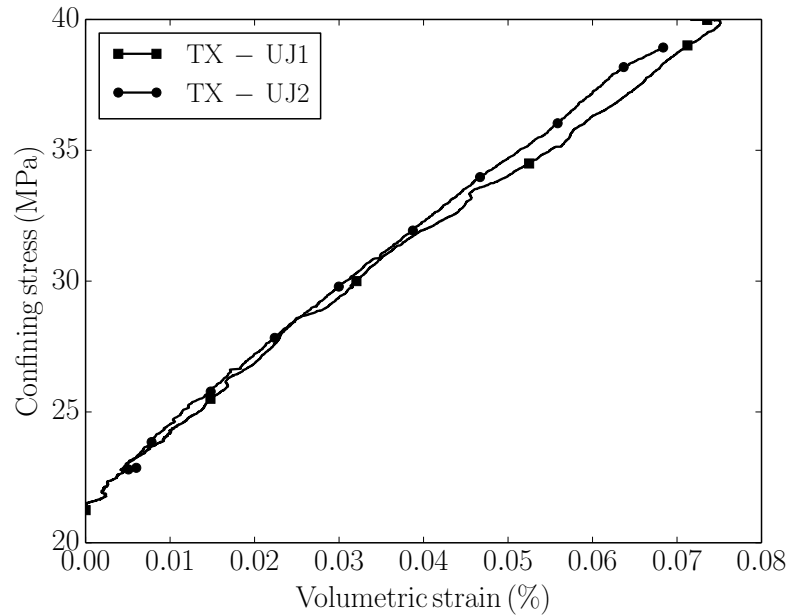
Figure 6.14: Confining stress – volumetric strain curves for isotropic unjacketed tests. The slopes correspond to solid bulk modulus K_s.

From the inspection of the experimental results we can, as before, assume the matrix response as independent of the confining stress. The average value of the solid bulk modulus determined over the complete loading path for both test is $K_s = 24.6$ GPa.

An important observation, already anticipated in the formulation of the constitutive model (Section 5.5.3), is the complete reversibility of the strains. As a result, we conclude that the solid phase behaves perfectly elastically in the range of stresses considered, as was shown to be the case for the same cement paste hydrated at higher temperature by Ghabezloo [18].

---

[1]In addition, if the changes in pore volume are measured, the Biot coefficient b can be determined. This requires, however, a large number of corrections regarding fluid and measurement system compressibility as well as changes in temperature. In the present work, we do not attempt this determination.

6.4.4 Deviatoric tests

The drained Young's modulus E_d and shear modulus G can be determined from drained deviatoric compression tests. It is important to note that in our experimental setup the determination of E_d relies on the measurements of the 2 axial LVDTs, since only the axial strain is required in its calculation. On the other hand, the shear modulus G depends on the information collected by all 6 LVDTs, since both axial and radial strains intervene in its calculation. Therefore, moduli E_d and G are independent experimental measurements .

The experimental curves of axial strains and stresses are presented in Figure 6.15, while the deviatoric strains and stresses can be observed in Figure 6.16. Tests TX-DV1 and TX-DV2 provide evidence of the repeatability of the experiments. Together with the remaining test, the results suggest an independence of the shear modulus with regards to the effective stress.

For all cyclic tests, the unloading phase exhibits the hysteresis loops already observed by Ghabezloo [18] and Vu [153] and attributed to creep strains. In a simplified analysis, we disregard such effects and will determine the drained Young modulus E_d and shear modulus G from the approximately linear response observed during the loading phases, over a load amplitude of at least 5 MPa. From the experimental results, we determine the average values $E_d = 20.6$ GPa with minimum and maximum values of 19.1 and 22.4 GPa respectively. Regarding the shear modulus, we obtain an average of $G = 7.3$ GPa with a minimum of 6.9 GPa and a maximum of 7.9 GPa.
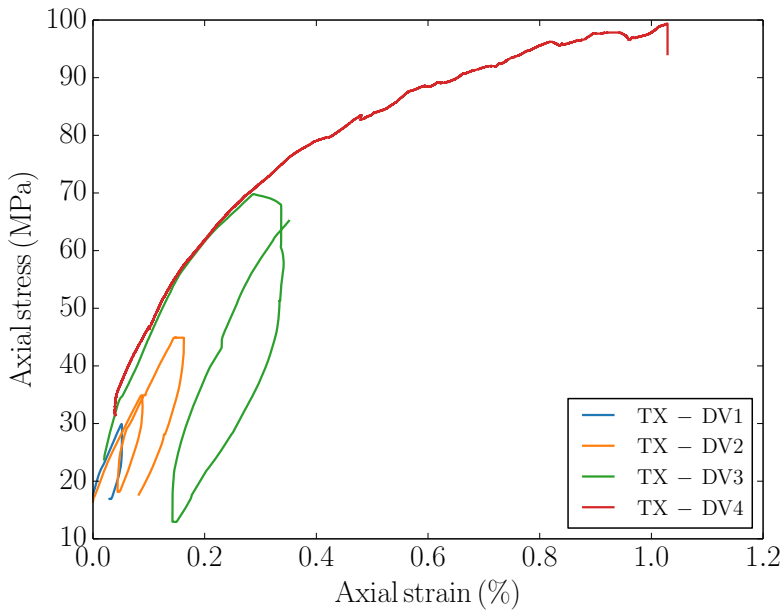

Figure 6.15: Axial stress – axial strain curves for drained deviatoric tests. The slopes in the linear loading response correspond to the drained Young modulus E_d.
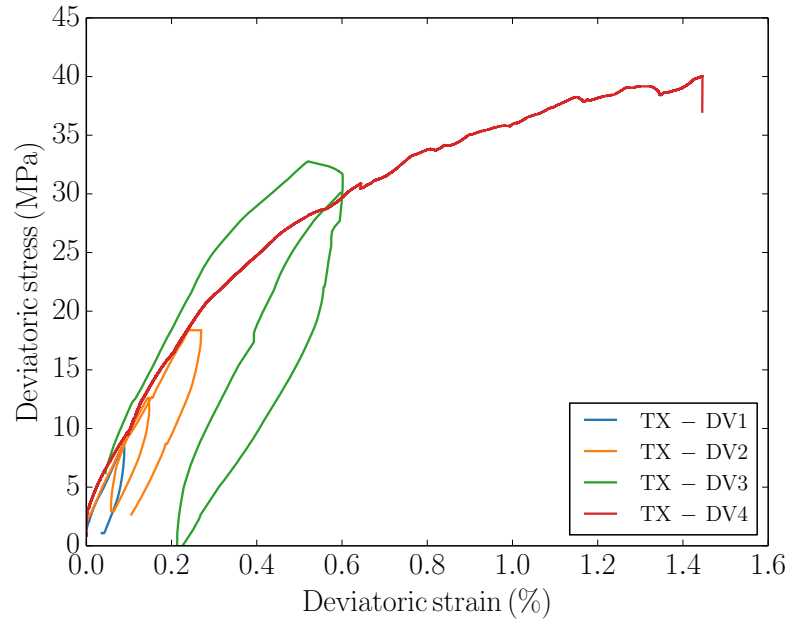
Figure 6.16: Deviatoric stress – strain curves. The slopes in the linear loading response correspond to the shear modulus G.

The existence of a yield stress and the generation of plastic strains is evidenced by the large loading cycle from TX - DV3. The yield stress for an initial effective confining stress of 5 MPa is in the order of $\tau = 25$ MPa, followed by a significant change in the shear stiffness. A similar inspection of test TX - DV4 suggests a yield stress of $\tau = 20$ MPa for an initial effective confining stress of 25 MPa. These results are in agreement with the assumption of Thiercelin et al. [205], Vu [8] and Agofack [16], who assumed a compressive cap for the yield surface, and not a purely Mohr-Coulomb or Drucker-Prager-type yield criteria, for which a monotonously increasing yield stress is predicted for increasing effective confining stress.

6.4.5 Compatibility analysis and determination of optimal set of poroelastic parameters

The complete set of experimentally-determined poroelastic parameters is presented in Table 6.1. We assume, based on the experimental evidence, that these properties are independent of the stress conditions, and thus remain valid for the entire poroelastic domain.

We now set to answer the impending question: *is there a set of compatible poroelastic parameters in agreement with the experiments?* If this is the case, we can apply the poroelastic framework for the modelling of cement paste, as done by Ghabezloo [74].

The description of the hydro-mechanical response of an isotropic poroelastic material

Table 6.1: Summary of poroelastic parameters determined from experiments, optimization and upscaling via the homogenization model with $\alpha = 0.85$.

Parameter	Value			Unit
	Experimental	Optimized	Upscaled	
K_d	10.6	11.1	12.1	GPa
K_s	24.6	24.9	22.1	GPa
K_u	14.5	13.9	14.2	GPa
G	7.3	7.9	7.2	GPa
E	20.6	19.2	18.0	GPa
B	0.36	0.36	0.33	-
$\nu_d{}^*$	0.22	0.21	0.25	-
ϕ^{**}	0.16	0.21	0.19	-

* Experimental value calculated from K_d and G.
** Experimental value from MIP.

requires four parameters: three bulk volumetric and one deviatoric moduli. A summary of some of the basic relations we used in the present discussion is available in Section 5.B. The determination of an optimal set of parameters is achieved by assuming a set of four basic parameters and deriving the remaining ones from this departure hypothesis. The application of an error-minimization algorithm yields a compatible and optimal set of poroelastic parameters, presented in Table 6.1. There is an excellent agreement between the experimental and optimized sets of poroelastic parameters, suggesting the overall compatibility of our triaxial experiments. In applications concerning the mechanical behaviour of a hardened cement paste, we consider the optimized values constitute a reliable set of poroelastic parameters in this range of curing temperatures and pressures.

It is interesting to note the difference among the porosity as measured from MIP (Figure 6.5) and the porosity determined from the poroelastic experiments (Table 6.1, according to the expression from Appendix 5.B). As discussed in Section 6.2, the MIP injection can only penetrate the capillary pores, and therefore does not include gel water. The slightly larger porosity derived from poroelastic parameters suggests there is a fraction of the gel porosity actively transporting pore fluid during the elastic loadings, i.e. quasi-instantaneously. This is in agreement with the hypothesis we have adopted in our mechanical model formulation (see Section 5.3.2), where we considered a fraction of the LD C–S–H porosity as active in fluid exchanges, in agreement with the Jennings model [1]. We therefore naturally expect the poroelastic active porosity to be larger than the capillary porosity. In general, however, the estimation of the poroelastic active porosity by MIP might be regarded as an acceptable first estimation.

The micromechanical elastic model described in Section 5.6.2 has been calibrated over the set of optimized and compatible poroelastic parameters. The upscaled values, also presented in Table 6.1, reproduce the results within a 10% precision range, a remarkable

result given the minimum number of fitted parameters: C–S–H globules bulk and shear modulus (Table 5.3).

6.5 Drained elastic parameters of hydrating cement paste

The series of uniaxial compression tests performed at different ages and curing temperatures have as objective the characterization of the evolution of elastic parameters with hydration degree and the evaluation of the effects of temperature.

The effects of the hydration degree are outlined for a cement paste hydrated at 7°C, in which case the main evolution trends of the material properties are captured thanks to the slow kinetics. An equal number of tests at multiple ages have been performed for higher hydration temperatures. We decided, however, to omit the presentation of these experiments because the fast evolution of the hydration degree makes it impossible to discern the tendencies clearly, since no points are available at low hydration degrees.

The results of uniaxial tests performed at different ages on a cement paste hydrated at 7°C are reproduced in Figure 6.17. The evolution of the drained Young modulus E_d, Poisson ratio ν_d, and compressive strength $\bar{\sigma}_1$ as a function of hydration degree are also presented. The results show the clear increase of all three mechanical parameters with hydration.

There is a significant increase in the uniaxial compressive strength $\bar{\sigma}_1$ with hydration degree. The results are in agreement with the experiments performed by Mindess et al. [206], who showed that the compressive strength grew as a function of the hydration degree following a trend that might be estimated as slightly over-linear. This result confirms the expression adopted for the chemical hardening of the yield surface of the cement paste. Although the yield and failure surface are not necessarily identical, we assume that, under the confinement-free conditions of an uniaxial test, there is no mechanical hardening and both surfaces coincide. In any case, both parameters can be reasonably supposed to be strongly correlated, and therefore the assumption of linear chemical hardening is supported by the experiments.

Regarding the elastic parameters, the more significant variation concerns E_d, which might be extrapolated to a zero value at $\alpha \approx 0.2$, suggesting an approximate percolation threshold in agreement with the results of UCA and STCA tests presented in Sections 6.6 and 6.7. For a hydration degree of 0.83, we obtain a $E_d = 20.2$ GPa, in excellent agreement with the results from triaxial tests (Table 6.1). The change in ν_d is less significant, going from 0.18 to 0.27.

The results might be compared to those obtained by other authors, among which we can cite the recent work of Irfan-Ul-Hassan et al. [207], who also observed a linear relation between Young modulus and hydration degree when probing cement pastes at similar
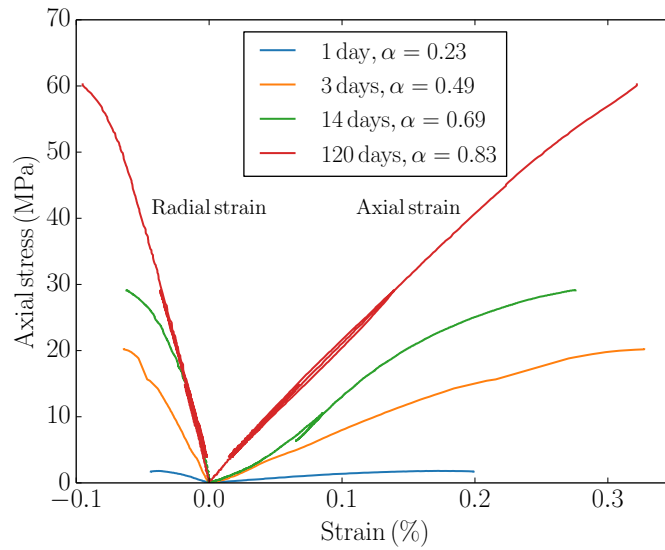
(a) Stress – strain response
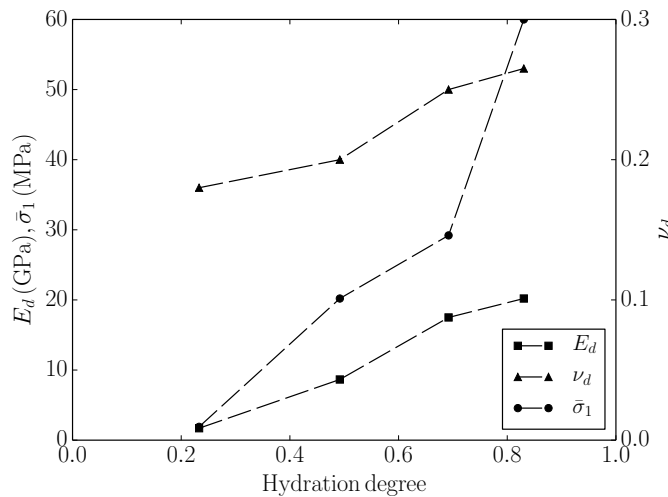
(b) Mechanical properties as a function of hydration degree

Figure 6.17: Results of the uniaxial tests on cement pastes hydrated at 7°C.

hydration degrees. Regarding the drained Poisson coefficient, the results are in agreement with the predictions of micromechanical elastic models, as exemplified in the work of Bernard et al. [144].

The experimental results regarding the effect of hydration temperature on mature cement pastes are presented in Figure 6.18. It is clear that increasing the hydration temperature degrades the elastic mechanical properties of the cement paste. The degradation is partly due to the significant increase in capillary porosity associated with higher temperatures –as confirmed by the MIP results (Figure 6.5)– among other reasons mentioned in the literature [23, 104].

The Young moduli for high temperatures are in agreement with the value determined by

Ghabezloo for the same cement paste cured and tested at 90°C [18]. We also observe that compressive strength decreases with increasing temperatures.
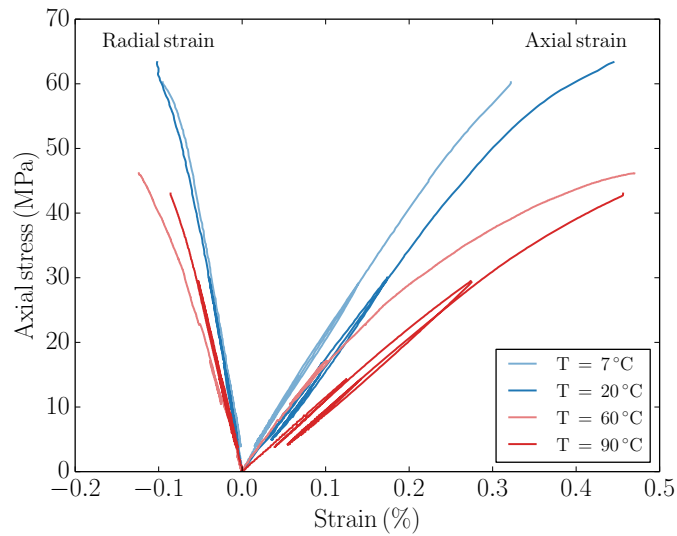
(a) Stress – strain response
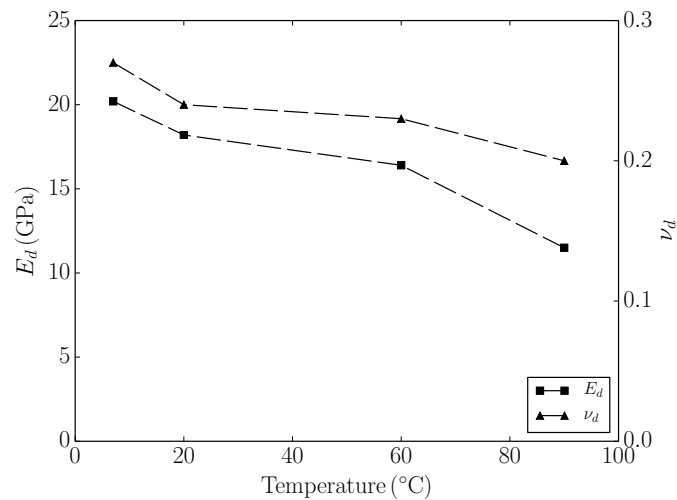
(b) Elastic properties as a function of hydration temperature

Figure 6.18: Results of the uniaxial tests on mature cement pastes hydrated at different temperatures. All specimens are 120 days old.

6.6 Continuous acoustic monitoring of hydrating cement paste

The series of UCA tests have been performed to evaluate the effect of temperature and pressure curing conditions on the mechanical properties of a hydrating cement paste. This analysis is complementary to the triaxial experiments, that allowed us to determine a

complete set of poroelastic parameters for a mature paste. It is also a complement to the uniaxial tests, useful for sketching the overall evolution trends of some of the essential elastic parameters. The UCA tests provide a continuous description of the evolution of the dynamic oedometric undrained modulus, unlike the discrete measurements provided by triaxial, uniaxial and STCA tests.

The analysis of the results requires their preliminary consideration from a poromechanical standpoint, notably in what regards the behaviour of the pore water as the mechanical pulse travels through the material. The subject has been extensively discussed in the literature (see, for instance, the seminal papers by Biot [71, 72]), although few references are available in what regards hydrating cement pastes [208–211].

As explained by Pimienta et al. [212], the bulk mechanical moduli determined from wave velocities display different regimes, depending on the excitation frequency of the mechanical wave. Starting from a low frequency, the porous material response changes from drained to undrained as the frequency increases, because of the inability to dissipate the pore water overpressure of the pores. At very high frequencies, the response becomes unrelaxed, a state in which the pore water pressure is not homogeneous inside the sample. We thus require the definition of the threshold frequencies separating the behaviour of the bulk water as drained or undrained, as these are the only behaviours described in the poromechanical framework. According to Biot's theory, the essential parameter is the skin depth

$$\delta = \left(\frac{2\eta}{\rho_l \, \omega} \right)^{1/2} \tag{6.8}$$

where η is the fluid viscosity and ω is the angular frequency of the excitation. The characteristic pore size l of the material is to be compared with the skin depth δ in order to adopt the appropriate response regime from Biot's theory, which is undrained if $\delta > l$.

For our experiments, since the excitation frequency of the UCA transducers is in the range of 1 MHz, and given the dependency of water viscosity on temperature, the skin depth can be estimated between 0.65 to 0.30 μm for temperatures ranging from 7 to 90°C. These values have to be compared with the characteristic pore size l of the cement paste. In order to do so, consider the MIP results of the hydrating cement paste (see Figures 6.1 and 6.2). We observe that, for the percolating cement paste, a main pore family is present in the range of 1 μm, but it very quickly shifts towards smaller pore sizes as the hydration progresses. Therefore, the characteristic pore size is comparable but not significantly larger than the skin depth δ early during the hydration, and it becomes considerably smaller later in the reaction. In consequence, as a simplification for our analysis, we adopt the low frequency response of the Biot theory throughout the reaction, and therefore the measured moduli in our UCA experiments will be considered as undrained for all ages. The undrained oedometric modulus E_{oed}^u of the cement paste can be determined from the longitudinal

wave velocity V_L as:

$$E_{oed}^u = \rho V_L^2 \tag{6.9}$$

where ρ is the density of the material, given by:

$$\rho = \frac{1 + w}{1/\rho_c + w/\rho_l} \tag{6.10}$$

In the remaining of the section we present the wave velocity V_L measured during the experiments as well as the evolution of E_{oed}^u with hydration. Whenever possible, the hydration degree has been calculated directly by correspondence of the UCA and isothermal calorimetry experiments. If the matching of UCA and calorimetry is not possible, the hydration degree has been calculated according to the hydration model.

6.6.1   Effect of temperature

The effect of temperature is presented in Figures 6.19 to 6.21, where we have separated the experiments according to the testing pressures. Initially, the wave velocity remains stagnant as a result of the fluid state of the cement slurry, and the measured wave velocity is in agreement with that of liquid water, which is in the order of 1500 m/s. The evolution of the solid skeleton is clearly evidenced in the increase of the wave velocity. Once the skeleton percolates, at a hydration degree that varies between 10 to 15%, the wave velocity increases nearly linearly with the hydration degree.

In general, all of the data series reflect a similar trend in what regards the effect of temperature on the elastic modulus E_{oed}^u. The effect of temperature seems to be nearly non-existent, or at least non-discernible, for temperatures ranging from 7 to 40°C. For temperatures of 60 and 90°C, however, E_{oed}^u is consistently lower when compared to experiments at lower temperatures at identical hydration degree. From the analysis of the results, we can observe a degradation of E_{oed}^u at the highest temperature of 15 to 20% when compared to the same cement paste cured at 7°C. This is in overall agreement with the conclusions drawn from the uniaxial experiments on mature cement pastes cured at different temperatures regarding the drained Young modulus and Poisson ratio (see Section 6.5).
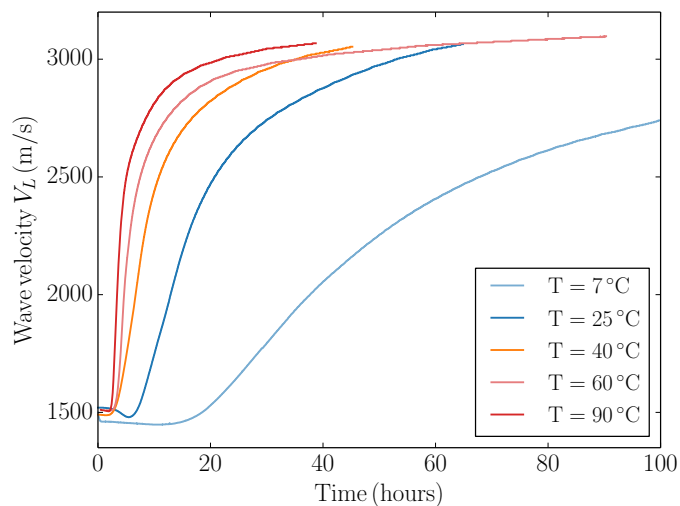
(a) Longitudinal wave velocity as a function of time
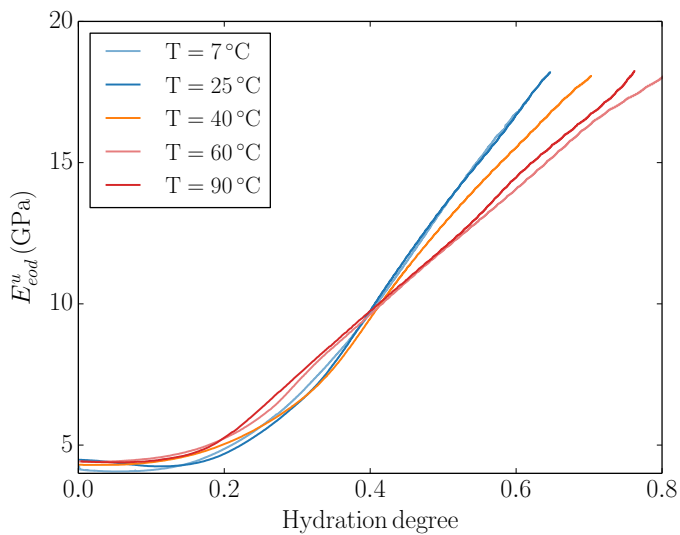
(b) Undrained oedometric modulus as a function of hydration degree

Figure 6.19: Results of the ultrasonic measurements for a pressure of 0.1 MPa.
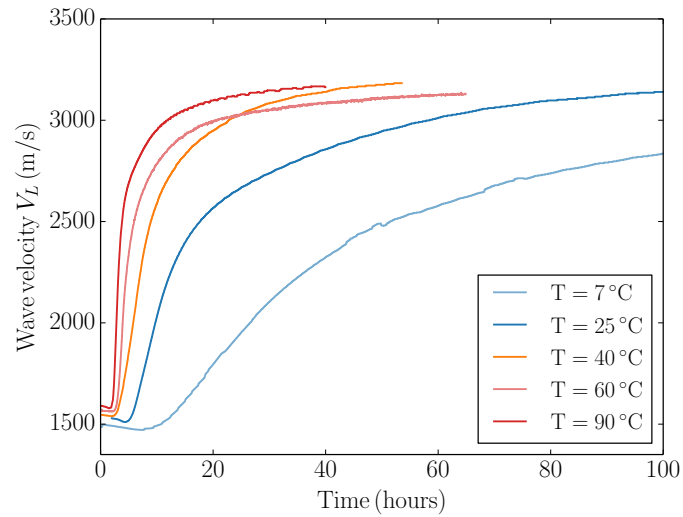
(a) Longitudinal wave velocity as a function of time
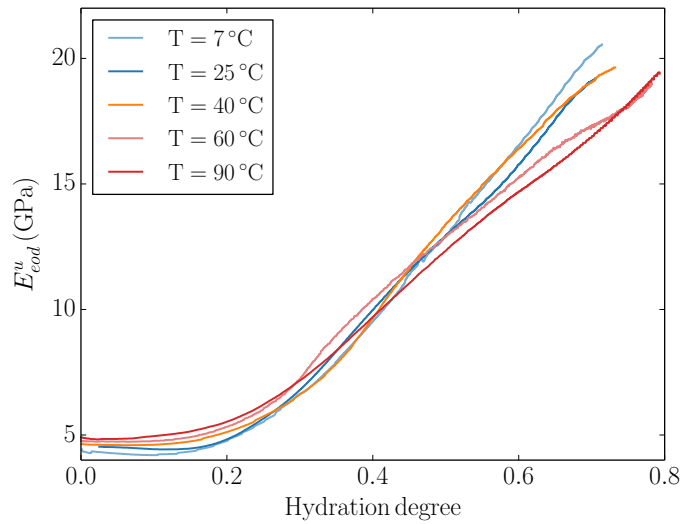
(b) Undrained oedometric modulus as a function of hydration degree

Figure 6.20: Results of the ultrasonic measurements for a pressure of 25 MPa.
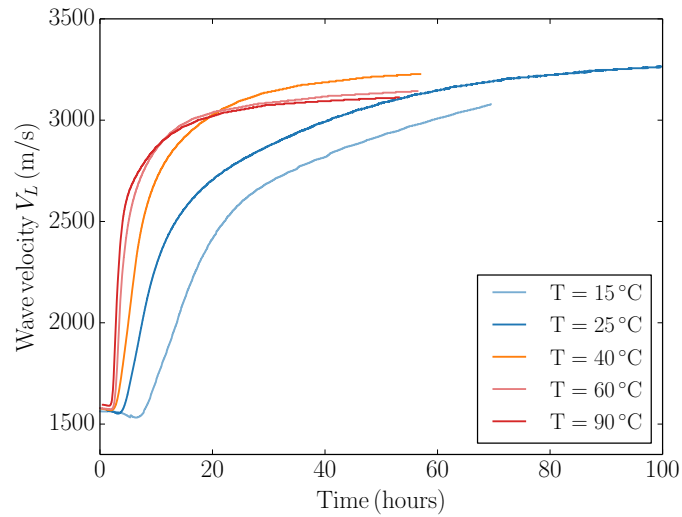
(a) Longitudinal wave velocity as a function of time
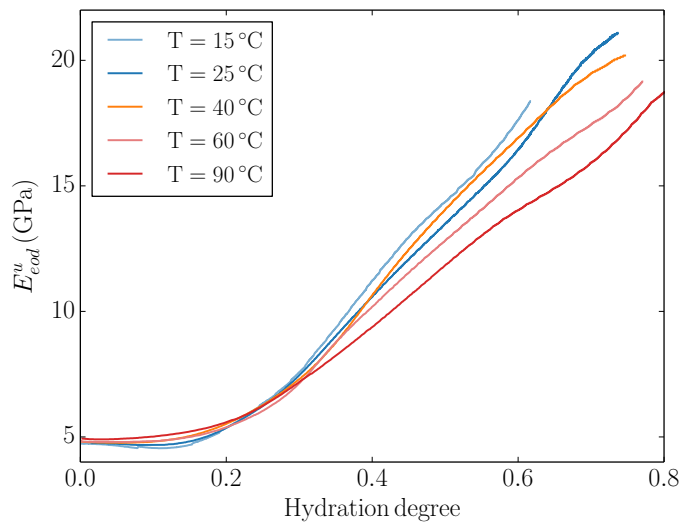
(b) Undrained oedometric modulus as a function of hydration degree

Figure 6.21: Results of the ultrasonic measurements for a pressure of 45 MPa. For T = 15°C, P= 40 MPa.

6.6.2   Effect of pressure

The effect of pressure in presented in Figures 6.22 to 6.26, where we have separated the results according to the testing temperatures. We observe that E^u_{oed} is slightly larger for the tests performed at higher pressures when comparing equal hydration degrees. This difference is presumably due to the presence of entrapped air bubbles incorporated during the slurry mixing, as mentioned by Sayers and Grenfell [208]. These small gas bubbles are dissolved in the liquid at higher pressures [151], hence reducing their effect on the measurements.

In any case, if the variation of the measured mechanical properties was due to the modification of the material due to the applied pressure, such effect can be neglected, given its magnitude. Overall, the hypothesis of independence of material properties with respect to hydrating pressure conditions can be justifiably adopted according to the experimental evidence.

The pressure-independence of the material properties implies that curing pressure conditions can be completely accounted for by their effect on hydration kinetics (e.g. by appropriate hydration models). Although the high-pressure testing equipments will likely remain a part of cement laboratories, the systematic examination of pressure effects on mechanical properties can henceforth be justifiably avoided in the range of pressures concerned by the present study. This conclusion might have a significant impact on the complexity of the equipment required for material testing, given the important economical investments and technical skill demanded by high-pressure experiments.
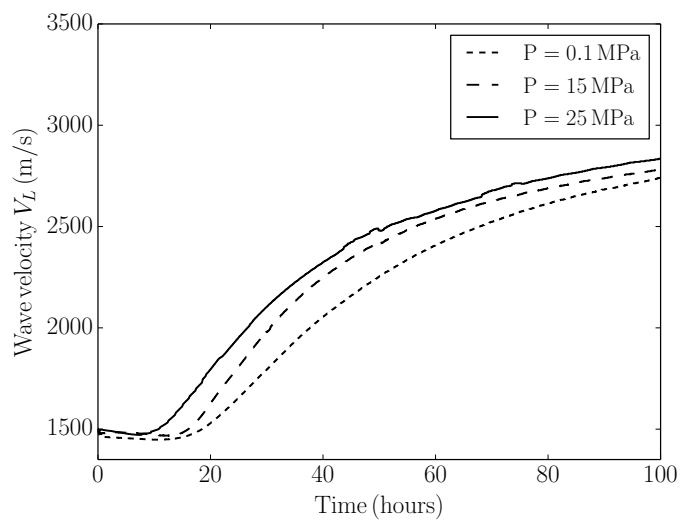
(a) Longitudinal wave velocity as a function of time
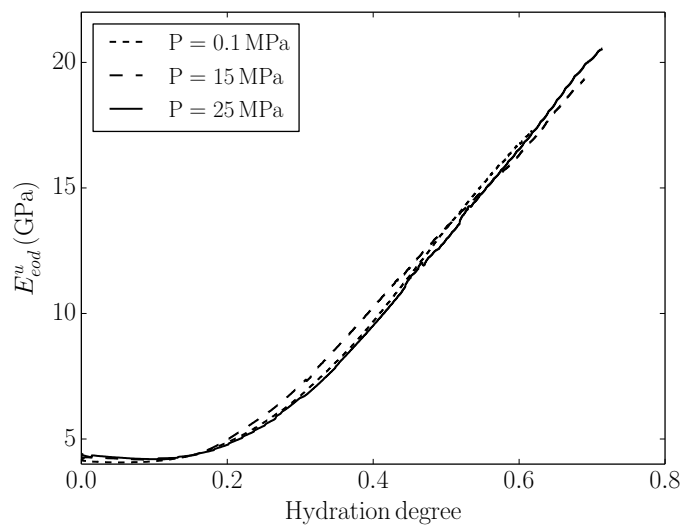
(b) Undrained oedometric modulus as a function of hydration degree

Figure 6.22: Results of the ultrasonic measurements for T= 7°C.
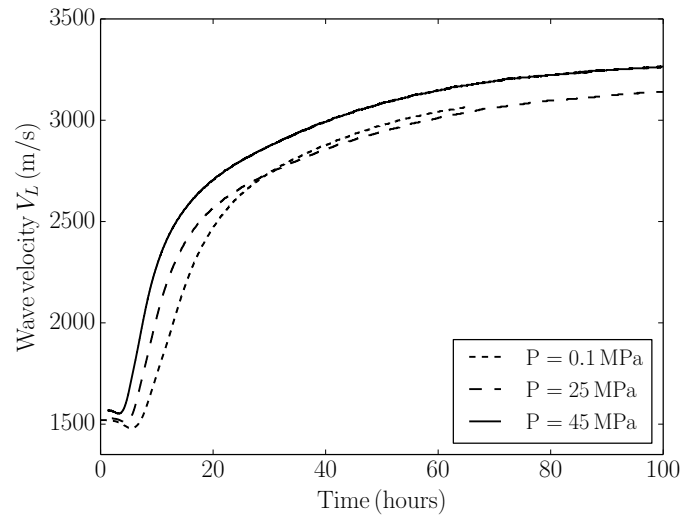
(a) Longitudinal wave velocity as a function of time
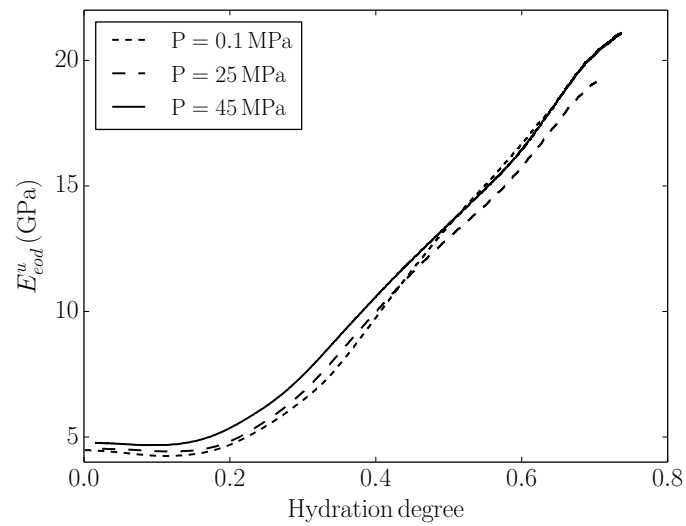
(b) Undrained oedometric modulus as a function of hydration degree

Figure 6.23: Results of the ultrasonic measurements for T= 25°C.
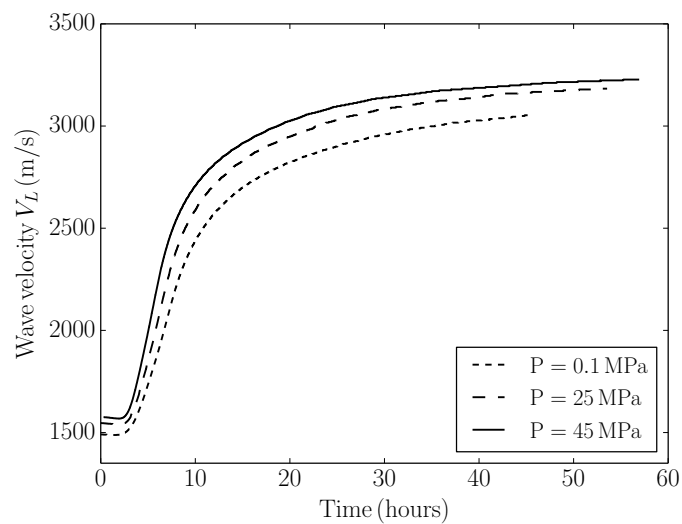
(a) Longitudinal wave velocity as a function of time
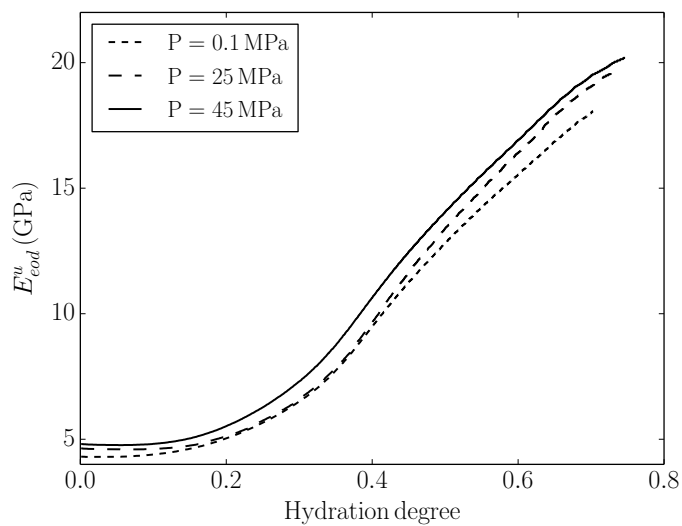
(b) Undrained oedometric modulus as a function of hydration degree

Figure 6.24: Results of the ultrasonic measurements for T= 40°C.
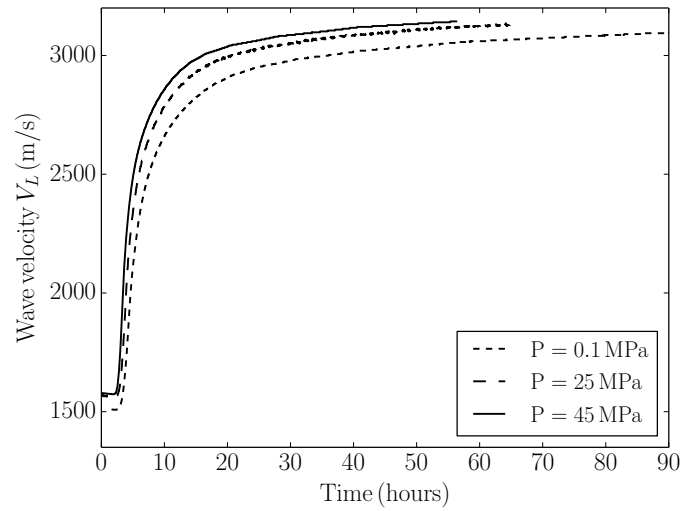
(a) Longitudinal wave velocity as a function of time
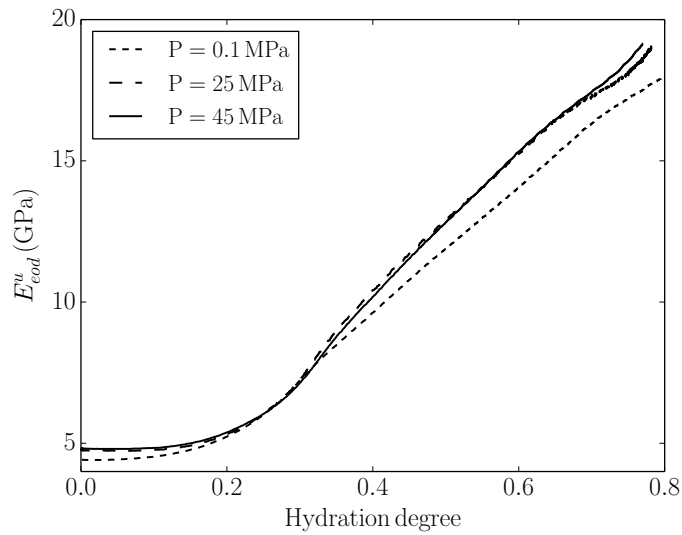
(b) Undrained oedometric modulus as a function of hydration degree

Figure 6.25: Results of the ultrasonic measurements for T= 60°C.
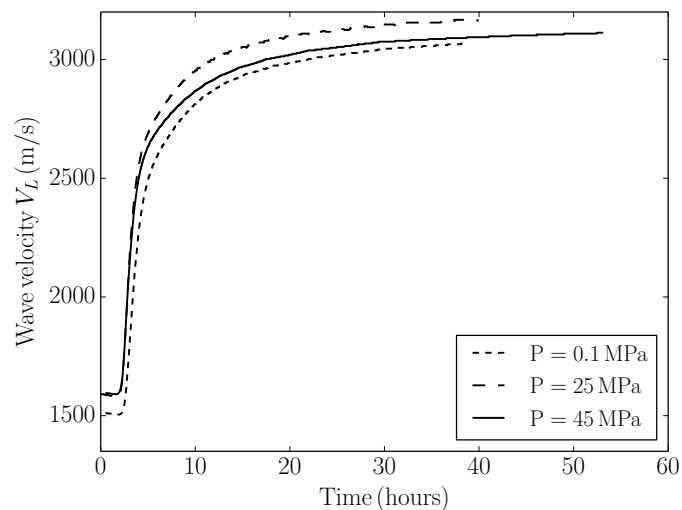
(a) Longitudinal wave velocity as a function of time
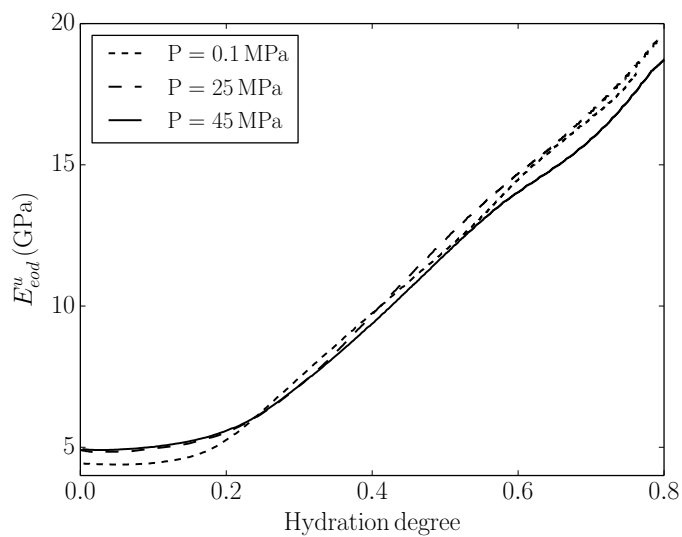
(b) Undrained oedometric modulus as a function of hydration degree

Figure 6.26: Results of the ultrasonic measurements for T= 90°C.

6.6.3 Remarks

The percolation of the skeleton has been assumed to coincide with the sharp increase in longitudinal wave velocity observed in the experiments. Rigorously, the shear wave velocity should also be measured in order to precisely determine the percolation threshold, characterized by the fluid-to-solid transition from a non-shearing to a shearing medium. There is, however, theoretical and experimental evidence of the simultaneity of increase of the longitudinal and shear waves in hydrating cement pastes, thus justifying our assumption [208].

The percolation hydration degree is consistently found between 10 to 15% for the different curing conditions. The determination of the percolation threshold is particularly precise for the cement pastes hydrated at very low temperature (7°C), in which case the wave velocity and hydration reactions evolution can be synchronized very precisely. The percolation threshold is higher than the value reported by some other authors, in the order of 5% [210, 211]. The reason for the slight discrepancy might be the specimen size, significantly larger in our experiments. A larger specimen not only provides a more representative averaged measure, but also minimizes the effect of boundary conditions and allows a more precise determination of the wave velocities. In addition, the hydration degree was not experimentally determined, but only estimated, in ref. [211]. In any case, there is no overall contradiction among the results, since the percolation threshold depends strongly on the cement paste formulation, cement powder properties and the morphology of the hydrates. The shape of hydrate particles has been found to weight decisively according to modelling results [34].

The quasi-linear increase of elastic properties with hydration degree is in agreement the observations of other authors using ultrasonic techniques [208, 210] and our own uniaxial (Section 6.5) and STCA experiments (Section 6.7).

The direct correlation proposed by Vu [8] between hydration degree and wave velocity, although appealing, is likely limited to a given water to cement ratio w and cannot be extrapolated to other values. An increase of w will result, because of the larger pore volume, in a higher hydration degree at percolation and lower wave velocities, as demonstrated experimentally by Boumiz et al. [210]. The hydration reaction, on the other hand, is accelerated by the excess of water (see Chapter 3), making the simple correlation implausible. In the limit case of a very diluted sample, complete hydration might be possible without solid percolation and hence no change in the wave velocity.

As previously mentioned, there seems to be no significant effect of the curing pressure on the resulting material properties or material microstructure (see our MIP results in Section 6.3 as well as ref. [139]). Therefore, the tests performed at low curing pressures (e.g. uniaxial experiments) can be deemed representative of the material properties.

6.7 Mechanical properties of cement paste hydrating under multiple temperatures and pressures

The current section presents the results of STCA tests performed on fresh cement slurries under different pressure and temperature conditions. The chemical shrinkage as well as the evolution of mechanical parameters of the hydrating material can be determined from the experiments. The trends concerning the material properties outlined by other experimental configurations can be verified under different pressures and temperatures in a complementary approach. Furthermore, the analysis of the loading cycles reveals interesting details about the evolution of the plastic yield of the hydrating material.

6.7.1 Early age behaviour of the cement paste: chemical shrinkage

The chemical shrinkage is defined as the stoichiometric volume imbalance of the hydration reaction (see Section 5.3.1). Under constant pressure and temperature, the chemical shrinkage strain is directly observable at the macroscopic scale as long as the skeleton remains non-percolating, as explained in Section 5.10. In the STCA cell, because the axial stress is held constant, the axial piston is continuously in contact with the cement paste specimen, hence providing a measurement of the chemical shrinkage before percolation.

The volumetric strain with respect to a unitary cement powder mass for a fluid slurry is given by:

$$\epsilon_{cm}(\alpha) = \left(\frac{1}{\rho_c} + \frac{w}{\rho_w} \right) \epsilon(\alpha) = \xi \, \alpha \tag{6.11}$$

where ξ is the chemical shrinkage of the cement powder, defined in terms of volume per unit of cement powder mass, assumed constant and independent of hydration degree (see Equation (5.26)). The procedure for the determination of chemical shrinkage hence relies in the linearity of the observed shrinkage and the hydration degree for a non-percolated specimen, as shown in Figure 6.27, for a hydration at 22°C and 25 MPa.

The chemical shrinkage values determined for STCA tests at different temperatures and pressures are presented in Figure 6.28. From the experiments, it seems reasonable to postulate the independence of chemical shrinkage with respect to pressure conditions. The most significant deviations for tests performed at the same temperature occur for parameters determined at very low pressures, in which case the results might be influenced by of the presence of air bubbles and the difficulties of the hydraulic piston to precisely exert the intended low pressure.

The pressure-independence of chemical shrinkage is a logical consequence of the absence of microstructural changes in cement pastes cured at different pressures (see remarks in Section 6.2). Furthermore, these results are in agreement with the conclusions regarding mechanical properties under different pressures as measured in the UCA experiments,
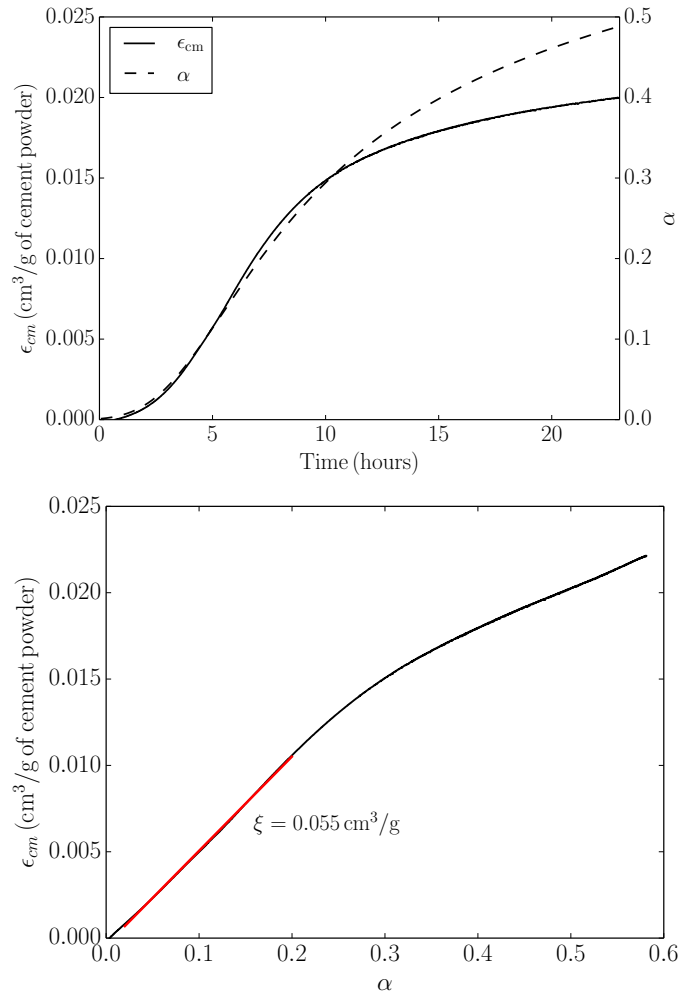
Figure 6.27: Sample chemical shrinkage fit. Test O - T22P25.

reinforcing the hypothesis of negligible changes of mechanical properties due to hydration pressures in the ranges we consider.

For low temperatures (7 and 20°C), the chemical shrinkage values are in agreement with those determined analytically from the stoichiometric balance equations, available in Table 5.1 (note, specifically, the C_3S and C_2S dominating phases). The results might also be compared with those obtained by Zhang et al. [62], who found a similar trend of the chemical shrinkage variation with temperature. Regarding magnitudes, however, their values of chemical shrinkage are larger for similar temperatures. The difference is likely due to the very low pressure condition –atmospheric– of the experiments of Zhang and co-workers. At very low pressures, a significant amount of entrapped air bubbles might remain undissolved in the cement paste and collapse during the hydration of the still-fluid slurry, increasing the total macroscopic strain and hence the apparent chemical shrinkage. The interest and novelty of the results we present reside partly in the high pressure under
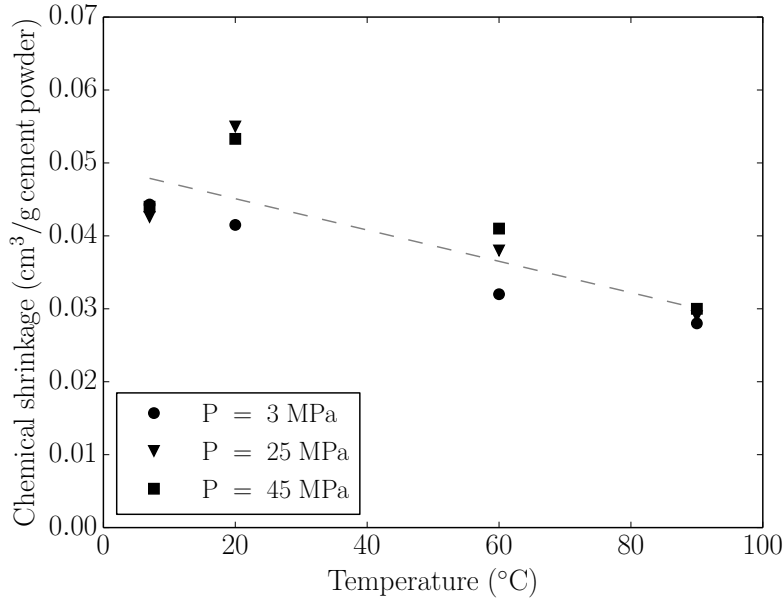
Figure 6.28: Chemical shrinkage dependency on temperature and pressure. Marks correspond to experiments. Dashed line corresponds to linear fit.

which the measurements are made, that eliminates these spurious effects.

For applications, we determine the chemical shrinkage from a simple linear regression of all the results assuming pressure independence:

$$\xi = \xi_0 + k_\xi T \tag{6.12}$$

where $\xi_0 = 0.049$ and $k_\xi = -2.15 \times 10^{-4}/°\text{C}$ and T is the temperature in Celsius.

6.7.2 Evolution of poroelastic parameters

From the oedometric multi-cyclic STCA experiments (Table 2.6), we can follow the evolution of the oedometric undrained modulus E_u^{oed} and the oedometric Skempton coefficient B_{oed}, given by:

$$B_{oed} = \frac{\delta p_w}{\delta \sigma_1} = \frac{1 + \nu_u}{3\left(1 - \nu_u\right)} B \tag{6.13}$$

in saturated undrained condition.

Typical responses of the multi-cyclic experiments are illustrated in Figures 6.29 and 6.30. The significant change of the response to the cyclic loading reflects the changes of the mechanical properties of the material. The evolution of the parameters is illustrated in Figures 6.31 and 6.32.

These results can be contrasted with the predictions from the micromechanical model formulated in Section 5.6.2, providing also a verification of the volume fraction model
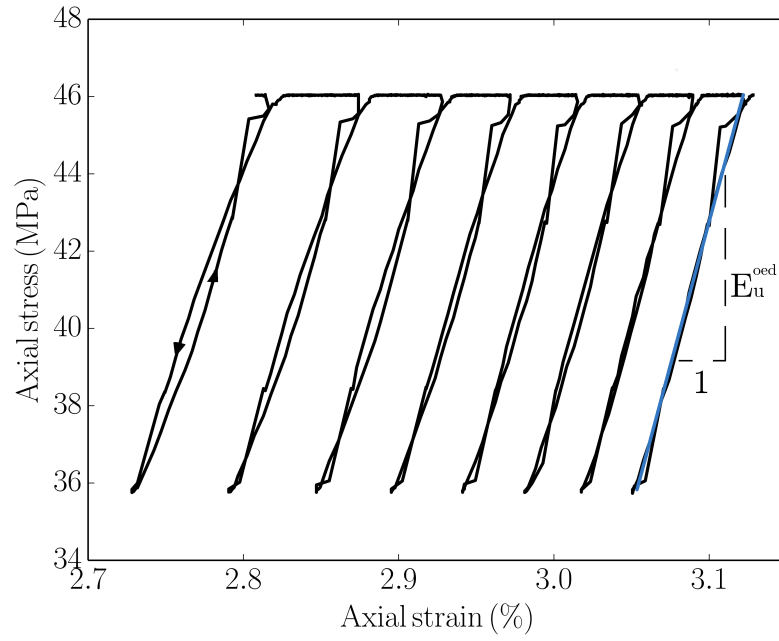
Figure 6.29: Determination of the oedometric modulus E_u^{oed} from the experimental results.
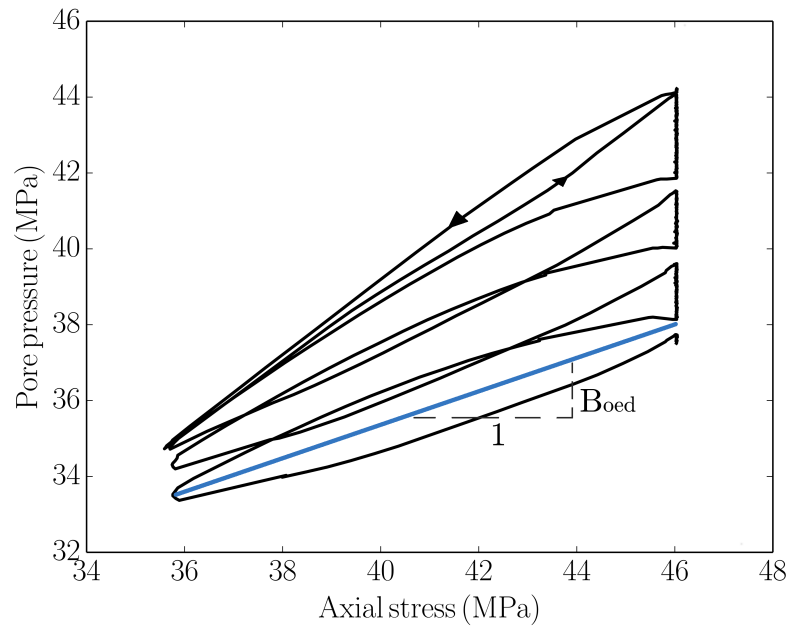
Figure 6.30: Determination of the oedometric Skempton coefficient B_{oed} from the experimental results.

from Section 5.3.1, given the hydration dependency of the parameters. The results of models and experiments are presented in Figures 6.33 and 6.34, where we can confirm the excellent predictive capabilities of the poroelastic micromechanical model. At the same time, this verification serves to assess the overall compatibility of the independent
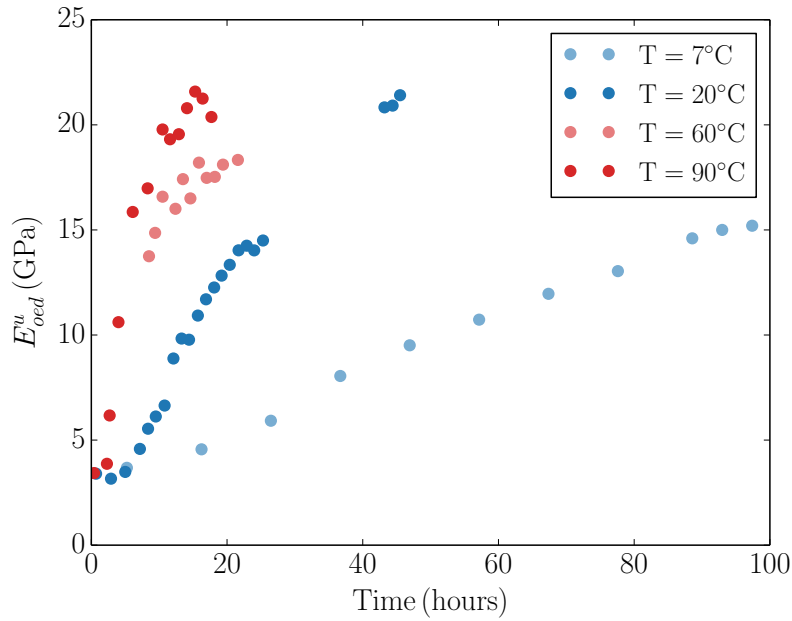
(a) E_u^{oed} as a function of time
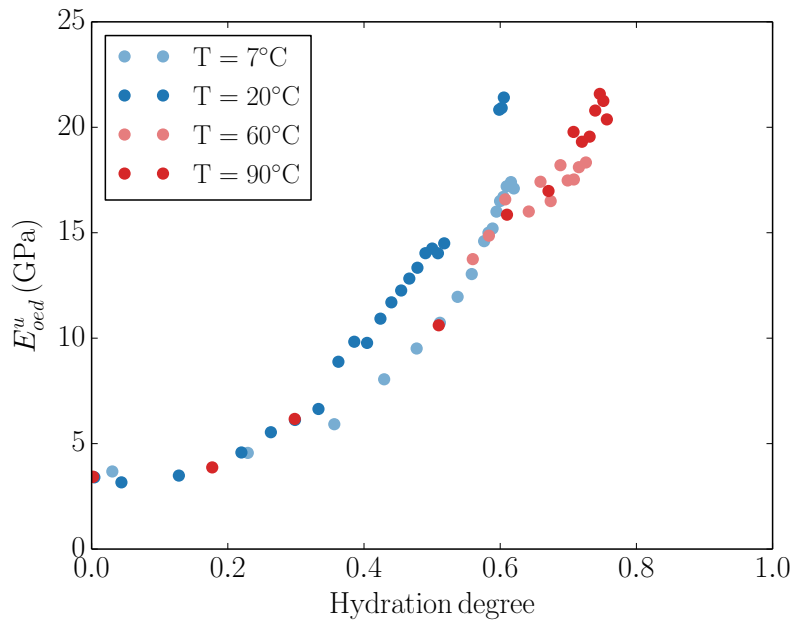
(b) E_u^{oed} as a function of hydration degree

Figure 6.31: Evolution of the undrained oedometric modulus in the STCA multi-cyclic tests.

experimental techniques: the micromechanical model is calibrated from triaxial results, and the predictions with time and hydration degree can be both obtained from the UCA and STCA tests. The compatibility of UCA and STCA measurements can also be evaluated in Figure 6.35.
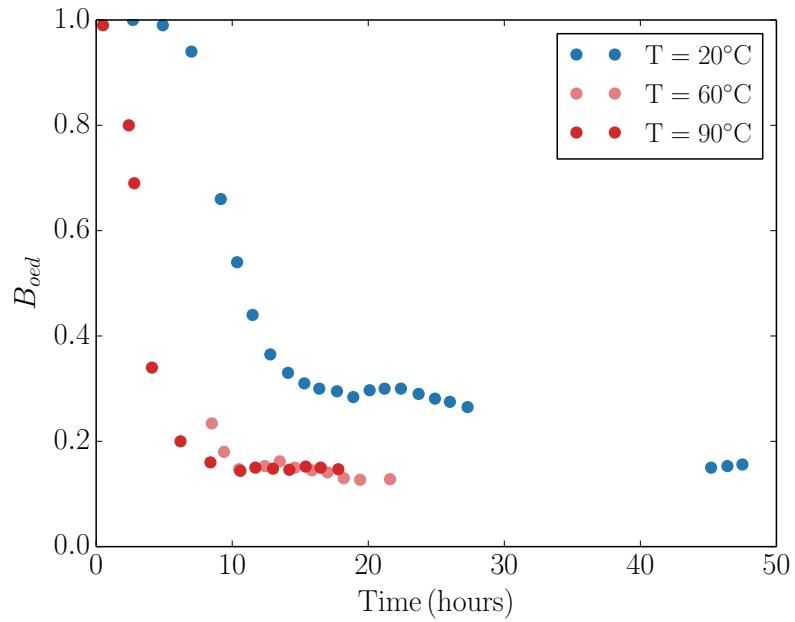
(a) B_{oed} as a function of time
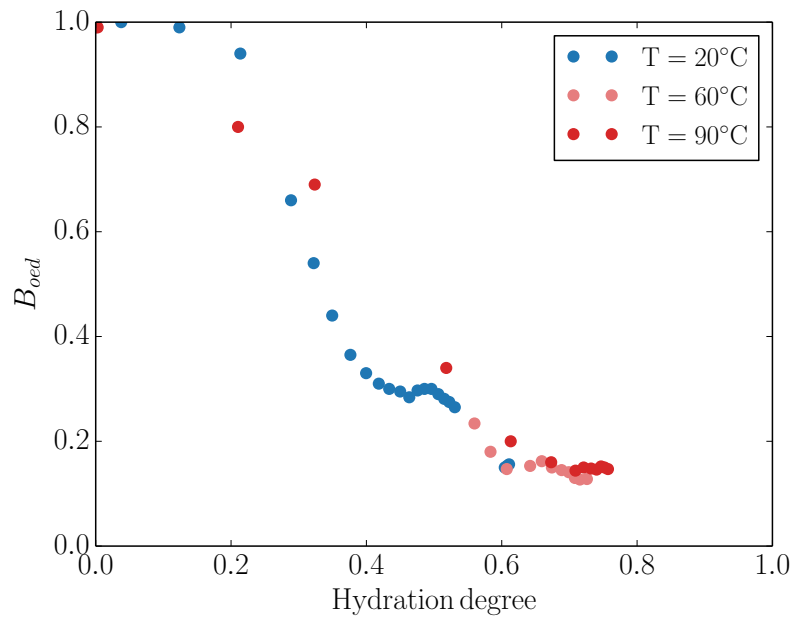
(b) B_{oed} as a function of hydration degree

Figure 6.32: Evolution of the oedometric Skempton coefficient in the STCA multi-cyclic tests.
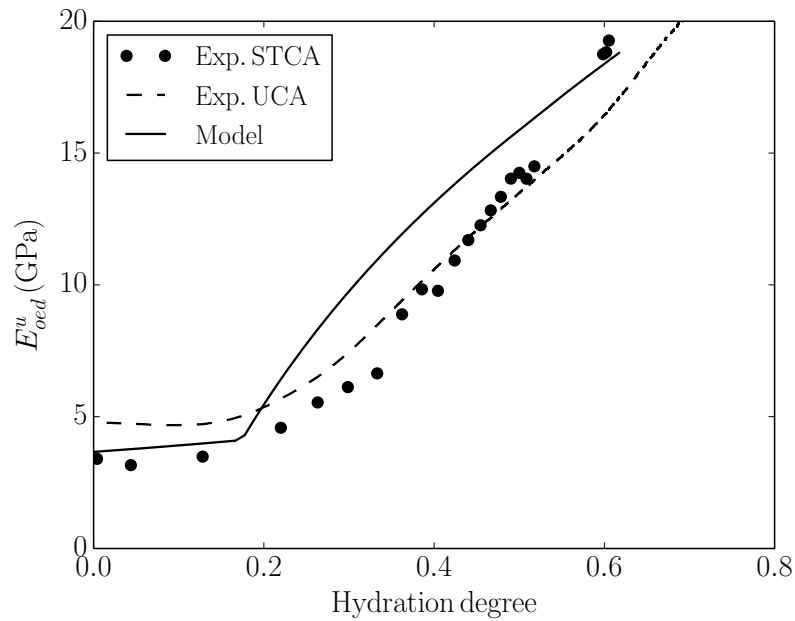
Figure 6.33: Evolution of the undrained oedometric modulus. Experimental measurements for hydration at 25°C and 45 MPa. Marks correspond to STCA and dashed lines to UCA measurements, respectively. Solid lines correspond to the micromechanical model predictions.
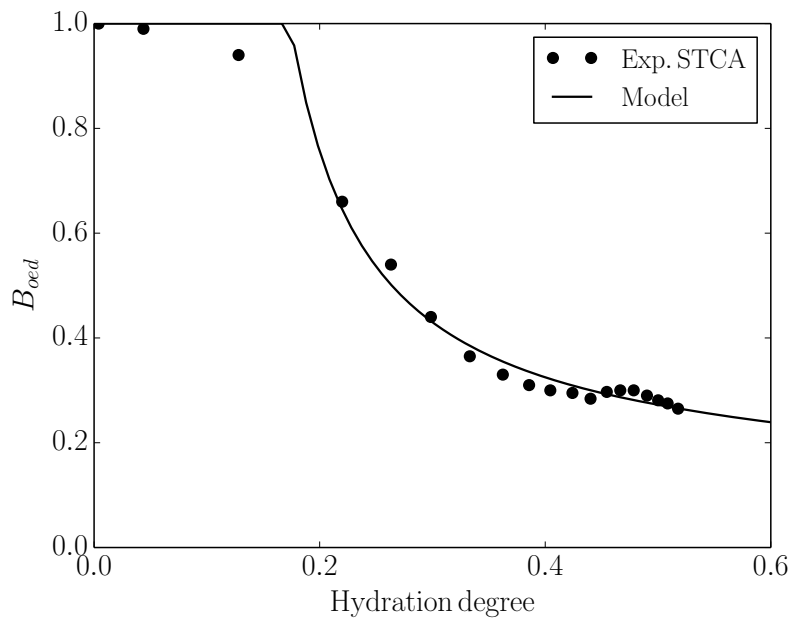
Figure 6.34: Evolution of the oedometric Skempton coefficient. Experimental measurements for hydration at 25°C and 45 MPa. Marks correspond to STCA experimental observations. Solid lines correspond to the micromechanical model predictions.
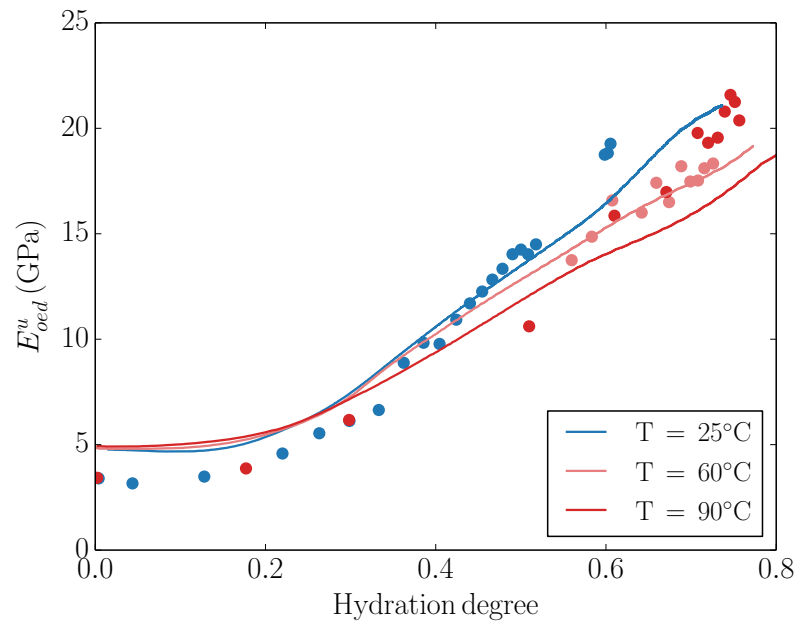
Figure 6.35: Evaluation of the compatibility of UCA (solid lines) and STCA (marks) experimental results.

6.7.3 Evolution of plastic behaviour

The evolution of the plastic properties can be assessed from the STCA tests performed by Agofack [16], in which cement paste specimens hydrated at 7°C under 25 MPa were subjected to two loading cycles at different times in their histories. An initial cycle is performed at varying ages (asynchronous), and a second cycle is performed in all samples at the same age (synchronous), as shown in Figure 6.36. The results are presented in Figures 6.37 and 6.38.
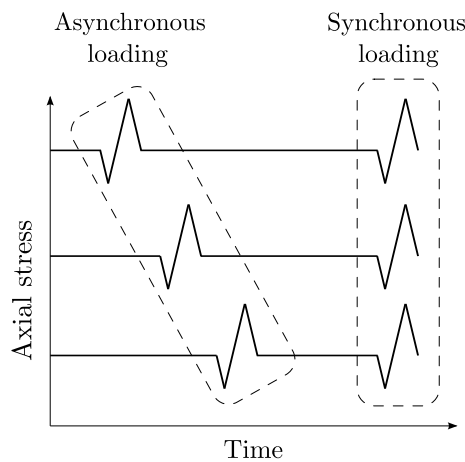
Figure 6.36: Loading paths of tests by Agofack [16]: early asynchronous cycle followed by synchronous cycle at 144 hours.
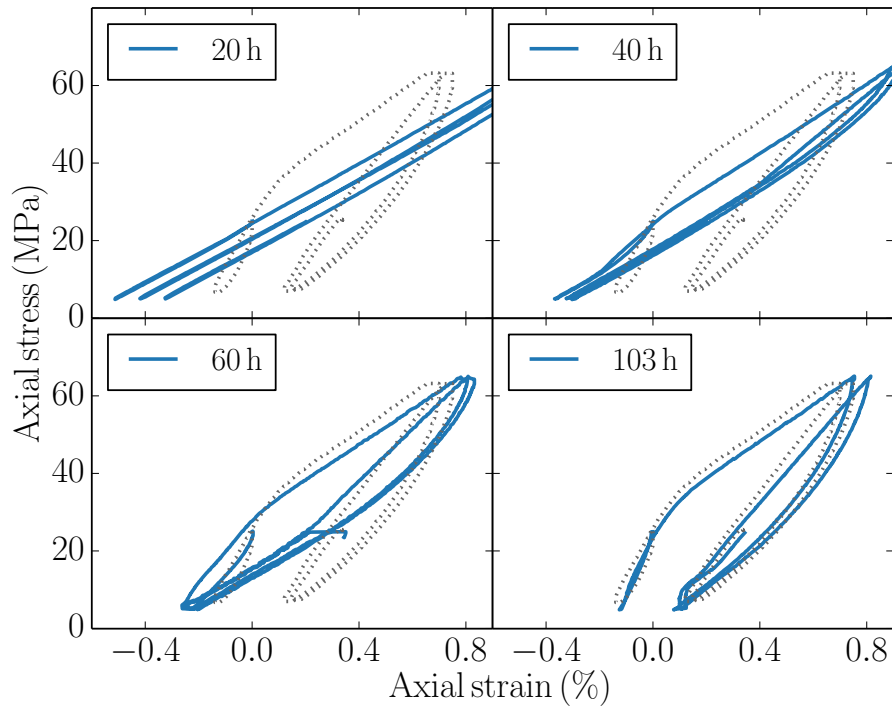
Figure 6.37: Response to the asynchronous loading cycles. Dashed lines correspond to the response at 144 hours. Adapted from Agofack [16].
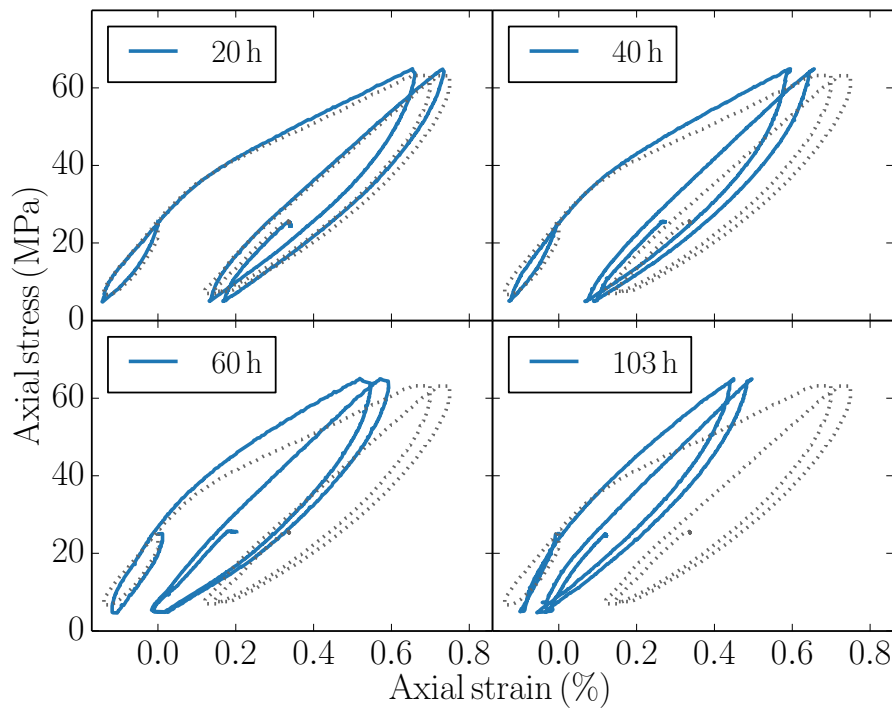
Figure 6.38: Response to the synchronous loading cycles at 144 hours. Legends indicate the time of the first loading in each case. Dashed lines correspond to the response of the specimen loaded after 144 hours. Adapted from [16].

The results clearly show that the history of the material has a decisive effect on the mechanical response observed later in its life, in agreement with the concept of yield surface and associated internal variables of our constitutive model from Chapter 5.

The superposition of the synchronous loadings, shown in Figure 6.39, evidences the change in yield stress of the chemically-active material. Such evolution can be better appreciated in Figure 6.40. The results verify the assumptions of the constitutive model, that postulate a linear chemical hardening of the yield stress. It is worth noting that, due to the different times at which the loading is applied, the amount of water consumed by hydration is not the same in all experiments. In consequence, the pore pressures and effective stresses, not measured in the experiments, are different for each of the results. The results should therefore be interpreted as indicative of the main trends.
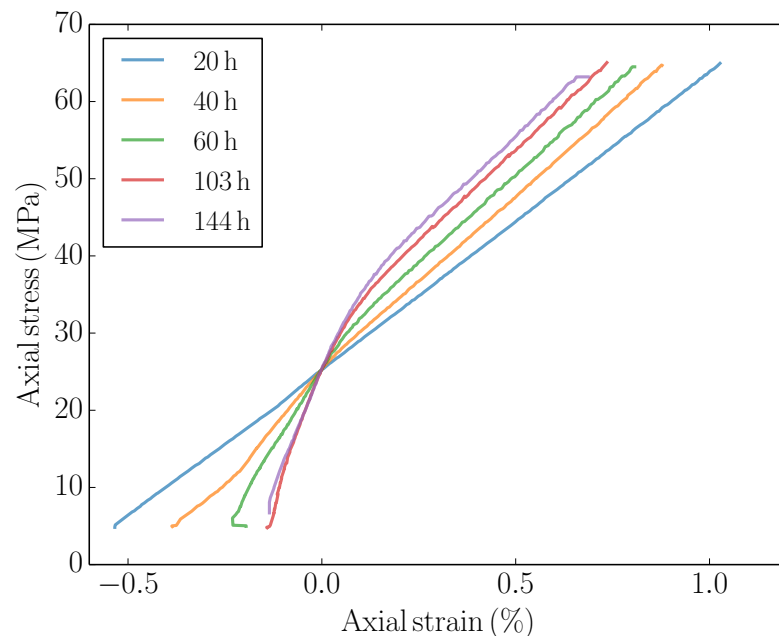
Figure 6.39: Superposition of response to the first loading cycle. Adapted from Agofack [16].
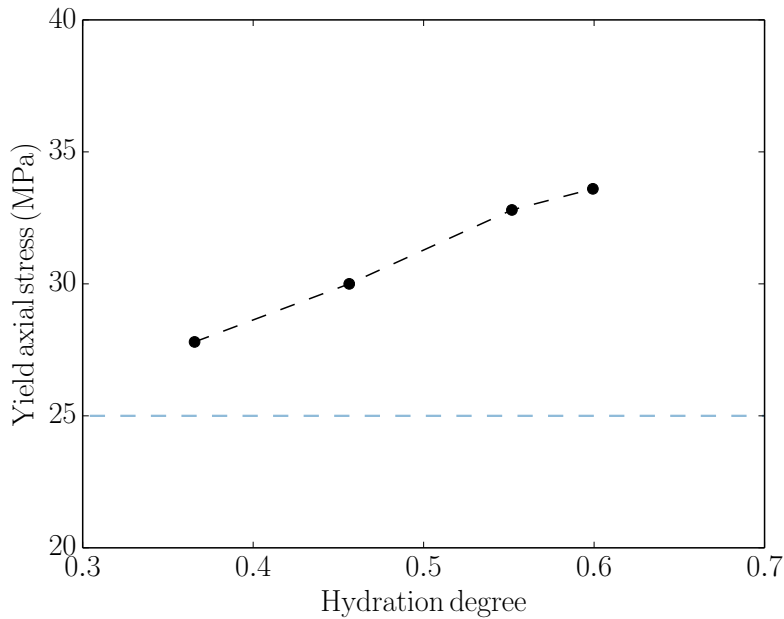
Figure 6.40: Evolution of plastic yield axial stress in oedometric condition. Blue dashed line corresponds to initial pore pressure. Black dashed line is a guide to the eye.

6.8 Comprehensive modelling of the behaviour from early age to hardened state

In this section, the constitutive model formulated in the preceding chapter is applied to the simulation of the STCA experimental results. The application constitutes a unique opportunity to assess the capabilities of the model in conditions simulating those found in an oil well. The model parameters are those presented in Table 5.5.

The simulation of the oedometric experiments requires the application of appropriate stress and strain conditions. The axial stress is imposed according to the experimental loading rates, while the radial strain is equal to zero. The event of a possible loss of contact between the specimen and the vessel wall of the oedometric cell can be readily accommodated in the formulation by assuring the non-negativity of radial stress.

The application will be divided in two parts, the first one concerning the initial monotonous loading phase, during which the axial stress is held constant. It will be demonstrated that the model can correctly capture the evolution of the axial strains, decomposed according to their nature in elastic, viscous or plastic. Furthermore, the evolution of the pore pressure predicted by the model will be shown to be in agreement with the pore pressure measurements when these are available from the experiments.

A second part is dedicated to the modelling of the cyclic loading phase, during which all the mechanisms –elastic, viscous and plastic– as well as the saturation state of the

specimen will take active part in the determination of the material response.

6.8.1 Monotonous axial loading

During the initial loading phase, the axial stress is held constant for a duration that spans from 24 to 144 hours (Table 2.6). The evolution of the strains with time for temperatures ranging from 7 to 90°C and three values of axial pressure are presented in Figure 6.41. There is an overall excellent agreement for all the results at high pressures. The most significant differences correspond to the low pressure results at 20, 60 and 90°C. The model consistently defines the same percolation threshold, derived from the micromechanical elastic model. For low values of curing pressure, the sample desaturates almost immediately after percolation, and therefore the value of strain corresponds essentially to the observable chemical shrinkage evolution before percolation.

(a) T = 7°C

(b) T = 20°C

(c) T = 60°C

(d) T = 90°C
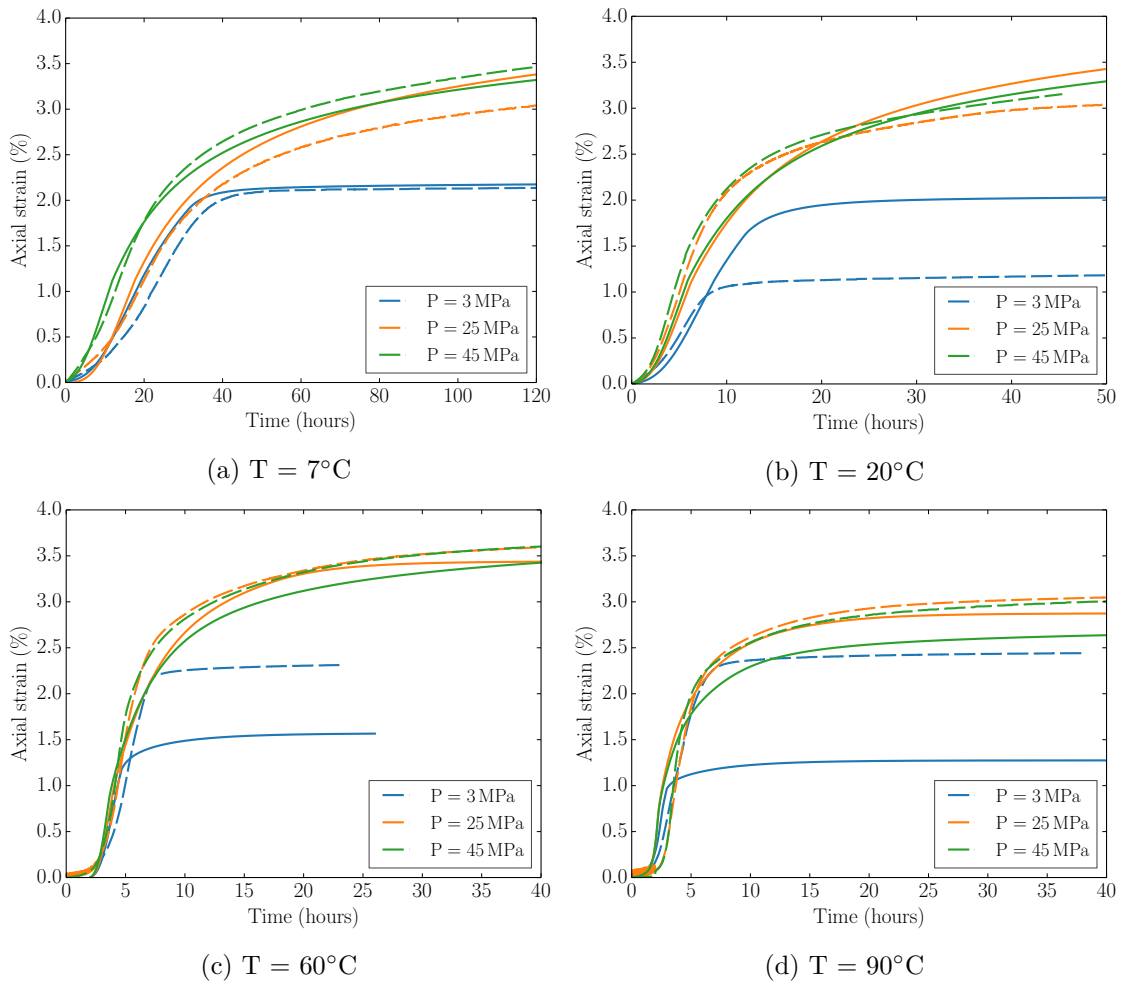
Figure 6.41: Axial strains as a function of time for multiple temperature and pressure conditions in oedometric STCA configuration. Solid lines correspond to model predictions, while dashed lines are the experimental results.

In the framework of our constitutive model, the strains might be discriminated according to their nature in elastic, viscous or plastic. The decomposition of the strains as a function of time and hydration degree is presented in Figure 6.42. Initially, only the purely chemical strain before percolation is observed. In the illustration, it is considered together with the plastic strains because of its purely irreversible character. The chemical strains are of course linearly related to the hydration degree, since the chemical shrinkage and hydration degree of all clinker components are assumed constant and homogeneous, respectively.

Once the solid skeleton percolates, the decrease of the pore pressure associated with the hydration reactions increases the effective stresses acting on the skeleton generating, as a result, both elastic and viscous strains. The viscous strains are dominant in this early phase, being responsible of about 80% of the total observable strain. Their evolution with the hydration degree is nearly lineal, except when the sample becomes partially saturated due to drying, as discussed in the following.

During this initial phase, no plastic strains are generated, since the yield surface remains beyond the effective stress state. This is in agreement with the experimental observations from Figure 6.37, where no plastic strains were observed for states of stress immediately above the applied hydration pressure, leading to conclude that the state of stress immediately before the loading was not on the yield surface.

After percolation, the radial stress changes during hydration result in the creation of a non-hydrostatic state of stress and, hence, the development of shear stresses into the specimen. The evolution of the state of stress will have an influential role in the model response to loading cycles.

Another consequence of the progress of hydration reactions is the reduction of the total pore pressure, as can be verified in Figure 6.43. It is important to note that the decrease in pore pressure is not linearly dependent on hydration degree, as confirmed by the experiments. The reasons for such behaviour are on one hand the non-linear evolution of the elastic material properties and on the other the gradual development of viscous strains.

Another important remark concerns the desaturation of the specimens, observed experimentally and reproduced by the model. Indeed, for low hydration pressures (i.e. 3 MPa), the desaturation occurs almost immediately after percolation. The capillary pressure in the long term is the order of 2 MPa, significantly lower than the values calculated with a non-ageing water retention curve by Agofack [16] . The relative humidity corresponding to 2 MPa capillary pressure is 98%, in excellent agreement with the results obtained for a cement paste of similar composition and age by Hua et al. [84].

The evolution of the saturation degree is presented in Figure 6.44, where it can be observed that, for the lowest hydration pressure, the saturation degree is close to 95% in the long term. More importantly, the effect of increments of mean stress on pore pressure,
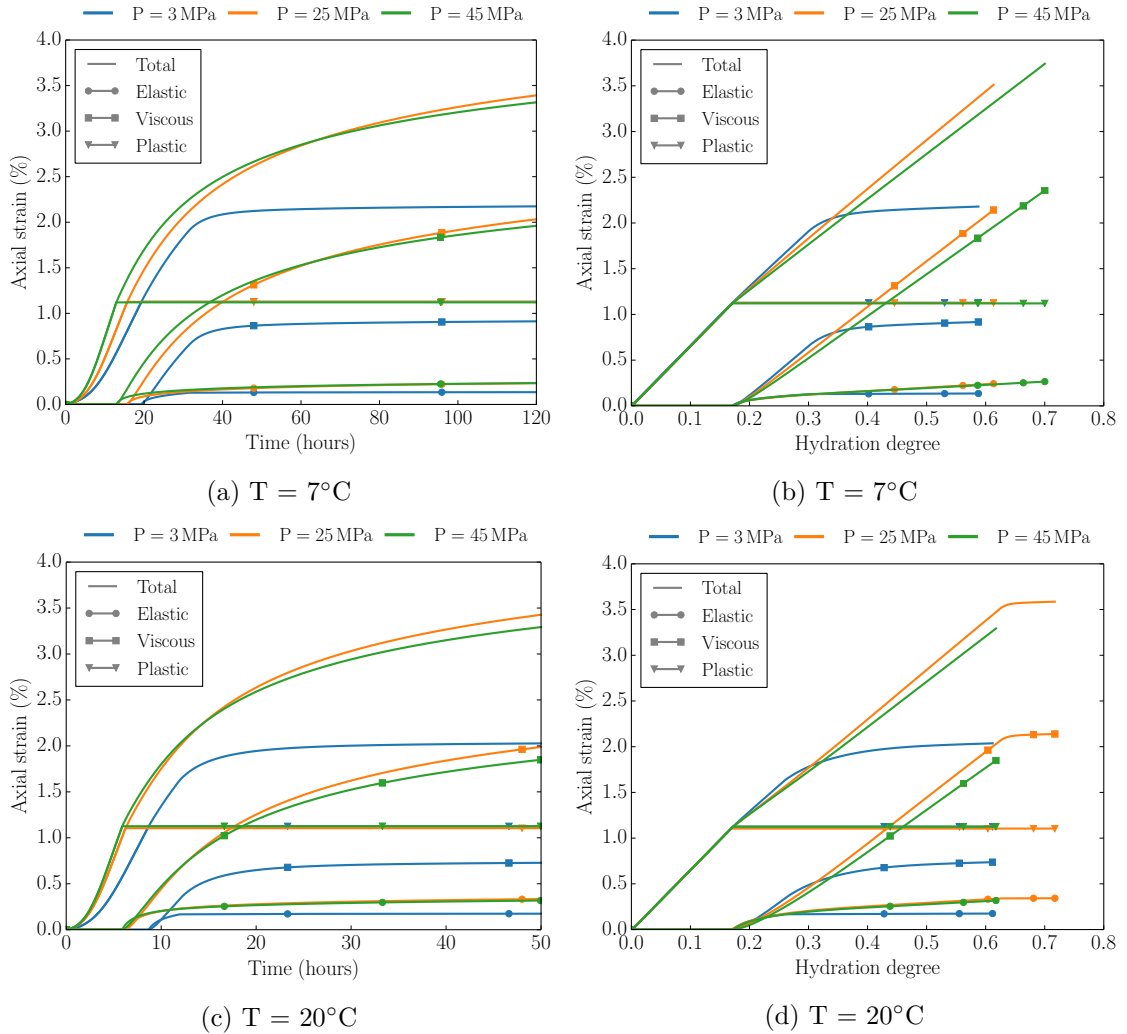
Figure 6.42: Components of the axial strains as a function of time and hydration degree for multiple temperature and pressure conditions in oedometric STCA configuration. The plastic strain includes the initial purely chemical strain.

reflected by the effective Skempton coefficient $\bar{B}$ we have identified in the previous chapter (Equation (5.122)), is dramatically affected by desaturation. A sharp drop of $\bar{B}$ occurs with desaturation resulting, subsequently, in a very low sensitivity of the pore pressure to mean stress changes, in what we might call quasi-drained conditions.
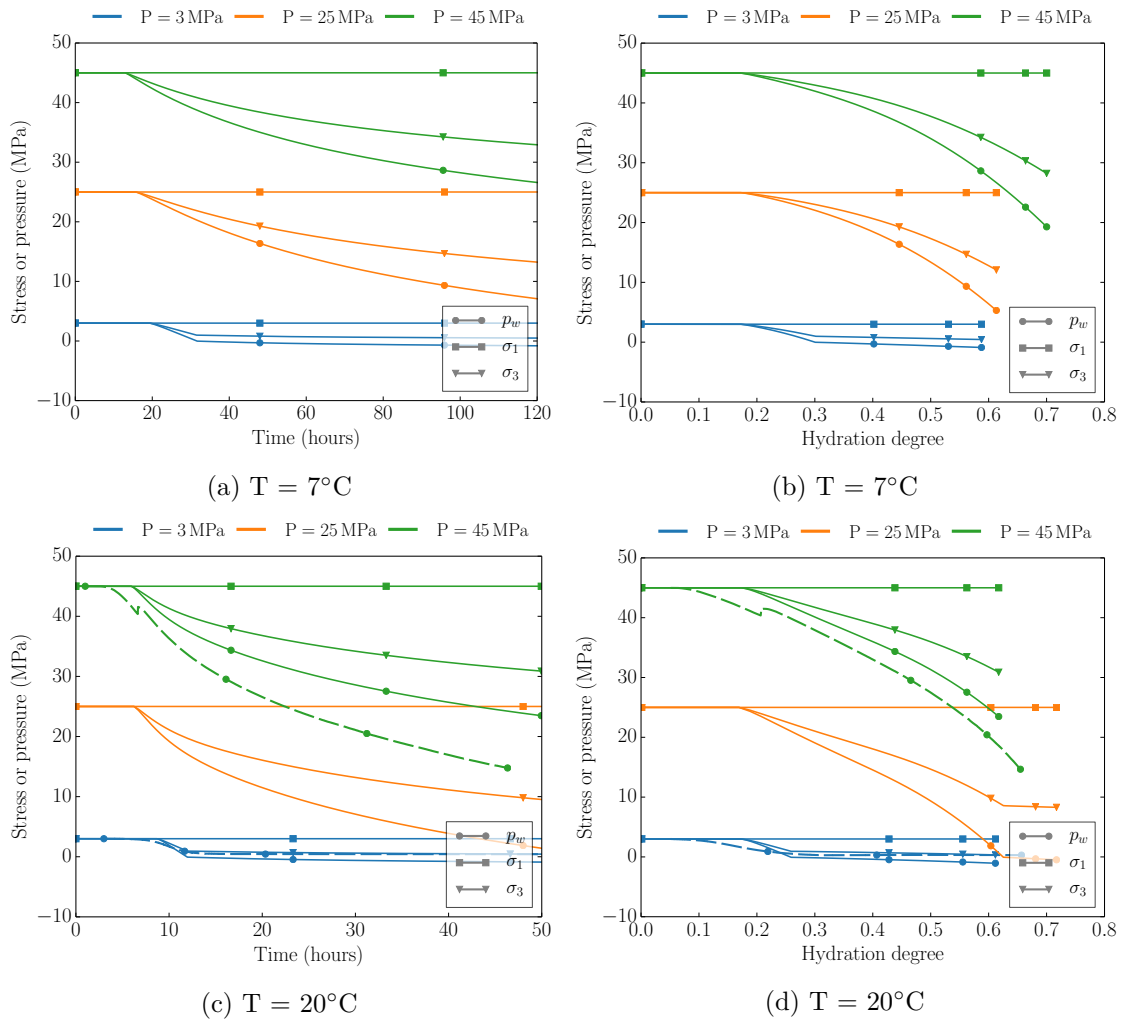
Figure 6.43: Pore pressure, axial and radial stresses as a function of time and hydration degree for multiple temperature and pressure conditions in oedometric STCA configuration.

(a) T = 7°C

(b) T = 7°C

(c) T = 20°C

(d) T = 20°C
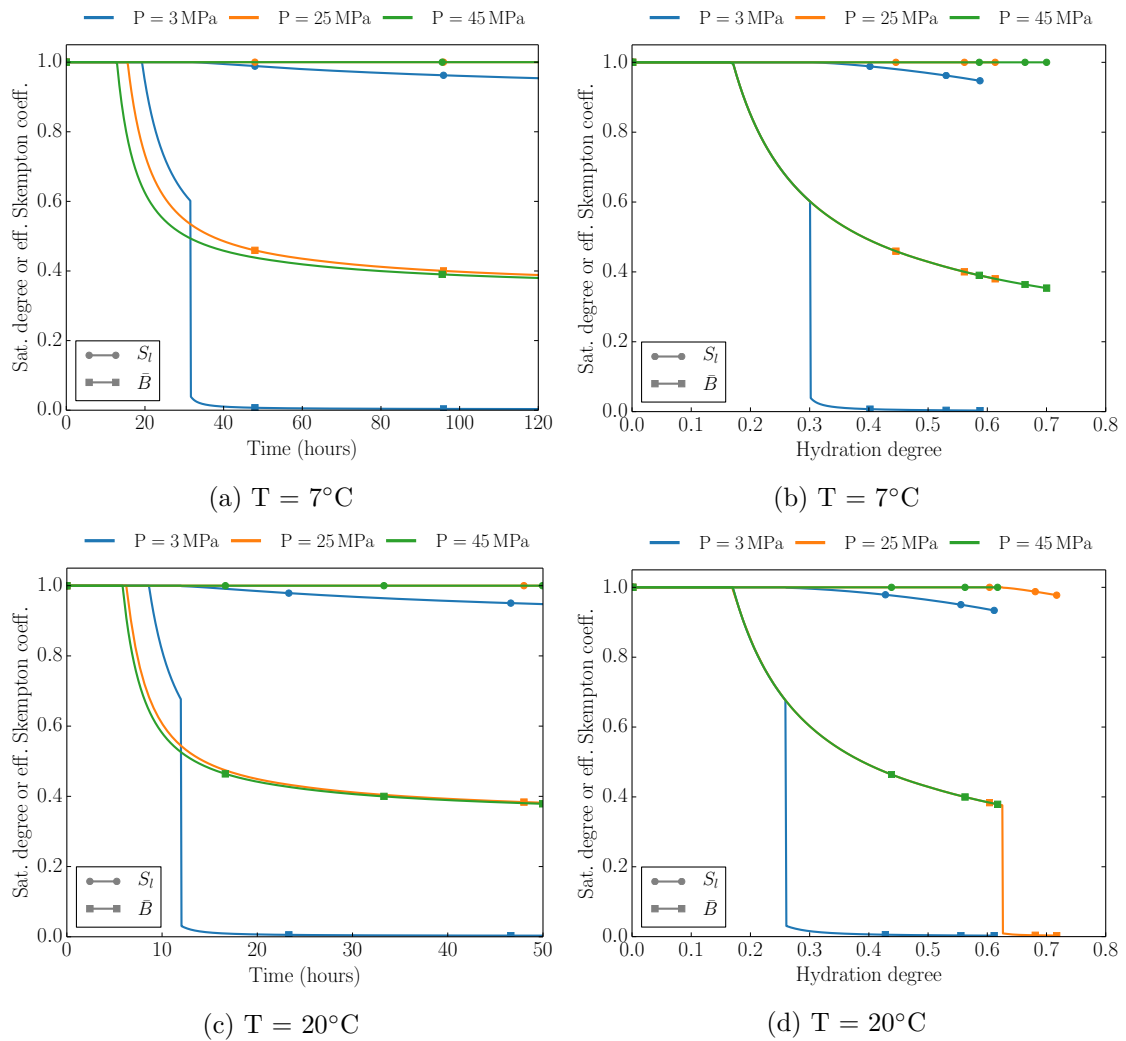
Figure 6.44: Saturation degree and effective Skempton coefficient as a function of time and hydration degree for multiple temperature and pressure conditions in oedometric STCA configuration.

6.8.2 Cyclic axial loading

The monotonous axial loading phase is followed by large loading cycles performed with the aim of probing the mechanical response of the cement paste and the effects of previous loading and temperature conditions on its long-term behaviour. The stress - strain response of all tests is presented in Figure 6.45.

The history of the specimen is clearly of major importance in the determination of the responses to loading. In no case is this more evident than for the tests at 7°C, in which a completely different response is observed depending on the previous history. For the lowest curing pressure, we observe a large strain plateau occurring at relatively low total stress, followed by a sharp increase in the stiffness. The response is entirely different for the intermediate curing pressure. Finally, at high pressure, the response is nearly reversible.
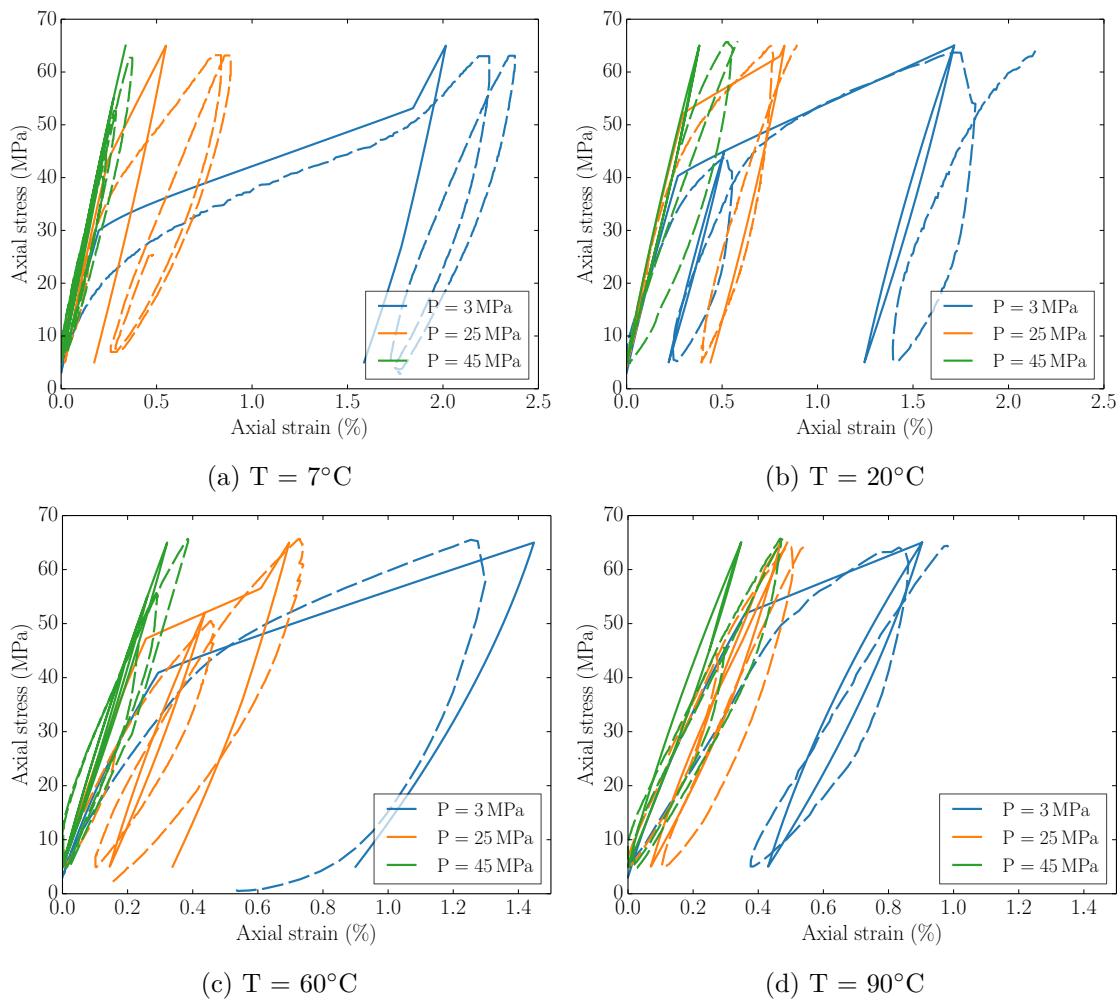
Figure 6.45: Stress-strain response of oedometric loading cycles. Cement pastes were hydrated under the indicated temperature and pressure conditions in oedometric STCA configuration. Solid lines correspond to model predictions, while dashed lines are experimental results.

The comparison of the experiments and the model results can be deemed acceptable. In all cases, the model succeeds in capturing the main features of the mechanical response of the material. The nature of the responses and their associated mechanisms will be made clear as we walk through the details underlying some of the most interesting simulation results.

The modelling results of the cyclic loading of the specimen cured at 7°C and 3 MPa (O - T7P3) is presented in Figure 6.46. All of the main components of the model actively intervene in the simulation. The initial stress state is of low mean and deviatoric stress, but a considerable desaturation, in the order of 95%, as shown in Figure 6.44. Three different regimes can be discerned according to the saturation state and the nature of strains:

- Partially saturated visco-elasticity

- Partially saturated visco-elasto-plasticity

- Saturated visco-elasto-plasticity

The strains are first purely viscoelastic in partially saturated state. At an axial stress in the order of 30 MPa, the yield surface is attained, and as a result, the plastic mechanism is activated. Partially-saturated plasticity yields very large plastic strains, of about 1.5%, until the porosity is sufficiently reduced as to re-saturate the pore space.

The saturation generates a drastic change in the plastic stiffness, causing plastic strains to increase at a much lower rate. In the loading path, the effect of the compacting plastic strains leads to a large increase in the pore pressure that results in a decrease of the total effective stress. Upon unloading, a large pore pressure hysteresis cycle is observed due to the residual plastic strains.

The radial stress at the beginning of the loading cycle is low, but remains positive (oedometric condition). The situation is different at lower curing pressures, in which case the specimen can detach from the walls of the oedometric cell and has to be considered in uniaxial state.

The comparison with the modelling results of the cyclic loading of the specimen cured at 20°C and 3 MPa (O - T20P3), presented in Figure 6.47, is very enriching. In this case, the axial loading up to 65 MPa is not sufficient to completely resaturate the pore space. This is due to the higher desaturation with respect to the previous case. Only partially-saturated behaviour is therefore observed throughout the loading cycles. This is confirmed by the experimentally-measured pore pressure, for which no increase was observed during the tests. The model successfully captures the behaviour of the material, including a part of the hysteresis loops associated with the viscosity of the material resulting from the multiple loading cycles.

Regarding intermediate pressures, the modelling of the cyclic loading of the specimen
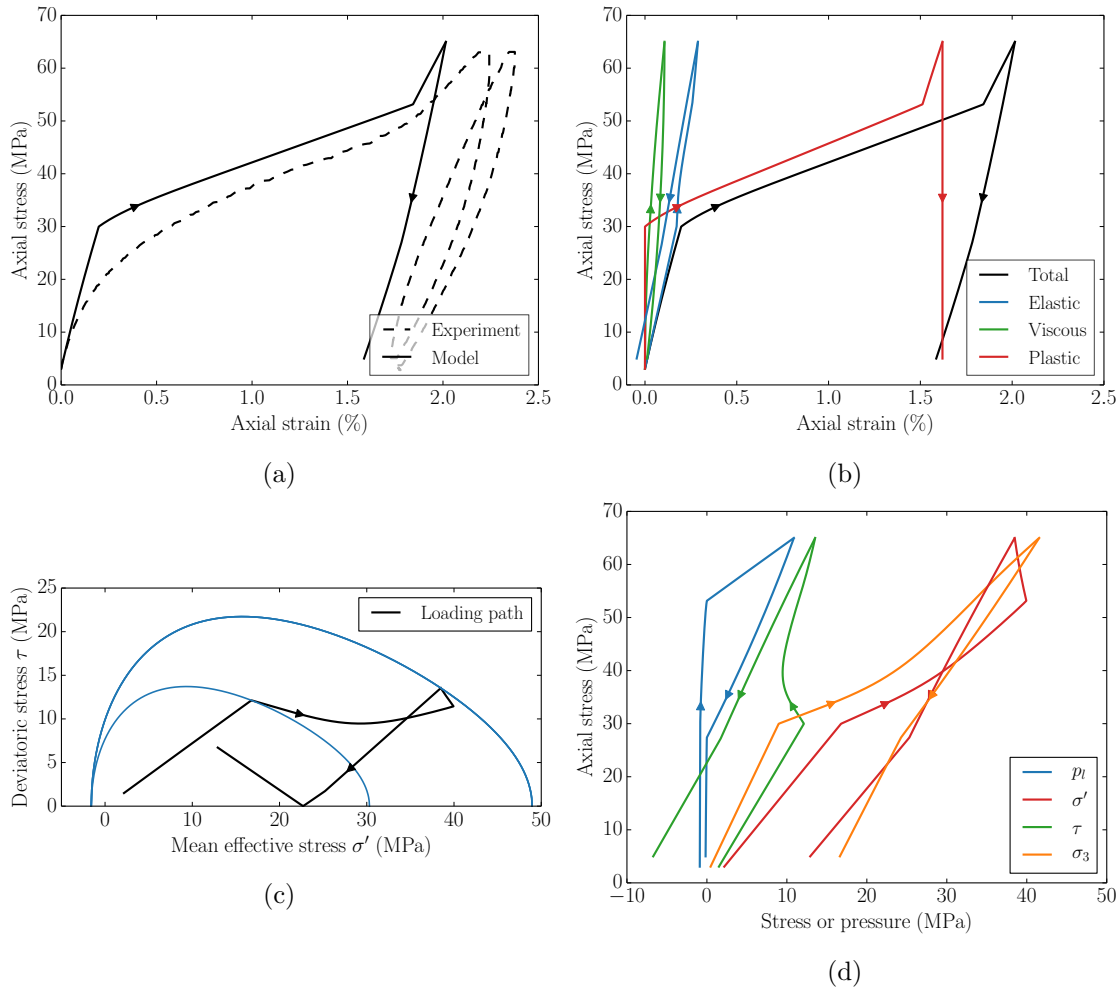
Figure 6.46: Simulation of the response to the cyclic loading for a specimen cured at 7°C and 3 MPa (O - T7P3): (a) axial stress and total strain (b) axial stress and strain decomposition (c) loading path and yield surface (d) stresses and fluid pressure. Solid lines correspond to model predictions, while dashed lines are the experimental results. Matched arrows correspond to the same state in all figures.

cured at 22°C and 25 MPa (O - T22P25) is presented in Figure 6.48. The simulations are again in reasonable agreement with the experiments. In this case, the model predicts the re-saturation of the material towards the end of the loading cycle.

Finally, concerning high curing pressures, we present the modelling results of the cyclic loading of the specimen cured at 20°C and 45 MPa (O - T20P45) in Figure 6.49. The result is completely different from the previous examples due to the total saturation of the material and the purely visco-elastic response. The experimental observations and the simulated response are in excellent agreement. Furthermore, we can note that the pore pressure evolution is fairly well captured by the model.
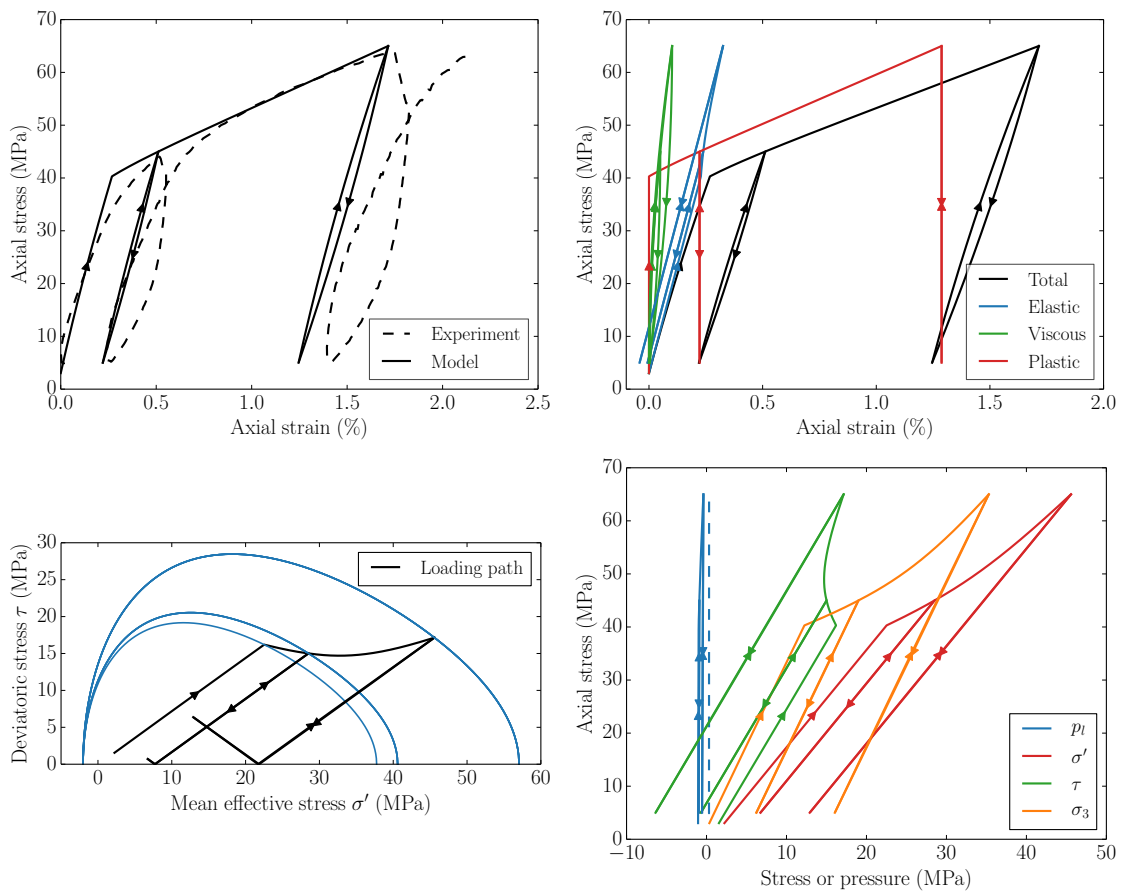
Figure 6.47: Simulation of the response to the cyclic loading for a specimen cured at 20°C and 3 MPa (O - T20P3): (a) axial stress and total strain (b) axial stress and strain decomposition (c) loading path and yield surface (d) stresses and fluid pressure. Solid lines correspond to model predictions, while dashed lines are the experimental results. Matched arrows correspond to the same state in all figures.
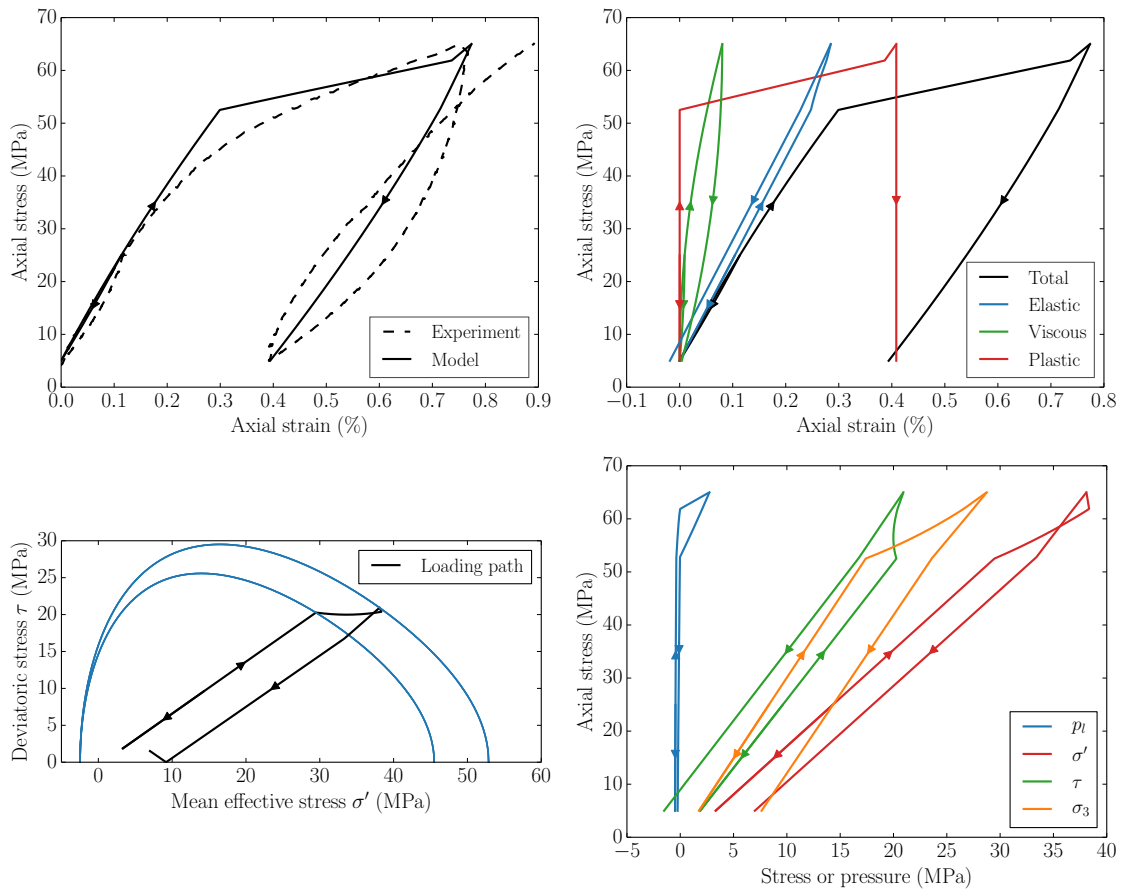
Figure 6.48: Simulation of the response to the cyclic loading for a specimen cured at 22°C and 25 MPa (O - T22P25): (a) axial stress and total strain (b) axial stress and strain decomposition (c) loading path and yield surface (d) stresses and fluid pressure. Solid lines correspond to model predictions, while dashed lines are the experimental results. Matched arrows correspond to the same state in all figures.
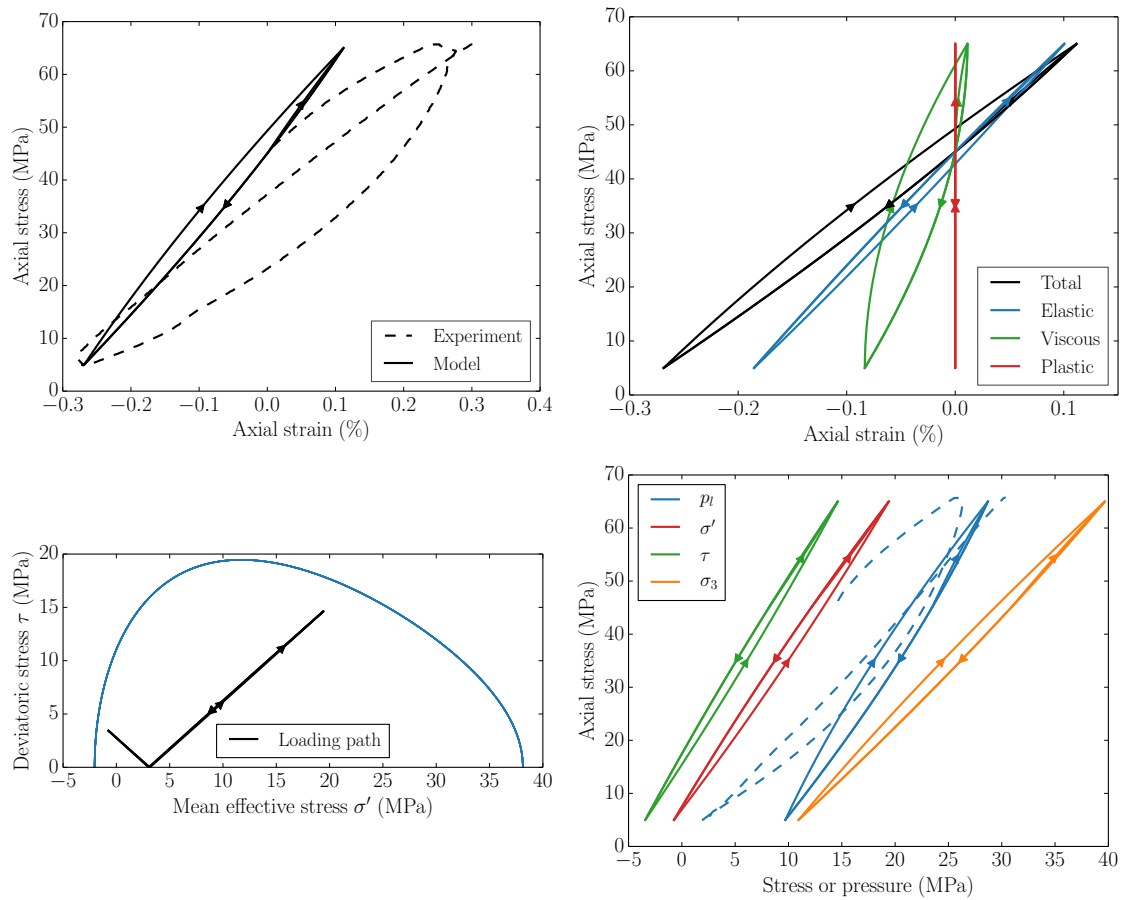
Figure 6.49: Simulation of the response to the cyclic loading for a specimen cured at 20°C and 45 MPa (O - T20P45): (a) axial stress and total strain (b) axial stress and strain decomposition (c) loading path and yield surface (d) stresses and fluid pressure. Solid lines correspond to model predictions, while dashed lines are the experimental results. Matched arrows correspond to the same state in all figures.

6.9   Conclusion

The experimental results presented in this chapter have served to thoroughly characterize the poromechanical properties and behaviour of a cement paste hydrating under different temperature and pressure conditions. The experiments combine a variety of techniques that allow us to probe the material in very different configurations.

From a series of experiments in a triaxial cell, a complete set of compatible poroelastic parameters has been determined for a mature cement paste hydrated at low temperatures.

The evolution of the poroelastic parameters with hydration has been characterized by uniaxial, UCA and STCA techniques. The experimental results show a good compatibility, despite the differences in techniques and test configurations. Acoustic and static experimental devices have been used to study the effect of temperature and pressure on the evolution and long term properties of the material. The effect of temperature is shown to be clearly dominating for the ranges we have examined. Pressure effects have consistently shown minor effects on macroscopic mechanical properties. The micromechanical poroelastic model predicts with good accuracy the observations stemming from experiments.

The constitutive model is evaluated in simulations of the results of mechanical loading experiments in the STCA oedometric configuration starting from the early stages of hydration under multiple temperatures, pressures and loading histories. The results show that the proposed model predicts with good accuracy the response of a hydrating cement paste when subjected to various loading paths from its early age. The importance of the loading history is outlined, as well as the need for the accurate determination of the effective stresses throughout the life of the material.

Chapter 7

Conclusions and Perspectives

7.1 General conclusions

The cement sheath, placed between the casing and the rock formation in oil, gas and geothermal wells, assures the vital role of zonal isolation, while guaranteeing well stability and protecting the steel casing from corrosion.

From its earliest age and during its lifetime, the cement sheath withstands a wide range of mechanical and thermal loadings that might span from below-zero temperatures to 250°C and from tens to hundreds of megapascals. These loadings can have a detrimental effect on the material performance and compromise the physical properties required to assure the proper fulfilment of the basic roles of the structure. Furthermore, the advent of sophisticated drilling and production technologies (e.g. hydraulic fracturing, steam injection, deepwater, high-pressure, high-temperature wells, and CO_2 sequestration) call into question the reliability of current industry standards, demanding further investigation of the material properties under such severe conditions. More than ever, the risk of integrity loss has to be properly assessed to avoid potential distressing scenarios.

These challenges call for robust numerical simulation tools to model the response of the cement sheath. In applications, therefore, it is essential to determine appropriate constitutive laws describing the evolution of the cement paste response spanning from the early to the advanced age in order to predict the behaviour of the structure. Furthermore, the history of loadings and the state of stress of the material can only be accounted for in a constitutive law integrating the material behaviour from its initial placing in the well.

The main objective of this thesis is to provide a comprehensive modelling framework for the mechanical behaviour of an oil well cement paste from its earliest age to its hardened state. The prediction of the performance of the material is based on a holistic approach integrating the progress of hydration reactions, the coupling between water consumption and strains, and the history of the applied loadings. The main findings and contributions

of the work can be identified according to our two modelling axes.

7.1.1   Hydration kinetics

Based on the classical notions of nucleation and growth models, a new general framework is proposed for the formulation of hydration models of cement-based materials. The formulation naturally introduces some of the most relevant parameters of cement paste mixtures, such as the cement powder composition, mass densities of the different phases, water to cement ratio, chemical shrinkage and hydrates properties.

The model considers the cement paste as a mixture of water and cement powder which, upon reaction, produce hydrates following a given stoichiometry. The hydrates nucleate on the boundaries and grow outwards isotropically, with a growth rate that transitions from boundary to diffusion control as the coating around the grains thickens. The reaction rate can be controlled by boundary growth, volume space constraints, nucleation site saturation, diffusion or limiting amounts of reactants. To the best knowledge of the authors, this constitutes one of the most complete, simple and physically intuitive models of its kind to feature such a wide range of mechanisms and a powerful tool for the analysis of the kinetics of cement hydration.

In addition, we successfully model the cement paste hydration kinetics at different curing conditions following a complementary approach based on chemical kinetic concepts. The model requires a simple mathematical expression coupling rates from activation theory (Arrhenius law) with conversion functions of solid-state kinetics.

Both temperature and pressure have the effect of increasing the reaction rates, although with different sensitivities. An average pressure increase in the order of 5 to 6 MPa is equivalent to a temperature increase of $1°C$. Temperature is therefore regarded as a far more critical parameter for both civil engineering and oil well practical applications.

The kinetic parameters agree with observations of the early hydration stages, where nucleation and growth is the rate-controlling mechanism. Later, other mechanisms might control the observed rate, among which we might consider the unavailability of reactants, lack of physical space and the tortuous microstructural diffusive barriers.

7.1.2   Poromechanical behaviour

We formulated a comprehensive hydro-chemo-mechanical constitutive model featuring the cement paste as a multi-phase chemically-active open porous medium. The model rests on basic physical laws, and the mechanisms involving dissipation sources (heat and mass transport, chemical reactions, viscous and plastic strains) have been formulated in strict respect of thermodynamic principles.

The model considers cement paste as a porous medium, chemically active, elastic, viscous,

plastic and conceivably partially saturated. Applications to the modelling of experiments performed on the material from its earliest age demonstrate the participation of each of the aforementioned mechanisms in the observed macroscopic behaviour of the material.

The experimental results characterize the mechanical properties and behaviour of a cement paste hydrating under different temperature and pressure conditions. The experiments combine a variety of techniques that allow us to probe the material in very different configurations.

From a series of experiments in a triaxial cell, a complete set of compatible poroelastic parameters has been determined for a mature cement paste hydrating at low temperatures (7 to 20°C). The evolution of the poroelastic parameters with hydration has been characterized by multiple techniques, with an excellent overall compatibility. Acoustic and static mechanical loading experimental devices have been used to study the effect of temperature and pressure on the evolution and long-term properties of the material. The effect of temperature is shown to be clearly dominating for the ranges we have examined. Pressure effects have consistently shown minor effects on macroscopic mechanical properties.

The model formulation relies on simple mechanical analogies. As a result, the model parameters have intuitive and clear physical meanings and their values reflect the intrinsic properties of the components of the cement paste skeleton. In consequence, these parameters can likely be extended to other compositions of cement paste with minimum modifications.

The constitutive model is evaluated in the simulations of the results of mechanical loading experiments in the STCA spanning from the early stages of hydration under multiple hydration conditions and loading histories. The results show that the proposed model predicts with good accuracy the response of a hydrating cement paste when subjected to various loading paths from its early age. The importance of the loading history is outlined, as well as the need for the accurate determination of the effective stresses throughout the life of the material.

7.2 Perspectives

The modelling of hydration kinetics based on elementary physical considerations provides a unique opportunity to gain insight on the relevant parameters that control the reaction. Subsequent efforts should be devoted to the description of the hydration kinetics of individual cement powder phases and the determination of their reaction parameters, with the ultimate objective of producing a predictive model capable of accounting for the effects of composition and curing conditions.

Advanced computational algorithms, such as neural networks or machine learning, also have an enormous potential to improve the predictive power of the current hydration modelling tools. Perhaps unsurprisingly, the consideration of additives, whose effects are

often not understood in detail, remains one of the main challenges for the modellers. These effects might also be addressed with similar computational techniques after collection of sufficient experimental data.

Regarding the poromechanical model, the consideration of viscoplastic strains for high loading stresses seems necessary to properly capture the important hysteresis cycles that characterize the material response. In addition, the consideration of damage and fracture mechanisms would contribute to add realism to the simulated behaviour of the material.

Among the avenues of future work, the implementation of the constitutive law in a robust field-scale simulation software, e.g. a finite element suite, is one of the foremost priorities. This would extend the modelling capabilities to more complex geometries, and ultimately allow the simulation of an oil well architecture, one of the main long-term ambitions of the ENPC-Total research project. It would constitute a powerful tool to answer compelling questions with immediate industrial applications. For instance, the knowledge of the history of loading for any given well could be considered and modelled to assess possible risks of integrity loss due to future planned loading schedules.

Concerning the experimental characterization techniques, experiments with different water to cement ratios would provide a simple mean to further test the solidification model hypothesis. In addition, the experiments in triaxial cells starting from the earliest age is a topic currently under development and will likely provide insightful information in the future. Also, the consideration of thermal cycles would provide complementary information necessary for the modelling of real oil well conditions.

Finally, the consideration of higher temperatures, above those considered in the present study, is necessary in some practical applications. In this regard, an experimental campaign and modelling tools are currently under development in the ANR THWellCement Project by S. Ghabezloo with the intention to assess the effect of temperatures up to 200°C.

Bibliography

[1] H. M. Jennings, Refinements to colloid model of C-S-H in cement: CM-II, Cement and Concrete Research 38 (3) (2008) 275–289.

[2] A. D. Blackie, The influence of PFA on the properties of structural concrete, in: Proceedings of the International Symposium on the use of PFA in concrete, Leeds University, England, 1982, pp. 14–16.

[3] J. J. Thomas, A new approach to modeling the nucleation and growth kinetics of tricalcium silicate hydration, Journal of the American Ceramic Society 90 (10) (2007) 3282–3288.

[4] X. Pang, C. Meyer, Modeling cement hydration by connecting a nucleation and growth mechanism with a diffusion mechanism. Part II: Portland cement paste hydration, Science and Engineering of Composite Materials 23 (6) (2016) 605–615.

[5] I. Carol, Z. P. Bažant, Viscoelasticity with Aging Caused by Solidification of Nonaging Constituent, Journal of Engineering Mechanics 119 (11) (1993) 2252–2269.

[6] Z. P. Bažant, S. Prasannan, Solidification Theory for Concrete Creep. II: Verification and Application, Journal of Engineering Mechanics 115 (8) (1989) 1704–1725.

[7] S. Ghabezloo, Association of macroscopic laboratory testing and micromechanics modelling for the evaluation of the poroelastic parameters of a hardened cement paste, Cement and Concrete Research 40 (8) (2010) 1197–1210.

[8] M. H. Vu, Effet des contraintes et de la température sur l'intégrité des ciments des puits pétroliers, Ph.D. thesis, Université Paris-Est (2013).

[9] X. Pang, W. Cuello Jimenez, B. J. Iverson, Hydration kinetics modeling of the effect of curing temperature and pressure on the heat evolution of oil well cement, Cement and Concrete Research 54 (2013) 69–76.

[10] P. Termkhajornkit, R. Barbarulo, Modeling the coupled effects of temperature and fineness of Portland cement on the hydration kinetics in cement paste, Cement and Concrete Research 42 (3) (2012) 526–538.

[11] U. Danielson, Heat of hydration of cement as affected by water-cement ratio, in: Proceedings of the 4th International Symposium on the Chemistry of Cement, Washington, 1962, pp. 519–526.

[12] V. Bonavetti, H. Donza, G. Menéndez, O. Cabrera, E. F. Irassar, Limestone filler cement in low w/c concrete: A rational use of energy, Cement and Concrete Research 33 (6) (2003) 865–871.

[13] L. Haar, NBS/NRC steam tables, CRC Press, 1984.

[14] N. Yavari, Effet de la temperature d'hydratation sur la microstructure et le comportement hydro-mecanique d'une pate de ciment, Tech. rep., Ecole des Ponts ParisTech (2011).

[15] S. Bahafid, A multi-technique investigation of the effect of hydration temperature on the microstructure and mechanical properties of cement paste, Ph.D. thesis, Université Paris-Est (2017).

[16] N. Agofack, Comportement des ciments pétroliers au jeune âge et intégrité des puits, Ph.D. thesis, Université Paris-Est (2015).

[17] E. B. Nelson, Well Cementing, Schlumberger Educational Services, 1990.

[18] S. Ghabezloo, Comportement thermo-poro-mécanique d'un ciment pétrolier, Ph.D. thesis, Ecole des Ponts ParisTech, France (2008).

[19] H. F. W. Taylor, Cement Chemistry, 2nd Edition, Thomas Telford, 1997.

[20] K. L. Scrivener, H. Van Damme, Construction Materials: From Innovation to Conservation, MRS Bulletin 29 (05) (2004) 308–313.

[21] API, SP 10A-1: Cements and Materials for Well Cementing, American Petroleum Institute, 2011.

[22] J. W. Bullard, H. M. Jennings, R. A. Livingston, A. Nonat, G. W. Scherer, J. S. Schweitzer, K. L. Scrivener, J. J. Thomas, Mechanisms of cement hydration, Cement and Concrete Research 41 (12) (2011) 1208–1223.

[23] S. Bahafid, S. Ghabezloo, M. Duc, P. F. Faure, J. Sulem, Effect of the hydration temperature on the microstructure of Class G cement: C-S-H composition and density, Cement and Concrete Research 95 (2017) 270–281.

[24] P. D. Tennis, H. M. Jennings, A model for two types of calcium silicate hydrate in the microstructure of Portland cement pastes, Cement and Concrete Research 30 (6) (2000) 855–863.

[25] D. P. Bentz, P. Lura, J. Roberts, Mixture proportioning for internal curing, Concrete International 27 (February) (2005) 35–40.

[26] H. M. Jennings, A model for the microstructure of calcium silicate hydrate in cement paste, Cement and Concrete Research 30 (1) (2000) 101–116.

[27] H. M. Jennings, J. J. Thomas, D. Rothstein, J. J. Chen, Cements as porous Materials, in: F. Schüth, K. S. W. Sing, J. Weitkamp (Eds.), Handbook of porous solids, Wiley-VCH Verlag GmbH, Weinheim, Germany, 2008, Ch. 6, pp. 2971–3028.

[28] T. C. Powers, Structure and Physical Properties of Hardened Portland Cement Paste, Journal of the American Ceramic Society 41 (1) (1958) 1–6.

[29] R. F. Feldman, P. J. Sereda, A model for hydrated Portland cement paste as deduced from sorption-length change and mechanical properties, Matériaux et Construction 1 (6) (1968) 509–520.

[30] A. J. Allen, J. J. Thomas, H. M. Jennings, Composition and density of nanoscale calcium-silicate-hydrate in cement., Nature materials 6 (4) (2007) 311–316.

[31] A. Muller, K. L. Scrivener, A. Gajewicz, P. J. McDonald, Densification of C–S–H measured by 1H NMR relaxometry, The Journal of Physical Chemistry C 117 (1) (2012) 403–412.

[32] R. J.-M. Pellenq, A. Kushima, R. Shahsavari, K. J. Van Vliet, M. J. Buehler, S. Yip, F.-J. Ulm, A realistic molecular model of cement hydrates, Proceedings of the National Academy of Sciences 106 (38) (2009) 16102–16107.

[33] H. M. Jennings, J. J. Thomas, J. S. Gevrenov, G. Constantinides, F.-J. Ulm, A multi-technique investigation of the nanoporosity of cement paste, Cement and Concrete Research 37 (3) (2007) 329–336.

[34] B. Pichler, C. Hellmich, J. Eberhardsteiner, Spherical and acicular representation of hydrates in a micromechanical model for cement paste: prediction of early-age elasticity and strength, Acta Mechanica 203 (3-4) (2008) 137–162.

[35] S. Ghabezloo, Effect of the variations of clinker composition on the poroelastic properties of hardened class G cement paste, Cement and Concrete Research 41 (8) (2011) 920–922.

[36] S. Ghabezloo, Micromechanics analysis of thermal expansion and thermal pressurization of a hardened cement paste, Cement and Concrete Research 41 (5) (2011) 520–532.

[37] K. Fuji, W. Kondo, Kinetics of the Hydration of Tricalcium Silicate, Journal of the American Ceramic Society 57 (11) (1974) 492–497.

[38] S. Bishnoi, K. L. Scrivener, uic: A new platform for modelling the hydration of cements, Cement and Concrete Research 39 (4) (2009) 266–274.

[39] J. W. Bullard, A determination of hydration mechanisms for tricalcium silicate using a kinetic cellular automaton model, Journal of the American Ceramic Society 91 (7) (2008) 2088–2097.

[40] R. Kondo, S. Ueda, Kinetics and Mechanisms of the Hydration of Cements, in: Proceedings of the Fifth International Congress on the Chemistry of Cements, Tokyo, 1968, pp. 203–248.

[41] P. Barnes, J. Bensted (Eds.), Structure and Performance of Cements, 2nd Edition, Spon Press, 2002.

[42] D. Damidot, A. Nonat, C3S hydration in diluted and stirred suspensions:(I) study of the two kinetic steps, Advances in Cement Research 6 (21) (1994) 27–36.

[43] S. Garrault, A. Nonat, Hydrated layer formation on tricalcium and dicalcium silicate surfaces: Experimental study and numerical simulations, Langmuir 17 (26) (2001) 8131–8138.

[44] P. Juilland, E. Gallucci, R. J. Flatt, K. L. Scrivener, Dissolution theory applied to the induction period in alite hydration, Cement and Concrete Research 40 (6) (2010) 831–844.

[45] J. J. Thomas, J. J. Biernacki, J. W. Bullard, S. Bishnoi, J. S. Dolado, G. W. Scherer, A. Luttge, Modeling and simulation of cement hydration kinetics and microstructure development, Cement and Concrete Research 41 (12) (2011) 1257–1278.

[46] K. L. Scrivener, P. Juilland, P. J. Monteiro, Advances in understanding hydration of Portland cement, Cement and Concrete Research 78 (2015) 38–56.

[47] A. Bezjak, I. Jelenić, On the determination of rate constants for hydration processes in cement pastes, Cement and Concrete Research 10 (1980) 553–563.

[48] L. J. Parrott, D. C. Killoh, Prediction of cement hydration, in: British Ceramic Proceedings, Vol. 35, London, 1984, pp. 41–53.

[49] R. Krstulović, P. Dabić, A conceptual model of the cement hydration process, Cement and Concrete Research 30 (5) (2000) 693–698.

[50] J. J. Biernacki, T. Xie, An advanced single particle model for C3S and alite hydration, Journal of the American Ceramic Society 94 (7) (2011) 2037–2047.

[51] K. van Breugel, Simulation of hydration and Formation of Structure in Hardening Cement-Based Materials, Ph.D. thesis, Delft University of Technology (1991).

[52] D. P. Bentz, Three-Dimensional Computer Simulation of Portland Cement Hydration and Microstructure Development, J. Am. Ceram. Soc. 80 (1) (1997) 3–21.

[53] J. W. Bullard, A Three-Dimensional Microstructural Model of Reactions and Transport in Aqueous Mineral Systems, Modell. Simul. Mater. Sci. Eng. 15 (2007) 711–738.

[54] S. Bishnoi, K. L. Scrivener, Studying nucleation and growth kinetics of alite hydration using μic, Cement and Concrete Research 39 (10) (2009) 849–860.

[55] W. A. Johnson, R. F. Mehl, Reaction kinetics in processes of nucleation and growth, Transactions of the American Institute of Mining & Metallurgical Engineers 135 (1939) 416–458.

[56] M. Avrami, Kinetics of phase change. I General Theory, The Journal of Chemical Physics 7 (12) (1939) 1103–1112.

[57] A. Kolmogorov, Statistical theory of crystallization of metals, Bull. Acad. Sci. USSR. Div. Chem. Sci. 3 (1937) 355–359.

[58] J. W. Cahn, The kinetics of grain boundary nucleated reactions, Acta Metallurgica 4 (5) (1956) 449–459.

[59] J. Christian, The Theory of Transformations in Metals and Alloys. Part I, Pergamon, 2002.

[60] A. J. Allen, J. C. McLaughlin, D. A. Neumann, R. A. Livingston, In Situ Quasi-Elastic Scattering Characterization of Particle Size Effects on the Hydration of Tricalcium Silicate, J. Mater. Res. 19 (11) (2004) 3242–3254.

[61] R. Berliner, M. Popovici, K. Herwig, M. Berliner, H. M. Jennings, J. J. Thomas, Quasielastic Neutron Scattering Study of the Effect of Water-to-Cement Ratio on the Hydration Kinetics of Tricalcium Silicate, Cement and Concrete Research 28 (2) (1998) 231–243.

[62] J. Zhang, E. A. Weissinger, S. Peethamparan, G. W. Scherer, Early hydration and setting of oil well cement, Cement and Concrete Research 40 (7) (2010) 1023–1033.

[63] A. Bazzoni, Study of early hydration mechanisms of cement by means of electron microscopy, Ph.D. thesis, École Polytechnique Fédérale de Lausanne (2014).

[64] M. Brown, D. Dollimore, A. K. Galwey, Chapter 3: Theory of Solid State Reaction Kinetics, in: C. H. Bamford, C. F. H. Tipper (Eds.), Comprehensive Chemical Kinetics: Reactions in the solid state, Vol. 22, Elsevier, 1980, pp. 41–113.

[65] J. L. Provis, On the use of the Jander equation in cement hydration modelling, RILEM Technical Letters 1 (2016) 62.

[66] Z. P. Bažant, S. Prasannan, Solidification Theory for Concrete Creep—I. Formulation, Journal of Engineering Mechanics 115 (8) (1990) 1691–1703.

[67] Z. P. Bažant, Creep and Damage in Concrete, in: J. Skalny, S. Mindess (Eds.), Material Science of Concrete IV, American Ceramic Society, 1995, pp. 355–389.

[68] Z. P. Bažant, Y. Xi, Continuous retardation spectrum for solidification theory of aging creep of concrete, Journal of Engineering Materials and Technology, Transactions of the ASME 121 (2) (1995) 281–288.

[69] V. Šmilauer, Z. P. Bažant, Identification of viscoelastic C-S-H behavior in mature cement paste by FFT-based homogenization method, Cement and Concrete Research 40 (2) (2010) 197–207.

[70] M. Vandamme, F.-J. Ulm, Nanoindentation investigation of creep properties of calcium silicate hydrates, Cement and Concrete Research 52 (2013) 38–52.

[71] M. A. Biot, Theory of Propagation of Elastic Waves in a Fluid-Saturated Porous Solid. I. Low-Frequency Range, The Journal of the Acoustical Society of America 28 (2) (1956) 168.

[72] M. A. Biot, Theory of Propagation of Elastic Waves in a Fluid-Saturated Porous Solid. II. Higher Frequency Range, The Journal of the Acoustical Society of America 28 (2) (1956) 179.

[73] F.-J. Ulm, G. Constantinides, F. H. Heukamp, Is concrete a poromechanics material?—A multiscale investigation of poroelastic properties, Materials and structures 37 (February) (2004) 43–58.

[74] S. Ghabezloo, J. Sulem, S. Guédon, F. Martineau, J. Saint-Marc, Poromechanical behaviour of hardened cement paste under isotropic loading, Cement and Concrete Research 38 (12) (2008) 1424–1437.

[75] S. Ghabezloo, J. Sulem, J. Saint-Marc, The effect of undrained heating on a fluid-saturated hardened cement paste, Cement and Concrete Research 39 (1) (2009) 54–64.

[76] J. Sanahuja, L. Dormieux, G. Chanvillard, Modelling elasticity of a hydrating cement paste, Cement and Concrete Research 37 (10) (2007) 1427–1439.

[77] S. Ghabezloo, Multiscale Modeling of the Poroelastic Properties of Various Oil-Well Cement Pastes, Journal of Multiscale Modelling 2 (3-4) (2010) 199–215.

[78] F.-J. Ulm, O. Coussy, Modeling of Thermochemomechanical Couplings of Concrete at Early Ages, Journal of Engineering Mechanics 121 (7) (1995) 785–794.

[79] F.-J. Ulm, O. Coussy, Strength Growth as Chemo-Plastic Hardening in Early Age Concrete, Journal of Engineering Mechanics 122 (12) (1996) 1123–1132.

[80] O. Coussy, F.-J. Ulm, Creep and plasticity due to chemo-mechanical couplings, Archive of Applied Mechanics 66 (8) (1996) 523–535.

[81] D. Gawin, F. Pesavento, B. A. Schrefler, Hygro-thermo-chemo-mechanical modelling of concrete at early ages and beyond. Part II: Shrinkage and creep of concrete, International Journal for Numerical Methods in Engineering 67 (3) (2006) 299–331.

[82] D. Gawin, F. Pesavento, B. A. Schrefler, Hygro-thermo-chemo-mechanical modelling of concrete at early ages and beyond. Part I: Hydration and hygro-thermal phenomena, International Journal for Numerical Methods in Engineering 67 (3) (2006) 299–331.

[83] B. Lecampion, A macroscopic poromechanical model of cement hydration, European Journal of Environmental and Civil Engineering 17 (3) (2013) 176–201.

[84] C. Hua, P. Acker, A. Ehrlacher, Analyses and models of the autogenous shrinkage of hardening cement paste. I. Modelling at macroscopic scale, Cement and Concrete Research 25 (7) (1995) 1457–1468.

[85] M. Abuhaikal, Expansion and Shrinkage of Early Age Cementitious Materials Under Saturated Conditions: The Role of Colloidal Eigenstresses, Ph.D. thesis, Massachusetts Institute of Technology (2016).

[86] W. Hansen, Drying Shrinkage Mechanisms in Portland Cement Paste, Journal of the American Ceramic Society 70 (5) (1987) 323–328.

[87] O. M. Jensen, P. F. Hansen, Autogenous deformation and RH-change in perspective, Cement and Concrete Research 31 (12) (2001) 1859–1865.

[88] Z. P. Bažant, Prediction of concrete creep and shrinkage: past, present and future, Nuclear Engineering and Design 203 (2001) 27–38.

[89] P. Acker, Why Does Ultrahigh-Performance Concrete (UHPC) Exhibit Such Low Shrinkage and Such Low Creep?, ACI Special Publication (2004) 1–14.

[90] H. M. Jennings, J. W. Bullard, J. J. Thomas, J. E. Andrade, J. J. Chen, G. W. Scherer, Characterization and modeling of pores and surfaces in cement paste: correlations to processing and properties, Journal of Advanced Concrete Technology 6 (1) (2008) 5–29.

[91] R. J. Flatt, G. W. Scherer, J. W. Bullard, Why alite stops hydrating below 80% relative humidity, Cement and Concrete Research 41 (9) (2011) 987–992.

[92] API, RP 10B-2: Recommended Practice for Testing Well Cements, American Petroleum Institute, 2010.

[93] A. W. Bishop, D. J. Henkel, The Measurement of Soil Properties in the Triaxial Test, 2nd Edition, Edward Arnold Ltd, 1962.

[94] Y. Guéguen, M. Boutéca (Eds.), Mechanics of Fluid-Saturated Rocks, Elsevier Ltd, 2004.

[95] S. Ghabezloo, J. Sulem, Effect of the volume of the drainage system on the measurement of undrained thermo-poro-elastic parameters, International Journal of Rock Mechanics and Mining Sciences 47 (1) (2010) 60–68.

[96] P. P. Rao, D. L. Sutton, J. D. Childs, W. C. Cunningham, An Ultrasonic Device for Nondestructive Testing of Oilwell Cements at Elevated Temperatures and Pressures, Journal of Petroleum Technology 34 (11) (1982) 2611–2616.

[97] Chandler Engineering, Instruction Manual Model 4265-HT High Temperature UCA (2014).

[98] A. H. Smith, A. W. Lawson, The Velocity of Sound in Water as a Function of Temperature and Pressure, The Journal of Chemical Physics 22 (3) (1954) 351–359.

[99] K. L. Scrivener, R. Snellings, B. Lothenbach (Eds.), A Practical Guide to Microstructural Analysis of Cementitious Materials, CRC Press, Taylor & Francis Group, 2016.

[100] C. Gallé, Effect of drying on cement-based materials pore structure as identified by mercury intrusion porosimetry: a comparative study between oven-, vacuum-, and freeze-drying, Cement and Concrete Research 31 (2001) 1467–1477.

[101] J. Zhang, G. W. Scherer, Comparison of methods for arresting hydration of cement, Cement and Concrete Research 41 (10) (2011) 1024–1036.

[102] S. Diamond, Mercury porosimetry: an inappropriate method for the measurement of pore size distributions in cement-based materials, Cement and Concrete Research 30 (2000) 1517–1525.

[103] R. Ghofrani, H. Plack, CaO- and/or MgO-Swelling Cements: A Key for Providing a Better Annular Sealing?, Proceedings of SPE/IADC Drilling Conference (1993) 199–214.

[104] E. Gallucci, X. Zhang, K. L. Scrivener, Effect of temperature on the microstructure of calcium silicate hydrate (C-S-H), Cement and Concrete Research 53 (November) (2013) 185–195.

[105] J. J. Thomas, A. J. Allen, H. M. Jennings, Hydration Kinetics and Microstructure Development of Normal and CaCl2-Accelerated Tricalcium Silicate Pastes, The Journal of Physical Chemistry C 113 (46) (2009) 19836–19844.

[106] A. K. Schindler, K. J. Folliard, Heat of hydration models for cementitious materials, ACI Materials Journal 102 (1) (2005) 24–33.

[107] D. Gawin, M. Wyrzykowski, Modelling and experimental study of hydration for ordinary portland cement, Architecture Civil Engineering Environment 3 (2010) 45–54.

[108] J. Tritthart, F. Häußler, Pore solution analysis of cement pastes and nanostructural investigations of hydrated C3S, Cement and Concrete Research 33 (7) (2003) 1063–1070.

[109] G. W. Scherer, J. Zhang, J. J. Thomas, Nucleation and growth models for hydration of cement, Cement and Concrete Research 42 (7) (2012) 982–993.

[110] ASTM, C 1608 - 06: Standard Test Method for Chemical Shrinkage of Hydraulic Cement Paste (2008).

[111] ASTM, C 1679 - 08: Standard Practice for Measuring Hydration Kinetics of Hydraulic Cementitious Mixtures Using Isothermal Calorimetry (2009).

[112] R. H. Mills, Factors influencing cessation of hydration in water cured cement pastes, Tech. Rep. 90, Highway Research Board (1966).

[113] F. Lin, C. Meyer, Hydration kinetics modeling of Portland cement considering the effects of curing temperature and applied pressure, Cement and Concrete Research 39 (4) (2009) 255–265.

[114] K. A. Riding, J. L. Poole, K. J. Folliard, M. Juenger, A. K. Schindler, Modeling hydration of cementitious systems, ACI Materials Journal 109 (2) (2012) 225–234.

[115] S. Kirkpatrick, C. D. Gelatt, M. P. Vecchi, Optimization by Simulated Annealing, Science 220 (4598) (1983) 671–680.

[116] D. J. Wales, J. P. K. Doye, Global Optimization by Basin-Hopping and the Lowest Energy Structures of Lennard-Jones Clusters Containing up to 110 Atoms, The Journal of Physical Chemistry A 101 (28) (1997) 5111–5116.

[117] K. J. Laidler, Chemical Kinetics, 3rd Edition, Pearson, 1987.

[118] L. D'Aloia, G. Chanvillard, Determining the "apparent" activation energy of concrete Ea - numerical simulations of the heat of hydration of cement, Cement and Concrete Research 32 (8) (2002) 1277–1289.

[119] G. W. Scherer, G. P. Funkhouser, S. Peethamparan, Effect of pressure on early hydration of class H and white cement, Cement and Concrete Research 40 (6) (2010) 845–850.

[120] X. Pang, D. P. Bentz, C. Meyer, G. P. Funkhouser, R. Darbe, A comparison study of Portland cement hydration kinetics as measured by chemical shrinkage and isothermal calorimetry, Cement and Concrete Composites 39 (2013) 23–32.

[121] S. Garrault, T. Behr, A. Nonat, Formation of the C-S-H layer during early hydration of tricalcium silicate grains with different sizes, Journal of Physical Chemistry B 110 (1) (2006) 270–275.

[122] B. Lothenbach, K. L. Scrivener, R. D. Hooton, Supplementary cementitious materials, Cement and Concrete Research 41 (12) (2011) 1244–1256.

[123] M. Wyrzykowski, P. Lura, Effect of relative humidity decrease due to self-desiccation on the hydration kinetics of cement, Cement and Concrete Research 85 (2016) 75–81.

[124] X. Pang, C. Meyer, Modeling cement hydration by connecting a nucleation and growth mechanism with a diffusion mechanism. Part I: C3S hydration in dilute suspensions, Science and Engineering of Composite Materials 23 (3) (2014) 345–356.

[125] A. Kumar, S. Bishnoi, K. L. Scrivener, Modelling early age hydration kinetics of alite, Cement and Concrete Research 42 (7) (2012) 903–918.

[126] J. W. Bullard, G. W. Scherer, J. J. Thomas, Time dependent driving forces and the kinetics of tricalcium silicate hydration, Cement and Concrete Research 74 (2015) 26–34.

[127] M. M. Costoya Fernandez, Effect of Particle Size on the Hydration Kinetics and Microstructural Development of Tricalcium Silicate, Ph.D. thesis, École Polytechnique Fédérale de Lausanne (2008).

[128] P. Šimon, Isoconversional methods, Journal of Thermal Analysis and Calorimetry 76 (1) (2004) 123–132.

[129] A. K. Schindler, Effect of temperature on hydration of cementitious materials, Materials Journal 101 (1) (2004) 72–81.

[130] J. L. Poole, Modeling temperature sensitivity and heat evolution of concrete, Ph.D. thesis, University of Texas at Austin (2007).

[131] A. Saul, Principles underlying the steam curing of concrete at atmospheric pressure, Magazine of Concrete Research 2 (6) (1951) 127–140.

[132] P. F. Hansen, J. Pedersen, Maturity computer for controlled curing and hardening of concrete, Nordic Beton 1 (1977) 19–34.

[133] A. K. Galwey, M. E. Brown, Application of the Arrhenius equation to solid state kinetics: can this be justified?, Thermochimica Acta 386 (1) (2002) 91–98.

[134] K. O. Kjellsen, R. J. Detwiler, O. E. Gjørv, Development of microstructures in plain cement pastes hydrated at different temperatures, Cement and Concrete Research 21 (1) (1991) 179–189.

[135] J. J. Thomas, The instantaneous apparent activation energy of cement hydration measured using a novel calorimetry-based method, Journal of the American Ceramic Society 95 (10) (2012) 3291–3296.

[136] J. Šesták, G. Berggren, Study of the kinetics of the mechanism of solid-state reactions at increasing temperatures, Thermochimica Acta 3 (1) (1971) 1–12.

[137] A. Khawam, D. R. Flanagan, Solid-state kinetic models: basics and mathematical fundamentals, Journal of Physical Chemistry B 110 (35) (2006) 17315–17328.

[138] X. Pang, C. Meyer, R. Darbe, G. P. Funkhouser, Modeling the effect of curing temperature and pressure on cement hydration kinetics, ACI Materials Journal 110 (2) (2013) 137–148.

[139] B. Bresson, F. Meducin, H. Zanni, C. Noik, Hydration of tricalcium silicate (C3S) at high temperature and high pressure, Journal of Materials Science 37 (24) (2002) 5355–5365.

[140] K. J. Krakowiak, J. J. Thomas, S. Musso, S. James, A. T. Akono, F.-J. Ulm, Nano-chemo-mechanical signature of conventional oil-well cement systems: Effects of elevated temperature and curing time, Cement and Concrete Research 67 (2015) 103–121.

[141] P. W. Brown, J. M. Pommersheim, G. Frohnsdorff, A kinetic model for the hydration of tricalcium silicate, Cement and Concrete Research 15 (1) (1985) 35–41.

[142] B. Lothenbach, F. Winnefeld, Thermodynamic modelling of the hydration of Portland cement, Cement and Concrete Research 36 (2) (2006) 209–226.

[143] B. Lothenbach, T. Matschei, G. Möschner, F. P. Glasser, Thermodynamic modelling of the effect of temperature on the hydration and porosity of Portland cement, Cement and Concrete Research 38 (1) (2008) 1–18.

[144] O. Bernard, F.-J. Ulm, E. Lemarchand, A multiscale micromechanics-hydration model for the early-age elastic properties of cement-based materials, Cement and Concrete Research 33 (9) (2003) 1293–1309.

[145] S. Vyazovkin, Evaluation of Activation Energy of Thermally Stimulated Solid-State Reactions under Arbitrary Variation of Temperature, Journal of Computational Chemistry 18 (1997) 393–402.

[146] H. Ziegler, An introduction to thermomechanics, 2nd Edition, North-Holland, Amsterdan, 1983.

[147] O. Coussy, Poromechanics, John Wiley and Sons, 2004.

[148] R. Lewis, B. A. Schrefler, Finite Element Method in the Deformation and Consolidation of Porous Media, 2nd Edition, John Wiley & Sons, Ltd, 1998.

[149] B. A. Schrefler, Mechanics and thermodynamics of saturated/unsaturated porous materials and quantitative solutions, Applied Mechanics Reviews 55 (4) (2002) 351.

[150] L. A. Richards, Capillary conduction of liquids through porous mediums, Journal of Applied Physics 1 (5) (1931) 318–333.

[151] P. Atkins, J. de Paula, Physical Chemistry, eighth Edition, Oxford University Press, 2006.

[152] M. A. Biot, Thermodynamic principle of virtual dissipation and the dynamics of physical-chemical fluid mixtures including radiation pressure, Quarterly of Applied Mathematics 39 (4) (1982) 517–540.

[153] M. H. Vu, J. Sulem, S. Ghabezloo, J.-B. Laudet, A. Garnier, S. Guédon, Time-dependent behaviour of hardened cement paste under isotropic loading, Cement and Concrete Research 42 (6) (2012) 789–797.

[154] S. J. Gregg, K. S. W. Sing, Adsorption, Surface Area and Porosity, 2nd Edition, Academic Press, London, 1982.

[155] O. Coussy, Revisiting the constitutive equations of unsaturated porous solids using a Lagrangian saturation concept, International Journal for Numerical and Analytical Methods in Geomechanics 31 (15) (2007) 1675–1694.

[156] A. W. Bishop, G. E. Blight, Some Aspects of Effective Stress in Saturated and Partly Saturated Soils, Géotechnique 13 (3) (1963) 177–197.

[157] O. Coussy, P. Dangla, Approche énergétique du comportement des sols non saturés, Mécanique des sols non saturés (2002) 137–174.

[158] B. D. Coleman, M. E. Gurtin, Thermodynamics with Internal State Variables, The Journal of Chemical Physics 47 (2) (1967) 597–613.

[159] W. M. Cornelis, M. Khlosi, R. Hartmann, M. Van Meirvenne, B. De Vos, Comparison of Unimodal Analytical Expressions for the Soil-Water Retention Curve, Soil Science Society of America Journal 69 (6) (2005) 1902.

[160] M. T. van Genuchten, A Closed-form Equation for Predicting the Hydraulic Conductivity of Unsaturated Soils (1980).

[161] O. Coussy, P. Dangla, T. Lassabatère, V. Baroghel-Bouny, The equivalent pore pressure and the swelling and shrinkage of cement-based materials, Materials and Structures 37 (1) (2004) 15–20.

[162] C. Pichler, R. Lackner, H. A. Mang, Multiscale Model for Creep of Shotcrete - From Logarithmic-Type Viscous Behavior of CSH at the μm-Scale to Macroscopic Tunnel Analysis, Journal of Advanced Concrete Technology 6 (1) (2008) 91–110.

[163] G. W. Scherer, Drying, Shrinkage, and Cracking of Cementitious Materials, Transport in Porous Media 110 (2) (2015) 311–331.

[164] R. H. Brooks, A. T. Corey, Hydraulic properties of porous media, Tech. rep., Colorado State University (1964).

[165] I. F. Collins, The use of Legendre transformations in developing the constitutive laws of geomechanics from thermodynamic principles, IUTAM Symposium on Mechanics of Granular and Porous Materials (1997) 151–159.

[166] R. K. P. Zia, E. F. Redish, S. R. McKay, Making Sense of the Legendre Transform, Am. J. Phys 77 (7) (2009) 614–622.

[167] A. Zaoui, Matériaux hétérogènes et composites (2000).

[168] L. Dormieux, D. Kondo, F.-J. Ulm, Microporomechanics, John Wiley & Sons, Ltd, 2006.

[169] J. D. Eshelby, The Determination of the Elastic Field of an Ellipsoidal Inclusion, and Related Problems, Proceedings of the Royal Society A: Mathematical, Physical and Engineering Sciences 241 (1226) (1957) 376–396.

[170] K. Velez, S. Maximilien, D. Damidot, G. Fantozzi, F. Sorrentino, Determination by nanoindentation of elastic modulus and hardness of pure constituents of Portland cement clinker, Cement and Concrete Research 31 (4) (2001) 555–561.

[171] P. J. Monteiro, C. Chang, The elastic moduli of calcium hydroxide, Cement and Concrete Research 25 (8) (1995) 1605–1609.

[172] C. J. Haecker, E. J. Garboczi, J. W. Bullard, R. B. Bohn, Z. Sun, S. P. Shah, T. Voigt, Modeling the linear elastic properties of Portland cement paste, Cement and Concrete Research 35 (10) (2005) 1948–1960.

[173] B. Pichler, C. Hellmich, Upscaling quasi-brittle strength of cement paste and mortar: A multi-scale engineering mechanics model, Cement and Concrete Research 41 (5) (2011) 467–476.

[174] Z. P. Bažant, Material Models for Structural Creep Analysis, in: Z. P. Bažant (Ed.), Mathematical modeling of creep and shrinkage of concrete, John Wiley & Sons, Ltd, 1988, pp. 99–215.

[175] J. Salençon, Viscoélasticité pour le calcul des structures, Editions de l'Ecole Polytechnique, 2009.

[176] Z. P. Bažant, A. B. Hauggaard, S. Baweja, F.-J. Ulm, Microprestresses-Solidification Theory for Concrete Creep. I : Aging and Drying Effects, Journal of Engineering Mechanics 123 (11) (1997) 1188–1194.

[177] O. Coussy, A general theory of thermoporoelastoplasticity for saturated porous materials, Transport in Porous Media 4 (3) (1989) 281–293.

[178] I. Vardoulakis, J. Sulem, Bifurcation analysis in geomechanics, Blackie Academic & Professional, 1995.

[179] J. Sulem, I. Vardoulakis, E. Papamichos, A. Oulahna, J. Tronvoll, Elasto-plastic modelling of Red Wildmoor sandstone, Mechanics of Cohesive-Frictional Materials 4 (3) (1999) 215–245.

[180] G. A. Maugin, The thermomechanics of plasticity and fracture, Cambridge University Press, 1992.

[181] K. H. Roscoe, A. N. Schofield, C. P. Wroth, On The Yielding of Soils, Géotechnique 8 (1) (1958) 22–53.

[182] A. N. Schofield, C. P. Wroth, Critical State Soil Mechanics, Soil Use and Management 25 (3) (1968) 310.

[183] D. Drucker, Conventional and Unconventional Plastic Response and Representation, Applied Mechanics Reviews 41 (4) (1988) 151.

[184] G. T. Houlsby, A. M. Puzrin, Thermodynamics of porous continua, in: W. Wu, H. S. Yu (Eds.), Modern trends in geomechanics, Springer, Berlin, Heidelberg, 2006, pp. 39–60.

[185] F.-J. Ulm, O. Coussy, Mechanics and durability of solids. Volume 1, Prentice Hall,, 2003.

[186] O. Coussy, J.-M. Pereira, J. Vaunat, Revisiting the thermodynamics of hardening plasticity for unsaturated soils, Computers and Geotechnics 37 (1-2) (2010) 207–215.

[187] I. F. Collins, G. T. Houlsby, Application of thermomechanical principles to the modelling of geotechnical materials, Proceedings of the Royal Society A: Mathematical, Physical and Engineering Sciences 453 (1964) (1997) 1975–2001.

[188] S. Mindess, J. F. Young, D. Darwin, Concrete, Prentice Hall, 2003.

[189] T. Engel, P. Reid, W. Hehre, Physical Chemistry, 3rd Edition, Pearson, 2002.

[190] P. Lura, J. Couch, O. M. Jensen, J. Weiss, Early-age acoustic emission measurements in hydrating cement paste: Evidence for cavitation during solidification due to self-desiccation, Cement and Concrete Research 39 (10) (2009) 861–867.

[191] S. D. Lubetkin, Why is it much easier to nugleate gas bubbles than theory predicts?, Langmuir 19 (2003) 2575–2587.

[192] P. Lura, O. M. Jensen, K. van Breugel, Autogenous shrinkage in high-performance cement paste: An evaluation of basic mechanisms, Cement and Concrete Research 33 (2) (2003) 223–232.

[193] M. Taiebat, Y. F. Dafalias, Simple Yield Surface Expressions Appropriate for Soil Plasticity, International Journal of Geomechanics 10 (4) (2010) 161–169.

[194] S. Brunauer, R. Mikhail, E. Bodor, Some remarks about capillary condensation and pore structure analysis, Journal of Colloid and Interface Science 25 (3) (1967) 353–358.

[195] R. A. Cook, K. C. Hover, Mercury porosimetry of hardened cement pastes, Cement and Concrete Research 29 (6) (1999) 933–943.

[196] D. Windslow, S. Diamond, A Mercury Porosimetry Study of the Evolution of Porosity in Portland Cement : Technical Publication, Tech. Rep. 3, Joint Highway Research Project (1969).

[197] V. Baroghel-Bouny, Water vapour sorption experiments on hardened cementitious materials. Part I: Essential tool for analysis of hygral behaviour and its relation to pore structure, Cement and Concrete Research 37 (3) (2007) 414–437.

[198] J. M. de Burgh, S. J. Foster, H. R. Valipour, Prediction of water vapour sorption isotherms and microstructure of hardened Portland cement pastes, Cement and Concrete Research 81 (2016) 134–150.

[199] S. Prapaharan, A. G. Altschaeffl, B. J. Dempsey, Moisture Curve of Compacted Clay: Mercury Intrusion Method, Journal of Geotechnical Engineering 111 (9) (1985) 1139–1143.

[200] Y. Mualem, Hydraulic conductivity of unsaturated soils: prediction and formulas., Methods of soil analysis. Part 1. Physical and . . . 1 (31) (1986) 799–823.

[201] B. M. Savage, D. J. Janssen, Soil physics principles validated for use in predicting unsaturated moisture movement in portland cement concrete, ACI Materials Journal 94 (1) (1997) 63–70.

[202] V. Baroghel-Bouny, M. Mainguy, T. Lassabatère, O. Coussy, Characterization and identification of equilibrium and transfer moisture properties for ordinary and high-performance cementitious materials, Cement and Concrete Research 29 (8) (1999) 1225–1238.

[203] G. Pijaudier-Cabot, J.-M. Pereira (Eds.), Geomechanics in CO 2 Storage Facilities, John Wiley & Sons, Inc., Hoboken, NJ USA, 2013.

[204] L. Luckner, M. T. van Genuchten, D. R. Nielsen, A consistent set of parametric models for the two-phase flow of immiscible fluids in the subsurface, Water Resources Research 25 (10) (1989) 2187–2193.

[205] M. Thiercelin, C. Baumgarte, D. Guillot, A Soil Mechanics Approach To Predict Cement Sheath Behavior, in: SPE/ISRM Rock Mechanics in Petroleum Engineering, Vol. v, Society of Petroleum Engineers, 1998, pp. 329–337.

[206] S. Mindess, J. F. Young, F. Lawrence, Creep and drying shrinkage of calcium silicate pastes I. Specimen preparation and mechanical properties, Cement and Concrete Research 8 (5) (1978) 591–600.

[207] M. Irfan-Ul-Hassan, B. Pichler, R. Reihsner, C. Hellmich, Elastic and creep properties of young cement paste, as determined from hourly repeated minute-long quasi-static tests, Cement and Concrete Research 82 (2016) 36–49.

[208] C. M. Sayers, R. L. Grenfell, Ultrasonic propagation through hydrating cements, Ultrasonics 31 (3) (1993) 147–153.

[209] R. D'Angelo, T. J. Plona, L. M. Schwartz, P. Coveney, Ultrasonic measurements on hydrating cement slurries. Onset of shear wave propagation, Advanced Cement Based Materials 2 (1) (1995) 8–14.

[210] A. Boumiz, C. Vernet, F. Tenoudji, Mechanical Properties of Cement Pastes and Mortars at Early Ages Evolution with Time and Degree of Hydration, Advanced Cement Based Materials 3 (3-4) (1996) 94–106.

[211] Z. Sun, G. Ye, S. P. Shah, Microstructure and early-age properties of Portland cement paste - Effects of connectivity of solid phases, ACI Materials Journal 102 (2) (2005) 122–129.

[212] L. Pimienta, J. Fortin, Y. Guéguen, Bulk modulus dispersion and attenuation in sandstones, Geophysics 80 (2) (2015) D111–D127.